Modelling and Analysis of Isotropic Thermal Conductivity Enhancement in Laser Melting and Welding

This thesis is submitted for the degree of Doctor of Philosophy

LANCASTER UNIVERSITY

School of Engineering

February 2024

Gabriel Lau Sin Hock

Abstract

Gabriel Lau Sin Hock

Modelling and Analysis of Isotropic Thermal Conductivity Enhancement in Laser Melting and Welding.

This thesis investigates the feasibility of simplifying laser welding simulations by introducing isotropic thermal conductivity enhancement while omitting the phase change mechanism. The aim is to simplify models without compromising accuracy in predicting conduction-based, mixed-mode, and keyhole-based laser welding scenarios.

The universal model's development involves iterative comparisons between simulation data and extensive experiments conducted across a range of laser powers (200 W to 1200 W) and traverse speeds (10 mm/s to 34 mm/s). This dataset enables comprehensive calibration, refining the model through an understanding of melt pool formation in diverse laser melting processes.

By excluding phase change and fluid flow simulations, the model strikes a balance between accuracy and computational efficiency. It successfully predicts melt pool dimensions, proving its ability to streamline simulations without compromising essential predictive aspects.

The deliberate simplification, while resulting in a decrease in absolute accuracy, addresses the practical challenges associated with computational demands in traditional phase change simulations. This contributes to the field by providing a practical and efficient alternative for laser welding simulations.

In conclusion, this work culminates in the development of a universal model to predict various laser melting and welding scenarios. It offers a streamlined approach for practical implementation and offers valuable insights to enable optimisation of laser material processing techniques of this type.

Contents

List of Figures

List of Tables

Acknowledgement

I dedicated this thesis to my loving parents, whose unwavering support and boundless love have been my pillars of strength throughout this journey. Their encouragement and belief in me have fuelled my perseverance.

I would also like to express my deepest gratitude to my supervisor, Dr Andrew Pinkerton, for his exceptional patience, unwavering support, and invaluable guidance. His mentorship has played a pivotal role in shaping my academic endeavours during my PhD study.

Declaration

I hereby declare that no portion of the work presented in this thesis has been submitted in support of an application for another degree or qualification at this or any other education institute.

1. Introduction

1.1. Overview

The term “LASER” is an acronym for “Light Amplification by Stimulated Emission of Radiation”. It refers to a device that produces a beam of coherent and monochromatic electromagnetic radiation by the stimulated emission occurring repeatedly within an optical resonator. A laser can be turned into a versatile and controllable heat source by altering parameters such as the frequency, intensity, and focus of the beam.

As laser technology has developed, considerable research has been put into developing laser processing techniques, leading to a wide variety of manufacturing methods with diverse levels of precision and complexity. Some examples include selective laser melting [1, 2], laser deposition, laser welding, laser cutting, laser cladding, laser-assisted milling, laser peening, laser chemical vapor deposition (LCVD), and laser-induced forward transfer (LIFT).

This work focusses on the Laser Melting and Welding processes. In the laser surface melting process, a laser beam is directed onto the surface of the work piece (or substrate), resulting in selective heating and melting of the material. As the laser is switched off or directed away, the molten surface undergoes rapid cooling, forming a new microstructure; this (and thus the resultant surface properties) may be similar to or quite different from the original material. The process can be applied to metals, ceramics, composites and polymers, although is most widely used with metals, which is the focus in this work.

A closely related technique is laser welding. This uses the same melt-resolidify cycle but for a different purpose. By directing the laser beam along the edge of two substrate closely placed together, the heat energy is used to melt both materials, fusing them together after solidification [3]. Important parameters for success in the two processes are similar – crucially, extent of the melt pool during melting and re-solidification conditions.

1.2. Major challenges and objectives of this work

The overall aim of this work is to investigate the modelling of these processes, over the full range of possible input parameters. It aims to achieve this by a single method, namely considering the material to remain in solid state throughout and excluding fluid flow and phase change functions.

To achieve and demonstrate this successfully the following objectives must be achieved:

- Develop an initial numerical model using Ansys Mechanical APDL to simulate the laser surface melting process.

- Advance the model; maintain modelling accuracy by compensating for removed heat transfer pathways with increased conductivity, and in some cases new sources as functions of the input parameters. Enable the model to select and extract the result data needed for later comparison.
- Using an experimental laser rig, based on IPG YLS-2000-S2 laser and ABB robot, quantify beam parameters and beam absorption. Establish conduction, mixed-mode and keyhole welding process windows.
- Design more advanced models to simulate conduction, mixed-mode and keyhole welding within the established process windows. Explore novel anisotropic conductivity enhancement and mixed mode modelling approaches.

  Compare the modelled and measured weld results across different parameters within the process windows. Evaluate the effectiveness of the models and techniques and highlight areas for further work.

Note, these objectives will not be achieved sequentially as listed, Parallel experimental and modelling work will aid both and be more efficient.

1.3. Thesis structure

This thesis has a total of six chapters, which are arranged:

Chapter 1 provides an introduction to the topic and defines the aims and objectives of the work.

Chapter 2 presents a literature review of laser surface melting processes. The focus is on how process parameters affect the melting process and quality. The content is further divided into three sub-categories (energy delivery system, motion system, and end product's properties).

Chapter 3 details how the experiments are conducted. This includes details of the material and equipment used for production of the samples and analysis of them.

Chapter 5 focusses on conduction-based welding and surface melting. This chapter describes the development of enhanced-conductivity numerical simulation models for conduction-based laser melting. The chapter also includes experimental work, investigating how laser power and traverse speed effects the cross-sectional shape of the melt pool, and comparisons between the experimental and numerical simulations results.

Chapter 6 considers mixed-mode and keyhole-based welding. This chapter builds on Chapter 5 for the intermediate and final stages of a numerical simulation model for keyhole-based and mixed-mode laser melting. Further experimental work, considering the effect of primary input parameters on the cross-sectional shape of a keyhole melt pool., allows further comparison of data from experiment and simulation.

Chapter 7 presents the general conclusions for this research and the recommendations for future work.

2. Literature Review

2.1. Introduction

This chapter presents a review of laser melt pool processes. The following topics are covered:

- An introduction to the use of laser systems in the manufacturing and engineering field and where melt pool processes fall within that.
- Identification of process parameters crucial to the formation of a laser melt pool.
- Mechanism that governs the flow of material within the melt pool or otherwise influence its geometry on solidification.
- The post-laser melting attributes important for quality control.

2.2. Laser-based material processing techniques

There are a wide range of laser processes. The major differences between the technique are the amount of laser energy used, the state of the material (solid, molten or vaporised) after interacting with the laser beam, the level of penetration achieve by the laser, and whether material is removed, formed or added [4, 5]. Figure 1 gives one example of the way laser processes can be divided.

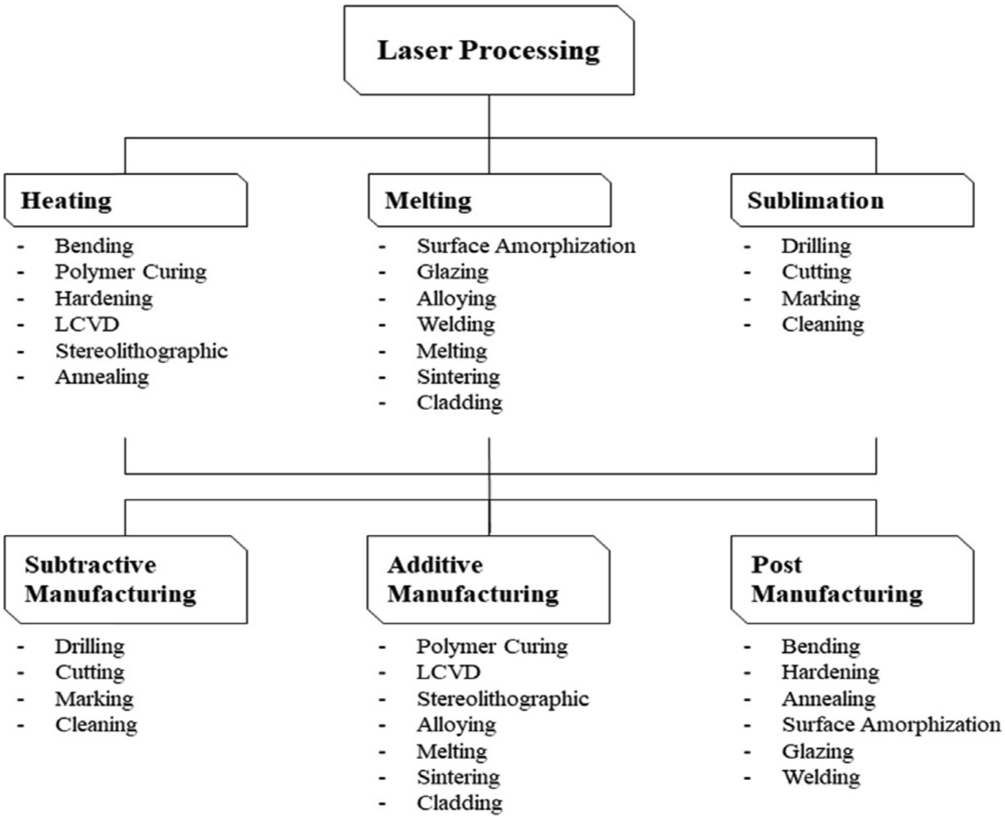

Figure 1 Spectrum of laser application in surface processing [6].

Figure 2 shows one method of categorizing laser manufacturing processes according to laser power density and interaction time. The melt pool processes that involve only melting lie in zone II and processes of Welding, Melting and Cladding are closely grouped so considered in more detail below. It must be remembered that processes are not single points as all can be performed with a range of parameters; for example, vaporisation becomes important in keyhole welding.

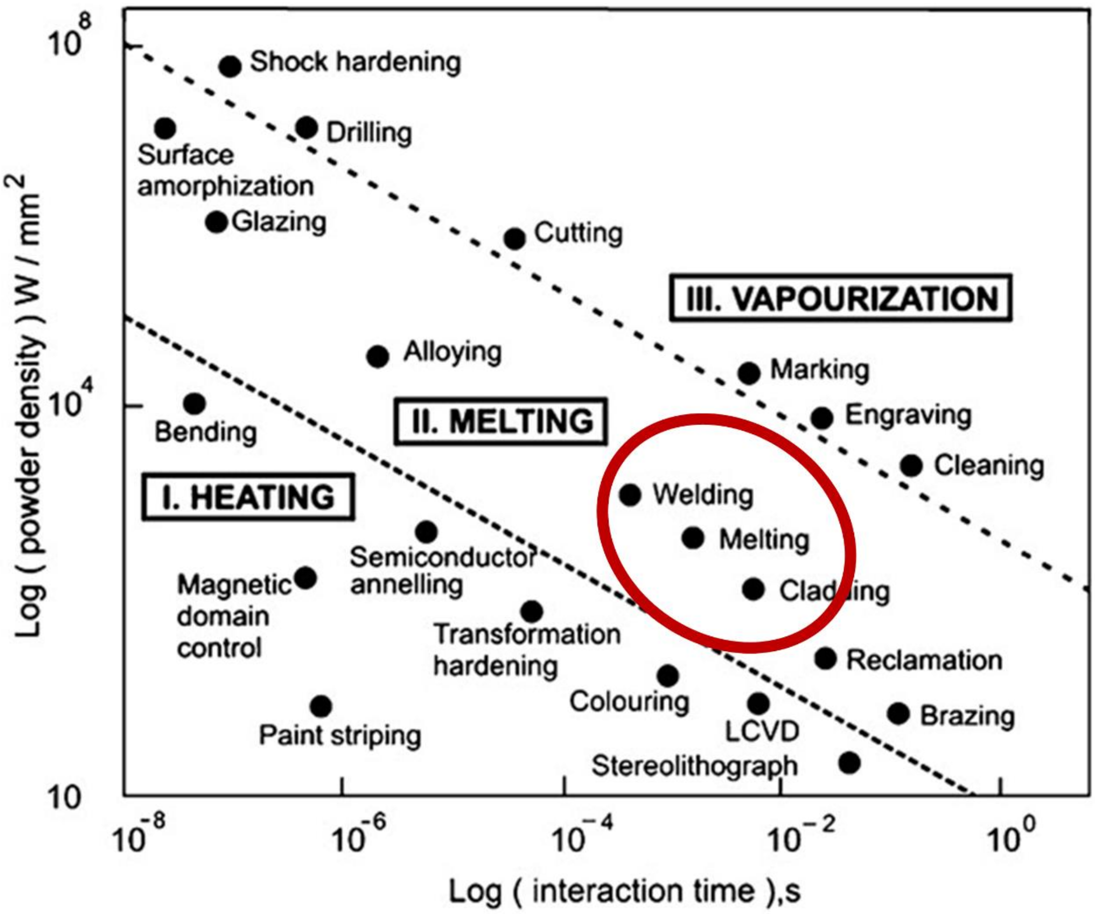

Figure 2. Schematic process map for different types of laser material processing [7].

2.2.1. Laser Cladding

Laser cladding, also known as a form of Laser Additive Manufacturing (LAM) or Directed Energy Deposition (DED), is a process that uses a laser as the primary heat source to add material to a substrate's surface, typically in powder or wire form. In this process, a nozzle delivers the material to the substrate surface, where it meets the focused laser beam. The intense energy of the laser instantly melts both the added material and a thin layer of the substrate, creating a molten pool. This simultaneous melting allows the added material to fuse with the substrate, forming a metallurgical bond upon solidification. Controlled by computer programming, the motion of the nozzle enables layer-by-layer deposition, which builds up a 3D structure or coating with precise control over thickness and material composition.

Several key process parameters play crucial roles in controlling the melting mechanism during the laser cladding process. These parameters include:

- Laser Intensity/Power: Determines the amount of energy available for melting the material.
- Laser Frequency: Affects the energy distribution and heat application rate on the substrate.
- Laser Modes: Influence the beam profile, impacting the shape and depth of the melt pool.
- Focal Point Positioning: The distance between both the laser focal point and the material focal point relative to the substrate surface impacts the efficiency and depth of melting.
- Mass Feed Rate: Controls the amount of material introduced into the melt pool, affecting layer thickness and uniformity.
- Nozzle Design and Feeding Methods: Optimise material delivery and interaction with the laser beam.
- Scanning Speed: Influences the cooling rate and shape of the molten pool.
- Ambient Atmosphere and Gas Flow: Helps control oxidation and stabilise the melt pool.

Careful selection and adjustment of these parameters are essential to ensure uniform cladding, minimise defects and enhance the final product's mechanical properties.

Here are the list of advantages of using LAM [8]:

- Able to manufacture parts with complex geometry [9]
- Able to use most material to create, repair and coat parts with different surface, mechanical and chemical properties [10-12].
- Flexible design space
- Low skill manufacturing
- Compact, portable manufacturing
- Less waste by-product. Possible of recycling and reconstituting by-products from LAM [13].
- Coating, cladding and 3D manufacturing are all possible [14-16].

A comprehensive discussion on laser-based additive manufacturing methods can be found in the book Additive Manufacturing for Designers by Elliott et al. [8]. This book provides insights into the history of additive manufacturing, its benefits, and standardization, as well as the materials used in the process. Additionally, Flemmer et al. [9] investigated Laser Metal Deposition and Computer-Aided Manufacturing (LMDCAM), highlighting how laser metal deposition can be integrated with computer-aided design systems to restore damaged components and directly manufacture complex geometries.

Dinda et al. [10] explored the microstructural evolution and thermal stability of Inconel 625 superalloy in laser deposition. Their findings show that Inconel 625 is an attractive material for laser cladding, as samples produced were free from defects such as cracks, bonding errors, and porosity. They concluded that directionally solidified components could be repaired or manufactured using direct metal deposition when appropriate processing strategies are followed. They also emphasised that consistent laser scanning direction is crucial for uniform microstructure formation across deposited layers.

Similarly, Pinkerton et al. [11] examined the feasibility of part repair using laser direct metal deposition and identified porosity formation as a major issue. Their study revealed that porosity severity increases with laser power and powder flow rate. Kamrani [12] provided a technological analysis of direct laser deposition methods, categorizing the process based on material feeding mechanisms, nozzle designs, material selection, surface hardness, crack formation, and treatment.

In terms of material efficiency and sustainability, Mahmood et al. [13] explored the reconsolidation of carbon steel machining swarf via laser metal deposition. They concluded that laser deposition can accommodate a wider range of particle geometries than previously considered, offering new possibilities for localised recycling. Further, Mahmood et al. [14] confirmed the viability of using low-cost Inconel 617 machining chips for laser surface modification, demonstrating the production of corrosion-resistant coatings.

Laser cladding has also been extensively studied for its impact on material properties. Qin et al. [15] investigated laser cladding of high Co-Ni secondary hardening steel on 18Cr2Ni4WA steel, revealing improved wear resistance and excellent metallurgical bonding. Their findings showed a gradual increase in microhardness from the substrate to the heat-affected zone, and then towards the laser-cladded coating. Likewise, Shishkovsky and Smurov [16] demonstrated the feasibility of synthesizing titanium nitride (TiN) coatings via 3D laser cladding in a nitrogen environment, producing coatings with high microhardness.

Material used in additive manufacturing exist in two primary forms: powder and wire. Wire material is usually fed through a nozzle during the manufacturing process, while powder material can be added in two distinct ways [17, 18]:

- Blown through a nozzle using an inert carrier gas;
- Preplaced as a layer of powder layer before the manufacturing (melting) process begins.

Despite the existence of various forms of material and feeding mechanism, both wire and powder feeding methods can coexist to achieve distinct manufacturing requirements simultaneously. This is frequently seen in surface coating and alloying processes, where materials with different compositions are used to create parts exhibiting diverse mechanical and chemical properties in different regions (functional grading). This approach allows for the achievement of location-specific properties, such as shape memory material or thermal reacting material [19-23].

Syed et al. [17] investigated a combined wire and powder feeding system for laser deposition. Their findings revealed that this hybrid process improved overall energy efficiency and surface finish quality while reducing porosity compared to powder deposition alone. Zhang et al. [18] further detailed laser metal deposition shaping systems, explaining their core sub-systems: energy supply, motion control, material delivery, and computer control.

The ability of laser cladding to create functionally graded materials (FGMs) is also well-documented. Syed et al. [19] successfully controlled composition gradients in nickel-copper FGMs by adjusting feed rates during the process. Similarly, Abioye et al. [20] showed that laser direct metal deposition could produce functionally graded structures with tailored thermal expansion properties. In a separate study, Abioye et al. [21] examined the microstructure of functionally graded Ni-Ti alloys, identifying the formation of NiTi and $NiTi_2$ phases, which varied in proportion depending on Ni powder feed rates.

Soodi and Masood [22] analysed the tensile strength of functionally graded and wafer-layered structures produced via laser direct metal deposition. They concluded that this technique is ideal for manufacturing complex structures with specific mechanical properties. Halani and Shin [23] explored the production of shape memory alloy nitinol via laser direct deposition, showing that the correct ratio of nickel and titanium powders, combined with optimal laser parameters and post-heat treatment, resulted in homogeneous, fully dense NiTi phases comparable to pre-alloyed nitinol powder.

After listing all the advantages of LAM technique, it isn't surprising to learn that the powder process in particular has been developed by multiple organisations since lasers were developed. Thus it is known by several names, including Laser Engineered Net Shaping (LENS), Direct Metal Deposition (DMD), Direct Light Fabrication (DLF) and Laser Deposition Welding (LDW) [24]. It is currently used in the medical field and space industries. This is mainly due to the portability and simplicity LAM provides and its ability to produce parts with complex geometry unlike most traditional manufacturing method [25, 26].

In space exploration, laser direct metal deposition has been proposed for in-situ fabrication of spare parts. Krantz et al. [25] explored its feasibility for space missions but identified challenges such as material feeding, vaporization, and heat dissipation in microgravity. Meanwhile, Vayre et al. [26] reviewed metallic additive manufacturing processes, categorizing them by raw material state (liquid, discrete particle, and solid sheet) and evaluating them based on quality, time, cost, and environmental impact.

A study by Pinkerton [24] focusing on the current status and potential future development of the lasers technology in manufacturing industries show how laser manufacturing methods is named and systematically categorised. In his papers, he also analysed the manufacturing market, barriers to addictive manufacturing, and the role of lasers in the future of manufacturing industry.

In conclusion, laser cladding is a versatile and widely researched additive manufacturing technique with significant advantages in material efficiency, component repair, and functionally graded material production. Ongoing research continues to refine its process parameters, expand material capabilities, and address existing challenges, ensuring its growing adoption in advanced manufacturing industries.

2.2.2. Laser Melting

Unlike the first group (LAM), this category of laser manufacturing does not involve the addition of materials during the process. Laser surface melting aims to modify the workpiece's surface through a melting-solidification process. After the laser passes over the material, the surface re-solidifies with a different microstructure, geometry, and, in some cases, altered elemental composition depending on the ambient atmosphere. This modification leads to changes in the material's surface properties [27].

Significant research efforts have been dedicated to improving the energy efficiency and final product quality of laser-induced melting processes. Several key process parameters have been identified as critical in controlling the melting and vaporization process:

- Laser path movement : The movement of the laser beam influences both the consistency of the keyhole depth and porosity formation within the melt track [28].
  Wu et al. [28] investigated high-frequency beam oscillation and its impact on keyhole dynamics in laser melting. Their findings indicate that an oscillating laser path results in a shallower but more stable keyhole due to a wider heat energy distribution, reducing porosity formation compared to a linear laser path.
- Process parameters : Laser power, scanning speed, and pulse duration play significant roles in determining the final microstructure and mechanical properties of the laser-treated surface [27],[29].
- Cui et al. [27] studied the microstructure and microhardness of hexagonal oxides formed after pulsed laser surface melting, finding that surface layer microhardness increases with laser treatment but gradually decreases as the distance from the laser spot centre increases. Similarly, Mallikarjuna et al. [29] examined the thermal behaviour of laser-processed titanium aluminide alloys and found that greater laser power and lower scanning speed lead to higher

maximum temperatures and deeper melt pools, directly influencing post-processing microhardness.

- Laser head offset and focal distance : The positioning of the laser beam in relation to the material surface affects weld quality, defect formation, and mechanical properties [30].

  Zhou et al. [30] investigated the influence of laser offset in the laser welding-brazing of dissimilar alloys. Their study revealed that shifting the laser beam toward one material side significantly affects microstructure formation, with defects such as cracks and lack of penetration occurring when the beam was offset toward the brass side instead of the Aluminium side. Additionally, they observed that shifting the laser beam from Aluminium to brass initially increased tensile strength before eventually decreasing.

- Substrate material properties and surface condition : The absorption efficiency of laser energy depends on the material's optical properties, surface roughness, and chemical composition [31].

  Wu et al. [31] studied laser ablation on different substrates and found that laser wavelength, initial surface roughness, and material composition are the primary factors affecting absorption efficiency. Their study concluded that rougher surfaces enhance laser absorption due to multiple reflections occurring on the material surface.

- Ambient atmosphere and/or gas flows : The presence and composition of shielding gases influence penetration depth, keyhole stability, and microstructure formation during laser melting [32-35].

  Shanmugarajan et al. [32] examined the effect of shielding gases on laser penetration depth, concluding that helium and nitrogen improve penetration, with nitrogen yielding slightly deeper penetration compared to helium. Xu et al. [33] investigated the effect of shielding gases on plasma plume behaviour in pulsed laser welding and found that a helium atmosphere enhances laser energy absorption by suppressing inverse bremsstrahlung absorption effects. They also observed that higher gas flow rates improve this suppression, leading to a more stable welding process. Miyagi and Wang [34] used in-situ X-ray imaging to study keyhole dynamics during laser melting of austenitic stainless steel, showing that keyhole depth fluctuates more in the absence of shielding gas and increases with laser defocus distance. Wang et al. [35] further analysed the effect of atmospheric composition on microstructure formation during the cooling process, particularly in press-hardened steel laser welding. Their findings showed that an argon atmosphere increased Aluminium content in δ-ferrite within the welded seam, reducing overall δ-ferrite formation compared to welding in normal air.

By carefully adjusting these parameters, laser melting processes can be optimised for improved material performance, enhanced surface properties, and reduced defect formation.

2.2.3. Laser Welding

Laser welding, unlike laser cladding (which involves material addition during the melting process) or laser surface melting (which typically affects only the surface), focuses on joining two or more workpieces through a deep melting and re-solidification process [5, 36, 37]. This process forms a robust metallurgical bond by creating a melt pool that penetrates the materials to the required depth, based on joint strength requirements and material thickness.

Key process parameters for laser welding include:

- Laser Path Movement: Controls the direction and pattern of the weld, affecting heat distribution and fusion quality [37, 38, 39].

  Tri et al. [37] investigated the oscillating laser welding process of Ti Grade 5 plates using a design of experiments (DoE) approach with the aim at developing empirical models to correlate the weld qualities with the process parameters. Jiang et al. [39] investigated the effect of oscillatory laser motion on the mixing zone of dissimilar substrates with different chemical compositions and the partial melting of strengthening phases in the weld. Their study showed that laser movement has a direct impact on the weld structure during solidification. Similarly, Tri et al. [38] explored the influence of processing parameters in laser welding using a beam oscillation method. Their work highlighted how oscillation affects joint properties and developed dependable models for evaluating the energy efficiency of both continuous-wave and pulsed laser welding processes.
- Laser Beam Characteristics: Parameters such as laser power, intensity, beam diameter, and focal point position directly influence the melt pool's depth, width, and stability [40-42].

  Ahsan et al. [40] conducted experimental investigations on porous structure fabrication using continuous and pulsed laser metal deposition. Their findings showed that different laser methods produce varying internal structures and that a range of part densities can be achieved by adjusting process parameters such as laser power and mass flow rate. Assunção and Williams [41] further supported this by showing that pulsed-wave lasers have higher spatial peak power density and greater penetration efficiency than continuous-wave lasers. However, they also found that when the laser-substrate interaction time exceeds 20 ms, penetration depth remains similar for both continuous-wave and pulsed-wave lasers.

- Scanning Speed: Affects the rate of energy application, influencing penetration depth, cooling rate, and heat-affected zone characteristics [42].

  Besnea et al. [42] studied laser welding of dissimilar materials, such as stainless steel and copper, and concluded that laser power and scanning speed (or laser interaction time) are critical parameters for achieving precision manufacturing.
- Laser Head Offset and Focal Distance: careful control of these parameters ensures optimum positioning of the laser beam focal plane relative to the surface for effective bonding and control of melt pool depth [43].

  Obratanski et al. [43] investigated the effect of laser focal positioning and beam incident angle on absorptivity. Their findings revealed that absorption efficiency increases as the laser focal point approaches the plate-pipe contact region, likely due to multiple reflections between the surfaces, enhancing energy absorption.
- Ambient Atmosphere and Gas Flow: All materials absorb and conduct heat differently, and surface conditions (e.g., cleanliness, roughness) affect the laser's interaction with the substrate [31, 43].

  The optical and geometric characteristics of the substrate significantly influence energy absorption, as showed in a study by Karmiris-Obratanski et al. [44]. Their research highlighted that material optical properties, laser beam characteristics, and surface geometry collectively determine how much laser energy is absorbed and how the melt pool is formed under the laser beam.

By carefully adjusting these parameters, laser welding can achieve a durable and high-quality joint, tailored for applications requiring strong bonds with minimal distortion. Additionally, precise variation of the process parameters allows control over the melt pool, enabling it to operate in either conduction-mode or keyhole-mode melting. This flexibility permits different levels of laser penetration, including the potential for full penetration, which produces a thorough weld covering the entire thickness of the material from top to bottom [44].

Details of the parameters mentioned are investigated and elaborated in the next section.

2.3. Process parameters

As mentioned earlier, processes do not in reality exist as a single point on the interaction-time vs intensity diagram. It is crucial to understand the relationship between the initial process parameters and the melt pool's mechanism to develop the analytical and numerical simulation models capable of explaining and predicting the formation of the melt pool during laser-based melting process, and how it affects the properties of the finished product [45, 46].

2.3.1. Laser wavelength

The choice of laser wavelength significantly influences the outcomes of laser welding and melting processes, as evidenced by recent studies. Rominger et al. [47] saw distinct melt-flow behaviours resulting from variations in laser radiation absorption properties on the surface of molten weld pools, emphasizing the dependence on wavelength and angle of incidence as shown in Figure 3. This variation serves as a fundamental distinction between different laser sources.

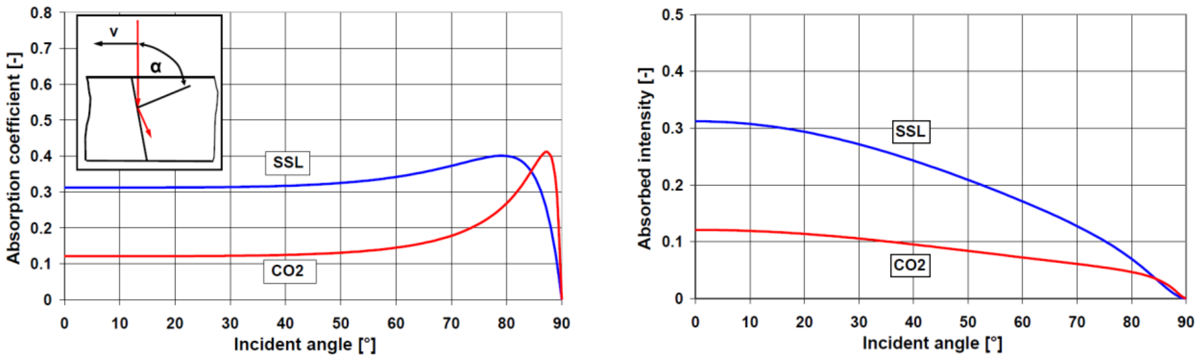

Figure 3. Absorption coefficient (left) and absorbed intensity (right) for iron at melting temperature [47].

Rudolf Weber et al. [48] highlighted the importance of angle of beam incidence, beam polarisation and scanning speed in industrial laser applications including cutting, welding and drilling. The different absorption characteristics of polarised beams in a cavity such as a keyhole were highlighted and test results showed that tangential polarisation of a laser with 1030nm wavelength can reduce spatter at lower welding speeds (<100 mm/s tested), although the effect of feed rate is more significant. Absorbed laser energy is a key factor in laser processing so understanding it is crucial for fine-tuning other parameters, such as laser power and scanning speed to achieve the best results. In one of their experiments investigating different polarization states of laser beams, they found that maximum cutting speeds are influenced by the magnitude and distribution of absorbed laser power. Consequently, to estimate achievable cutting velocities, it is necessary to determine the actual differences in absorbed laser power between different polarization states. This concept is also applicable to laser melting and welding processes.

Grabowski et al. [50] conducted a comprehensive investigation into the effects of electromagnetic laser radiation wavelengths on laser surface melting of metal matrix composites, specifically AlSi/SiC. Their analysis, using lasers with wavelengths of 0.808, 1.06, and 10.6 µm, elucidated the intricate interplay between optical absorption, reflectance, material composition and wavelength (Figure 4) and how these change with temperature (Figure 5). Particularly noteworthy was the observed jump in absorptivity during the solid to liquid transition, indicative of significant changes in energy absorption dynamics.

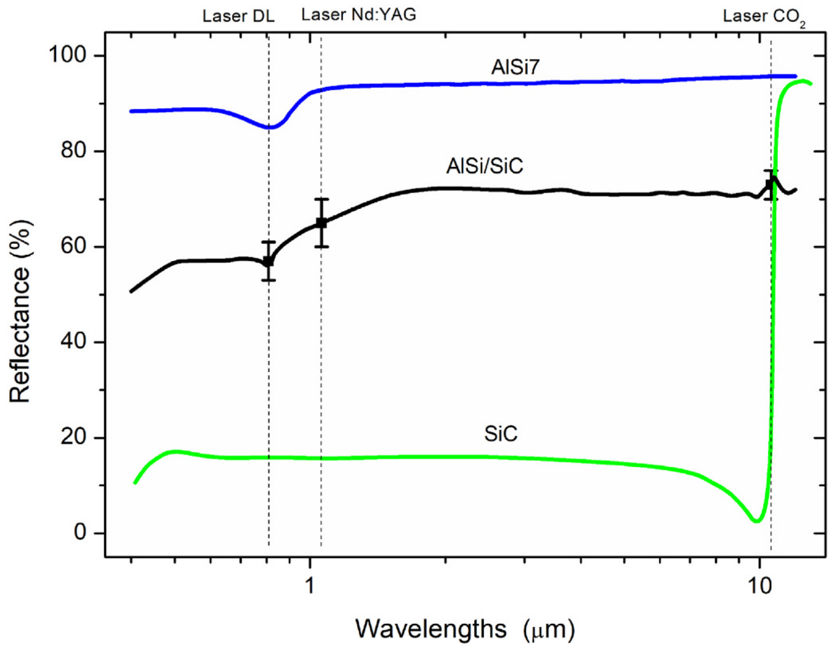

Figure 4. Reflectance of electromagnetic radiation as a function of wavelength for AlSi7, AlSi/SiC and SiC at room temperature (T = 293 K) [50].

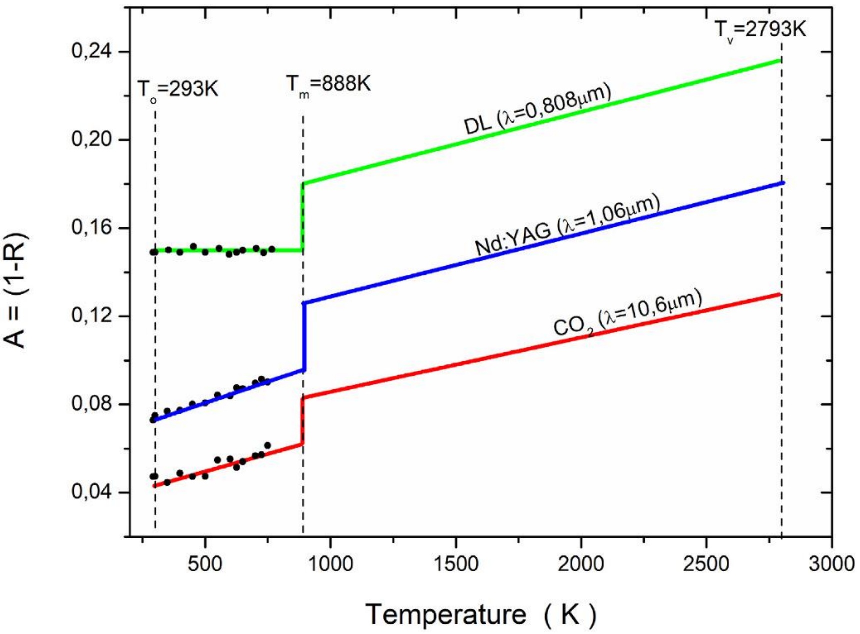

Figure 5. Absorptivity of AlSi7 for three electromagnetic wavelengths: 0.808 μm, 1.06 μm and 10.6 μm [50].

2.3.2. Pulsed vs continuous wave

Laser types, such as pulsed wave laser and continuous wave laser, show distinct characteristic and properties. These differences affect the formation of the melt pool and how material is melted and deposited onto the surface of a workpiece.

A study conducted by Assuncao and Williams [41] , which compares the effects of continuous wave and pulsed wave laser welding at the same power density, yielded the following findings:

- Pulse wave lasers have deeper weld penetration.
- Continuous wave lasers show a larger transition mode region.

Pulsed laser parameters can vary widely. For pulses in the millisecond range, Tzeng [51] found that pulse duration, average peak power density and speed were major factors affecting surface roughness with the longest pulse duration yielding the shallowest slumping between pulses.

For instance, a study investigating the effects of the type of laser on melt pool formation and the finishing quality of the final product reveals that the use of a pulsed laser results in a product with lower surface roughness. Another study by Kuo [52], used different ratios of continuous and pulsed beams to weld Inconel alloy and compare the relative influences of modes on the weld properties. They found a more pulsed wave allowed full penetration welds to be obtained at lower powers and higher speeds. Weld porosity decreased but weld spatter increased.

Another study comparing laser beams pulsed in the nanosecond range with ones in continuous beam mode was performed by Coroado et al. [53]. For the welding of stainless steel to Aluminium, it was found that the pulsed beam produced a lower heat-affected zone, more precise control of the heat input and high aspect ratio welds.

2.3.3. Beam geometry

In addition to the operational mode of the laser system, beam geometry also plays a crucial role, directly influencing the distribution of thermal energy across the workpiece surface interacting with the laser beam. Safdar et al. [54] conducted a study focusing on the numerical analysis of laser beam geometries during laser melting. They explored the impact of non-conventional beam geometry on melt pool characteristics in the laser melting of mild steel. Using a finite volume model, their study analysed various beam shapes, such as circular, rectangular, and diamond, showing the significant role of laser beam geometry in controlling temperature distribution across the workpiece. Different beam geometries resulted in distinct heat and cooling rates within the melt pool, influencing phase transformations and solidification cracking. For instance, the diamond beam exhibited the lowest heating rate and the highest cooling rate within the melt pool, making it suitable for applications requiring precise control over phase transformation and reduced solidification cracking.

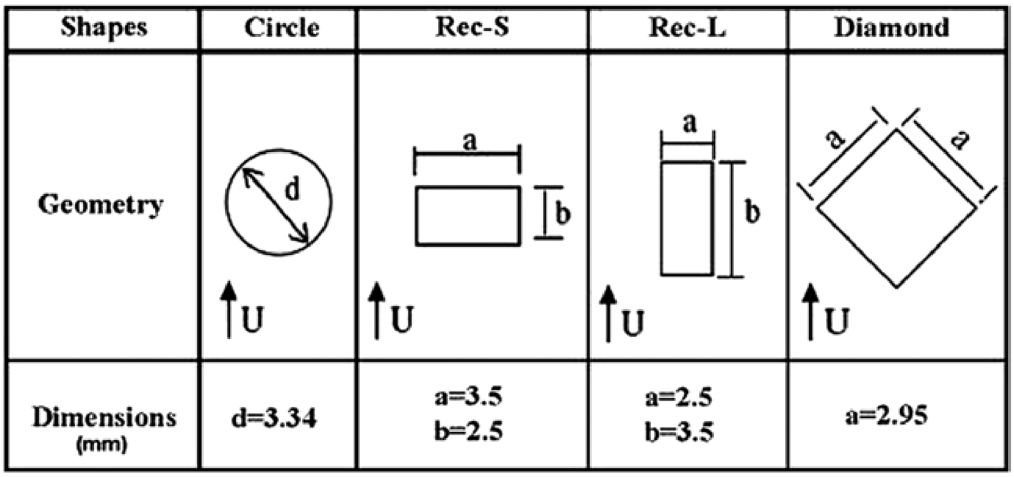

Figure 6. Laser beam geometries [54].

Additionally, Sheikh and Li [55] provided a review of non-conventional laser beam geometries used to improve and optimise laser material processes across various applications. They highlighted methods for modifying beam geometry, such as beam integrators and diffractive optical elements, and simulated five different beam shapes, including circular, rectangular, and triangular shapes.

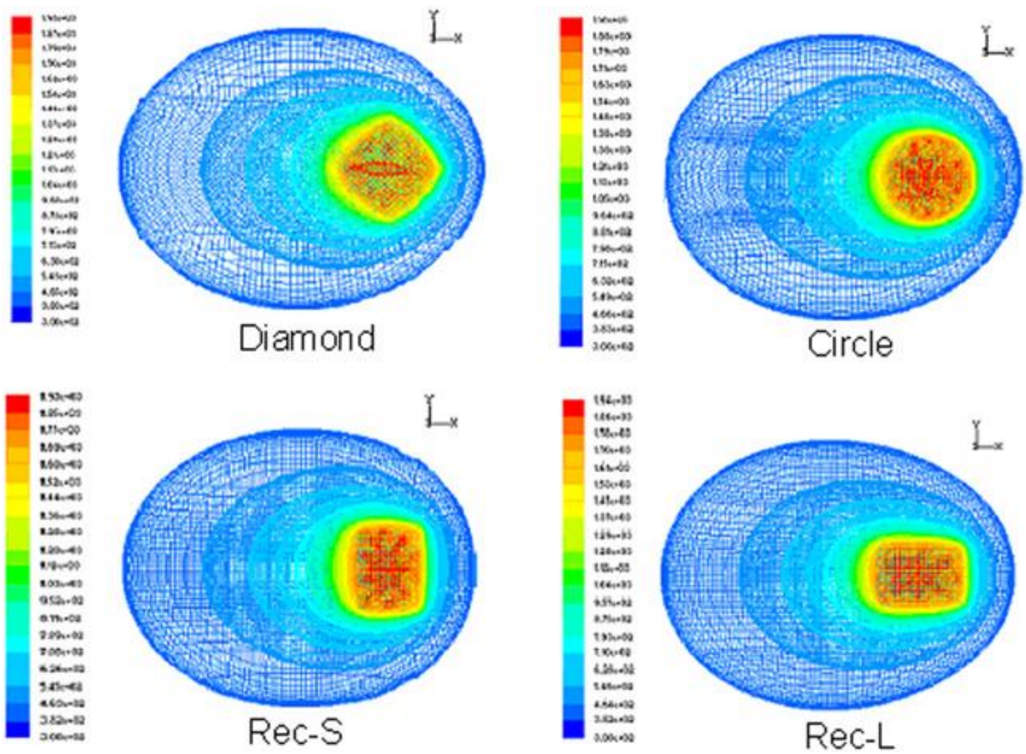

Figure 7. Isotherms on the top surface due to different shapes of moving laser beam [54].

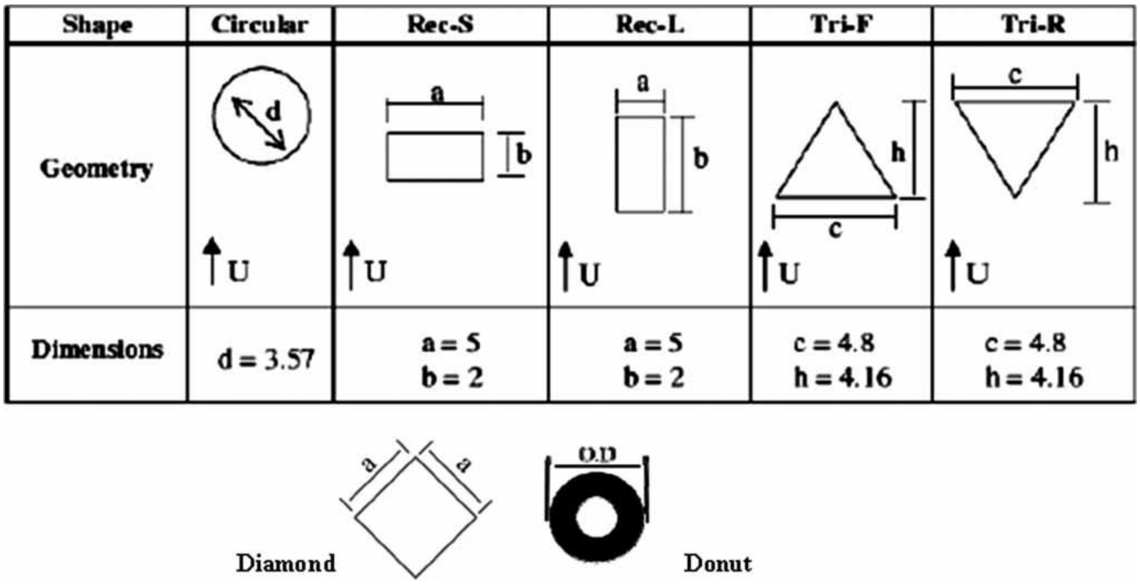

Figure 8. Laser beam shapes [55].

The findings of Sheikh and Li [55] demonstrated significant variations in temperature distribution and heating rates among different beam geometries, with the circular beam exhibiting the highest attainable temperature and the triangular beam (Tri-F) displaying the lowest heating rate. Collectively these studies underscore the importance of laser beam geometry in optimizing laser melting and welding processes. By manipulating beam geometry, researchers and practitioners can precisely control temperature distribution, heat input, and melt pool characteristics, ultimately enhancing process efficiency, quality, and performance.

2.3.4. Laser power and traverse (scanning) speed

Laser power and scanning speed are two crucial factors in laser surface melting and welding. The combination of laser power and scanning speed (power/speed) is often referred to as line energy density and is a measure of the energy absorbed per length of weld. This factor holds significant importance, influencing aspects such as thermal accumulation, cooling rate and other essential factors that contribute to shaping the final product [56, 57].

Research conducted by Cui et al. [58, 59] into the influence of laser power on microstructure evolution and subsequent mechanical properties during laser surface melting emphasises the significance of laser power as a crucial parameter affecting the overall quality of Nd:YAG pulsed laser melted surfaces.

Another investigation carried out by Faraji et al. [60] focused on the influence of welding parameters (laser power, welding current and welding speed) on weld pool characteristics. The findings of this study led to the following conclusions:

- the temperature of the weld pool decreases, and the thermal distribution slightly wider with increasing welding (scanning) speed.
- The depth of the weld increase with higher laser power.

The relationship between scanning speed and melt pool dimensions is further supported by studies conducted by Mallikarjuna et al. [61], which focused on understanding thermal behaviour in laser processing [29], and a study conducted by Gu and Dai, who focused on understanding the role of melt behaviour in selective laser melting.

In a study conducted by Bal et al. [62] on the calculation of the melting efficiency on laser welding, the researchers aimed to explain the relationship between process parameters and melt pool geometry using melting efficiency. This approach allowed them to identify the best parameters for laser melting with minimum energy losses. They found:

- Lower traverse speed leads to lower melting efficiency.
- Higher laser power combined with material of low conductivity results in higher melting efficiency.

The researchers also discovered that there is a limit to what melting efficiency can be achieved by increasing the traverse speed. Further increasing the traverse speed beyond a certain limit means the material has insufficient interaction time with the laser for the melting process to occur effectively.

A study conducted by Miyagi and Wang [34], aiming to understand keyhole dynamics and morphology through X-ray imaging, yielded the following results:

- Keyhole depth and width increase with higher laser power but decrease with higher traverse speed, as shown in Figure 9.
- Keyhole depth fluctuates when no shielding gas is supplied during laser melting.

Another study conducted by Saadlaoui et al. [63] on the thermomechanical processes of laser welding identified that an increasing in traverse speed results in:

- A longer and shallower melt pool.
- Lower longitudinal residual stress and distortions.

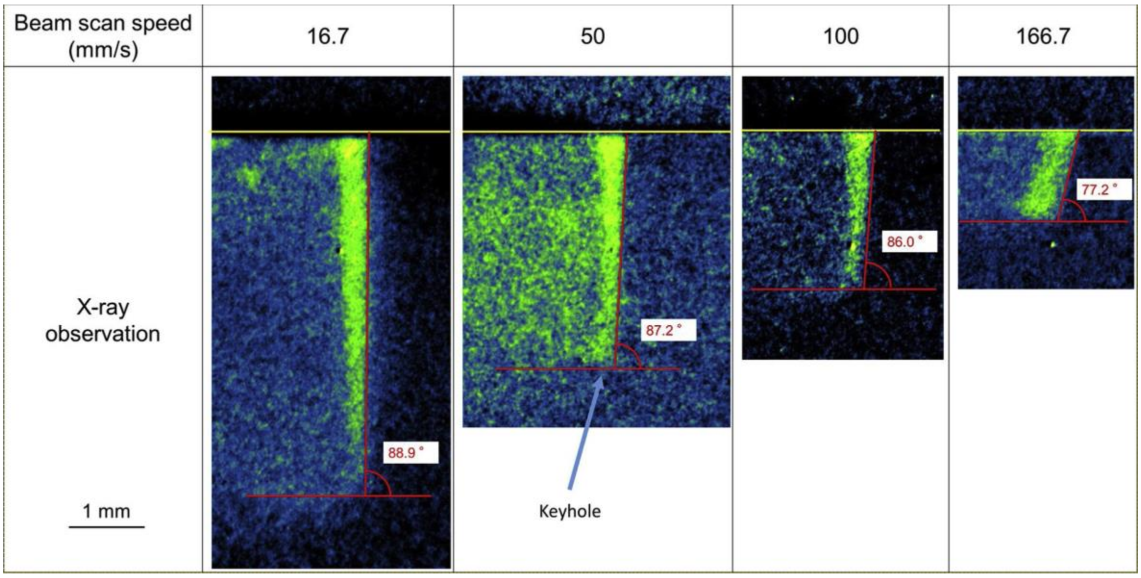

Figure 9. X-ray imaging of the keyhole under different traverse speed. (Laser power, defocus distance and shielding gas remain the same for all cases) [34]

2.3.5. Laser head offset and focal distance

In this category, parameters associated with nozzle positioning during laser-based manufacturing are discussed. Accurate nozzle positioning is crucial for precision melting or joining as it determines the laser spot area and position where interaction between the laser beam and the workpiece takes place. This interaction affects energy density and factors such as laser overlap region on the melt pool. These factors combined will affect the finishing quality, microstructure evolution and the mechanical properties of the final product [30].

A study conducted by Luo et al. [64] on the effect of the laser beam on laser energy absorption characteristics has identified that laser focusing is crucial in laser welding, as it influences energy distribution on the workpiece and the formation of the keyhole. As shown in Figure 10, the workpiece experiences the maximum thermal effect and creates the deepest keyhole when the laser focal point lies directly on the surface of the workpiece, resulting in the smallest laser beam diameter and the highest energy density.

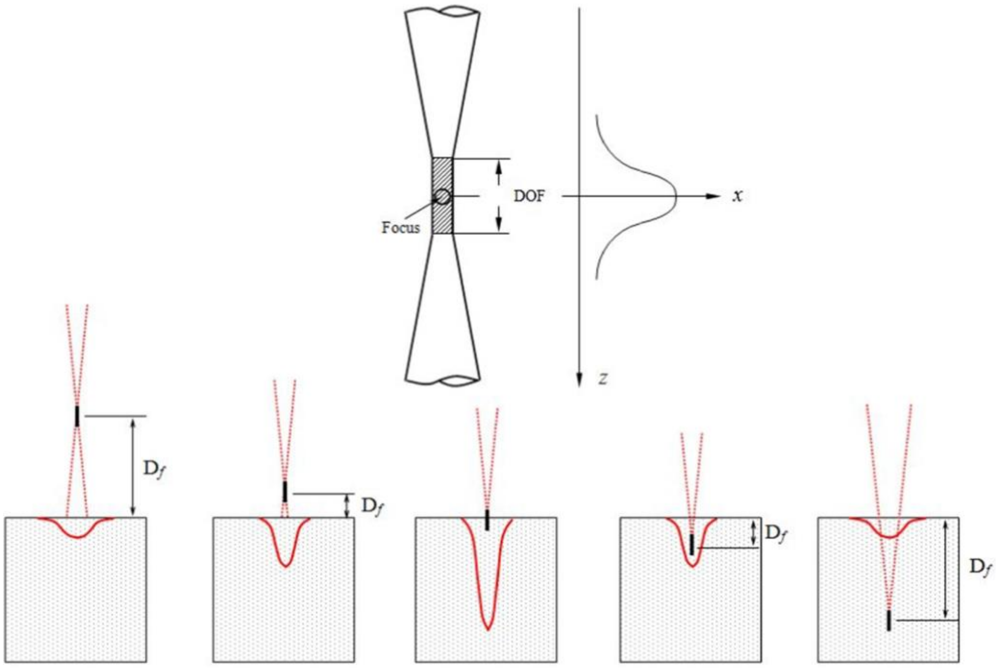

Figure 10. Influence of depth of field offset on welding thermal effect [64].

This is further supported by a study conducted by Miyagi and Wang [34] on keyhole dynamic and morphology. As shown in Figure 10, when the laser focal point moves away from the workpiece surface, the depth of the keyhole will decrease, and the width of the keyhole will increase. Another study conducted by Karmiris-Obratanski et al. [43] also supports these findings, as they state that the absorbed laser power increases when the focal point is closer to the workpiece surface.

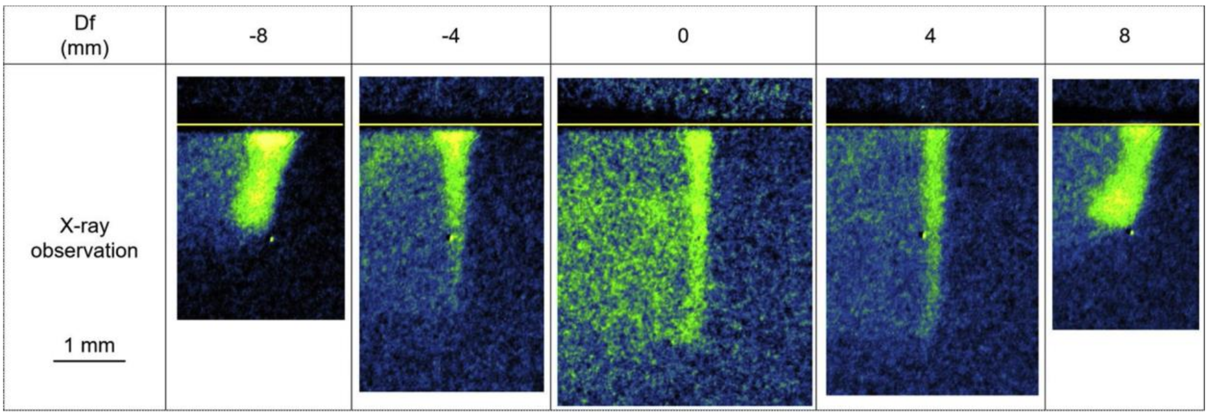

Figure 11. X-ray imaging of keyhole under different defocusing distance (Laser power, laser traverse speed and shielding gas remain the same for all cases) [34].

2.3.6. Substrate material properties and surface condition

Section 2.3.1 but in addition to this, both the material of the substrate and its surface condition can initially affect the absorption of the laser.

A study conducted by McDaniel et al. [65], focussed on reflectivity, where reflectivity = (1 – absorptivity) for a non-transmitting material such as a metal. Following multiple pulse incubation of a smooth platinum stainless steel (Pt:SS) surface, authors concluded that increasing the number of pulses decreases the reflectivity. This is due to the increase in surface roughness caused by a higher ablation effect.

Another study conducted by Wu et al. [31], focussing on the interactions of a picosecond Nd:YVO4 laser (532 nm) and a continuous wave (1064 nm) laser with different materials, supports the above study. They concluded:

- Higher surface roughness increases absorption due to non-uniform reflection on the surface.
- Higher wavelengths result in lower absorptivity in 9Cr18 stainless steel.

In addition, the wide variety of metals, with different mechanical and thermal properties (e.g. density, conduction, melting and vaporisation points), affect all aspects of a surface or weld melt pool, and if or when a keyhole is formed.

2.3.7. Ambient atmosphere and/or gas flows

An inert shielding gas, either within an enclosure around the process or as a flow around the melt pool prevents oxidation. A flow coaxial with the beam also protects the laser lens by preventing dirty or hot gases or debris from flowing back into the nozzle. In fact, a study conducted by Miyagi and Wang [34] highlights the importance of shielding gas in preventing fluctuation in keyhole depth.

Another study conducted by Campbel et al. [66] aimed to understand how various shielding gases can influence the flow within the melt pool. They found that between helium and argon, using helium as shielding gas leads to a higher Marangoni number, indicating a stronger and faster outward flow velocity. Based on their findings, they've concluded that helium induces a flow vector opposite to that of argon.

Moreover, research conducted by Shanmugarajan et al. [32] demonstrates that using helium and nitrogen as shielding gas reduces the fusion zone, heat affected zone while improving the penetration depth of the weld.

In addition to how the type of shielding gas can influence the formation of melt pool, the atmosphere in which the manufacturing process is conducted is also crucial as it can influence the absorption efficiency of the materials and also the microstructure evolution of the workpiece. According to a study by Xu et al. [33], a helium atmosphere can effectively suppress the inverse bremsstrahlung absorption effect induced in the laser welding process's plasma, thus enhancing the absorption efficiency of the process. Another study by Wang et al. [35] aimed at understanding the formation mechanism of δ-ferrite and metallurgy reaction in molten pool, demonstrating that workpiece welded in an argon atmosphere produce less δ-ferrite compare to those welded in normal air atmosphere.

2.4. Melt pool mechanisms

This chapter delves into fundamental aspect that govern the formation of the melt pool including energy absorptivity and melt pool flow. An understanding of the mechanisms driving melt pool formation is necessary for the development of a dependable simulation model.

2.4.1. Energy absorptivity

The terms absorptivity [67] and absorption coefficient [68] are sometime used interchangeably to measure the proportion of laser power supplied to a surface that is absorbed. It is important they are not confused with other terms used to measure process efficiency such as 'melting efficiency' [69].

In addition to factors such as laser type and material properties, the traverse speed of the laser also plays a role in affecting absorptivity during laser manufacturing. A study conducted by Tadamalle et al. [70], centred on the impact of welding (traverse) speed on non-keyhole laser welding, indicates that an increase in welding speed results in an increase in the total power absorbed by the material. This is due to the increase in energy absorptivity and melting efficiency during the melting process.

Another study conducted by Wang et al. [71] on the effects of welding speed on absorption rate during keyhole laser welding has led to the following conclusions:

- The maximum absorption rate for full penetration welding is 61%, and the absorption rate increases with higher welding speed.
- The maximum absorption rate for partial penetration welding is 73%, and the absorption rate decreases as welding speed increases. Additionally, the mass loss rate increases with higher welding speed.

This is further supported by a study conducted by Kawahito et al. [72], focusing on laser absorption characteristic in laser welding with partial penetration. They have concluded the following:

- Laser absorption increases as the laser power increases, due to the increase in the keyhole depth and diameter.

- Laser absorption decreases as the welding speed increases. This is because the keyhole is no longer coaxial with the laser, causing more laser energy to directed onto the material's surface instead of entering the keyhole. Consequently, there is more energy lost due to increased reflection.

Moreover, other researchers have pointed out that a shallower keyhole has a negative impact on energy absorptivity. This is due to the reduction in successive reflections (Fresnel reflections) of laser rays within the keyhole as the laser enters it. This results in a negative feedback loop within the entire system, centred around energy efficiency [5, 44, 73-77].

This relationship is further substantiated by the graph below, which illustrates the connection between the keyhole depth and the energy absorptivity. The alignment of peaks and the valleys in both graphs leads to the conclusion that energy absorptivity is directly linked to keyhole geometry [78]. Another study conducted by Kawahito et al. [76], also yields similar results and conclusions.

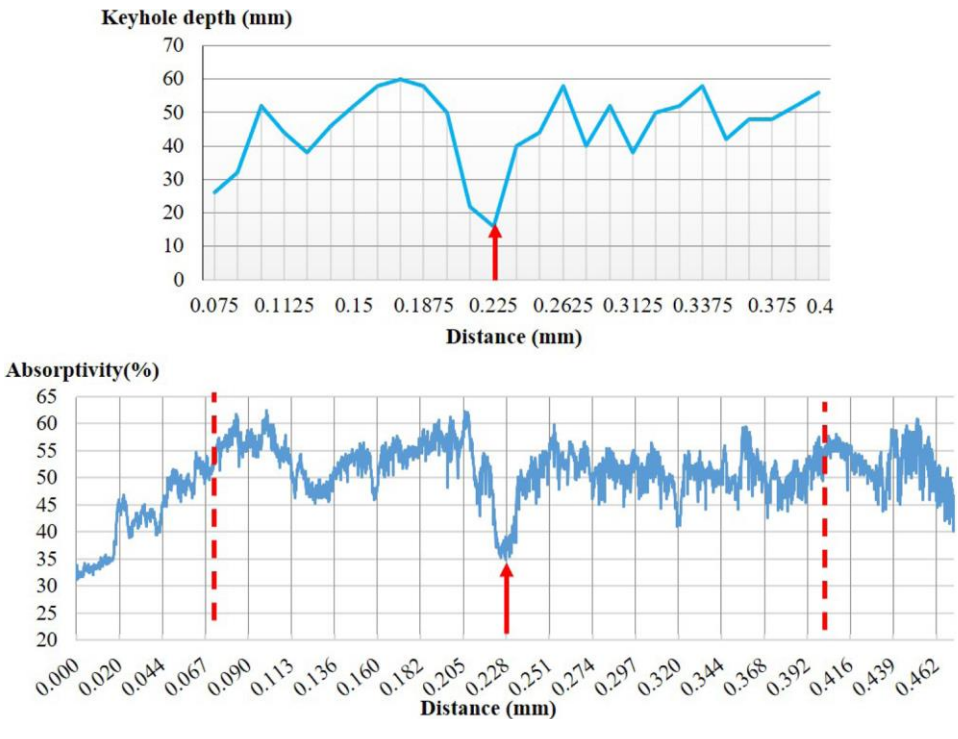

Figure 12. Evolution of keyhole depth and energy absorptivity along the scan distance under the scan speed of 0.5 m/s and laser power of 100 W [78].

This theory gains further support from researchers who have conducted studies aiming at understanding the phenomena behind Fresnel reflections using computational simulations. By integrating models with ray tracing functions, these researchers are able to simulate how laser rays are trapped, reflected and absorbed within the keyhole, thereby enhancing the overall energy absorptivity of the laser melting (or welding) process [74, 75, 79].

A study conducted by Tan et al. [80], focusing on the investigation of keyhole plume and molten pool, has managed to identify and plot the distribution of laser absorptivity intensity.

As shown in Figure 13, the keyhole bottom has the highest laser absorption, as reflections are concentrated within this region. This is followed by the upper half of the keyhole, near the cavity entrance. Lastly, the lower half of the keyhole (adjacent to the keyhole bottom) and the top surface of the melt pool show the least laser absorption. The former is because it has a vertical keyhole wall resulting in minimal interaction with the laser beam, while the latter is due to it being distant from the laser beam. Interestingly, Tan et al. [80] noticed that as the total keyhole absorption increases, the proportion of absorption by the keyhole bottom decreases.

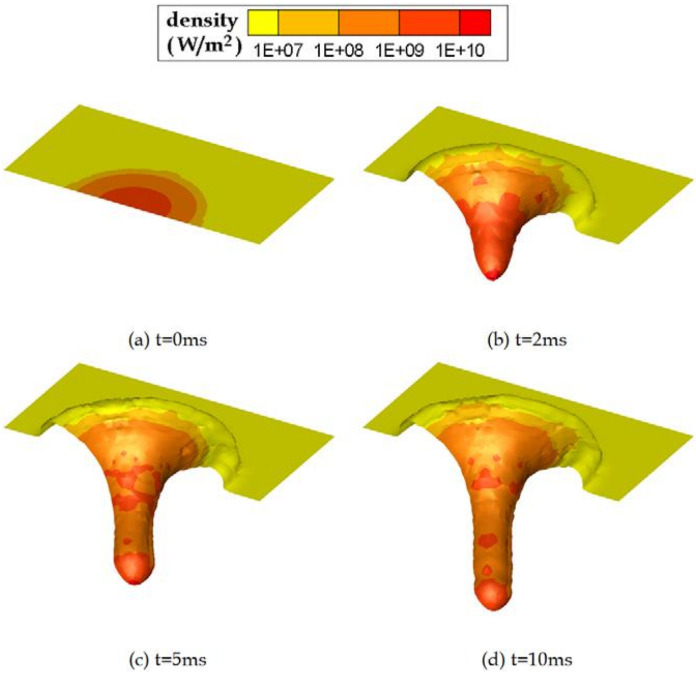

Figure 13. Distribution of laser absorptivity intensity [80].

Beyond laser-related factors, consideration of material properties also plays a crucial role in understanding the energy absorptivity during laser melting process. In an exploration of temperature-dependent absorption coefficient, Nguyen and Yang concluded that the absorption coefficient should not remain constant but rather exhibit temperature dependent behaviour. Accordingly, they introduced the following function to represent the temperature-dependent absorption coefficient [81]:

A study conducted by Ebrahimi et al. [77], aiming at understanding the influence of laser characteristics on internal flow behaviour, also supports the above theory by highlighting the importance of temperature's impact on material properties, thus affecting the overall energy absorptivity. In their study, they went further to enhance absorption in order to account for the influence of various laser characteristic (including laser wavelength, surface temperature, laser-ray incident angle, and material composition) on the melt pool flow, all while striving to maintain simplicity when developing the simulation model for laser melting.

2.4.2. Melt pool flow and keyhole formation

Several forces have been identified as drivers of the flow within a melt pool. These forces include [74, 82-88]:

- Marangoni force
- Convection
- Buoyancy force
- Surface tension
- Electromagnetic forces
- Viscous force
- Lorentz force
- Recoil pressure (only for keyhole formation)

The melt pool formed from laser melting can be categorised into three different types: conduction-mode, mix-mode (transition), and keyhole-mode melt pool [44, 89-92].

In a conduction-mode melting/welding heat transfer primarily occurs through conduction [92]. A shallow melt pool which tends to extend outward, away from the laser spot is formed. Flow in the pool is dominated by Marangoni forces, although there may other forces such as buoyancy. The conduction of heat and flow of molten material are responsible for determining the width of the melt pool [85]. But, the direction of the flow when viewed in the cross section of the melt pool can vary as it is driven by a gradient in surface tension and the relationship between surface temperature and tension is not the same for all materials as shown in Figure 14 [87].

In a transition-mode melt pool formation, which occurs between conduction-mode and keyhole-mode, the energy intensity is strong enough to cause the vaporisation of material at the bottom of the melt pool, initiating the formation of a keyhole. However, the energy intensity is not sufficient to generate a temperature high enough for vaporisation and recoil pressure to take place, overcoming surface tension and thus preventing the formation of a cavity in the centre of the melt pool. Without a cavity at the centre of the keyhole, there is no improvement in absorptivity to further drive the formation of the keyhole and deepen its structure, preventing a complete transition from conduction-mode to keyhole-mode [44, 90, 93, 94].

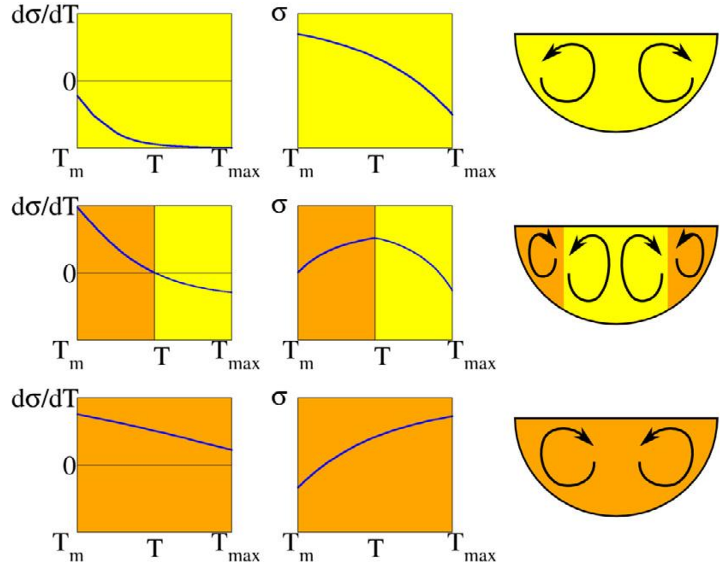

Figure 14. Illustration of the relation between the surface tension and temperature between the melting temperature (Tm) and the maximum weld temperature (Tmax), and the Marangoni flow direction [87].

In the formation of a keyhole-mode melt pool formation, convection is the primary method of heat transfer due to the higher melt pool temperature and stronger flow movement within the melt pool. The two main driving forces are recoil pressure and Marangoni flow, which result from the intense laser power and vaporization effect. These forces lead to the formation of the keyhole and the cavity at the centre. With the formation of the keyhole's cavity, molten material is forced to flow upward from the bottom of the keyhole, moving through the sides of the keyhole. The continuous upward flow of molten material results in the formation of a crown at the top surface, which then pushes outward from the centre towards the edge of the melt pool. This leads to the cross-sectional shape of the keyhole resembling a nail. Besides pushing material away from the bottom of the keyhole, recoil pressure also plays a role in maintaining the cavity located at the centre of the keyhole, preventing the backflow of molten material from the rear and the top [44, 74, 80, 86, 88, 93-96].

To understand deep penetration during the formation of the keyhole melt pool, Pang et al. created a 3D transient multiphase model of keyhole-mode laser welding. Using a high-speed camera, they saw the formation of a vapor plume during laser welding, leading to the assumption that the temperature of the keyhole wall is approximately the material boiling point [97].

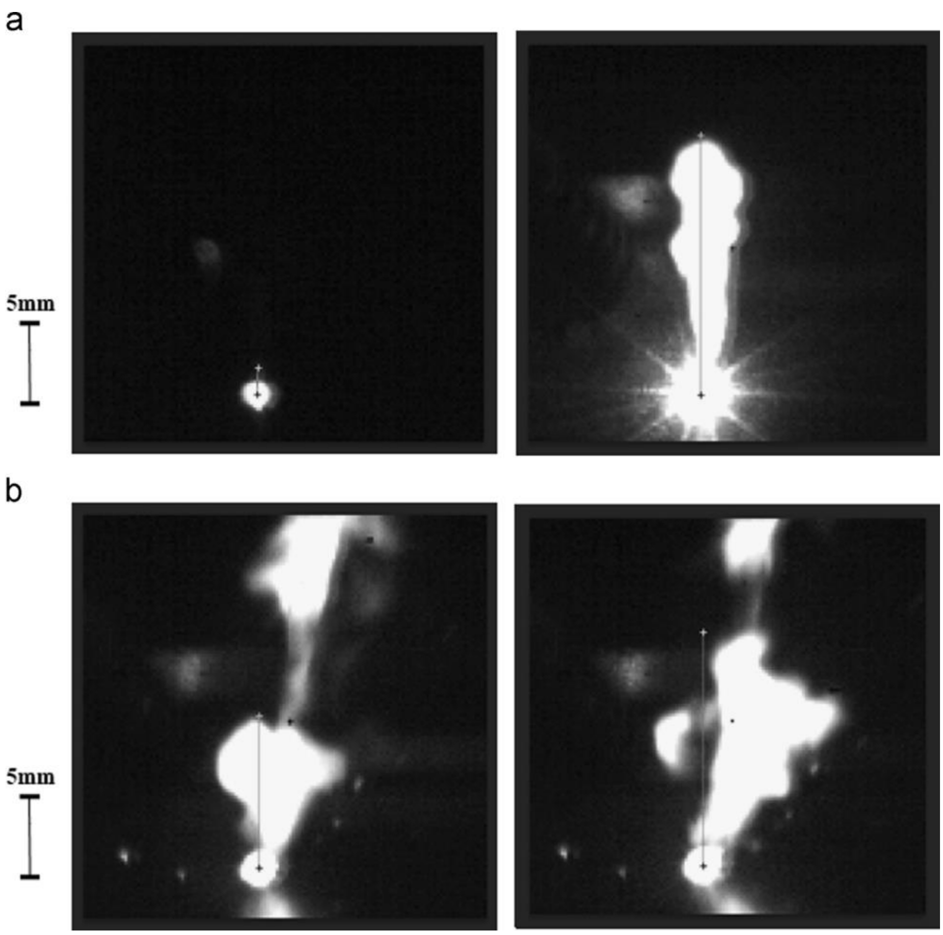

Figure 15. High-speed cameral images of vapour plume in laser welding: (a) unseparated metallic vapour; (b) separated metallic vapour [97].

According to Hu et al. [74], the flow located at the bottom of the keyhole is stronger that the wall of the keyhole, mainly due to the high temperature (above boiling point) and recoil pressure cause by vaporising material. However, due to the gravitational force acting on the molten material, parts of the material unable to rise all the way up and falls down into the keyhole instead, resulting in porosity due to cavity entrapment [98].

Figure 16 shows the result of simulations by Sohail et al [98] illustrating the relationship between penetration depth, laser power and the direction of flow within the laser keyhole. Additionally, it demonstrates the formation of a liquid bridge and an entrapped cavity resulting from the keyhole wall's collapse due to gravitational forces.

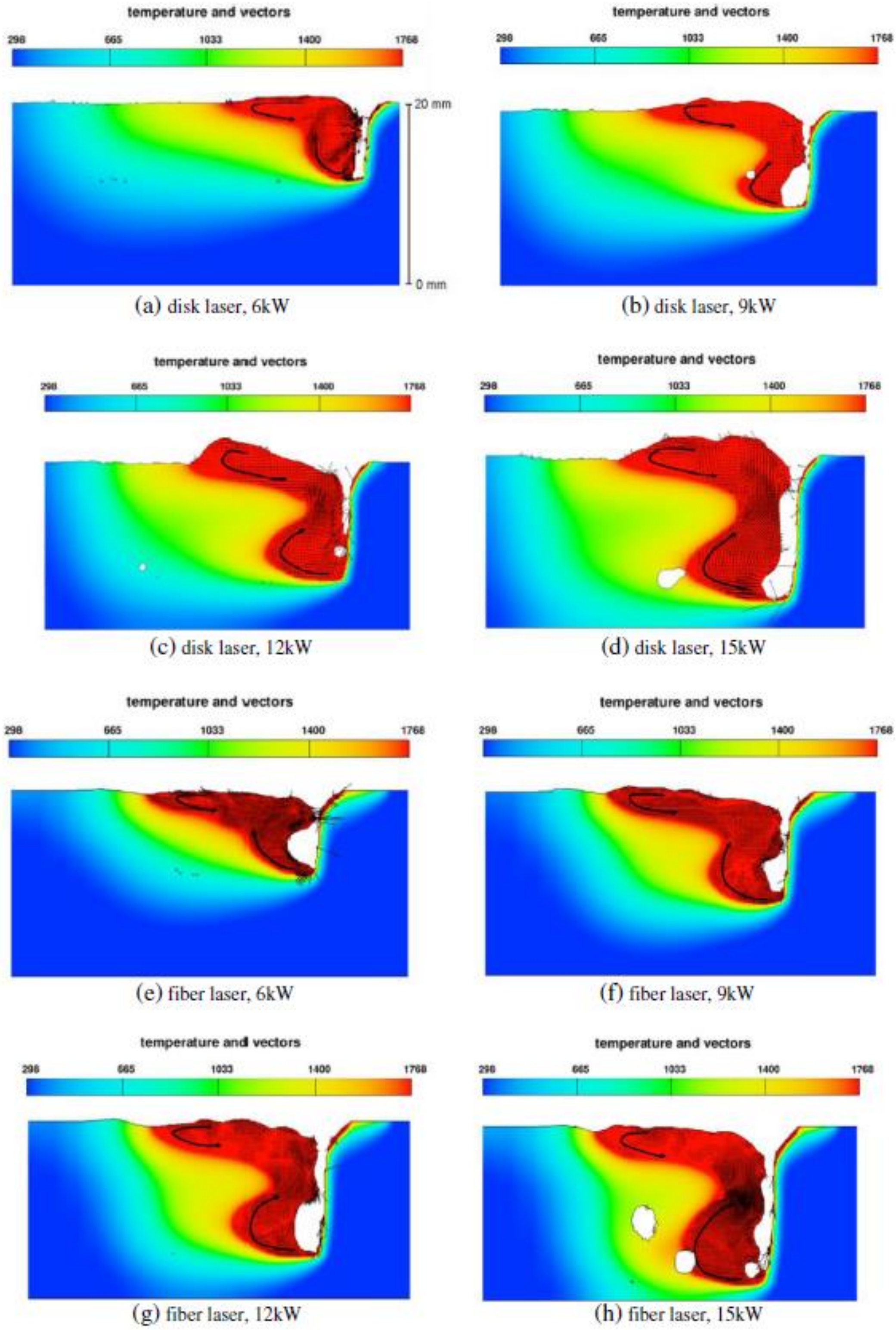

Figure 16. Flow patterns at different powers of disk and fibre laser [98].

As mentioned earlier, the keyhole depth is maintained through the constant removal of material by the laser beam. This can only be maintained by the laser beam vaporising materials and generating recoil pressure to force the material upwards. Consequently, any deviation of the laser beam away from the keyhole bottom will disrupt the keyhole mechanism, resulting in the fluctuation in the keyhole depth as shown in Figure 17 [99].

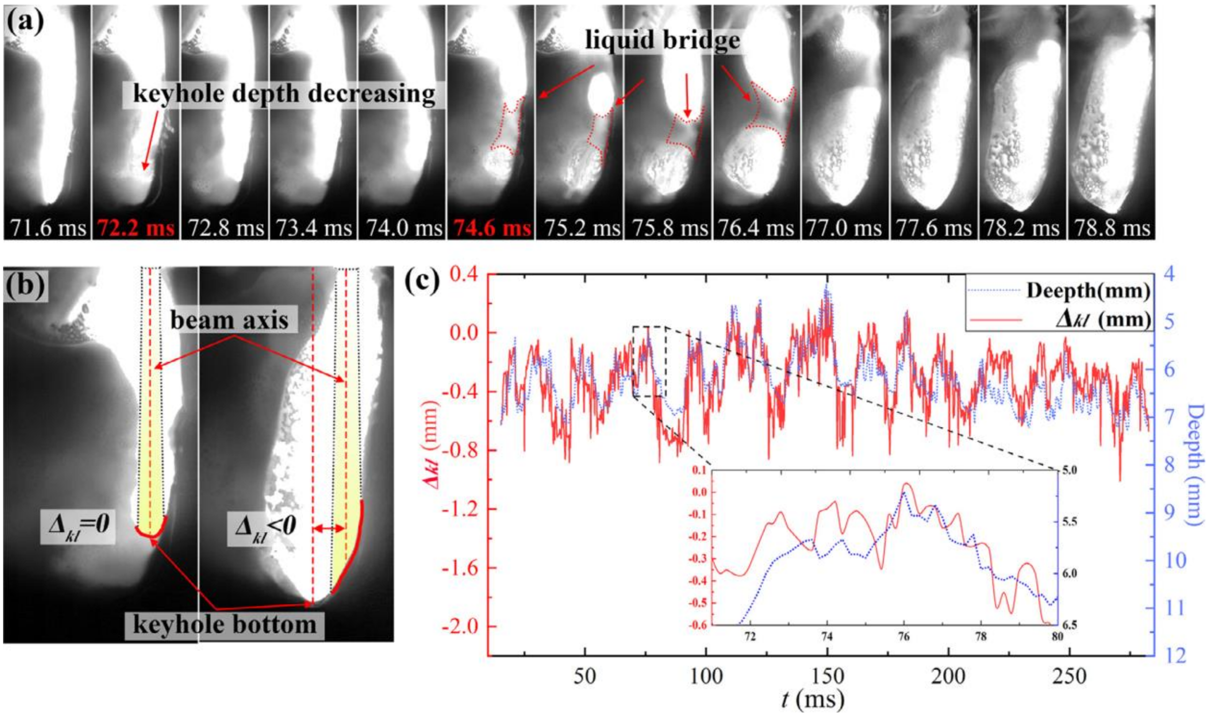

Figure 17. The keyhole-beam deviation and keyhole depth fluctuation: (a) keyhole profiles in a fluctuation cycle; (b) the illustration of keyhole-beam deviation (Δkl). When Δkl < 0, the laser spot locates on the front keyhole wall. When Δkl = 0, the laser spot locates on the keyhole bottom; (c) comparison between the variation of Δkl and keyhole depth [99].

Given the complexity of the melt pool mechanism in laser welding, some researchers have concentrated on developing a simplified model for simulating melt pool formation during laser melting and welding: In a study conducted by Franco et al. [100], which was centred on simulating the laser welding process, they proposed a theoretical model using a double moving heat source to predict the outcome of laser welding. They concluded that linear functions for defining the position of the heat source within the material (acting as the heat source for laser energy which enters the keyhole) and the power balance (involving variables such as laser power, welding speed and focal spot diameter) are necessary for ensuring the model's reliability.

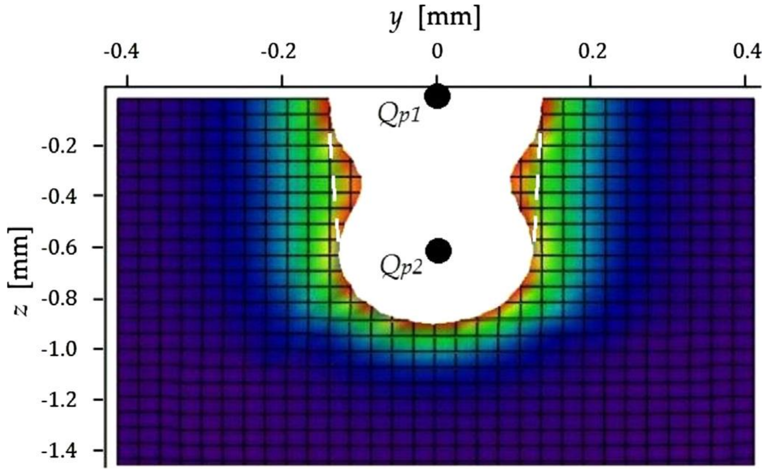

Figure 18. Contour plot of the temperature field for a model showing the concept of double moving heat source [100].

Over the past decade, the enhanced thermal conductivity (ETC) approach—particularly in its anisotropic form—has gained increasing attention as a simplified yet effective alternative to full fluid dynamics-based models for simulating melt pool formation. Among the earlier works, Kamara et al. [135] applied directional modifications to thermal conductivity to replicate convective effects during laser deposition, demonstrating how anisotropic enhancements can influence melt pool geometry. Since then, many studies have adopted and further developed this strategy across various laser-based manufacturing processes and materials.

To replicate the conduction-mode laser melting process while maintaining modelling simplicity, Safdar et al. employed both isotropic and anisotropic versions of the enhanced thermal conductivity approach. The underlying concept involves multiplying the thermal conductivity by a constant factor [101]:

$$k' = \alpha k$$

Here, k represents the normal thermal conductivity value at the corresponding temperature and α is the enhancement factor which is defined as:

$$\alpha = \begin{cases} 1 & if \quad T < T_{liquidus} \,\&\, T_{solidus} \\ Multiplying\ factor & if \quad T > T_{liquidus} \end{cases}$$

While they were successful with the anisotropic enhanced thermal conductivity approach (An Iso ETC x 1 x 5 x 1), they were unable to replicate the results using the isotropic enhanced thermal conductivity approach.

Recent contributions further demonstrate the practicality and accuracy of the anisotropic enhanced thermal conductivity method. For instance, Nikam et al. [136] introduced directional correction factors along the x, y, and z axes to emulate Marangoni convection in laser-based powder bed fusion (PBF), achieving strong agreement with experimental melt pool geometries under varied processing conditions. Ghosh et al. [137] and Siao and Wen [138] similarly validated the anisotropic enhanced thermal conductivity method in laser welding and selective laser melting (SLM), respectively, highlighting its capability to predict melt pool characteristics while substantially reducing computational cost compared to full CFD-based models. Liu et al. [139] also applied anisotropic enhanced thermal conductivity method to SLM of AlSi10Mg, linking improved predictions of melt pool dimensions and thermal gradients to grain structure evolution.

Ancellotti et al. [140] compared both anisotropic and isotropic enhancement strategies in simulating L-PBF of Ti6Al4V, proposing a calibration approach based on surface roughness and melt pool dimensions. Their findings suggest that model selection may depend on the specific application and calibration objectives. Nevertheless, anisotropic enhanced thermal conductivity method continues to be widely recognized as a flexible and computationally efficient means of approximating convective heat transfer in melt pool modelling.

2.5. Final part properties and attributes

This section considers the factors that determine the quality of the final melt or weld, such as microstructure, stress-strain properties, faults such as cracks, porosity and oxidation, and other surface properties. By reviewing these aspects, the chapter aims to gain a comprehensive understanding of how materials respond and evolve after the laser melting or welding process.

2.5.1. Microstructure

In laser melt pool processes, final microstructure is highly dependent on solidification conditions, which can be engineered by the process parameters considered above, including laser power, traverse speed and beam parameters. Other factors include the type of material used , substrate geometry and initial temperature [102].

Many researchers have agreed that the final cooling rate experienced by the material during the solidification process is one crucial factor in determining the material's microstructure [103-107]. In one study conducted by Dinda et al., differences in microstructure at various locations of a wall created through laser direct metal deposition were observed. Their findings are summarised as follows [10]:

- A fine dendritic structure with secondary dendrite arms is observed at the top layer due to slow cooling rate.

- Primary dendrites, without the growth of secondary dendrites, are predominantly seen at the bottom layer due to fast cooling rate.
- As the cooling rate decreases from the bottom to the top layer, the microstructure of the deposited wall gradually transitions from a fully columnar to a dendritic structure.

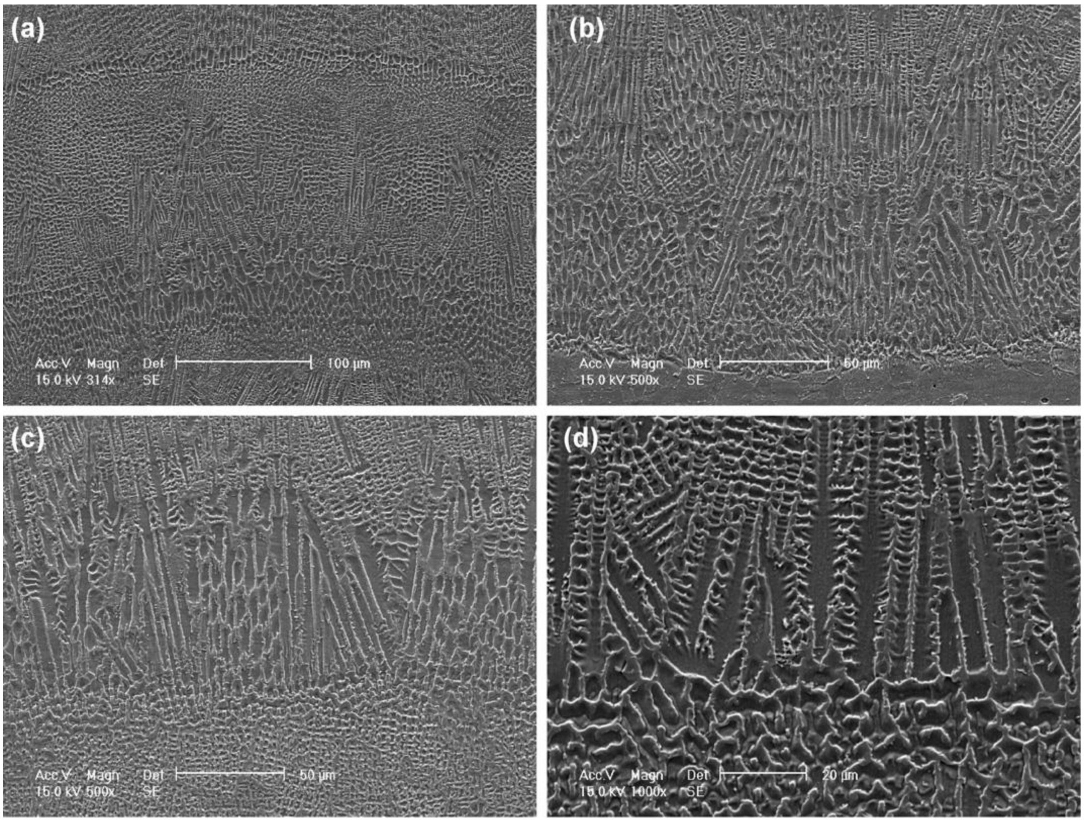

Figure 19. Transverse-section microstructures at different locations of the sample [10].

Dezfoli et al. [108] found that by manipulating the laser scanning speed, it is possibility to control the shape of the grain structure. They also proposed the use of secondary laser heat source as another method of regulating grain structure growth, which can lead to changes in the mechanical properties of the final product. The findings demonstrate it could be possible to engineer the material properties of different regions of a metallic component to meet the functional requirements.

In addition to the initial microstructure formation during the melting or welding process, there can be more microstructure development. Heat treatment due to laser processing of nearby areas (particularly for laser surface melting) or deliberate heat treatment or shock peening of welds for control of residual stress, can cause further changes [109, 110].

A study conducted by David et al. [111] to investigate the effects of solidification on stainless steel weld microstructures found a wide range of variations in microstructure, from duplex to fully austenitic and fully ferritic, could be formed by varying cooling rate and composition. They named laser welding with a 400 W pulsed Nd:YAG laser as producing high cooling rates.

In a study conducted by Tian et al. to investigate the effects of anneal temperature and cooling rate on microstructure and tensile properties, the following results were obtained [106]:

- Higher cooling rates results in a finer microstructure, which contributes to the overall strength of the structure.
- Increasing the annealing temperature leads to an increase in the strength of the specimens.

In a study comparing the metallurgical behaviours of stainless steel manufactured through selective laser melting and laser cladding deposition, Ma et al. [112] concluded that different manufacturing methods have varying impacts on the cooling rate during the manufacturing process. These variations result in distinct microstructure evolutions during the solidification process, which leads to differing mechanical properties in the final product.

2.5.2. Stress, strain and crack formation

In laser manufacturing process, to achieve better quality control of the final product, it is essential to understand the effects of stress and strain and how they can contribute to the formation of cracks.

Stress and strain, resulting from the thermal distribution during laser manufacturing process, represent a material's resistance to and deformation under forces caused by thermal expansion and contraction during laser melting and solidification (cooling) [113, 114]. Such thermal stress and strain, if left unchecked, can impact the structural integrity of the final product.

In laser manufacturing, the concentrated thermal energy creates a significant temperature gradient, leading to the accumulation of thermal stress. If this stress surpasses the material's ultimate tensile strength, the region under the highest stress will undergo permanent deformation. Continued strain can lead to the formation of fractures and cracks, serving to relieve the accumulated stress [114].

By understanding the microstructure of the material, it is possible to understand and predict the formation of cracks or even microcracks within the material. Zhang et al. [89] observed that cracks tend to form in the lower beads, which are the regions closer to the substrate or previously deposited layers. These cracks often propagate along the grain boundary and can sometimes extend into the newly deposited upper beads. Sun et al. [115] in a related study, further supported these findings by noting that:

- In cases of small stress, crack tend to distribute along dendrites and propagate along the crystalline direction.

- In cases of large stress, cracks propagating normal to the crystalline direction can break through dendrites, generating intergranular cracks.

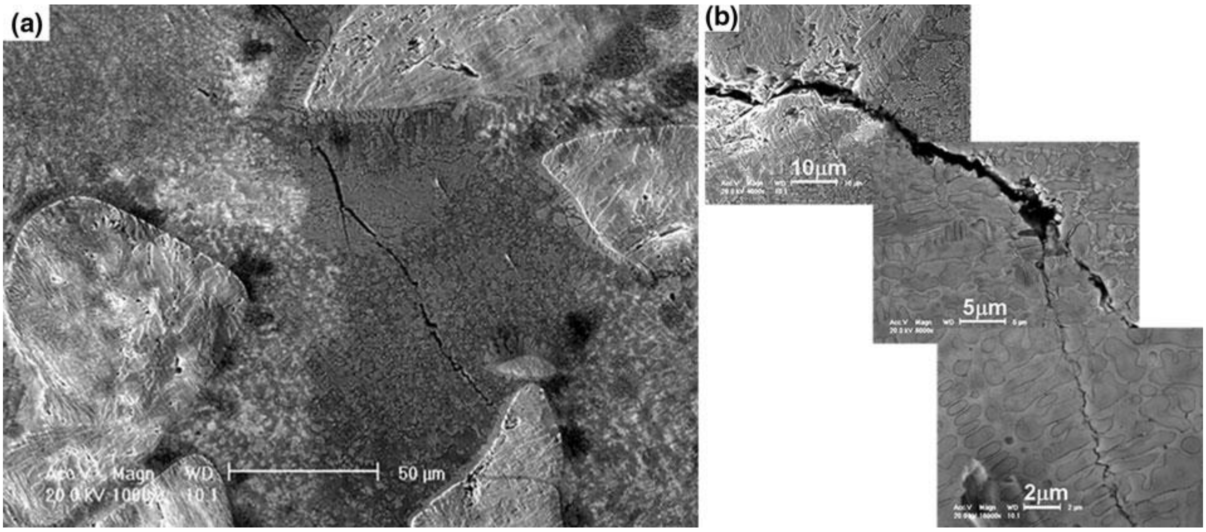

Figure 20. Morphology of cracks [115].

To avoid crack formation, some researchers suggest the use of preheating treatment [12, 116, 117], while others have suggest the application of post-processing treatment to eliminate the inconsistencies within the product produced [118].

In a related study by Liu et al. [119], the effect of heat treatment on crack control and microstructure refinement in laser beam welded TiAl-based alloy was investigated. The study emphasised the importance of in situ post-weld heat treatment in crack mitigation, with optimal results achieved at elevated temperatures. In situ heating at 800°C effectively inhibited crack formation, leading to crack-free welds. Additionally, conventional post-weld annealing induced grain refinement, further enhancing weld quality and integrity.

Understanding the interplay between stress, strain, and microstructure evolution is essential for developing effective strategies to mitigate crack formation and ensure the production of high-quality laser-manufactured components.

2.5.3. Surface properties

In the manufacturing industry, the pursuit of excellence in the final product is paramount, with surface finishing being an important aspect. While surface quality is just one facet of the overall quality commonly aimed to achieve, it is often the most conspicuous as it forms the first impression. This sub-chapter delves into the critical realm of surface properties and finishing in laser-based manufacturing processes.

To achieve a good finishing surface, it is crucial to understand the relationship between process parameters and the melting mechanism. Gharbi et al. [120] concluded that in additive manufacturing, the use of thin additive layers and large melt pool area helps improve the surface finish of the final product. They also stated that increasing the distance between the nozzle and the surface, affecting powder-laser interaction, enhances particle melting, thus benefiting surface finish.

Further support was seen in a study conducted by Gharbi et al. [121], adding that the operation mode of the laser has an impact on the surface finish. They found out that the use of quasi-continuous laser irradiation is better than fully continuous laser irradiation. This was attributed to the reduction in thermal gradient and Marangoni lateral flow in the melt pool, reducing the mean velocity of the flow within the melt pool. Additionally, they mentioned that when using continuous wave laser, the use of top-hat laser head which provides a uniform beam distribution, is beneficial for surface improvements.

Aside from improvement on surface roughness, it is also possible to improve corrosion resistance through the selection of the right process parameters. Yu et al. [122] demonstrated that through careful manipulation of the process parameters such as single-pulse energy density, spot overlap rate and laser scanning times, it is possible to influence the corrosion resistance of the laser melting layers. This is further supported by another study conducted by Hashemi et al. [123]. These authors showed it was possible to improve the microstructure and corrosion resistance of a surface through the use of laser surface treatment with changes in laser scanning speed.

2.5.4. Oxidation

If the melting or welding process is not fully shielded by inert gases or another controlled atmosphere and oxygen is present, there is the potential for oxidation. A study by Cui et al. [124] focussing on the novel morphologies and growth mechanism of oxides induced by pulsed laser, managed to categorise the morphologies of oxides into 4 types, as shown in Figure 21.

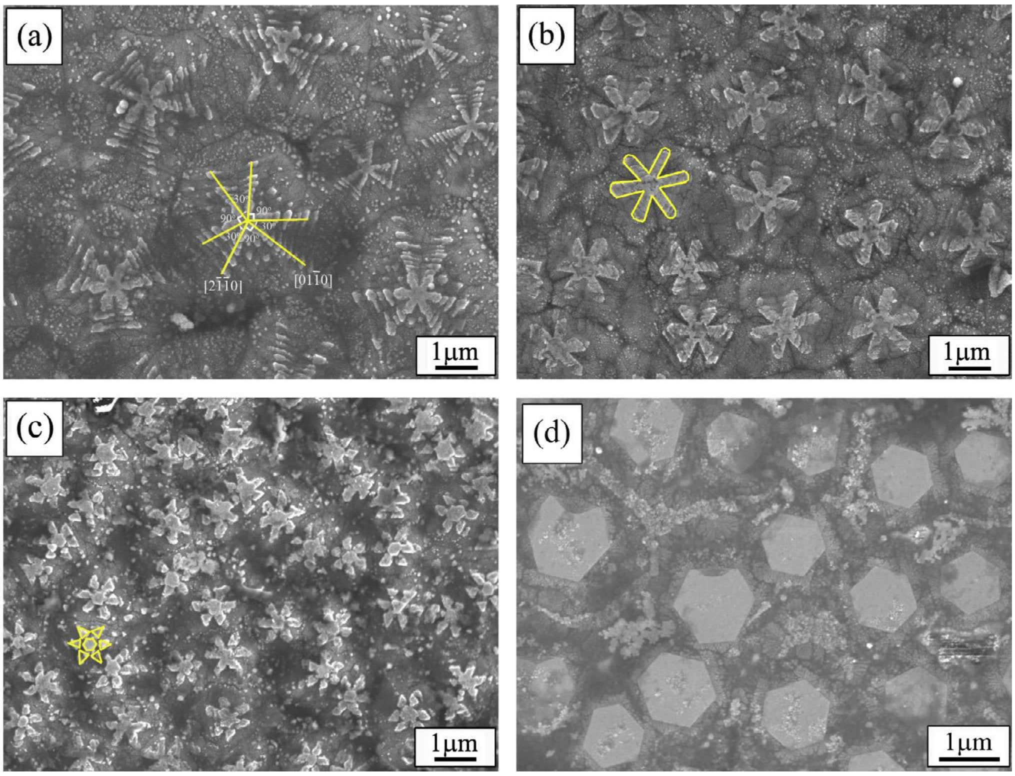

Figure 21. FESEM images of different Cr2O3 morphologies formed on stainless steel surface after laser oxidation: (a) dendritic Cr2O3 (type 1); (b) flower-like Cr2O3 (type 2); (c) gear-like Cr2O3 (type 3); regular hexagonal Cr2O3 (type 4) [124].

Through comparison, they concluded that types 1-3 morphologies are basically the evolution of the hexagonal shape, except for type 4, which shows regular hexagonal Cr_2O_3 morphology.

In a subsequent study of surface oxidation phenomenon and mechanism, Cui et al. [125] concluded that the common oxides found on stainless steel after laser processing were Cr_2O_3, Fe_2O_3 and MnO_2. They also discovered that the composition and morphologies of the oxides formed are not uniformly distributed across the laser spot. Cr_2O_3 and MnO_2 are mainly found at the edge while Fe_2O_3 is found at the centre of the laser spot.

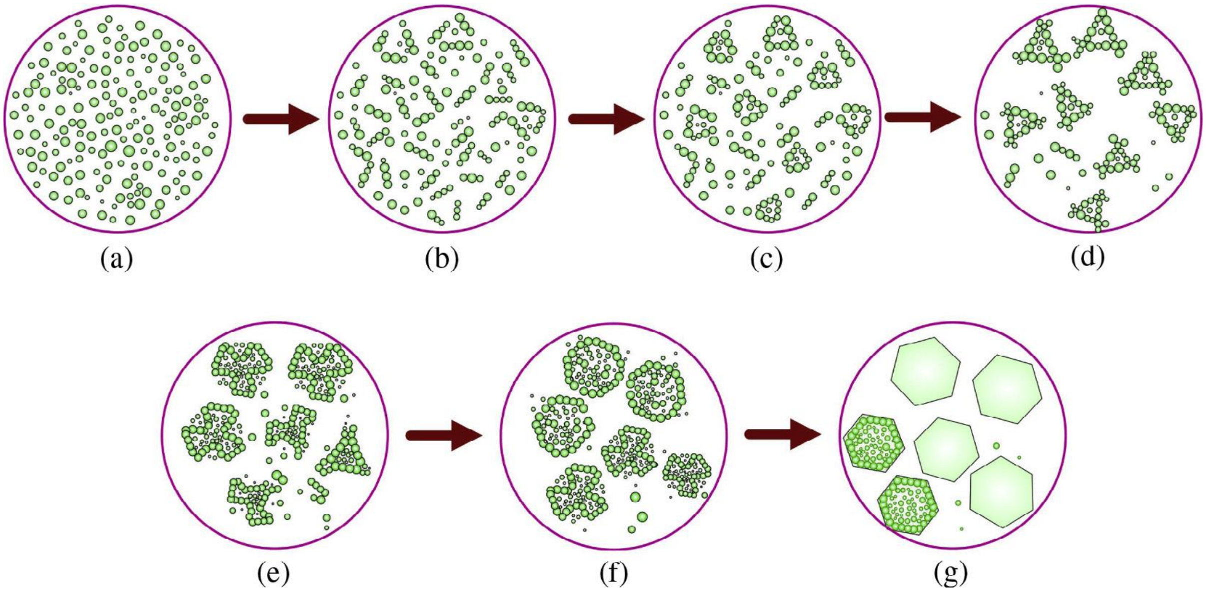

Figure 22. Schematic growth model of the regular hexagons [124].

In a study of oxide growth and effects, Adams et al. [126] were able to create distinguishable metal oxide colour layers by controlling the laser scanning speed. They discovered that the faster the scanning speed, the thinner the oxides formed. Through experiments with a range of laser scanning speeds, they categorised the oxide coatings formed into two types:

- Thick oxide coating (>250 nm), which consists of a Fe-rich oxide solution forms at the top half and a Cr-rich oxide containing Mn develops in the bottom half.
- Thin oxide coating (<200 nm), which consists of a Cr-rich oxide solution containing Mn and Fe with compositional gradients throughout the thickness.

Other studies also support the theory of surface colouration through controlled oxide formation. Li et al. [127] managed to achieve different colours by controlling process parameters such as laser power, focal plane offset and scanning direction. In addition to the mentioned parameters, they also experimented with varying numbers of laser scan passes and laser scanning speeds. Their findings concluded that various laser processing parameters can influence the oxide formation and, consequently, surface colouration on stainless steel.

Similarly, Antonczak et al. [128] and Nanai et al. [129] also support the theory of surface colouration through controlled oxide formation. Figure 23 shows results by Antonczak et al. demonstrating the effects of laser pulse repetition rate and hatching pattern.

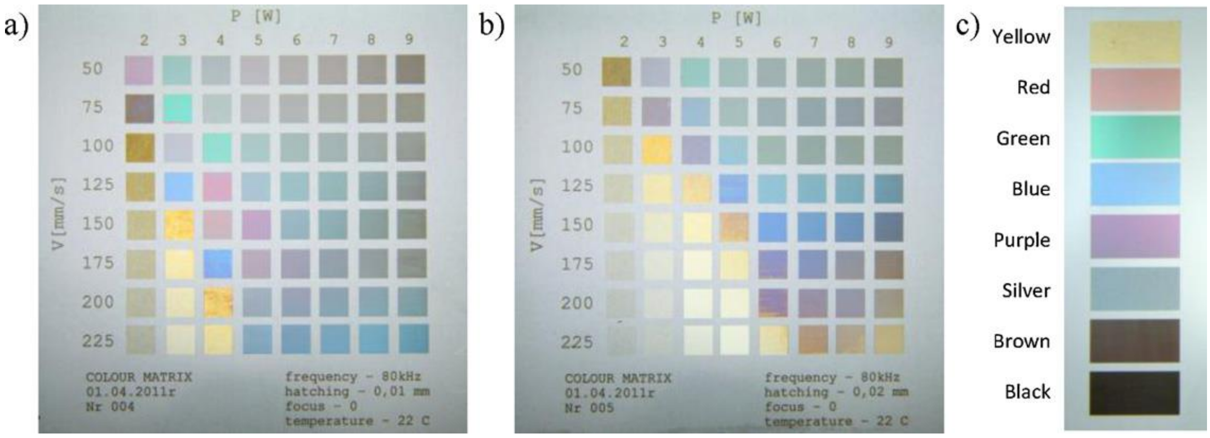

Figure 23. The influence of average power and speed of scanning of the sample on the colour palette: (a) example for pulse repetition rate FR=80 kHz and hatching h=0.01 mm, (b) example for pulse repetition rate FR=80 kHz and hatching h= 0.02 mm and (c) eight representative colours selected for study [128].

2.5.5. Porosity

In a study conducted by Huang et al. [130], it was observed that the use of different materials in laser welding leads to variations in porosity density. Furthermore, they concluded that porosity formation within a keyhole is a result of the following factors:

- Bubble formation caused by instability in keyhole formation.
- Bubble formation that becomes trapped during solidification process.

The SEM micrographs presented in Figure 24 present visual evidences of microscopic pores and voids within high strength 316L steel structures generated using Direct Metal Deposition (DMD). These microscopic pores, commonly referred to as micro-pores, have a direct influence on the structural integrity of the material, affecting its stress and strain characteristics. Therefore, meticulous selection of process parameters is paramount for controlling the growth of porosity and ensuring quality control.

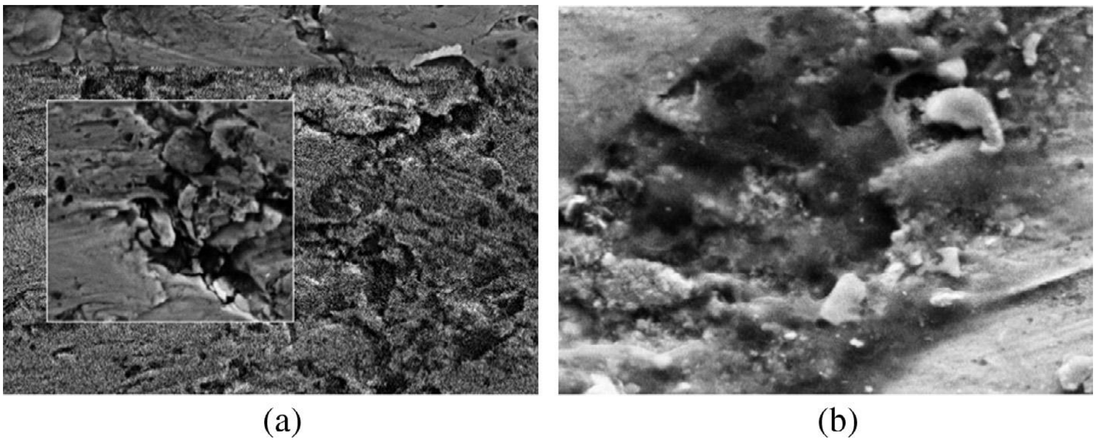

Figure 24. SEM micrographs showing microscopic pores and voids in direct metal deposition generated high strength 316L steel structures at (a) Magnification of 8.91 k, and (b) Magnification of 3.92 k [118].

2.6. Summary

This literature review explores laser melt pool processes, starting with an introduction to the widespread application of laser systems in manufacturing and engineering. It delves into the identification of key process parameters and their influence on the formation and flow mechanism within the melt pool. Additionally, it underscores the importance of the post-laser melting attributes for quality control purposes (Figure 25). The reviewed studies review the intricate interplay between laser process parameters, material properties, melt pool formation dynamics, and the resulting post-laser melting attributes. These findings shed light on the complexity inherent in the laser melting mechanism, highlighting the need for a comprehensive understanding of these factors to optimise process outcomes.

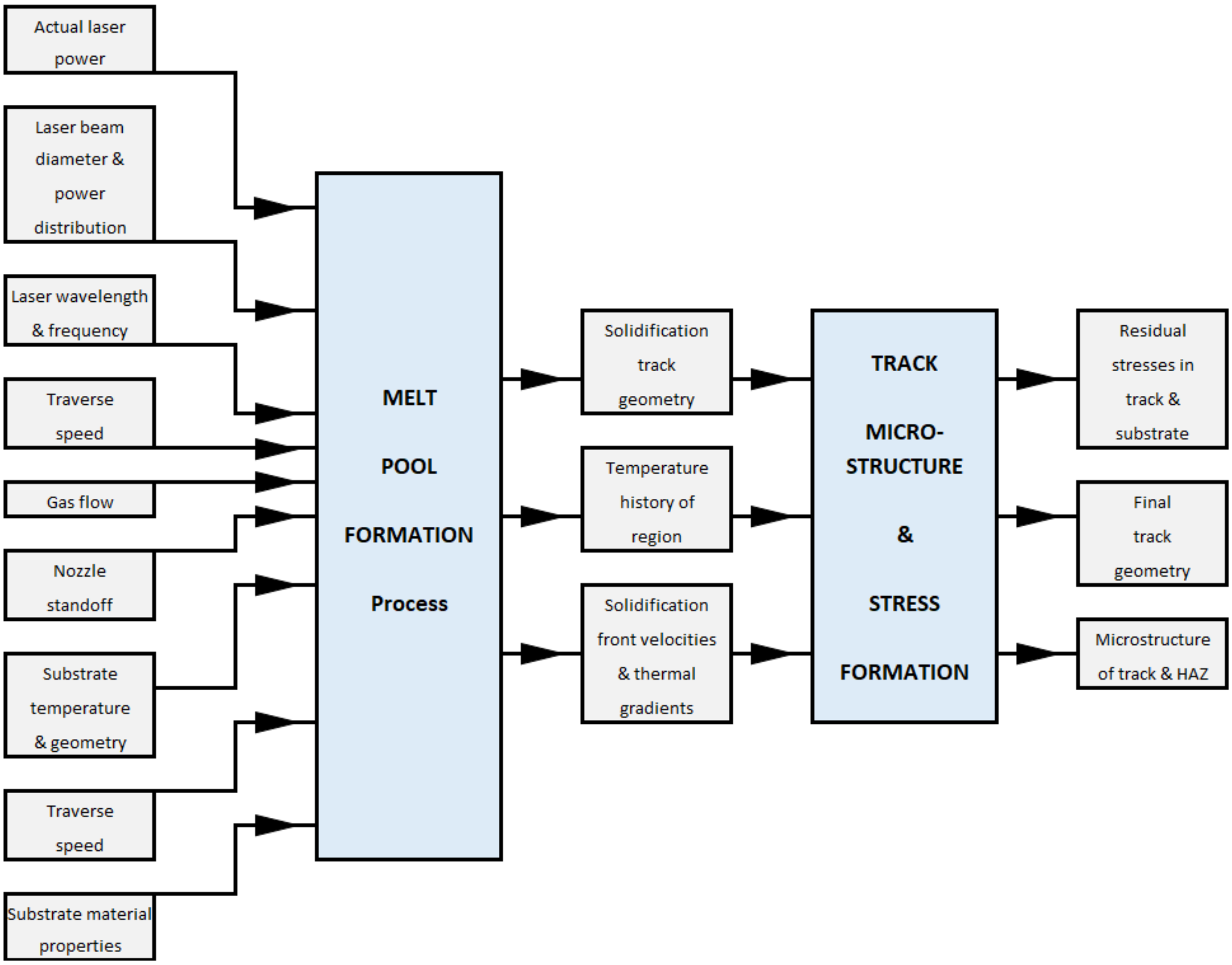

Figure 25. Parameters at different stages of laser surface melting and welding (adapted from [45]).

3. Equipment and Techniques used in this work

This chapter presents an introduction to the equipment used in this research. In this chapter, the following topics are covered:

- Equipment used for conducting laser melting and welding experiments.
- Equipment used for analysing the samples obtained from the experiments.

3.1. Material used for laser melting experiments

The material used in this work of laser melting is stainless steel 316. It has the following basic properties [131]:

- Molecular mass: 55.9354
- Melting point: 1430 °C (1703 K)
- Boiling point: 2817 °C (3090 K)
- Heat of vaporization: 7450.0 kJ/kg
- Heat of fusion: 270.0 kJ/kg

The following properties are temperature dependent properties during solid state:

- Density, (kg/m^3):

$$\rho = 8084 - 0.4209\, T - 3.894 \times 10^{-5}\, T^2$$

- Heat capacity, [J/(kg·K)]:

$$C_p = 462 + 0.134 \times T$$

- Thermal conductivity, [W/(m·K)]:

$$\lambda = 9.248 + 0.01571 \times T$$

The following properties are temperature dependent properties during liquid state:

- Density, (kg/m^3):

$$\rho = 7433 - 0.0393\, T - 1.801 \times 10^{-4}\, T^2$$

- Heat capacity, J/(kg·K):

$$C_p = 775$$

- Thermal conductivity, [W/(m·K)]:

$$\lambda = 12.41 + 0.003279 \times T$$

3.2. Laser and Optics

3.2.1. Physical Specifications

The laser system employed for this research is an IPG Photonics continuous-wave laser system with a maximum power of 2.0 kW. The system comprises a multimode Ytterbium fibre laser (IPG YLS-2000-S2) equipped with an Ethernet interface for systems monitoring and control using LaserNet software cooled by a remote water-to-air chiller unit (IPG LC-71). The laser is connected via a multimode optical fibre to a vertical configuration welding head (IPG FLW-D30) with water-cooled collimating and focussing optics, which culminates with a downwards-facing copper nozzle. The chiller unit has a cooling capacityof 3.8 kW and delivers cooling water to the laser at 20 – 22 ^{o}C and to the laser optics at 27 – 33 ^{o}C.

Figure 26. The IPG YLS-2000 unit in the engineering building located within the Lancaster University: a) Laser unit (IPG YLS-2000-S2); b) Chiller unit (IPG LC-71).

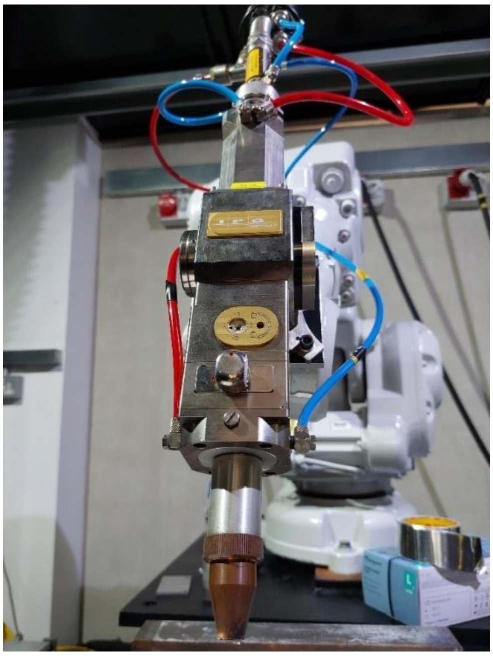

Figure 27. The welding head (IPG D30) mounted at the end of the ABB robotic arm.

3.2.2. Beam parameters

The beam parameters as supplied by the manufacturers IPG Photonics, are given in Table 1. Some of these are values inherent to the system, others are actual values, measured after installation of the system. Figure 28 shows the beam profile measured at the laser waist and further information from those installation measurements.

Table 1. Beam parameters

Beam parameter	Value
Beam wavelength	1068 – 1080 nm
Polarization	Random
Optical fibre diameter	100 µm
Beam Parameter Product (BPP)	3.94 mm.mrad
M^2	11.5
Minimum beam radius	0.14 mm
Beam divergence half-angle	28.9 µrad

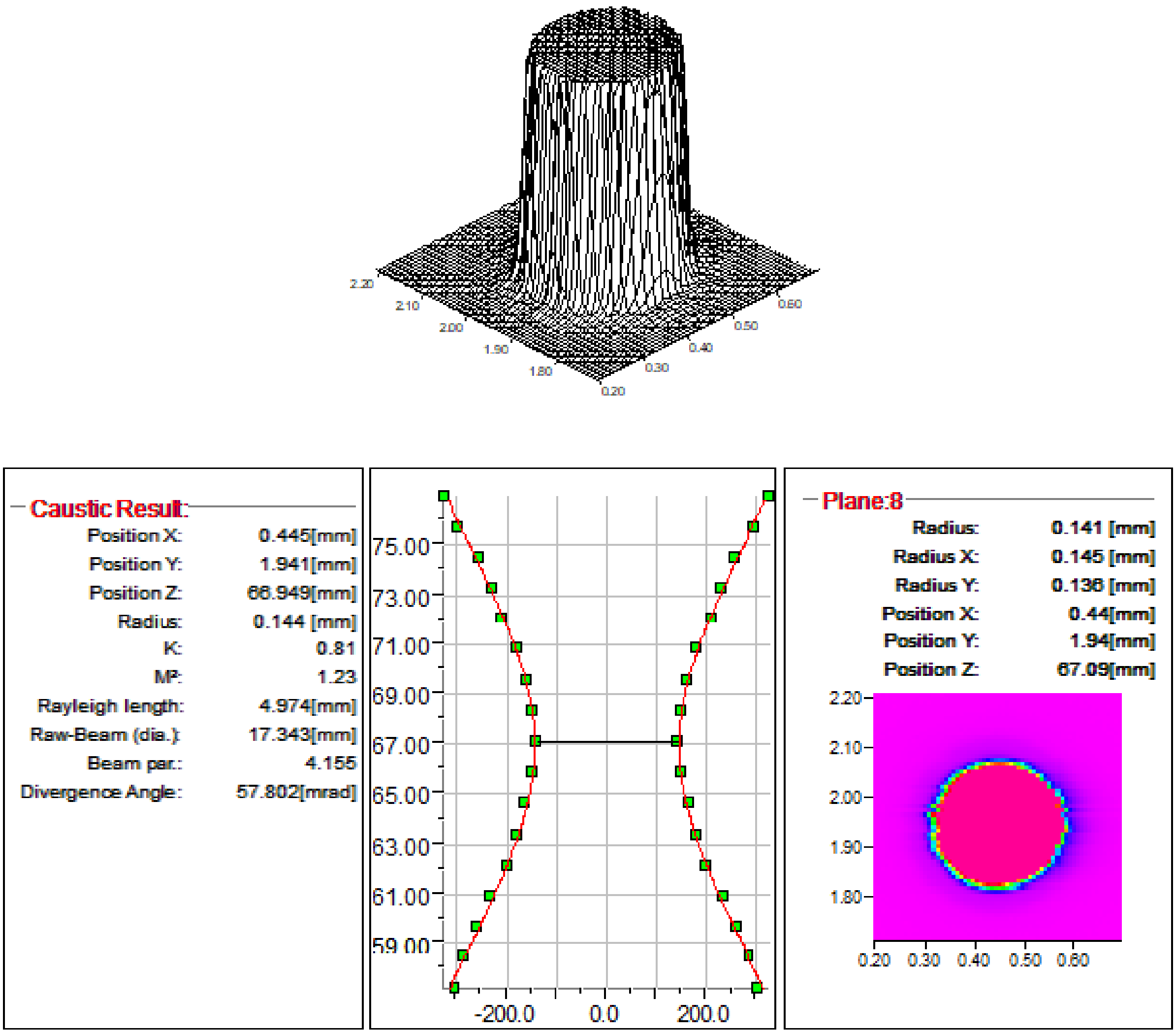

Figure 28. Detail information of the laser focus and the beam profile measured at the laser waist.

3.2.3. Beam focal position

Manufacturer's data and measurements did not position the beam waist on the axis relative to the end of the copper nozzle so an experiment was initially performed to establish this.

A 'burn test' method was employed: placing a material likely to be damaged by direct impact of the laser at different positions on the axis, exposing it to the laser for a brief period and then measuring the extent of the damage to determine the beam diameter. The experiment was carried out using plastic and then with metal plates sprayed with red paint. A laser power of 250 W is used, with an offset from the nozzle tip ranging from 3 to 30 mm; the offset is increased by 3 mm for each measurement. In the first set of experiments, an exposure time of 0.2 second is used. Following an understanding of the programming limits of ABB RobotStudio, a second set of experiments is carried-out using an exposure time of 0.1 second.

After conducting the experiments, all samples were taken to the metallography lab where the Leica digital microscope and Software Application Suite (LAS) allowed precise measurement of the laser damage (see section 3.5). Figure 29 is one of the results obtained. The measured results at each offset from the experiments was compiled and the mean value taken as the measured beam diameter.

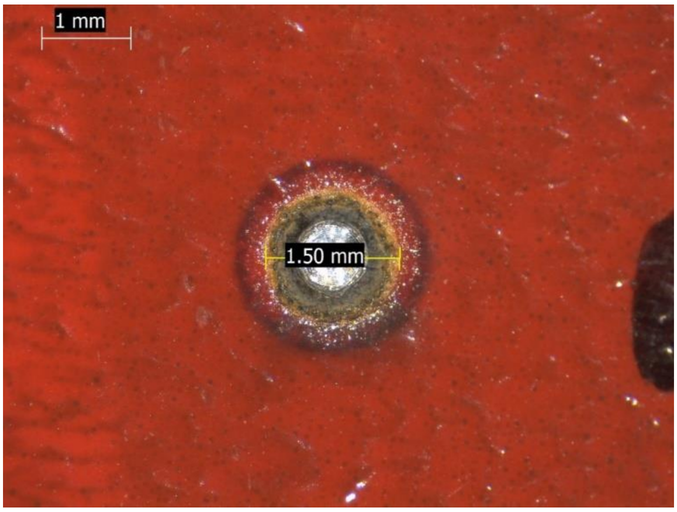

Figure 29. Laser ablation formed on a metal plate sprayed with red paint.

The theoretical beam profile was calculated from the information in Table 1, assuming the beam waist was positioned at the tip of the copper nozzle. Figure 30 compares the experimental and theoretical profiles. The curves are similar although the measured far-field divergence is slightly larger than the theoretical value (approximately 67 mrads compared to a theoretical value of 57 mrads) and the minimum radius slightly larger. These differences are possibly due to conducted heat damaging the samples beyond the limits of the beam and do not affect the experimental trends seen.

The minimum beam diameter shown experimentally occurred between 3 and 5 mm below the copper nozzle tip and it was thus concluded this was the position of the focal plane of the laser. Based on this, it will be possible to predict the beam diameter at different positions below the nozzle, a crucial input for the simulation models in this work. Placing a substrate at offsets of 3 mm or greater should be sufficient to act an outlet for shielding gas from the nozzle.

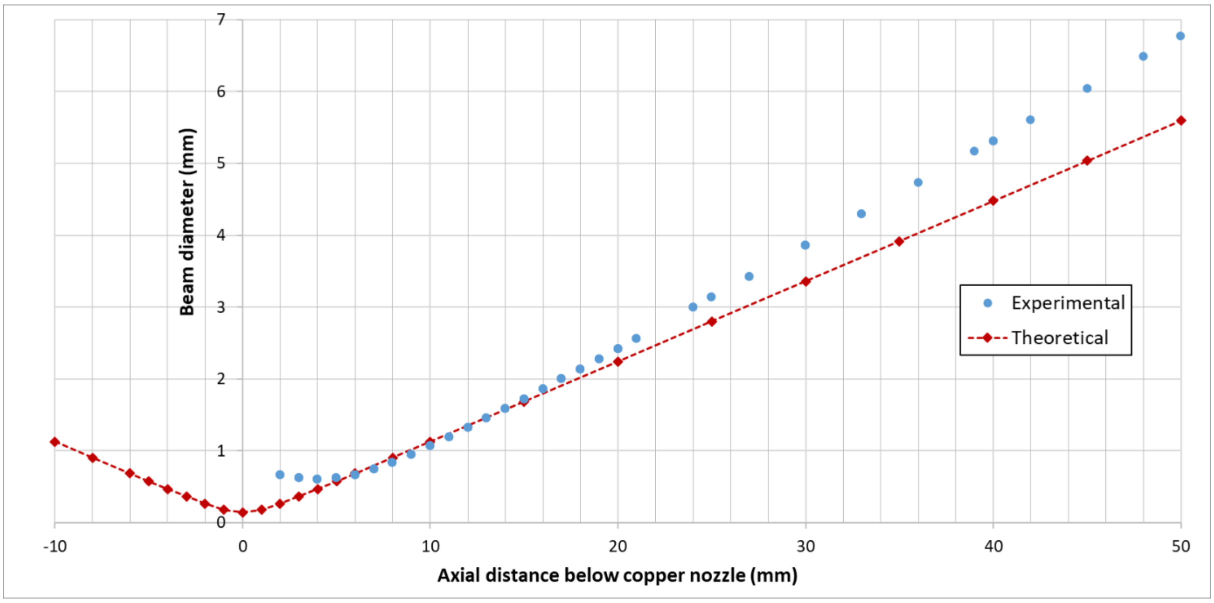

(a)

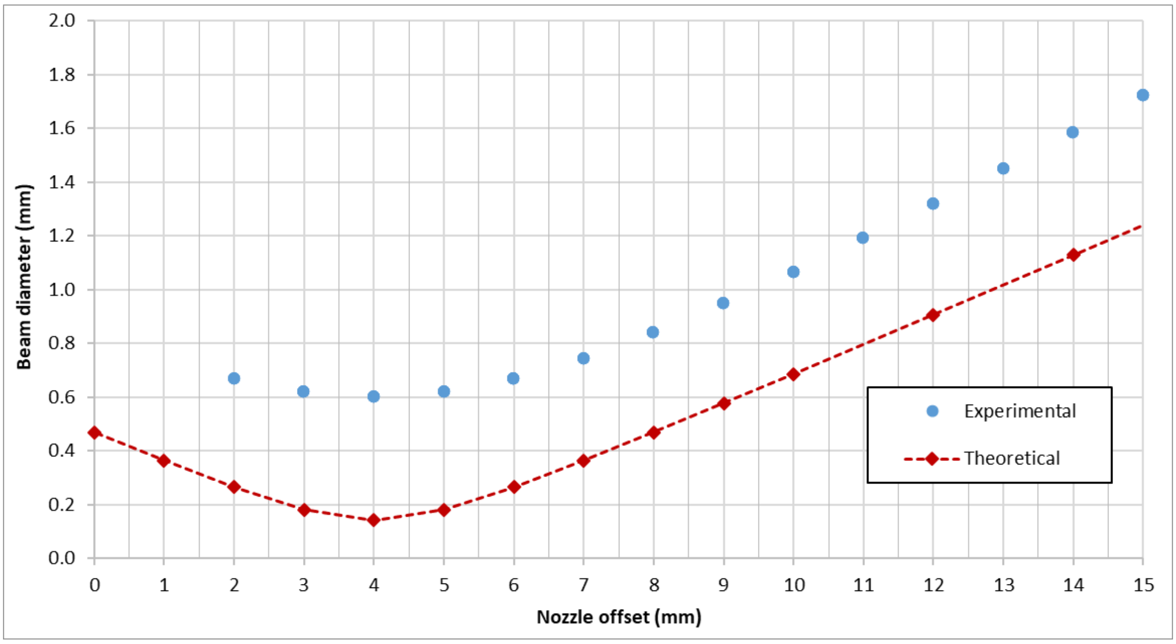

(b)

Figure 30. Beam diameters below the welding head nozzle (a) initial data, (b) fitted data for 4 mm beam waist offset.

3.3. Integrated Laser Processing System

The research involves a series of experiments, including laser absorptivity, laser melting and bead-on-plate welding experiments. To conduct these, an experiment setup comprising a the laser system from section 3.2, a 6-axis robot, a safety enclosure and coordinating computers was used. The system is shown schematically in Figure 31.

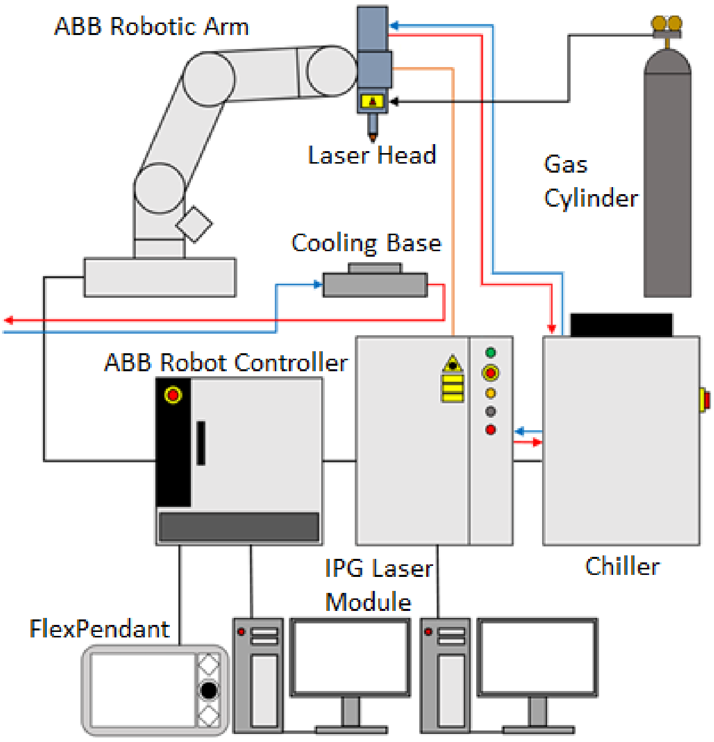

Figure 31. Schematic diagram of the Integrated Laser Processing System

The motion system for processing is a 6-axis robot manufactured by ABB Robotics. It controls the laser scanning speed and positioning the laser focal point. Integration with the laser system is achieved through the RobotStudio software package, which allows control of the robotic arm movement plus most laser parameters through the RAPID programming language.

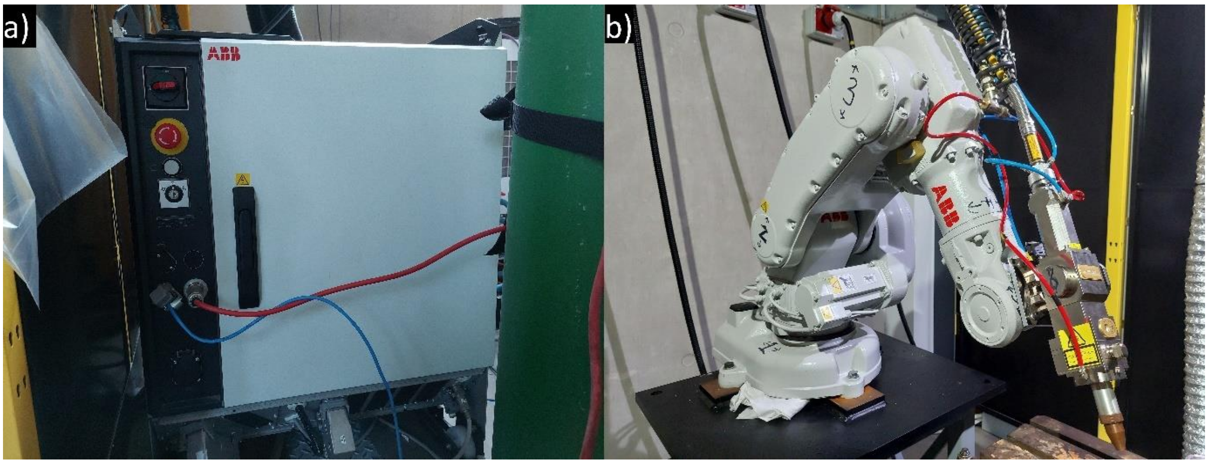

Figure 32. The ABB Units used in this work: a) IRC5 Industrial Robot Controller; b) ABB IRB140 6-axis robot, with IPG laser head

Control of the combined laser-robot system was from a desk installed with two desktop computers, one connected to the IPG laser system and the other to the ABB robotic system. The dedicated IPG computer displayed the controls and feedback information from LaserNet software. dedicated ABB robotic system used two monitors: the first displayed the RobotStudio software for controlling and programming the robot's movements and the laser firing mechanism, the second showed the conditions within the safety chamber that fully enclosed the experimental area.

Figure 33. The control desk used in the experiments.

3.4. Post-processing of laser melted samples

After the laser melting experiment, all samples underwent several post-processing steps. A bandsaw was initially used to cut the substrate into workable size samples. These were then mounted with in black resin using a fully automated hot mounting press machine known as an OPAL 410 machine manufactured by QATM company (Figure 34a).

After mounting, samples were ground and then polished using a SAPHIR 520 machine, also manufactured by QATM (Figure 35). This fully automated machine can process up to 5 samples simultaneously.

During the grinding and polishing process, the following consumables were used:

- Silicon carbide grinding papers with plain backs adhering to FEPA (grain) standards: P240, P600, P800, P1200 and P2500.
- Polishing cloth mounted on a magnetic foil.
- Diamond paste (syringe) with grain sizes of 1 µm and 6 µm

- QPREP diamond lubricant in yellow (water-based)

(a) (b)

Figure 34. (a) An OPAL 410 hot mounting press and (b) an example mounted sample

Figure 35. The SAPHIR 520 in action during the polishing process.

After completing the grinding and polishing process, all the samples were transferred to the chemical laboratory for etching. Here, samples were etched in Kalling's No.2 Reagent, prepared using the following components:

- Cupric Chloride ($CuCl_2$) 3 g
- Hydrochloric acid 6 ml
- Isopropanol alcohol 56 ml

Work with this reagent indicates that Cupric Chloride controls the final image brightness, while hydrochloric acid regulates the reaction rate and erosion. During the etching process, there were two distinct stages after the reagent was added to the surface via dropper or swab. In the first stage, the top layer of the surface was removed, revealing the microstructure of the melt track; in the second stage, further erosion and darkening occur, resulting in excessive darkening of the revealed surface, reducing the visibility of the melt track and microstructure after etching is stopped by rinsing the sample under water..

To achieve desirable results, precise timing of a rinsing process is crucial, as it needs to happen between the two erosion stages. Using 6 ml of hydrochloric acid, a lower proportion than appears in many references for this reagent, was found to provide the optimum reaction rate. The first stage of erosion did not take too long, while the second stage of erosion does not immediately follow, allowing sufficient time for the rinsing process.

3.5. Microscopy and image capture

After completing the post processing process involving grinding, polishing and etching, the samples are taken to the metallography laboratory for microscopic observation and analysis.

A Leica DM2700 M Upright Materials Microscope with a Leica DFC295 digital microscope colour camera attached was used for image capture (Figure 36). The microscope is designed specifically for material analysis with a focus on high-resolution imaging of surface structures and materials. This model includes advanced features like LED illumination for consistent and bright lighting, essential for reducing sample heating during prolonged observation. The objective lenses provide a magnification of 5x, 10x, 20x, 50x, and 100x. With this magnification range, the microscope allows precise examination of microstructural details.

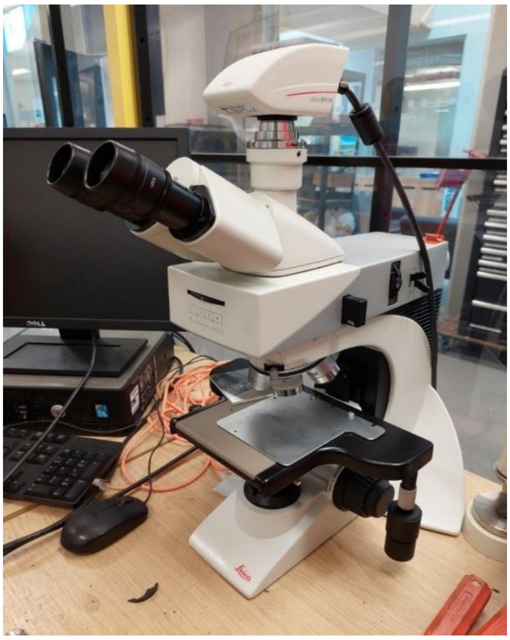

Figure 36. The Leica DM2700 M Upright Materials Microscope with DFC295 digital microscope colour camera attached.

For image capture, a Leica DFC295 Digital Colour Camera was mounted in place of the standard camera on the Leica DM2700 M microscope. This 3-megapixel digital colour camera enhances imaging capabilities by delivering high-quality colour representation, which is essential for detailed material analysis. The camera supports real-time viewing and adjustable exposure settings, critical for effectively documenting findings and adjusting for variations in sample composition.

The camera was connected to a desktop computer with the Leica Application Suite (LAS) software installed. The LAS software was used for image acquisition, preview, and archiving. This software not only allows real-time monitoring of images on a desktop monitor but also includes advanced features such as image stitching. In this work, higher magnifications such as 20x limited the visible field to only a section of the microstructure so the stitching function proved especially valuable as it enabled the creation of a single, continuous image that provided a comprehensive view of the entire microstructure, revealing details that would otherwise be unobservable. it also allows precise measurement of samples and features by input of the magnification used during image capture.

4. Conduction-based welding and surface melting

4.1. Introduction

Laser welding is a welding technique that uses a laser beam as a heat source to melt materials and join separate parts through the re-solidification of the molten material. By adjusting the power intensity, the heat flux on the designated surface can be controlled, allowing for precise modification of the cross-sectional shape of the melt track and the penetration depth achieved during welding.

As the power of a laser moving on a metal surface increases, there is a transition from heating-only to melting, with an oval shape, (conduction mode), to a nail-shaped profile (keyhole mode). This occurs when the material temperature exceeds its boiling point, leading to vaporization. The resulting vapor pressure causes the laser beam to drill into the substrate, forming a keyhole, which significantly alters the heat transfer and penetration characteristics.

This chapter focuses on conduction-based laser welding, which occurs at lower laser intensities and does not involve keyhole formation. Figure 37 illustrates the conduction mode laser welding process. In this study, the laser power range for conduction-mode welding is set between 200 W and 250 W, as power levels exceeding 250 W were found to initiate the transition to keyhole mode.

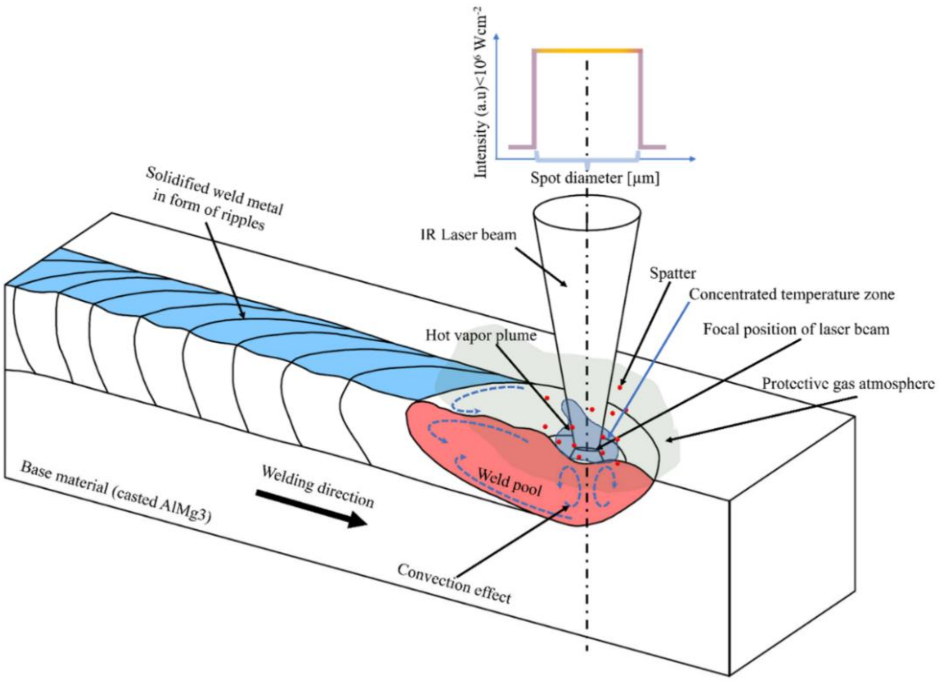

Figure 37. Schematic representation of laser welding process in conduction mode [133].

The chapter will develop a series of models, beginning at the most basic and then sequentially adding additional features. This will allow testing at each stage to assess if newly introduced complexities are operating correctly. For convenience, models are labelled M1, M2, M3…The models are be based on an orthogonal axis system, with the origin at the first intersection of the substrate and laser axis and the laser considered to move in the positive y direction.

4.2. Single phase conduction model, M1

4.2.1. Model Design

A numerical simulation model with a single moving heat source has been developed. The moving heat source comprises the following properties:

- Circular heat flux, representing a circular laser beam
- Evenly distributed heat flux, simulating a flat-top laser beam

To simulate the movement of the heat source, the simulation is divided into numerous cycles, depending on the distance travelled and the time required for each time step (within each simulation cycle). This approach aims to ensure a smooth flow of heat flux across the surface, rather than a 'jumping' heat flux movement. Striking a balanced between two key factors is crucial:

- Achieving smooth heat flux movement: Smaller time step result in smoother movement.
- Maintaining an acceptable simulation duration: Shorter simulations require longer time steps and fewer simulation cycles.

This simulation model is created with the following assumption:

- The mass remains constant throughout the entire simulation process.
- There is no phase change between solid, liquid and gas during the entire simulation process.

Figure 38 shows a simplified simulation flowchart for the model.

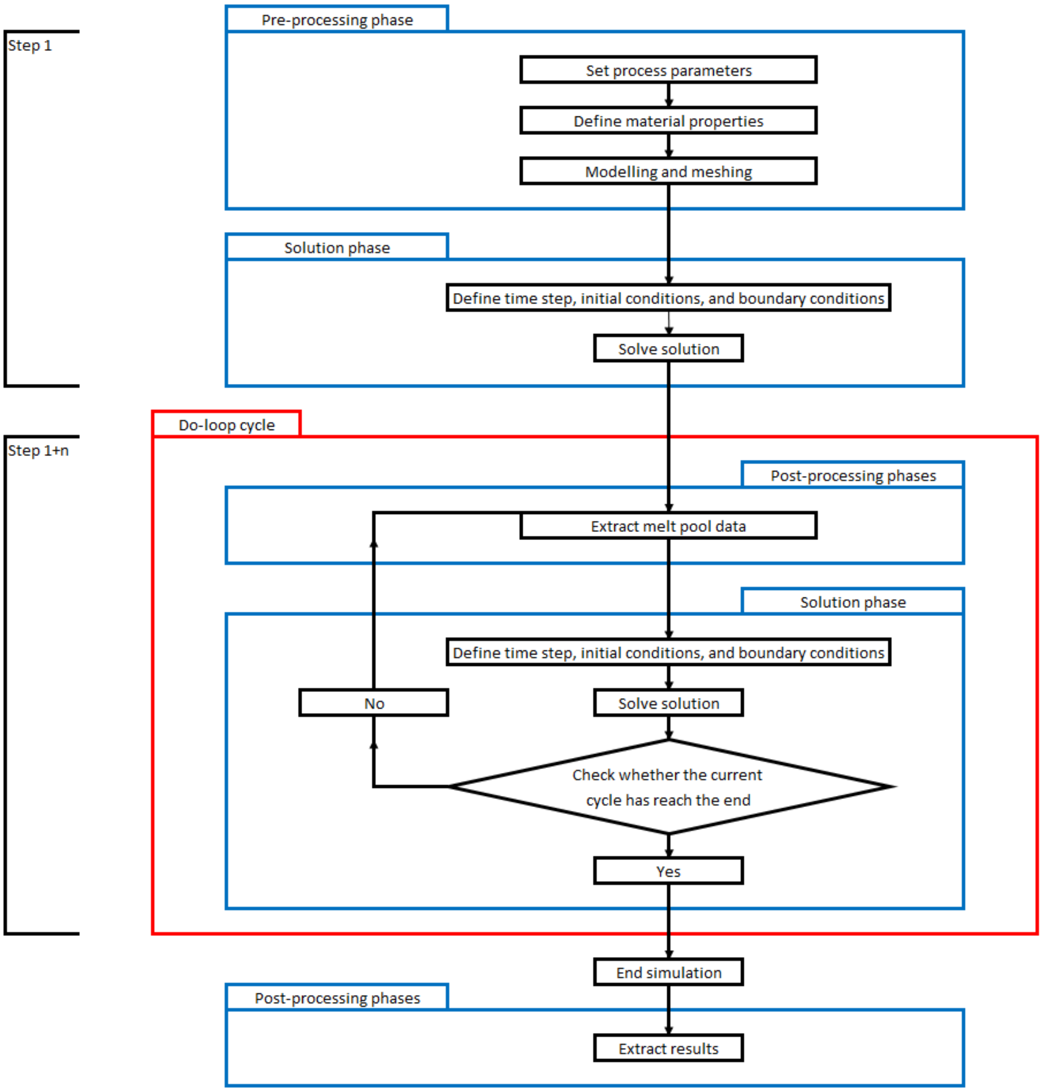

Figure 38. Simplified representation of the first model. (n stands for number of cycles after the first)

The boundary conditions used throughout the simulations are as follows:

1. Initial Temperature:

   The entire volume of the model is assigned an initial temperature value representing the ambient temperature of the surrounding environment before the simulation begins.

2. Convection Conditions:

   Five out of the six surfaces are subjected to convection conditions to simulate natural heat loss due to the convection process.

   Convection coefficient used: 20 $W/m^2 \cdot K$

3. Symmetry Constraint:

The remaining surface, which does not have convection conditions applied, is defined with a symmetry constraint. This is because the model is designed to represent half of the actual volume/geometry, thereby reducing computational resource requirements.

4. Heat Flux Application:

Heat flow fundamentals in Ansys APDL follows the first law of thermodynamics, states that thermal energy is conserved.

$$\rho c\left(\frac{\partial T}{\partial t}+\{v\}^T\{L\}^T\right)+\{L\}^T\{q\}=\ddot{q}$$

Where,

$$\begin{array}{ccc}
\rho & = & density \\
c & = & specific\ heat \\
T & = & temperature \\
t & = & time \\
\{L\} & = & \begin{Bmatrix} \frac{\partial}{\partial x} \\ \frac{\partial}{\partial y} \\ \frac{\partial}{\partial z} \end{Bmatrix} = vector\ operator \\
\{v\} & = & \begin{Bmatrix} v_x \\ v_y \\ v_z \end{Bmatrix} = velocity\ vector\ for\ mass\ transport\ of\ heat \\
\{q\} & = & heat\ flux\ vector \\
\ddot{q} & = & heat\ generation\ rate\ per\ unit\ volume
\end{array}$$

Along the edge where the convection surface meets the surface defined with the symmetry constraint, heat flux is applied to the top ‘convection’ surface to represent the heat input from the laser beam interacting with the substrate surface.

The heat flux area is determined based on the laser beam diameter, where a semicircular surface area is selected to overwrite the convection condition with the heat flux condition.

The heat equation used in the first simulation cycle is as follows:

$$Heat\ Flux=\left\{\frac{Used\_Laser\_Power\times\left[\frac{(Laser\_Absorption+Surface\_Absorption)}{2}\right]}{(\pi\times(Heat\_Radius)^2)}\right\}$$

After the first cycle, once the initial heat flux has triggered the system and the temperature profile has reached the desired condition, allowing the keyhole logic system to function, a second set of heat flux equations is applied to overwrite the first:

$$Top\ Surface\ Heat\ flux=\left\{\frac{(Used\_Laser\_Power\times Surface\_Absorption)}{(\pi\times(Heat\_Radius)^2)}\right\}$$

$$Keyhole\ Heat\ Flux = \left\{\frac{[Used\_Laser\_Power \times (Laser\_Absorption - Surface\_Absorption)]}{KHoleInterior\_Area}\right\}$$

Heat Flux : Represents the heat source from the laser beam interacting with the top surface.

Top Surface Heat Flux : The heat flux applied to the top surface area.

Keyhole Heat Flux : The heat flux applied to the side surface area where the symmetry constraint function is applied.

Used_Laser_Power : The heat energy from the laser beam.

Laser_Absorption : The total laser absorption for the entire model.

Surface_Absorption : The laser absorption on the top surface.

Heat_Radius : The radius of the laser beam.

KHoleInteriar_Area :The area representing the keyhole formed during the laser welding/melting process. In this simulation, the dimensions used to calculate this area are determined by the keyhole logic system, which takes the temperature profile obtained after each simulation cycle as input.

This simulation model consists of three main sections. The first section, referred to as 'Step 1' in Figure 38, begins with the pre-processing phase. During this phase, all the necessary process parameters and input temperature dependent material properties for the model is defined. Once all the values for process parameters and material properties are defined, the programmed code proceed to establish the model's dimension and initiate the meshing process. This concludes the pre-processing phase and transitions to the solution phase.

In the solution phase, the initial time step and conditions required for the simulation, such as simulation properties and the initial starting temperature, are defined. Subsequently, the boundary conditions, including heat flux properties and convection conditions, are specified. Finally, the solve function is initiated and the simulation is performed.

The second section, referred to as 'Step 1+n' in Figure 38, commences with the post-processing phase. During this phase, the results required for subsequent simulation cycles are extracted. Once all necessary information has been extracted, the simulation proceeds to the solution phase.

In this phase, the time step and conditions for the simulation are defined. Instead of specifying the initial starting temperature, the temperature results from the previous simulation cycle are used as the starting temperature for this cycle. Subsequently, the boundary conditions are redefined and the solve function is initiated to run the simulation.

Upon completing the current simulation cycle, the system enters a checking process to determine if it has reached the final cycle. If the simulation has not reached the final cycle, the system triggers a do-loop function and initiates the next simulation cycle by repeating the post-processing and solution phases mentioned earlier.

Once the simulation completes the final cycle and passes the checking process, it exits the do-loop cycle. At this stage, it enters the third and final section. In this section, only the post-processing phase is present, where all result data will be extracted and stored.

4.2.2. Experimental verification

A laser absorption experiment was conducted using stainless steel plates measuring 50 mm X 20 mm X 3 mm in dimensions. Before the experiment, all stainless-steel plates were sandblasted and cleaned with isopropanol. Sandblasting was performed to enhance the laser absorptivity of the stainless steel since the material originally had a smooth and shiny surface, indicating high reflectivity.

Prior to commencing the experiments, three thermocouples were attached underneath the stainless-steel plate. One thermocouple was affixed at the centre of the plate, while the other two were positioned 10 mm apart on each side along the designated path where the laser was intended to move. A CompactDAQ module and a DAQ chassis by National Instruments were used to receive voltage generated by the thermocouples and convert it into digital signals. These signals were then sent to a computer with LabView software installed for further interpretation and recording.

Table 2 and Figure 39 show temperature data collected by the three thermocouples for cases involving different laser powers and scanning speeds. From Figure 39, it is noticeable that some readings from the thermocouple appear inconsistent and scattered. This may be attributed to the poor contact between the thermocouple and the bottom surface.

Table 2. Peak temperatures measured by each sensor for laser power of 200W and 250W at scanning speed of 12, 16, 20, 24, 28 mm/s.

Laser power, W	200	200	200	200	200
Speed, mm/s	12	16	20	24	28
sensor 1, °C	32.2	31.5	30.1	28.1	27.5
sensor 2, °C	29.8	30.1	32.5	24.3	27.9
sensor 3, °C	27.3	29.7	26.5	23.0	27.3

Laser power, W	250	250	250	250	250
Speed, mm/s	12	16	20	24	28
sensor 1, °C	39.4	37.5	31.5	28.3	29.6
sensor 2, °C	40.0	31.8	29.6	26.2	27.7
sensor 3, °C	28.5	33.5	25.9	24.2	24.3

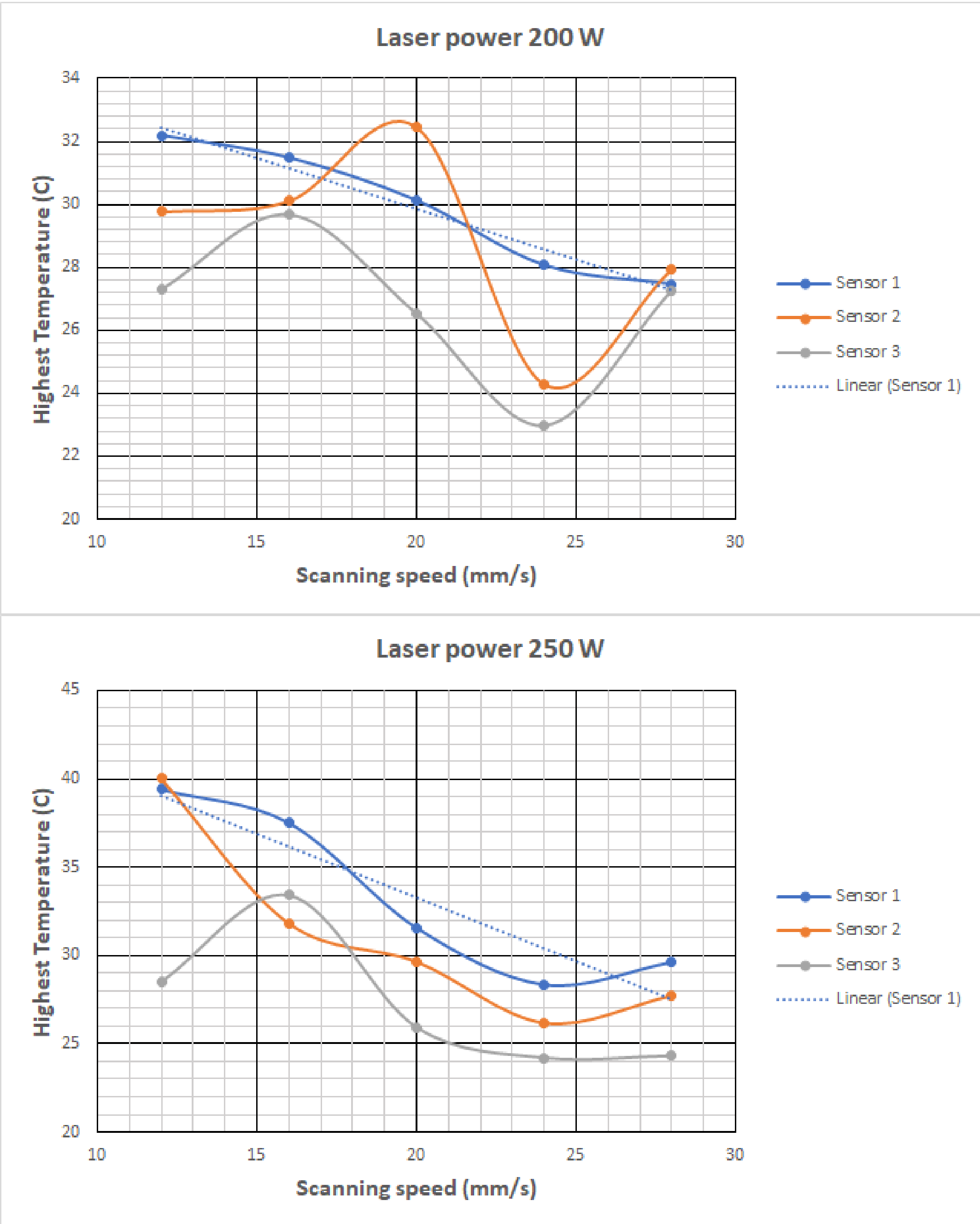

Figure 39. Temperature data collected at different laser powers and scanning speed.

4.2.3. Comparison of M1 modelled and experimental results

To compare the modelled and measured results for the laser absorptivity, multiple simulations were conducted. Table 3 shows the results and compares experimental and M1 simulated temperature results (measured in Celsius). The section highlighted in red represents a comparison of results that indicate an absorption rate greater than 100%, which is not possible due to the law of conservation of energy. For cases involving laser power of 200 W and scanning velocity between 12 mm/s and 24 mm/s, the absorption rate increases from 0.3 to 1.0. for cases involving laser power of 250 W and scanning velocity between 12 mm/s and 24 mm/s, the absorption rate increases from 0.4 to 1.0.

Table 3. Comparison between experimental and M1 simulated temperature data.

Absorption Experiment		Simulated temperature, °C				Experimental temperature, °C		Prediction	
Laser Power	Scanning Velocity	0.25	0.35	0.45	0.55	0.2	0.6	Absorption	
200 W	12 mm/s	28.9	33.1	37.2	41.4	32.2	32.2	0.325	
200 W	16 mm/s	24.7	27.1	29.6		31.5	31.5	0.52	
200 W	20 mm/s	22.3	23.7	25.2		30.1	30.1	0.78	
200 W	24 mm/s	20.9	21.8	22.7	23.6	28.1	28.1	1	
200 W	28 mm/s	20.1	20.6	21.2		27.5	27.5	1	Limit
250 W	12 mm/s	31.5	36.7	42.0	47.2	39.4	39.4	0.4	
250 W	16 mm/s	26.2	29.2	32.3		37.5	37.5	0.61	
250 W	20 mm/s	23.2	25.0	26.9		31.5	31.5	0.73	
250 W	24 mm/s	21.5	22.6	23.7	24.8	30.0	30.0	1	
250 W	28 mm/s	20.4	21.1	21.8		29.6	29.6	1	Limit

The predicted absorption is determined by identifying the intersection point between two lines, where one line represents the experimental results and the other represents the simulated results. This is shown in Figure 40. For the first case (200 W, 12 mm/s), the predicted absorption is 0.325 (or 32.5%), as the intersection between the two lines occurs at the coordinates X=0.325 and Y=32.193. Further work is needed because the results of the temperature comparison are not fully conclusive.

After completing with the temperature measurements, another experiment was conducted using a stainless-steel block measuring 70 mm X 68 mm X 10 mm in dimensions. Prior to the experiment, all stainless-steel block were sandblasted and cleaned with isopropanol. The choice of a 10 mm thickness, as opposed to 3 mm, was made because all samples obtained from this experiment will undergo cutting and mounting at a later stage. This would not be feasible with a thin plate as it cannot stand upright during the mounting process. The 3 mm thickness used during the temperature measurement experiment was intended to detect obvious temperature changes during the laser melting process. Using a thicker substrate block would result in less noticeable temperature variation, as most of the heat would conduct away before reaching the bottom surface.

Similar as the experiment earlier. two different laser power (200 W and 250 W) and a range of scanning speed (12, 16, 20, and 24 mm/s) is chosen for this experiment. After finishing the experiment, all samples were cut into smaller pieces. They were then mounted, ground, polished, and etched before viewing under the microscope.

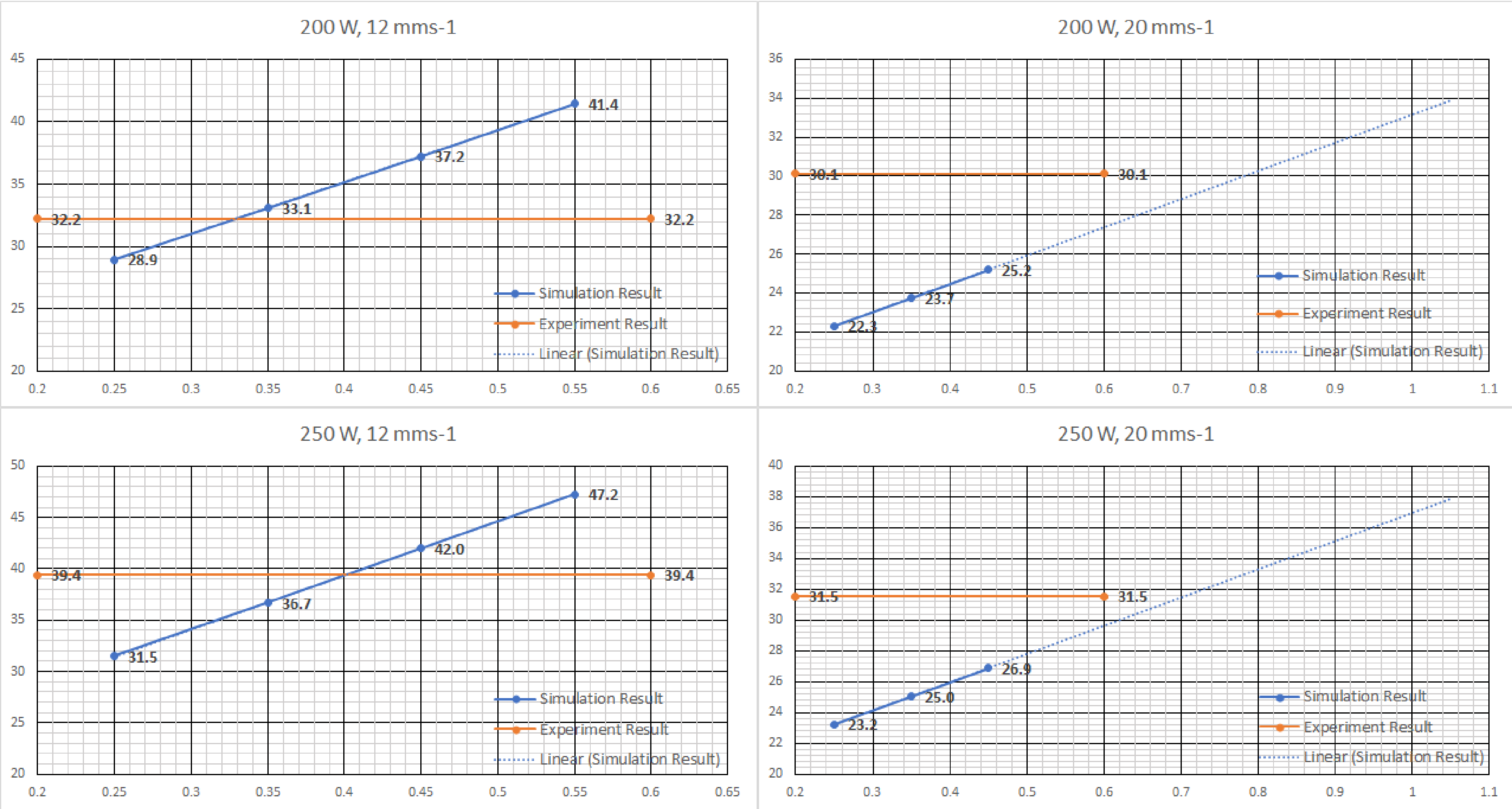

Figure 40. Graph of comparison between experimental and simulated results.

Figure 41 is a cross-sectional view of a melt track form under the laser power of 200 W and a scanning speed of 12 mm/s. The cross-sectional area and the dimension of the melt track is measured using the Leica DFC295 microscope and LAS software.

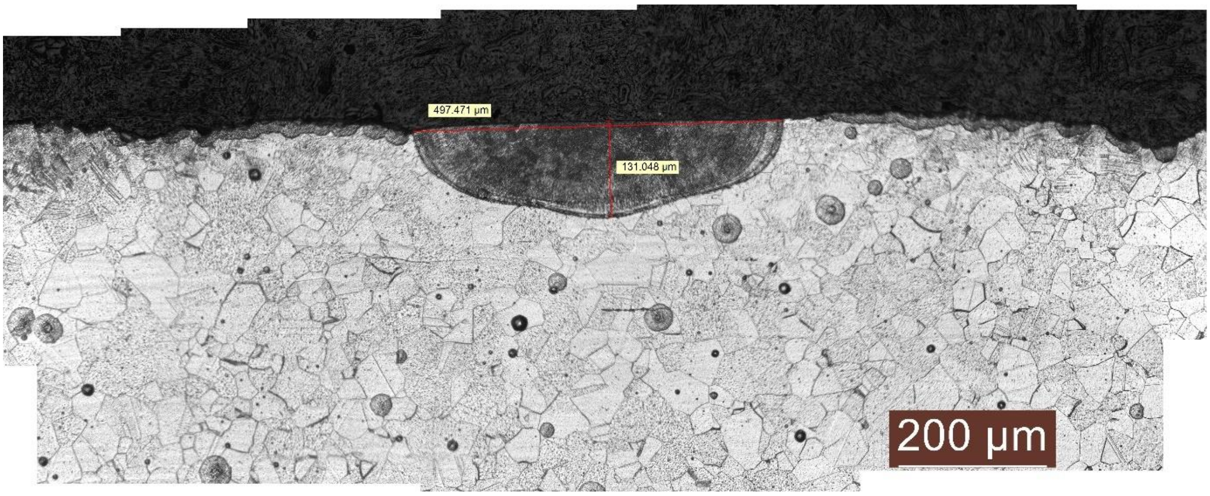

Figure 41. The cross-section of a melt track prepared at 200 W and 12 mm/s.

In the series of simulations using the first model to obtain the laser absorptivity, the dimensions of the melt track from the cross-section (as shown in Figure 41) were compared; however, the simulation results showed that the cross-sectional geometry of the melt track did not match the experimental results.

Microscopic images captured from the experimental samples clearly show a semi-oval-shaped melt pool, where the half-width ('surface radius', or semi-major axis if the melt pool is considered a half ellipse) is greater than the depth of the melt pool. Additionally, the cross-sectional results from the simulations show a melt track with a width slightly larger than the radius of the laser beam. Even though, as shown in Figure 42, the half-width-to-depth ratio in the experimental results (1.9:1) and the simulation results (2:1) for an absorptivity of 0.35 are closely comparable, the size of the cross-sectional melt track does not match the experimental observations.

This deviation occurred because the simulation model does not account for Marangoni flow or convection effects, which play a crucial role in expanding the melt pool horizontally. In laser melting and welding, surface tension gradients—caused by temperature variations—induce a convective flow within the melt pool, known as the Marangoni effect, which redistributes molten material outward, increasing the melt pool's width relative to its depth. As a result, experimental observations typically show a shallow melt track with a semi-oval geometry, where the half-width (radius) is greater than the depth.

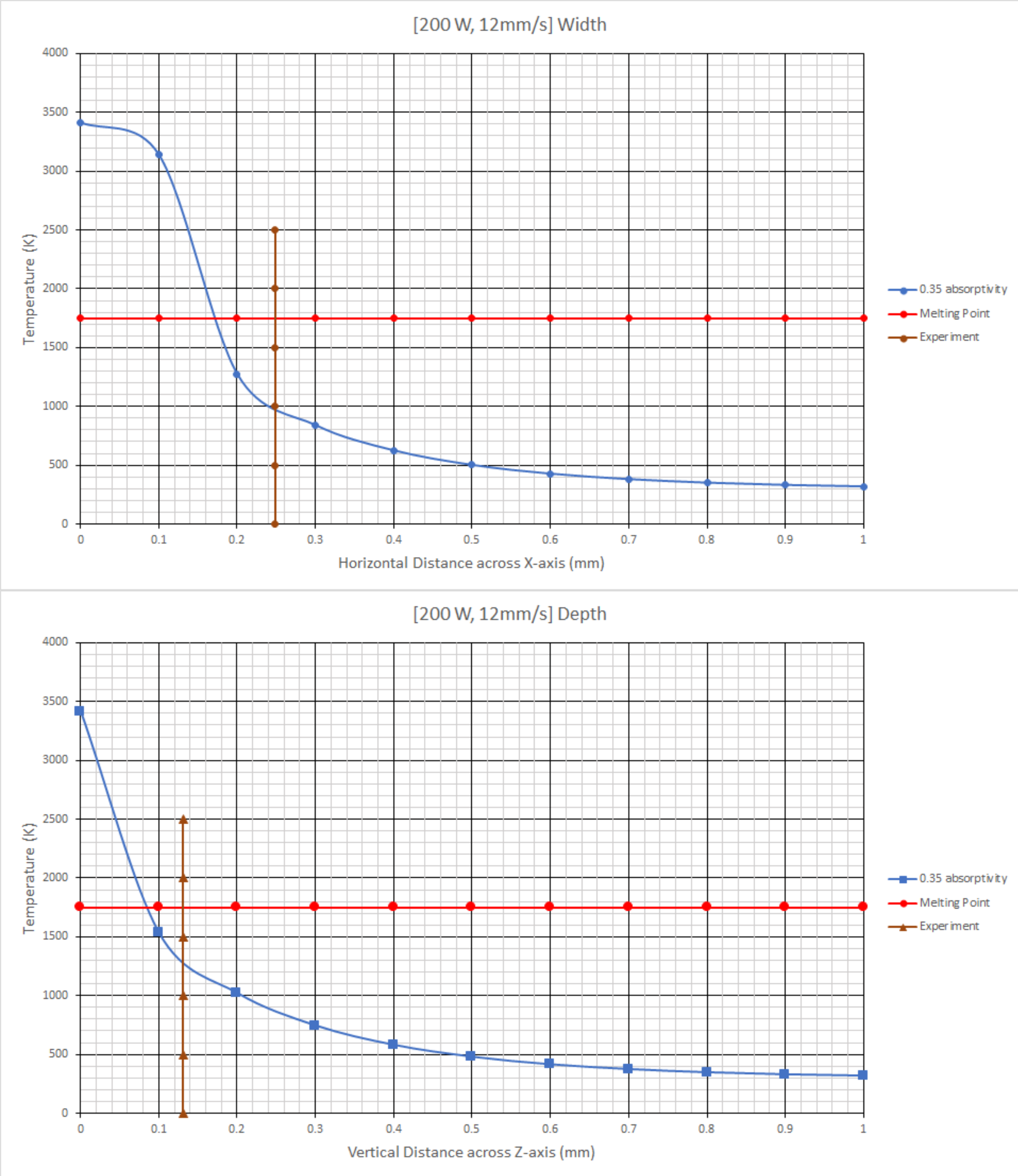

Figure 42. Simulation results of melting experiment with absorptivity of 0.35, using laser power of 200 W and velocity of 12 mm/s.

Although the half-width-to-depth ratio in the simulation is similar to that observed in the experiments, this similarity is likely coincidental. Since the simulation lacks fluid flow effects, the slight increase in width seen in the results is more likely due to direct laser heating rather than convective redistribution. Furthermore, as the width of the simulated melt track is only slightly larger than the beam diameter, it suggests that the melt track dimensions are due to the laser beam alone rather than any redistributive flow mechanisms. Additionally, the overall cross-sectional size of the simulated melt track is still smaller than the experimental results, further emphasizing the limitations of the current model in capturing the full extent of the melting dynamics.

4.3. Enhanced conduction model, M2

4.3.1. Introduction

Scientific literature indicates that conduction-based melting doesn't always result in a semi-circular shape when viewed in cross-section. The dimensional value obtained for the width of the melt track is usually larger than that for the depth of the melt track or that predicted purely by heat conduction simulation due to heat flow movement in the melt pool.

To compensate for the inaccuracies identified in section 4.2, the second model, M2, includes a change in thermal conductivity for the liquid phase. This accounts for the increased heat flow by convection due to intrapool fluid flow. M2 does this via anisotropic conductivity enhancement. This develops the anisotropic enhanced thermal conductivity approach first identified by Safdar et al. [101].

4.3.2. Model design

An overview of the second model, M2, is provided in Figure 43. Building upon model M1, shown in Figure 38, this model incorporates the functionality to modify the material's thermal conductivity during the simulation process. The modification enables it to compensate for the increased heat transfer due to flow movement in the melt pool. The model's simplicity without the need to introduce complex fluid flow mechanisms is maintained.

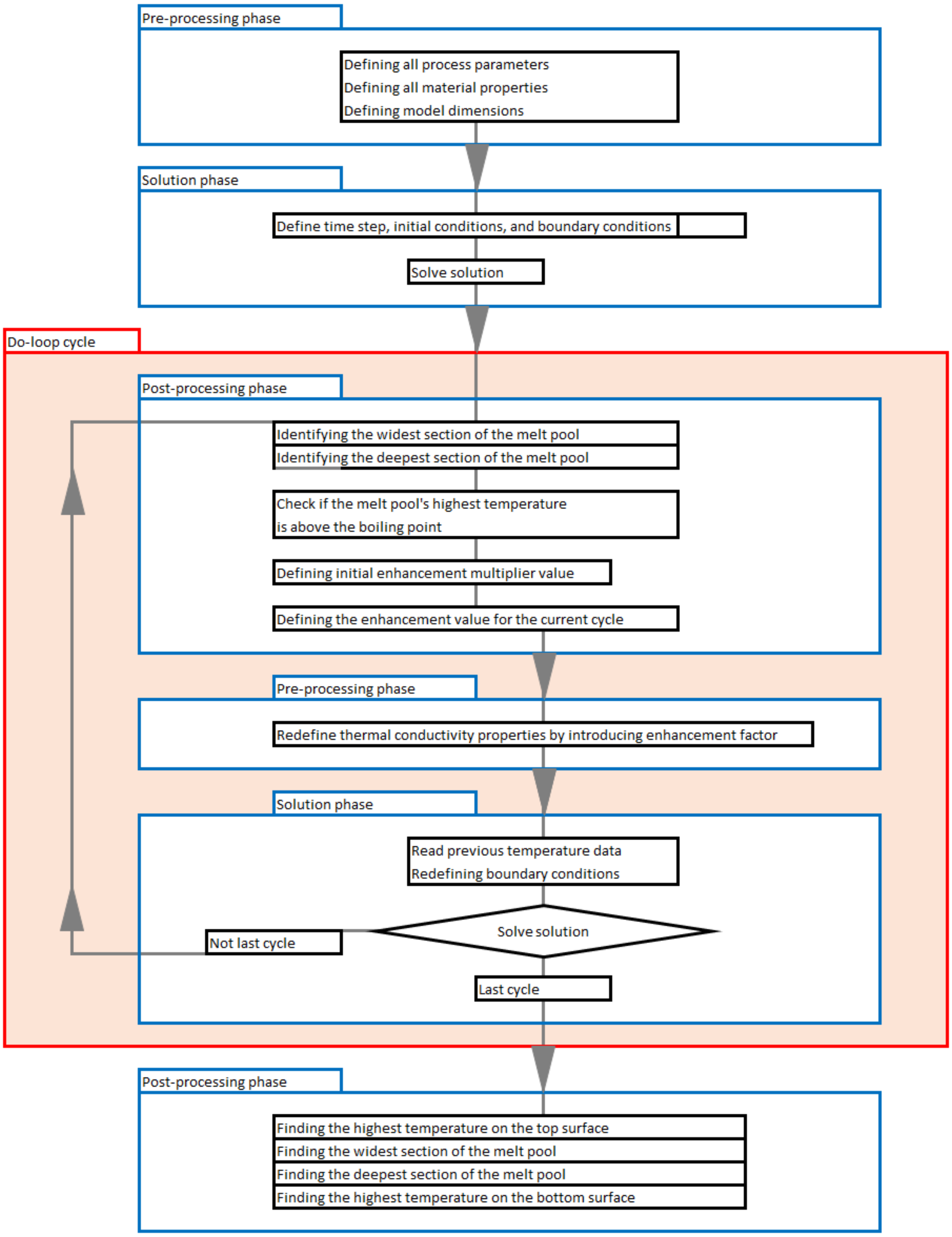

Figure 43. Simulation flowchart for the second, M2, model to run conduction-based laser melting/welding process.

The first cycle depicted in Figure 43 is shown in more detail in Figure 44. This section initiates the initial cycle of the simulation, a critical step as it establishes the foundational temperature data for subsequent simulation processes involving modifications to material properties.

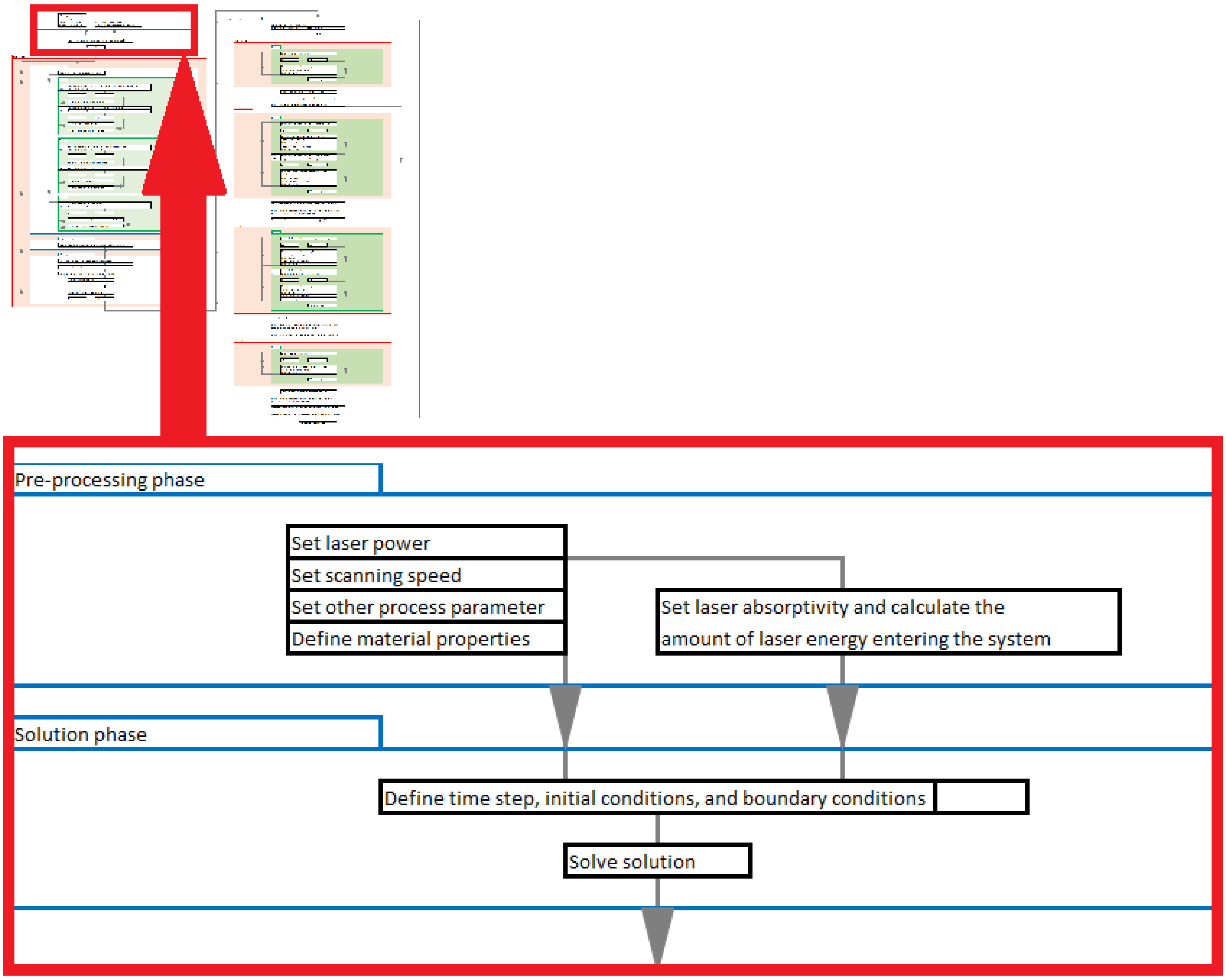

Figure 44. First cycle of the simulation process.

Within the first cycle shown in Figure 44, two distinct simulation phases are introduced: the pre-processing phase and the solution phase. In the pre-processing phase, all properties, including process parameters and temperature-dependent material properties, are defined before commencing the simulations. Subsequently, the model is constructed based on the dimensions and mesh properties inputted earlier.

Upon entering the solution phase, the simulation properties and boundary conditions are established. The solution phase concludes when the 'Solve' command is executed, and any remaining boundary conditions are cleared.

Figure 45 presents the first half of the loop cycle, which follows the initial cycle shown in Figure 44. This section comprises of three 'if-functions' (highlighted by three green boxes) within the post-processing phase.

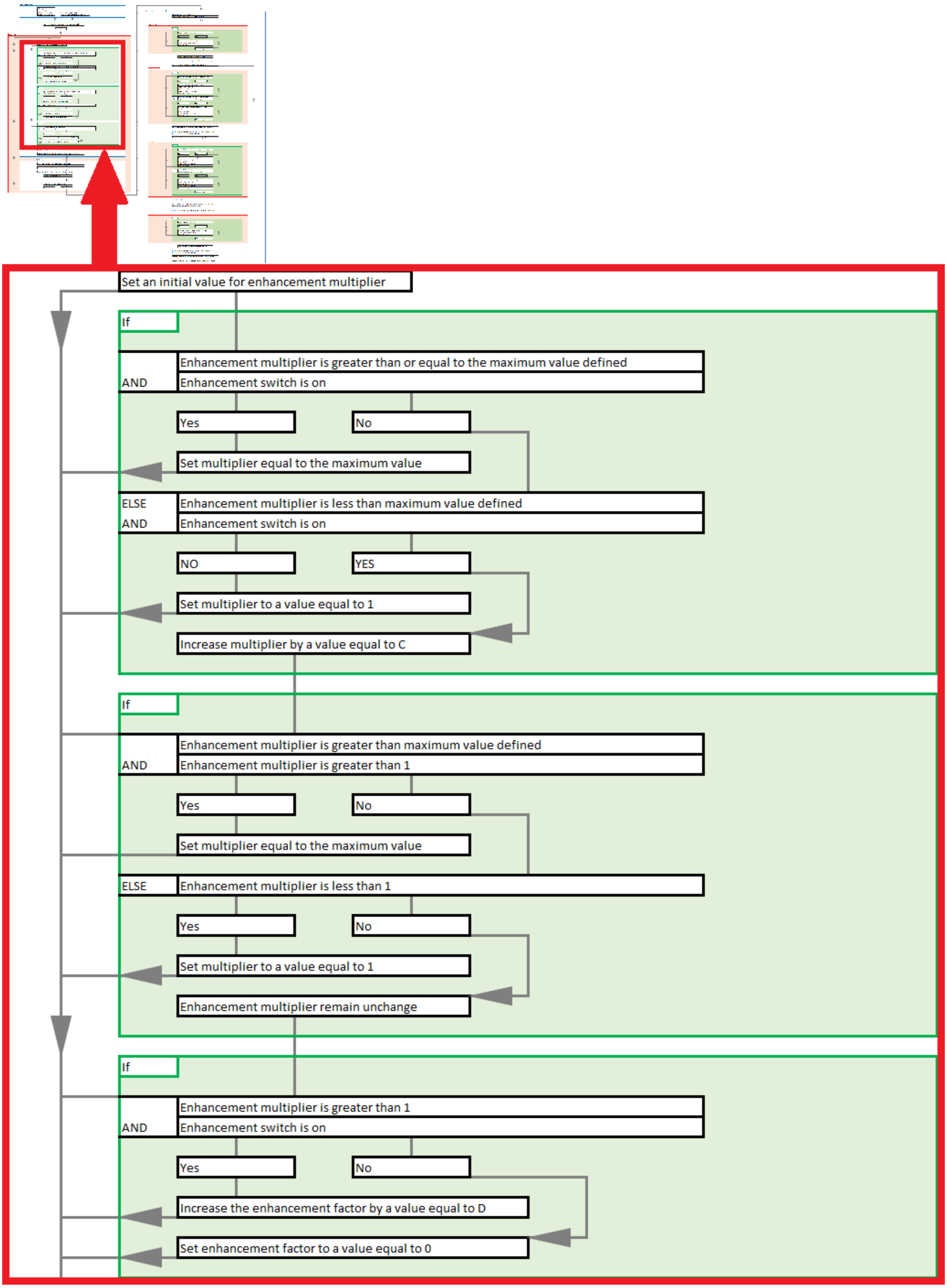

Figure 45. First half of the loop cycle of the simulation process.

The first 'if-function' governs modifications to the thermal conductivity properties of the material in the x, y, and z directions. Three different outcomes are established based on the conditions fulfilled by the results from the previous cycle.

Upon entering the first 'if-function', the results are checked against the following conditions:

- The enhancement multiplier is greater than or equal to the maximum value defined.
- The enhancement switch is on.

If both conditions are met, the thermal conductivity multiplier is set to the maximum value defined before the start of the simulation. Otherwise, the results are checked against the next set of conditions:

- The enhancement multiplier is less than the maximum value defined.
- The enhancement switch is on.

If both conditions are met, the thermal conductivity multiplier is increase by a value defined before the start of the simulation. Otherwise, the multiplier is set to a value equal to one. The increase in value is govern by the equation below ('I' equals to the current number of loop cycles):

$$EnFacX\_Multiplier = \big(EnFacX\_Initial + \big(En\_Increment \times (i-2)\big)\big)$$

Overall, the logic behind this 'if-function' can be presented by the two equation below:

$$EnFacX\_Multiplier = \begin{cases} \text{EnMultiplier\_Max} & if \quad \begin{pmatrix} EnFacX\_Multiplier \geq \text{ maximum value defined} \\ Switch\_X = 1 \end{pmatrix} \\ \big(EnFacX\_Initial + \big(En\_Increment \times (i-2)\big)\big) & if \quad \begin{pmatrix} EnFacX\_Multiplier < \text{ maximum value defined} \\ Switch\_X = 1 \end{pmatrix} \\ 1 & if \quad (Switch\_X = 0) \end{cases}$$

$$EnFacY\_Multiplier = \begin{cases} \text{EnMultiplier\_Max} & if \quad \begin{pmatrix} EnFacY\_Multiplier \geq \text{ maximum value defined} \\ Switch\_Y = 1 \end{pmatrix} \\ \big(EnFacY\_Initial + \big(En\_Increment \times (i-2)\big)\big) & if \quad \begin{pmatrix} EnFacY\_Multiplier < \text{ maximum value defined} \\ Switch\_Y = 1 \end{pmatrix} \\ 1 & if \quad (Switch\_Y = 0) \end{cases}$$

Exiting the first 'if-function', the simulation process proceeds to the second 'if-function', where the results are checked against the following conditions:

- The enhancement multiplier is greater than maximum value defined.
- The enhancement multiplier is greater than one.

If both conditions are met, the thermal conductivity multiplier is set to the maximum value defined before the start of the simulation. Otherwise, the results are checked against the next condition:

- The enhancement multiplier is less than one.

If this condition is met, the thermal conductivity multiplier is set to a value of one. Otherwise, the multiplier remains unchanged.

Overall, the logic behind this 'if-function' can be presented by the two equation below:

$$EnFacX\_Multiplier = \begin{cases} \text{EnMultiplier\_Max} & if \quad \begin{pmatrix} EnFacX\_Multiplier > \text{ maximum value defined} \\ \text{EnMultiplier\_Max} > 1 \end{pmatrix} \\ 1 & if \quad (EnFacX\_Multiplier < 1) \\ EnFacX\_Multiplier & if \quad (Fail\ to\ meet\ the\ above\ conditions) \end{cases}$$

$$EnFacY\_Multiplier = \begin{cases} \text{EnMultiplier\_Max} & if \quad \begin{pmatrix} EnFacY\_Multiplier > \text{ maximum value defined} \\ \text{EnMultiplier\_Max} > 1 \end{pmatrix} \\ 1 & if \quad (EnFacY\_Multiplier < 1) \\ EnFacY\_Multiplier & if \quad (Fail\ to\ meet\ the\ above\ conditions) \end{cases}$$

The purpose of implementing the second 'if-function' is to prevent the multiplier from exceeding the intended maximum value or falling below one. This 'if-function' serves as a safety check.

After exiting the second 'if-function', the simulation process advances to the third 'if-function', where the results are checked against the following conditions:

- The enhancement multiplier is greater than 1
- The enhancement switch is on

If both conditions are met, the thermal conductivity enhancement factor is increased by a certain value. Otherwise, the enhancement factor is set to a value equal to zero. The increase in value is governed by a series of equations listed below ('n' represents the numbering system given to the total count of the data points representing temperature-dependent thermal conductivity):

- For $5 \leq n \leq 7$

$$Mod\_KXXn = \left\{ \left[\left((18.1 + Hor\_EnFactor) \times (EnFacX\_Multiplier - 1) \right) + Mod\_KXXn \right] \times \frac{2 \times (n-4)}{7} \right\}$$

- For $8 \leq n \leq 10$

$$Mod\_KXXn = \left[\left(\left(KXXn_{original} + Hor_{EnFactor}\right) \times EnFacX\_Multiplier\right) \times (EnMultiplier\_SL - 1)\right]$$

- For n = 11 or 12

$$Mod_{KXXn} = \left\{\left[(20.6 + Hor_{EnFactor}) \times EnFacX_{Multiplier}\right] \times \left[EnMultiplier\_SL \times \left(\left((EnMultiplier\_LG - 1) \times \frac{n-10}{3}\right) + 1\right)\right]\right\}$$

- For 13 ≤ n ≤ 21

$$Mod_{KXXn} = \left[\left((20.6 + Hor\_EnFactor) \times EnFacX\_Multiplier\right) \times (EnMultiplier\_SL \times EnMultiplier\_LG - 1)\right]$$

Table 4 shows the variables used in the equations that helps governs the values used in the IF-functions.

Table 4. Unknowns variables used in the equations for governing the values used in the IF-functions.

Manipulated factor	Meaning
$KXXn_{original}$	The original temperature-based thermal conductivity in x-axis
Hor_EnFactor	The horizontal enhancement factor
EnFacX_Initial	0
En_Increment	2.0
EnFacX_Multiplier	Multiplying factor for conductivity enhancement
EnMultiplier_SL	2.0
EnMultiplier_LG	1.5

In more detail:

- $KXXn_{original}$ represents the original thermal conductivity corresponds to the n^{th} of the temperature listed in the thermal conductivity properties found at the preprocessor phase of the simulation modelling.

- Hor_EnFactor (a.k.a. horizontal enhanced factor) has the original value (35.9-18.1)+(35.9-34.4), derived from the conductivities in Table 4.

Table 5. thermal conductivity of the substrate at different temperatures

Temperature in Kelvin	Corresponding thermal conductivity (original)
1600 K (solid phase)	34.4
1700 K (solid phase)	35.9
1750 K (liquid phase)	18.1

The purpose of this equation is to ensure a smooth transition of thermal conductivity between the solid and liquid phases, preventing any sudden decrease during phase change. This equation is part of a larger system implemented to approximate heat transfer effects typically associated with fluid flow in the liquid phase, thereby enhancing the material's effective thermal conductivity in the absence of an actual fluid dynamics model.

The following equations are used to calculate the thermal conductivity shown in Table 5, above [131]:

1. [Solid state] Thermal conductivity, [W/(m·K)]:

$$\lambda = 9.248 + 0.01571 \times T$$

2. [Liquid state] Thermal conductivity, [W/(m·K)]:

$$\lambda = 12.41 + 0.003279 \times T$$

- As for the variables En_Increment, EnMultiplier_SL, and EnMultiplier_LG, they are designed to control the rate of change in the enhancement value, which governs the transition of thermal conductivity from the solid phase to the liquid phase and then to the gaseous phase. Based on a series of simulations, values of 2.0 for En_Increment and EnMultiplier_SL, and 1.5 for EnMultiplier_LG were deemed the most suitable for achieving an optimal rate of change in thermal conductivity enhancement.

The above equations applied to thermal conductivity in the x-axis (KXX). Similar equations are used for thermal conductivity in the y-axis (KYY), with the only difference being the substitution of KXX with KYY.

Another component of the system, which approximates heat transfer effects typically associated with phase changes, is the implementation of the third 'if-function'. This function ensures a smoother transition of temperature-based thermal conductivity from the solid to the liquid phase. It also helps regulate heat transfer from the melt pool to the surrounding solid region, preventing heat from becoming trapped within the melt pool.

Upon entering the third ‘if-function’, the results are checked against the following conditions:

- The EnFacX_Multiplier is greater than 1
- The enhancement switch is on

If both conditions are met, the thermal conductivity enhancement represented by Mod_KXXn is defined by the equations shown in Table 6.

Table 6. Definition for Mod_KXXn variables.

Mod_KXXn	Corresponding temperature	Defined values / equations
Mod_KXX1	1100 K	0
Mod_KXX2	1200 K	0
Mod_KXX3	1300 K	0
Mod_KXX4	1400 K	0
Mod_KXX5	1500 K	((((18.1+Hor_EnFactor)*(EnFacY_Multiplier-1))+Mod_KYY8)*2/7)
Mod_KXX6	1600 K	((((18.1+Hor_EnFactor)*(EnFacY_Multiplier-1))+Mod_KYY8)*4/7)
Mod_KXX7	1700 K	((((18.1+Hor_EnFactor)*(EnFacY_Multiplier-1))+Mod_KYY8)*6/7)
Mod_KXX8	1750 K	(((18.1+Hor_EnFactor)*EnFacY_Multiplier)*(EnMultiplier_SL-1))
Mod_KXX9	2000 K	(((19.0+Hor_EnFactor)*EnFacY_Multiplier)*(EnMultiplier_SL-1))
Mod_KXX10	2250 K	(((19.8+Hor_EnFactor)*EnFacY_Multiplier)*(EnMultiplier_SL-1))
Mod_KXX11	2500 K	((((20.6+Hor_EnFactor)*EnFacY_Multiplier)* (EnMultiplier_SL*(((EnMultiplier_LG-1)*1/3)+1)-1)))
Mod_KXX12	2750 K	((((20.6+Hor_EnFactor)*EnFacY_Multiplier)* (EnMultiplier_SL*(((EnMultiplier_LG-1)*2/3)+1)-1)))
Mod_KXX13	3000 K	(((20.6+Hor_EnFactor)*EnFacY_Multiplier)* (EnMultiplier_SL*EnMultiplier_LG-1))

Mod_KXX14	3250 K	(((20.6+Hor_EnFactor)*EnFacY_Multiplier)*(EnMultiplier_SL*EnMultiplier_LG-1))
Mod_KXX15	3500 K	(((20.6+Hor_EnFactor)*EnFacY_Multiplier)*(EnMultiplier_SL*EnMultiplier_LG-1))
Mod_KXX16	3750 K	(((20.6+Hor_EnFactor)*EnFacY_Multiplier)*(EnMultiplier_SL*EnMultiplier_LG-1))
Mod_KXX17	4000 K	(((20.6+Hor_EnFactor)*EnFacY_Multiplier)*(EnMultiplier_SL*EnMultiplier_LG-1))
Mod_KXX18	4250 K	(((20.6+Hor_EnFactor)*EnFacY_Multiplier)*(EnMultiplier_SL*EnMultiplier_LG-1))
Mod_KXX19	4500 K	(((20.6+Hor_EnFactor)*EnFacY_Multiplier)*(EnMultiplier_SL*EnMultiplier_LG-1))
Mod_KXX20	4750 K	(((20.6+Hor_EnFactor)*EnFacY_Multiplier)*(EnMultiplier_SL*EnMultiplier_LG-1))
Mod_KXX21	5000 K	(((20.6+Hor_EnFactor)*EnFacY_Multiplier)*(EnMultiplier_SL*EnMultiplier_LG-1))

Otherwise, all Mod_KXXn (from Mod_KXX1 to Mod_KXX21) is equal to the value of zero.

Figure 46. Second half of the loop cycle of the simulation process. shows the second half of the loop cycle, depicting two distinct simulation phases: the pre-processing phase and the solution phase.

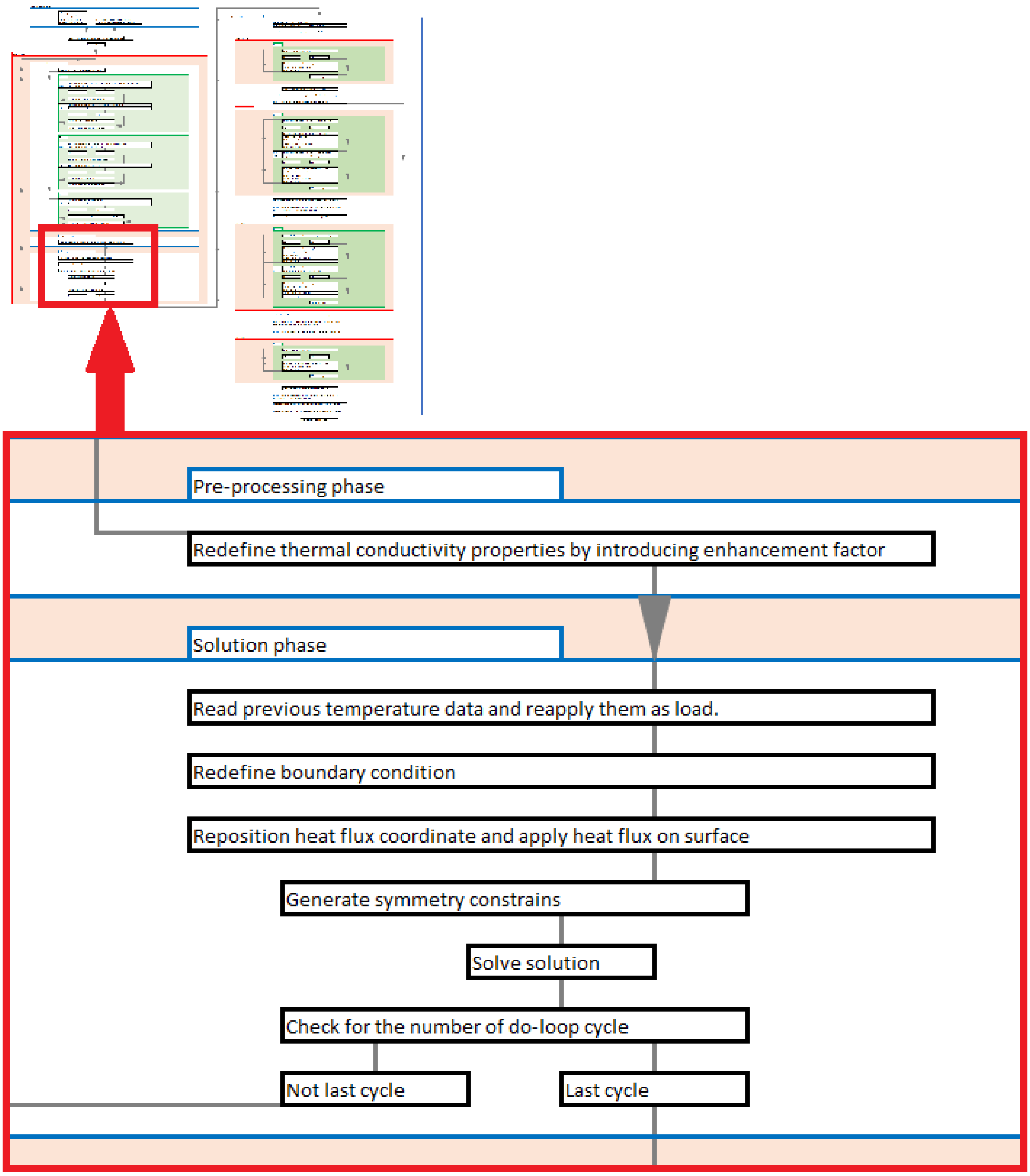

Figure 46. Second half of the loop cycle of the simulation process.

In the pre-processing phase, all temperature-dependent material properties are redefined before commencing the simulations. This redefinition is governed by the equation below (where $KXXn_{original}$ represents the original thermal conductivity at the corresponding temperature):

$$Thermal\ Conductivity, KXXn$$
$$= \left[\left(KXXn_{original} + \mathrm{Hor\_EnFactor}\right) \times \mathrm{EnFacX\_Multiplier}\right] + Mod\_KXXn$$

Upon entering the solution phase, the simulation properties and boundary conditions are established. The solution phase concludes when the 'Solve' command is executed, and any remaining boundary conditions are cleared.

Figure 47 illustrates a section within the final post-processing phase. In this section, its purpose is to identify the highest temperature along the path where the centre of the heat flux moves.

This function begins by defining the 'checking range' along the y-axis. The 'checking range' serves the purpose of extending the temperature checking distance on the top surface to prevent the accidental exclusion of nodes with high temperature values. Following this, the mesh dimensions are identified to match the initial meshing factor set during the modelling process in the pre-processing phase.

Once the initial parameters are prepared, this function begins by identifying the first two temperature data for comparison. These data are then stored as Temp00 and Temp01. After the data is stored, the function enters a do-loop process and repeats the if-function until it achieves its objective of finding the highest temperature.

When entering the 'if-function', the stored data is checked against the following condition:

- Temp01 is greater than Temp00.

If the condition is true, the checkpoint coordinate is shifted by one node along the y-axis. Temp00 is then overwritten with the original data from Temp01, and subsequently, Temp01 is overwritten with the temperature data found in the next node.

If the condition is not met, the 'if-function' executes the 'Exit' command, which stops the do-loop function with Temp00 defined as the highest temperature on the surface.

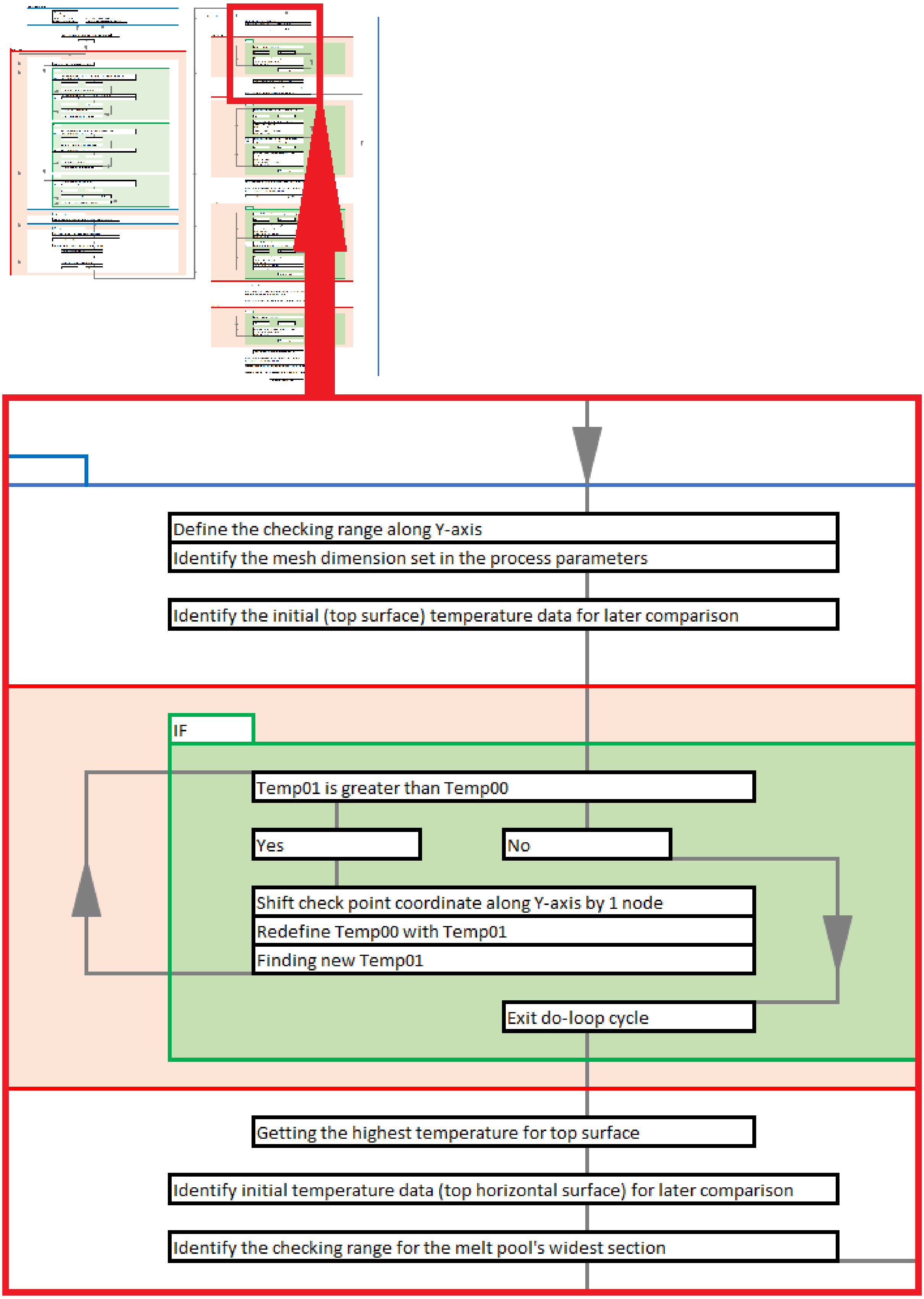

Figure 47. Final post-processing phase: Identification of the highest temperature on the top surface.

Figure 48 shows a section within the final post-processing phase. In this section, its purpose is to identify the widest section of the melt pool in the x-axis direction.

This function begins by comparing the width of the current checkpoint coordinate and the one before it. The width for the current checkpoint coordinate is stored as No_MeltMax_W2, and the temperature at the edge of the melt pool is stored as TempW1. The checkpoint coordinate in front of No_MeltMax_W2 is stored as No_MeltMax_W1, and its corresponding temperature is stored as TempW0. The function enters a do-loop process and repeats the if-function until it successfully identifies the widest section of the melt pool.

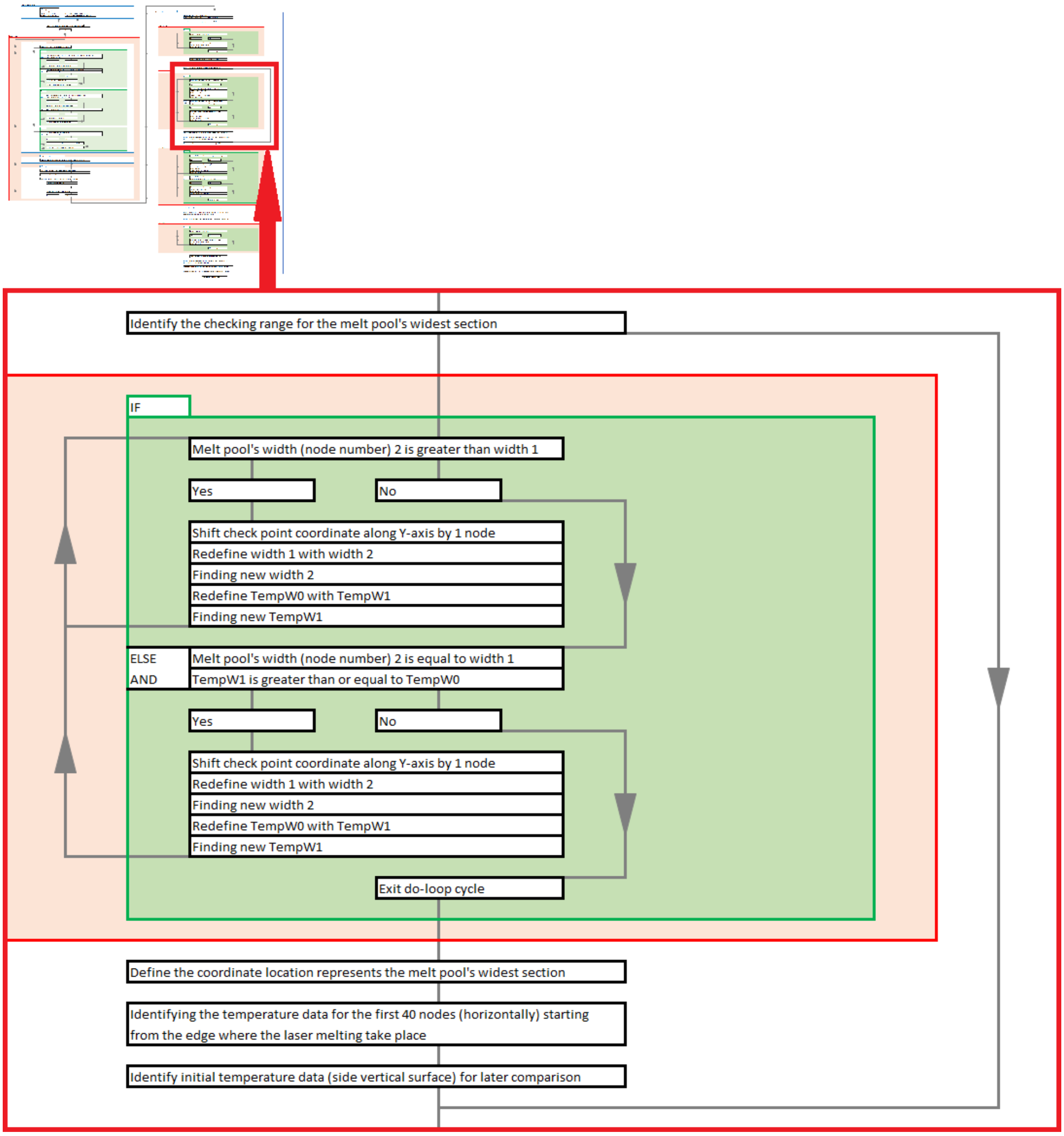

Figure 48. Final post-processing phase: Identification of the widest melt pool section on the top surface.

When entering the 'if-function', the stored data is checked against the following condition:

- The width of the melt pool (No_MeltMax_W2) at position 2 is greater than the width (No_MeltMax_W1) at position 1.

If the condition is true, the checkpoint coordinate is shifted backwards by one node. No_MeltMax_W1 is overwritten with the original data from No_MeltMax_W2, and TempW0 is overwritten with the original data from TempW1. New No_MeltMax_W2 and TempW2 are redefined using temperature data from the next node.

Otherwise, the results are checked against the next set of conditions:

- The width of the melt pool (No_MeltMax_W2) at position 2 is equal to the width (No_MeltMax_W1) at position 1.
- TempW1 is greater than or equal to TempW0.

If both conditions are true, No_MeltMax_W1 is overwritten with the original data from No_MeltMax_W2, and TempW0 is overwritten with the original data from TempW1. New No_MeltMax_W2 and TempW2 are redefined using temperature data from the next node.

If one or both conditions are not met, the 'if-function' executes the 'Exit' command, which stops the do-loop function with MaxMelt_Y_Loc written with the latest coordinates obtained from the if-function. Using that coordinate, a series of temperature data obtained from 41 nodes across the x-axis direction is stored as Temp_H00 to Temp_H40.

Figure 49 illustrates a section within the final post-processing phase. In this section, it serves as a function of identifying the deepest point of the melt pool (in the z-axis direction).

Similar to the previous function (depicted in Figure 48), this function begins by comparing the depth of the current checkpoint coordinate and the one before it. The depth for the current checkpoint coordinate stored as No_MeltMax_D2, and the temperature at the edge of the melt pool is stored as TempD1. The checkpoint coordinate in front of No_MeltMax_D2 is stored as No_MeltMax_D1, and its corresponding temperature is stored as TempD0. The function enters a do-loop process and repeats the if-function until it successfully identifies the deepest section within the melt pool.

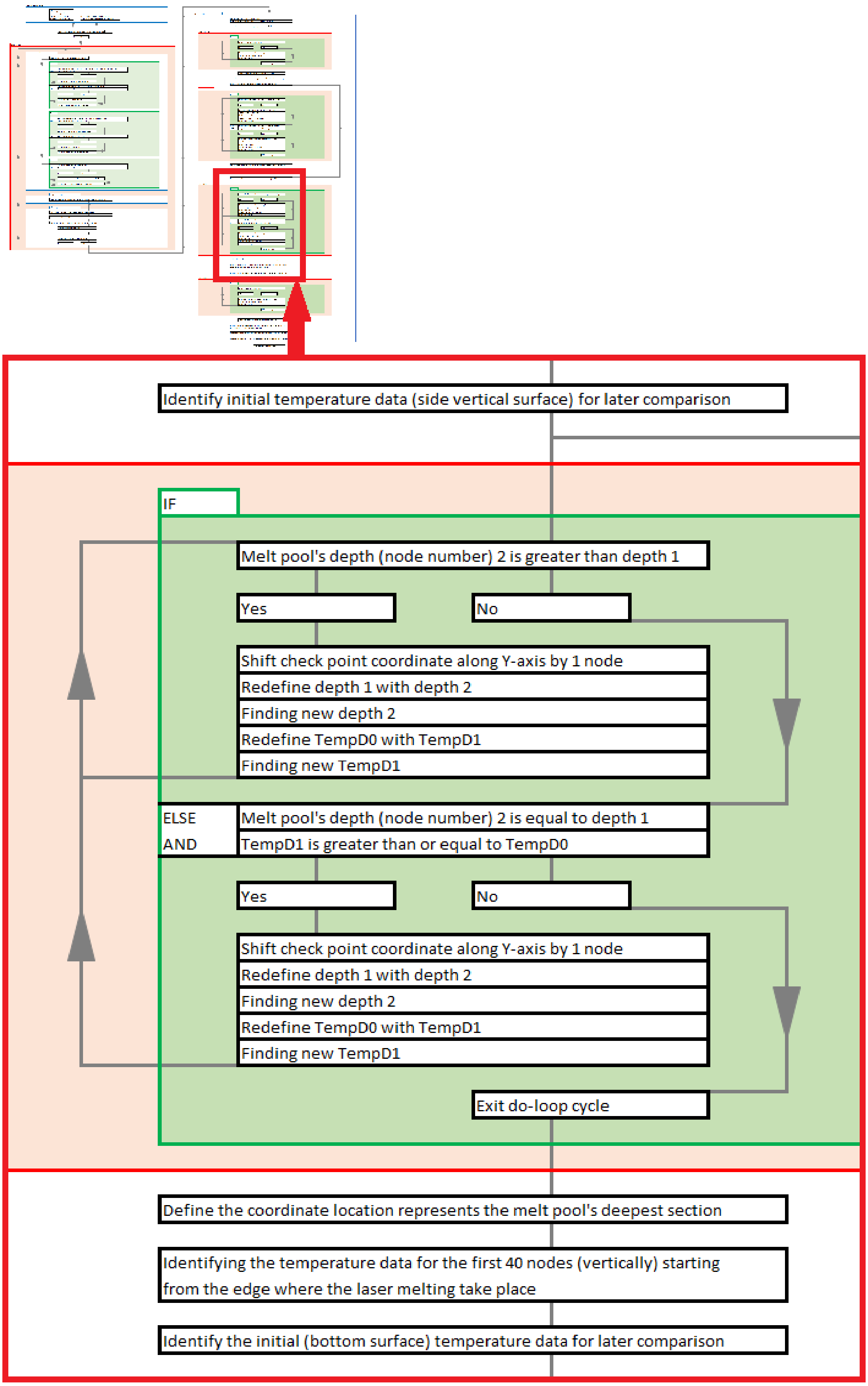

Figure 49. Final post-processing phase: Identification of the deepest melt pool section on the side (symmetry boundary) surface.

When entering the ‘if-function’, the stored data is checked against the following condition:

- The width of the melt pool (No_MeltMax_D2) at position 2 is greater than the width (No_MeltMax_D1) at position 1.

If the condition is true, the checkpoint coordinate is shifted backwards by one node. No_MeltMax_D1 is overwritten with the original data from No_MeltMax_D2, and TempD0 is overwritten with the original data from TempD1. New No_MeltMax_D2 and TempD2 are then redefined using temperature data from the next node.

Otherwise, the results are checked against the next set of conditions:

- The width of the melt pool (No_MeltMax_D2) at position 2 is equal to the width (No_MeltMax_D1) at position 1.
- TempD1 is greater than or equal to TempD0

If both conditions are true, No_MeltMax_D1 is overwritten with the original data from No_MeltMax_D2, and TempD0 is overwritten with the original data from TempD1. New No_MeltMax_D2 and TempD2 are then redefined using temperature data from the next node.

If one or both conditions are not met, the ‘if-function’ executes the ‘Exit’ command, which stops the do-loop function with MaxMelt_Y_Loc written with the latest coordinates obtain from the if-function. Using that coordinate, a series of temperature data obtained from 61 nodes across the z-axis direction is stored as Temp_V00 to Temp_V40.

Figure 50 presents a section within the final post-processing phase. In this section, its primary function is to identify the highest temperature on the bottom surface, directly beneath the path where the centre of the heat flux moves. It also aims to collect temperature data from the first 11 nodes behind the most recent heat flux coordinate.

This function initiates by identifying the first two temperature data for comparison. These data are then used to overwrite the previously stored data, namely Temp00 and Temp01. Once the data is overwritten and stored, the function enters a do-loop process and iterates through the if-function until it achieves its objective of finding the highest temperature.

When entering the ‘if-function’, the stored data are checked against the following condition:

- Temp01 is greater than Temp00.

If the condition is true, the checkpoint coordinate is shifted by one node’s distance along the y-axis. Temp00 is then overwritten with the original data from Temp01, and subsequently, Temp01 is updated with the temperature data found in the next node.

If the condition is not met, the ‘if-function’ executes the ‘Exit’ command, which terminates the do-loop function with Temp00 defined as the highest temperature on the bottom surface.

After identifying the highest temperature on the bottom surface, it proceeds to execute the next function, show in Figure 50, whose objective is to obtain the temperature data from the first 11 nodes, starting from the most recent heat flux coordinate and moving backwards. Those temperature data are then stored as Temp00 to Temp10.

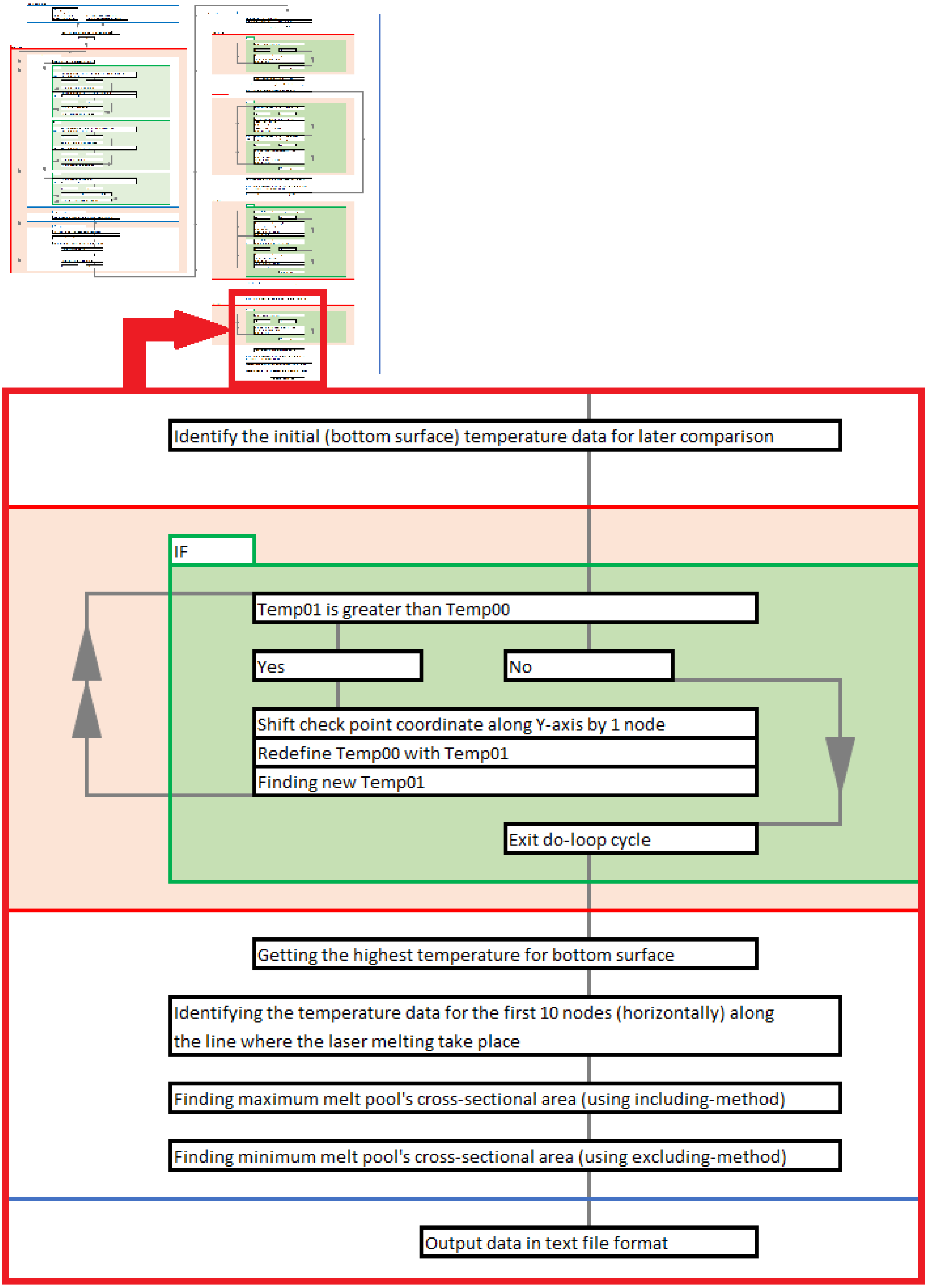

Figure 50. Final post-processing phase: Identification of the highest temperature on the bottom surface.

4.3.3. Settings used in for the simulations

After creating the models to simulate a convective heat flow via enhanced thermal conductivity, the next step is to choose the initial conditions and suitable settings for conduction-based laser melting simulations.

For the laser process parameters, the settings defined are as such:

- Laser power: 200 W – 250 W
- Scanning speed: 12, 16, 20, and 24 mm/s
- Beam diameter: 0.4 mm
- Ambient temperature: 292 K

For the model's dimension used in this chapter:

- Width: 5 mm
- Length: 30 mm
- Thickness: 3 mm

For the simulation settings used in this chapter:

- Number of steps: 100
- Total travel distance: 10 mm

4.3.4. Experimental verification

It was decided to conduct both thermal conductivity enhancement comparison and laser absorptivity comparison simultaneously.

In this section, the results obtained from the conduction-based laser melting experiment are shown in Figures 51 and 52. The following process parameters were used in this experiment:

- Laser power: 200 W and 250 W
- Laser scanning speed: 12, 16, 20, 24, and 28 mm/s
- Laser beam diameter on the surface: 0.5 mm

Using image stitching function available in the Leica Software Application Suite (LAS) software, multiple images obtained with the Leica DFC295 digital microscope colour camera are merged into a single image that displays the entire cross-sectional area of the melt track. This enables precise measurements of the dimension and the area coverage of the melt tracks.

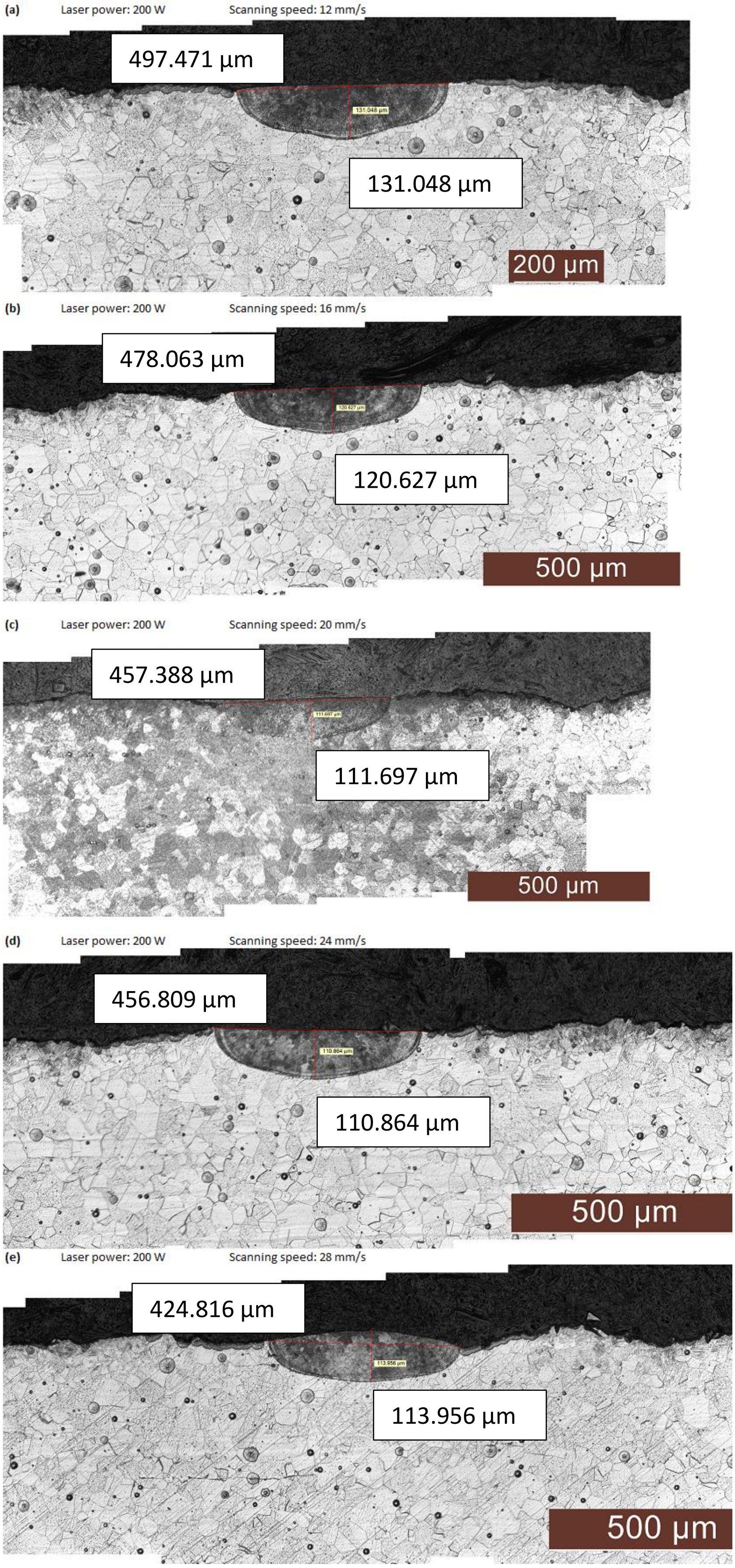

Figure 51. Conduction-based laser melting using 200 W laser power with different scanning speed.

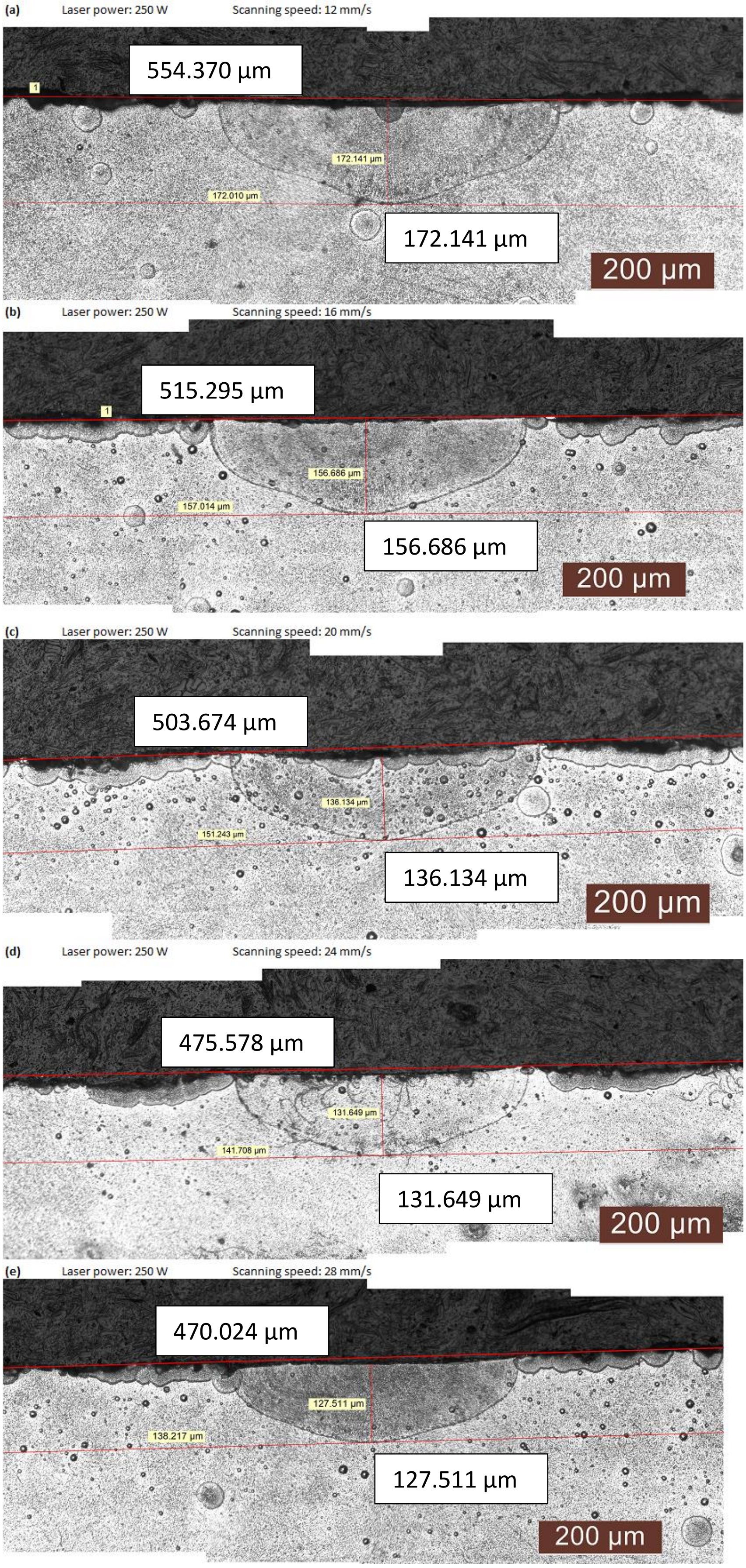

Figure 52. Conduction-based laser melting using 250 W laser power with different scanning speed.

Table 7 shows that the width of the melt track increases from 497.5 µm to 554.4 µm, and the depth increases from 131.0 µm to 172.1 µm as the laser power increases from 200 W to 250 W at a traverse speed of 12 mm/s. A similar trend is observed across a range of traverse speeds from 16 mm/s to 28 mm/s.

Table 7. Results obtained from conduction-based laser melting experiment.

Laser power (W)	Speed (mm/s)	Width (µm)	Depth (µm)	Area (µm^2)
200	12.0	498	131	50231
200	16.0	478	121	44444
200	20.0	457	112	40347
200	24.0	457	111	40144
200	28.0	425	114	37050
250	12.0	554	172	65466
250	16.0	515	157	59544
250	20.0	504	136	54527
250	24.0	476	132	48727
250	28.0	470	127	46005

When the laser power remains constant at 200 W, the width of the melt track decreases from 497.5 µm to 424.8 µm, and the depth decreases from 131.0 µm to 114.0 µm as the traverse speed increases from 12 mm/s to 28 mm/s. A similar trend is observed when the laser power is kept constant at 250 W, where the width of the melt track decreases from 554.4 µm to 470.0 µm, and the depth decreases from 172.1 µm to 127.5 µm as the traverse speed increases from 12 mm/s to 28 mm/s.

Based on these results, it can be concluded that increasing the laser power leads to an increase in both the width and depth of the melt track, as well as its cross-sectional area. Conversely, increasing the traverse speed results in a decrease in the width, depth, and cross-sectional area of the melt track.

4.3.5. Comparison of model concepts

After the experiment results were obtained, a series of simulations was conducted with different process parameters using different concepts. This was achieved by changing the settings available within model M2. The settings available include

- a switch for enabling and disabling the thermal enhancement function (with the enhancement switch OFF, the model reverts to the M1 model).
- A switch for anisotropic or isotropic function. If the switch is ON and the model is in the anisotropic enhanced thermal conductivity mode, the direction of thermal conductivity enhancement and the multiplier factor of the enhancement can be set. For experiments below it was to be in the x direction (i.e. lateral direction at right angles to beam movement).
- A switch for the transition function of thermal conductivity from solid to liquid, including the magnitude of transitioning (applicable when thermal enhancement is ON).

The previous comparison of laser absorptivity, based on the highest temperature recorded at the bottom surface of the substrate, yielded unrealistic, and in some cases physically impossible, solutions. As an alternative, a novel approach has been proposed, in which laser absorptivity is evaluated by comparing the dimensions (width and depth) of the melt track between experimental results and simulation results obtained using a model that incorporates the anisotropic enhanced thermal conductivity method. Simultaneously, this approach serves to validate the theory of thermal conductivity enhancement proposed by Safdar et al. [101].

The equation used to guide the thermal conductivity (λ) enhancement function at this current stage is:

$$\lambda\ [W/(m \cdot K)] = (12.41 + 0.003279 \times T) \times EnFacX\_Multiplier$$

Where λ represents the enhanced thermal conductivity, T is temperature and EnFacX_Multiplier represents a multiplying factor for conductivity enhancement.

Figure 53 shows the impact of the enhancement multiplier, EnFacX_Multiplier, on the surface half width (width measured from the centre to the edge of the melt pool) of the melt track and temperature profile of the melt track formed. It can be seen that as the multiplier increased from x10 to x100, the width of the melt track increased, but the rate of width expansion gradually decreased, indicating a decline in the effectiveness of further thermal conductivity enhancement for expanding the width of the melt pool. It can be concluded that anisotropic enhancement approach has been validated for expanding the width of the melt pool to align with the result obtained from the experiment but the amount of expansion possible is limited.

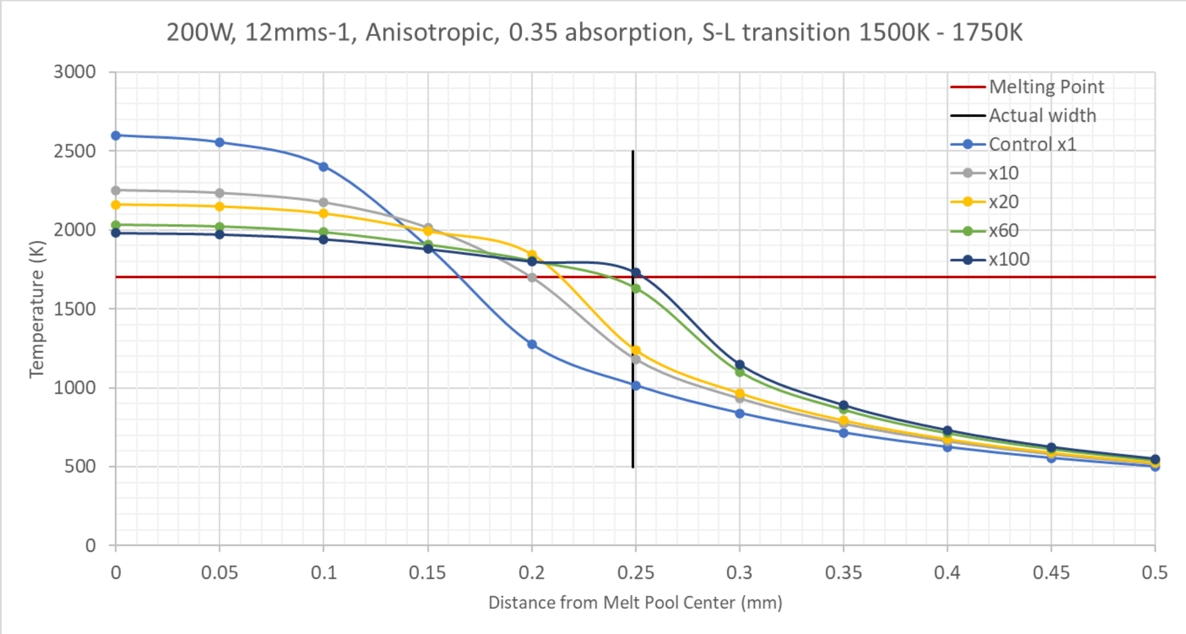

Figure 53. The M2 model with 0.35 absorption, anisotropic thermal enhancement and the solid-liquid transition function.

The next step after proving the validity of the enhancement approach is to identify the best fit composition between the laser absorptivity and the enhancement factor. Figure 54 shows the impact of the enhancement multiplier towards half the width (width measured from the centre to the edge of the melt pool) of the melt track and temperature profile of the melt track formed.

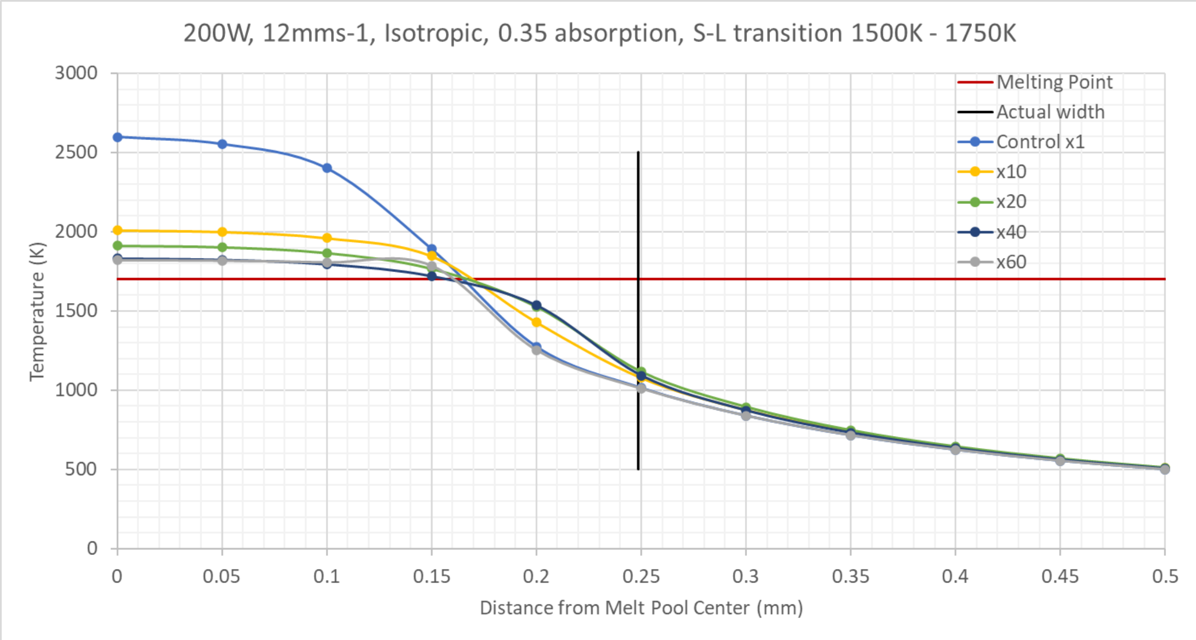

Figure 54. The M2 model with 0.35 absorption, isotropic thermal enhancement and the solid-liquid transition function.

It can be seen that changes in the width of the melt track are minimal, with the edge remaining between 0.16 mm and 0.17 mm from the centre of the melt track, regardless of variations in the multiplier value for the isotropic enhancement. Consequently, an alternative approach by modifying the temperature range for the solid-to-liquid transition function, was explored.

Figure 55 shows the results obtained by reducing the temperature range for solid to liquid transition function. This alteration shows a change in the width of the melt track. The negative change in the width is due to the reduction in the temperature profiles, showing that the increase in temperature range for the transition function results in a stronger conduction of thermal energy away from the melt pool into the solid region.

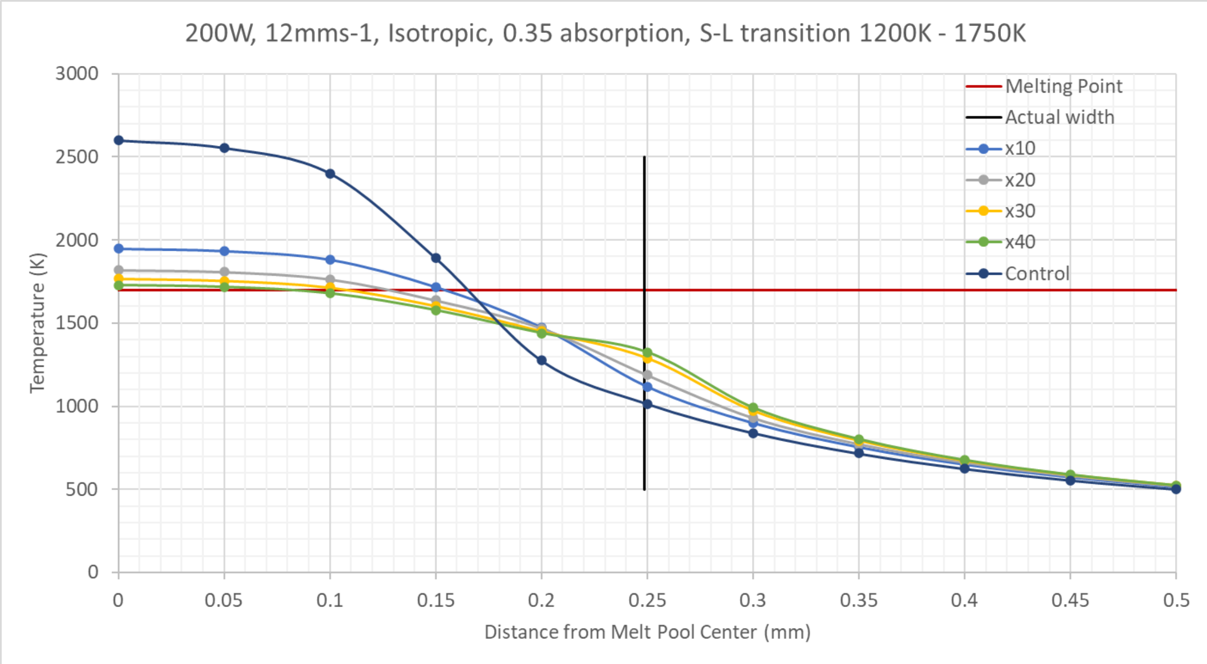

Figure 55. Melt pool half width according to the M2 model with 0.35 absorption, isotropic thermal enhancement and the solid-liquid transition function between 1200K – 1750K.

At this stage, the decision was made to increase the laser absorptivity with the aim of shifting the graph line upwards in the hope of achieving an increase in the width of the melt track. Figures 56 and 57 show the effect of laser absorptivity and thermal conductivity enhancement on pool temperatures and predicted dimensions. From these graphs, it has been learned that the current equation guiding the enhancement function does not yield promising results. It results in a reduction in the depth of the melt pool without a significant increase in the width of the melt pool.

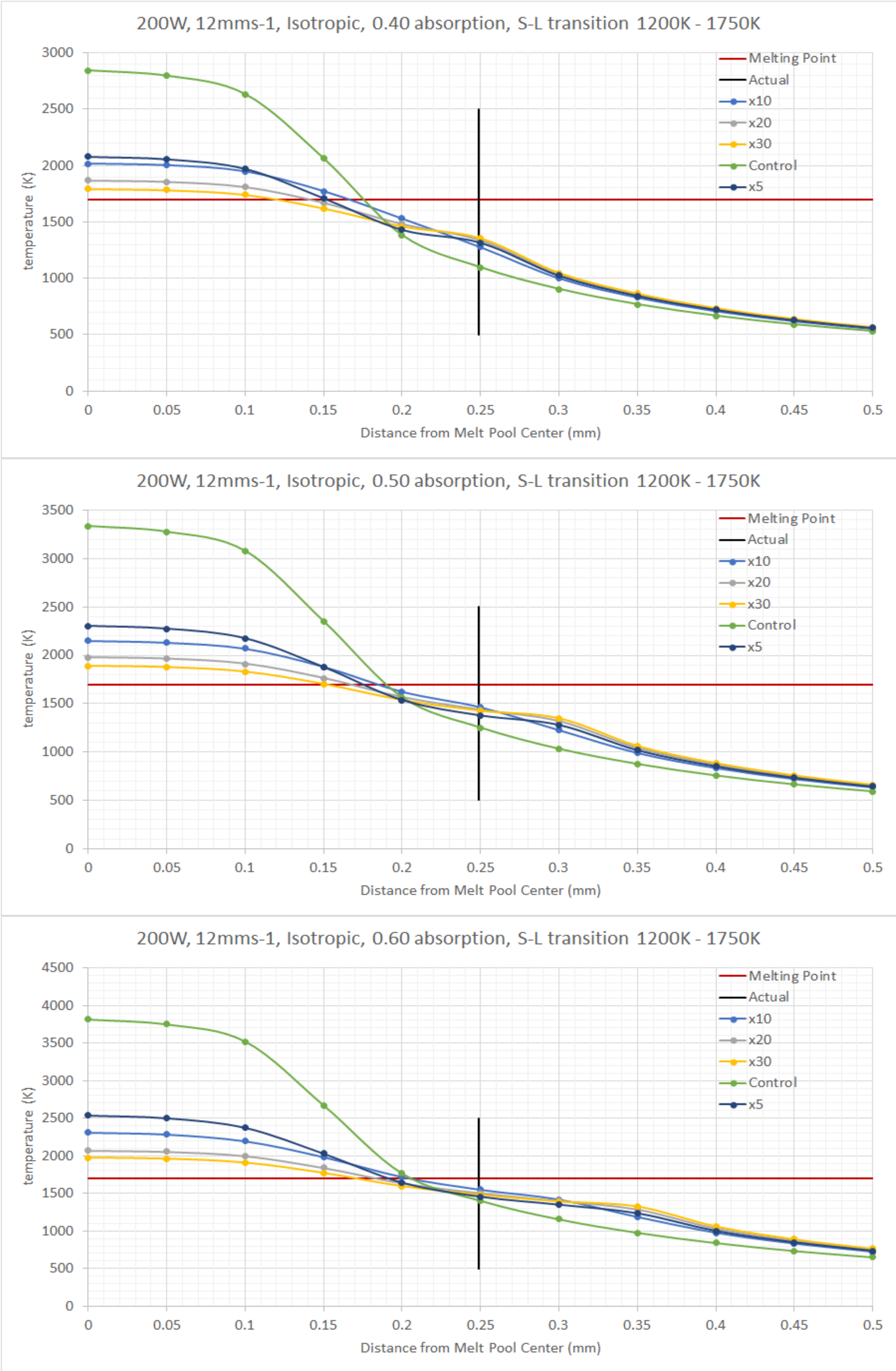

Figure 56. Melt pool half width according to the M2 model with isotropic thermal enhancement and 0.5, 0.6 and 0.7 absorption

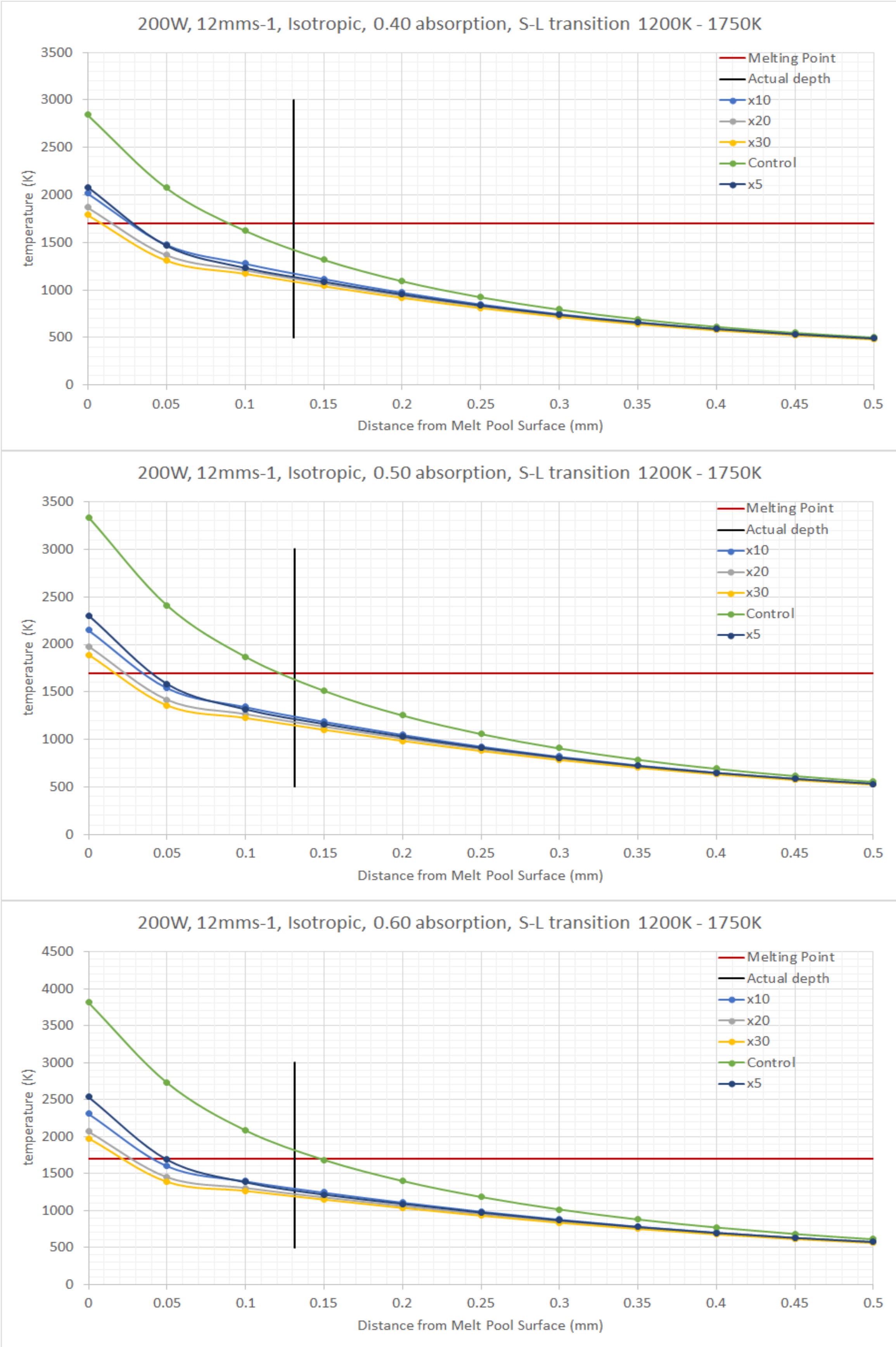

Figure 57. Melt pool depth according to the M2 model with isotropic thermal enhancement and 0.5, 0.6 and 0.7 absorption.

Figure 58 shows the bar chart of the half width comparison using results obtained from M1 (or M2 with the conduction enhancement function switched off). From the bar chart, it is noticeable that instead of producing a result with a wider melt pool, the results of this model show a reduction in the melt pool's width.

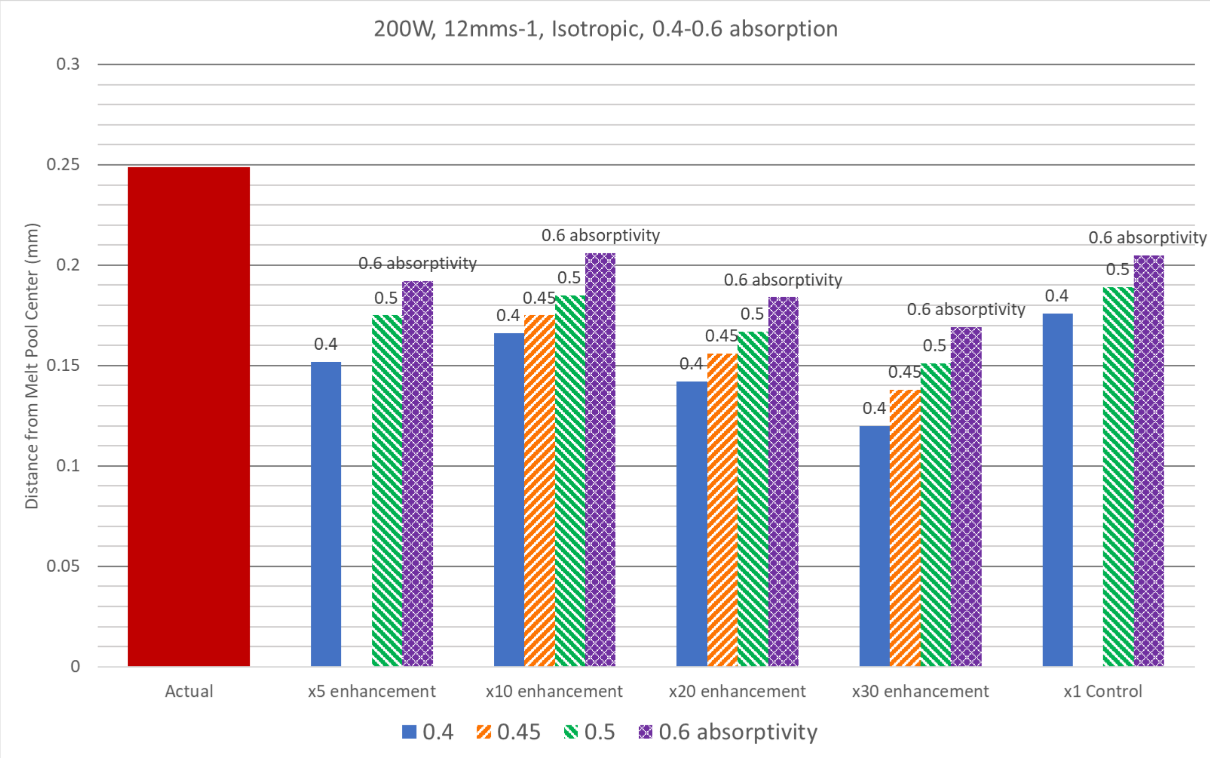

Figure 58. Half width at different laser absorption and thermal conductivity enhancement values, calculated using model M2 with isotropic thermal enhancement

The primary reason for this reduction is the lack of a mechanism to account for the effects of fluid flow when the thermal enhancement function is off. In an actual laser welding process, molten material spreads due to surface tension and convective heat transfer, allowing the melt pool to expand laterally. However, the absence of such effects limits the lateral distribution of heat, preventing the melt pool from widening properly.

Table 8. Melt pool half widths simulated using different laser absorption and thermal conductivity enhancement factors compared to experimental results

Absorptivity	Experiment result	x5 enhancement	x10 enhancement	x20 enhancement	x30 enhancement	x1 Control case
0.4	0.25 mm	0.15 mm	0.17 mm	0.14 mm	0.12 mm	0.18 mm
0.45	0.25 mm	-	0.18 mm	0.16 mm	0.14 mm	-
0.5	0.25 mm	0.18 mm	0.19 mm	0.17 mm	0.15 mm	0.19 mm
0.6	0.25 mm	0.19 mm	0.21 mm	0.18 mm	0.17 mm	0.21 mm

Table 9. [Width] Relative Error Analysis of Thermal Conductivity Enhancement for 200 W laser power at traverse speed of 12 mm/s

Absorptivity	x5 enhancement	x10 enhancement	x20 enhancement	x30 enhancement	x1 Control case
0.4	38.9 %	33.3 %	42.9 %	51.8 %	29.2 %
0.45	-	29.6 %	37.3 %	44.5 %	-
0.5	29.6 %	25.6 %	32.9 %	39.3 %	24.0 %
0.6	22.8 %	17.2 %	26.0 %	32.1 %	17.6 %

The equation used to calculate the relative error (RE) in Table 9 is as follow:

$$RE = \frac{|Simulated\ result - Experiment\ result|}{Experiment\ result} \times 100$$

To address this limitation, the thermal conductivity enhancement equation was modified to improve lateral heat transfer. Specifically, the introduction of the Hor_EnFactor increases the thermal conductivity in the temperature range above the melting point, compensating for the lack of fluid motion and promoting better heat distribution. This adjustment helps achieve a more accurate melt pool width in the simulation.

4.3.6. Results comparison using data generated by model M2

Figure 59 illustrates the different approaches used to enhance the thermal conductivity. The line labelled 'original', is the default temperature-dependent thermal conductivity found in reference [131].

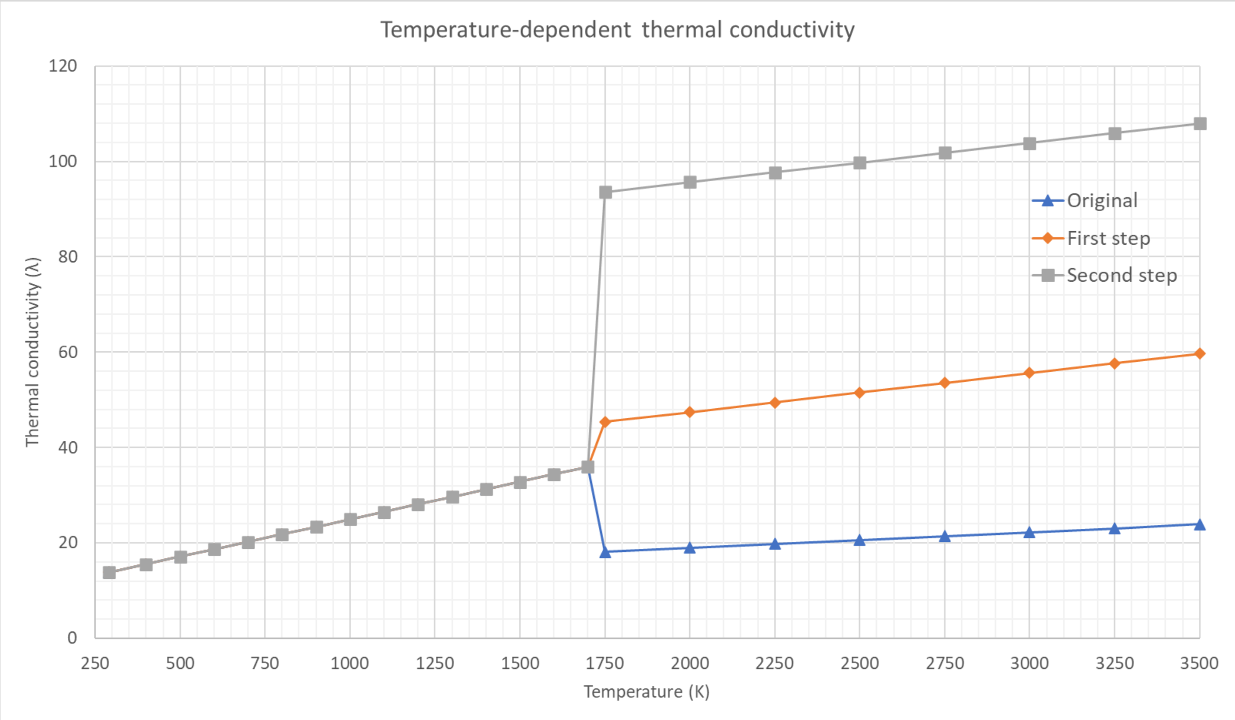

Figure 59. Different approaches in modifying the thermal conductivity – model M2.

The modification of thermal conductivity is intended to compensate for the absence of fluid flow in the 'solid-only' simulation model. Without fluid flow to redistribute heat from the heat flux region, the melt pool would not reach its expected dimensions, as observed in the comparison between the M1 model and the experimental results. To address this limitation, an increased thermal conductivity beyond the liquid phase is introduced to approximate the enhanced heat transfer effect typically facilitated by fluid flow within the melt pool.

For line representing 'Original', the equation used is:

$$\lambda = 12.41 + 0.003279 \times T$$

Where λ represents the thermal conductivity of the material (W/(m·K)) and T represents the temperature of the material (K).

For the line representing 'First step enhancement', the equation used is:

$$\lambda = (12.41 + 0.003279 \times T) \times EnFacX\_Multiplier$$

Where EnFacX_Multiplier is represented by the 2 conditional equations below:

$$EnFacX\_Multiplier = \begin{cases} \text{EnMultiplier\_Max} & if \begin{pmatrix} EnFacX\_Multiplier \geq \text{ maximum value defined} \\ Switch\_X = 1 \end{pmatrix} \\ \left(EnFacX\_Initial + \left(En\_Increment \times (i-2)\right)\right) & if \begin{pmatrix} EnFacX\_Multiplier < \text{ maximum value defined} \\ Switch\_X = 1 \end{pmatrix} \\ 1 & if \quad (Switch\_X = 0) \end{cases}$$

$$EnFacX\_Multiplier = \begin{cases} \text{EnMultiplier\_Max} & if \begin{pmatrix} EnFacX\_Multiplier > \text{ maximum value defined} \\ \text{EnMultiplier\_Max} > 1 \end{pmatrix} \\ 1 & if \quad (EnFacX\_Multiplier < 1) \\ EnFacX\_Multiplier & if \quad (Fail\ to\ meet\ the\ above\ conditions) \end{cases}$$

The first equation is designed to calculate the required value during the simulation process, while the second equation serves as a safety check to ensure that the inputted value is correct and as intended during the simulation.

For the line representing ‘Second step enhancement’, the equation used is:

$$\lambda = [(12.41 + 0.003279 \times T) + Hor\_EnFactor] \times EnFacX\_Multiplier$$

Hor_EnFactor is represented by the equation below:

$$Hor\_EnFactor = (35.9 - 18.1) + (35.9 - 34.4)$$

Using these equations, Figures 60 and 61 were obtained. These show that the increase in thermal conductivity has resulted in a wider melt track; however, the current modifications are still unable to achieve a width comparable to the experimental results. This is something to be tackled in future developments of the model.

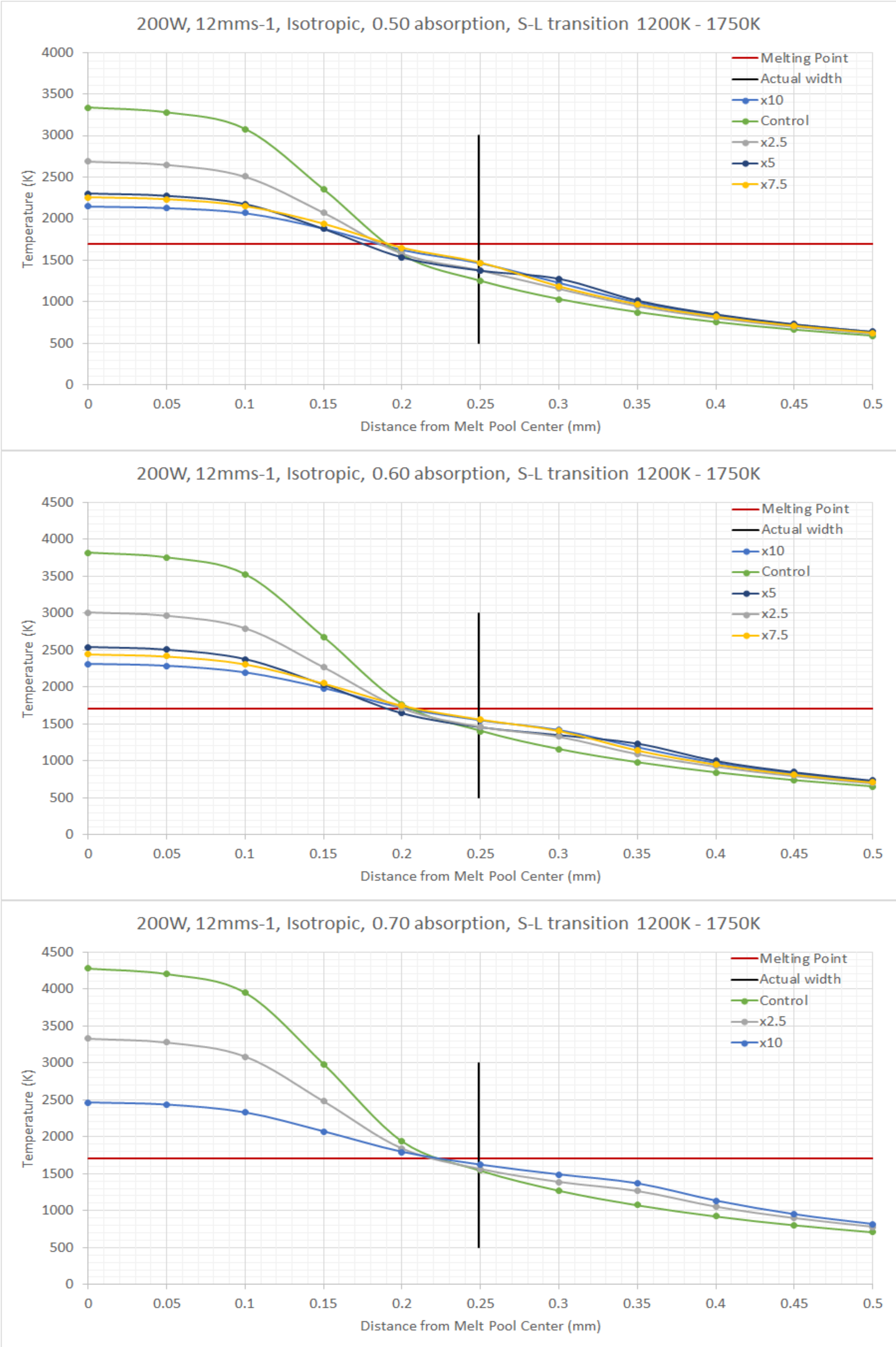

Figure 60. Melt pool half widths according to the M2 model with isotropic thermal enhancement and 0.5, 0.6 and 0.7 absorption.

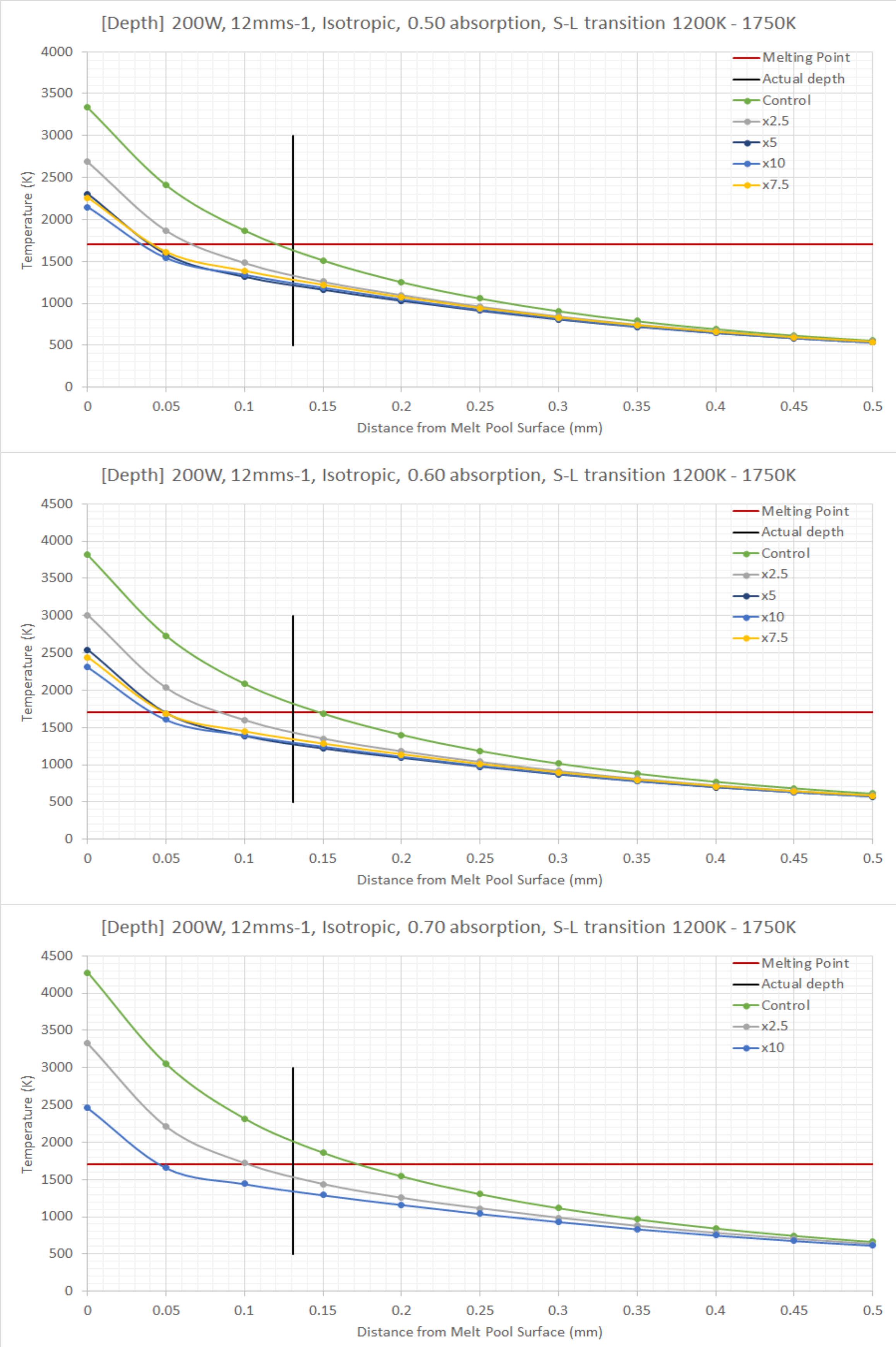

Figure 61. Melt pool depths according to the M2 model with isotropic thermal enhancement and 0.5, 0.6 and 0.7 absorption.

The bar chart comparing the half width results obtained from the M2 model is shown in Figure 62. Similar to the findings in Figure 58, the results presented in Figure 62 are not entirely in agreement with those obtained from the experiment. However, when combined with the findings in Figure 60, some improvements are evident. However, it can be concluded a tenfold increase in the thermal conductivity is physically unrealistic.

Figure 62. Melt pool half widths according to the M2 model with isotropic thermal enhancement and 0.4, 0.5, 0.6 and 0.7 absorption.

4.4. Advanced enhanced conduction model, M3

4.4.1. Introduction

A third model was developed based on M2. Model M3 is designed to improve the way thermal conductivity changes are governed in order to prevent insufficient lateral heat dissipation leading to localised heat accumulation beneath the laser beam. The models' simplicity, without the need to introduce complex fluid flow mechanisms, is maintained.

No new experimental results are necessary as this model can be verified using the same results used for M2 in the previous section.

4.4.2. Model design

The structure of M3 is the same as that of M2, but it incorporates improved governing equations to enhance thermal conductivity. The development of this model was guided by the following two key objectives:

- Further increase the enhancement factor for temperature above melting point.
- Modify thermal conductivity near the melting and boiling point using an interpolation method. This adjustment aims to better simulate the expansion of the melt pool's boundary, accounting for phase change from solid to liquid and the fluid flow away from the centre due to both Marangoni flow and vapour pressure generated by the vaporisation of material (for cases involving higher laser power).

Figure 63 shows how conductivity is modified in model M3.

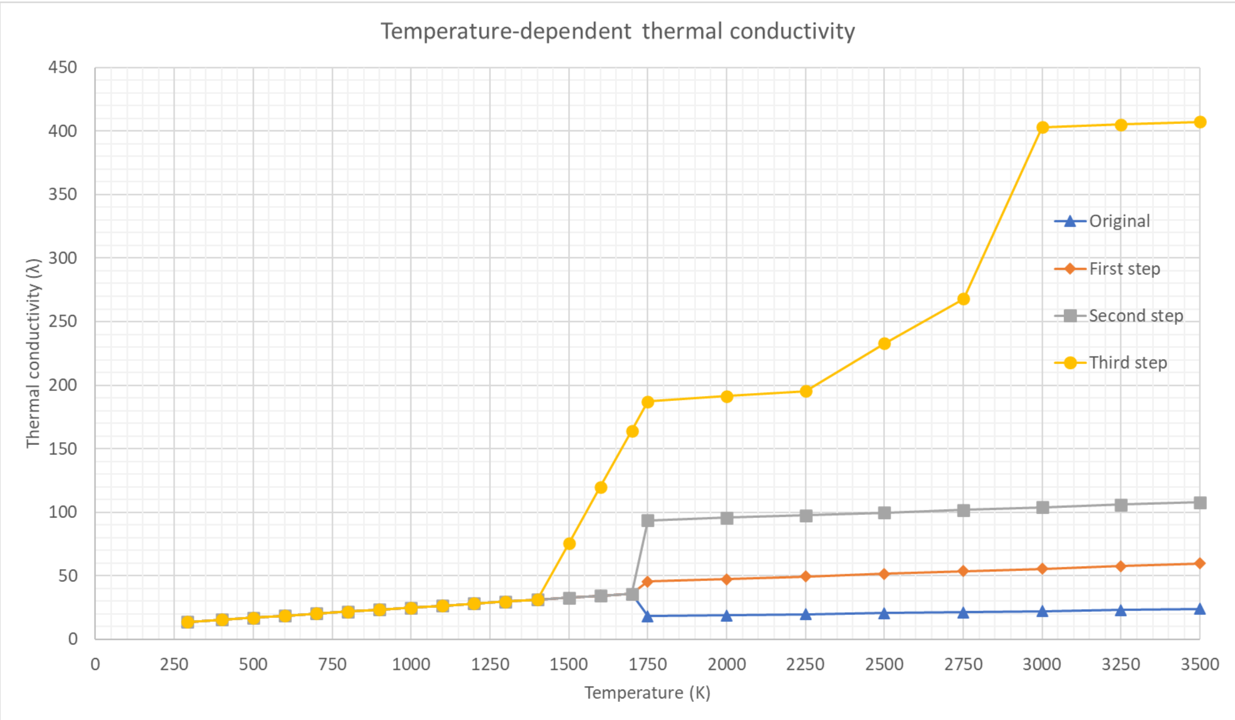

Figure 63. Different approaches in modifying the thermal conductivity – model M3.

As shown in the flowcharts in Figure 45 and Figure 46, several functions have been incorporated into the model to govern modifications to the properties of the material. The increase in conductivity is determined by a series of equations listed below, where 'n' represents the numbering system assigned to the total count of data points representing temperature-dependent thermal conductivity. The conditions under which each equation is applied are listed below and summarised in Table 6.

- For $8 \leq n \leq 10$, temperature range: 1750 K – 2250 K

$$Mod_{KXXn} = \Big[\big((KXX_{original} + Hor\_EnFactor) \times EnFacX\_Multiplier\big) \times (EnMultiplier\_SL - 1)\Big]$$

Where EnMultiplier_SL = 2.0

- For n equals to 11 or 12, temperature range: 2500 K – 2750 K

$$Mod_{KXXn} = \left\{[(20.6 + Hor\_EnFactor) \times EnFacX\_Multiplier] \times \left[EnMultiplier\_SL \times \left(\left((EnMultiplier\_LG - 1) \times \frac{n-10}{3}\right) + 1\right)\right]\right\}$$

Where EnMultiplier_LG = 1.5

- For $13 \leq n \leq 21$, temperature range: 3000 K – 5000 K

$$Mod_{KXXn} = \Big[\big((20.6 + Hor\_EnFactor) \times EnFacX\_Multiplier\big) \times (EnMultiplier\_SL \times EnMultiplier\_LG - 1)\Big]$$

- For $5 \leq n \leq 7$, temperature range: 1500 K – 1700 K

$$Mod_{KXXn} = \left\{\Big[\big((18.1 + Hor\_EnFactor) \times (EnFacX\_Multiplier - 1)\big) + Mod_{KXX8}\Big] \times \frac{2 \times (n-4)}{7}\right\}$$

Table 10. Overview of Thermal Conductivity Enhancement Parameters.

Factor	Definition and Purpose
Hor_EnFactor	Increment factor for thermal conductivity in the X and Y directions, applied through an additive method. This factor raises the thermal conductivity of the liquid phase above that of the solid phase, ensuring a higher overall value.
EnFacX_Multiplier	Multiplicative enhancement factor for thermal conductivity in the X direction. This factor is central to the research, as it explores the feasibility of using enhanced thermal conductivity as a substitute for fluid flow modelling in solid-only simulations.

Mod_KXXn	Additional enhancement of thermal conductivity based on the second model. This third-step enhancement is reflected in Figure 63, demonstrating its impact on heat transfer.
EnMultiplier_SL	Modification of thermal conductivity near the melting point to simulate convective heat transfer. This adjustment facilitates faster heat dissipation from the 'liquid' region to the surrounding 'solid' region, improving the representation of heat flow in the absence of fluid dynamics.
EnMultiplier_LG	Modification of thermal conductivity near the boiling point to simulate heat transfer during keyhole welding. This adjustment enhances heat transfer from the 'gas' region to the surrounding 'liquid' region, better capturing the thermal behaviour associated with vaporization and keyhole formation.

In the equations shown above, the two factors, namely EnMultiplier_SL and EnMultiplier_LG, are the multiplication factors used to represent the increase in flow in the liquid and the gas phases. Similarly, EnFacX_Multiplier is the factor used to determine the rate of increase in thermal conductivity every time a loop completes during the simulation process.

The thermal conductivity value for temperature range between 1500 K and 5000 K is modified, while the thermal conductivity value below 1500 K remains untouched. As such, the new thermal conductivity represented by 'Third step' in Figure 63 is determined by the following equation:

$$\lambda = \left(\left(\lambda_{original} + Hor\_EnFactor\right) \times EnFacX\_Multiplier\right) + Mod_{KXXn}$$

Reason behind the logic of choosing temperature range 1500 K – 1700 K and 2500 K – 2750 K for applying modification at the thermal conductivity is because selected temperature range is the range below both the melting point (1703 K) and the boiling point (3090 K) of the material chosen. These temperature range are redefined as the phase change region where the material is susceptible to changes state from solid to liquid and from liquid to gases. The aim of implementing this functions is to greatly increase the efficiency of heat transfer between different state especially within the selected temperature range of 1500 K – 1700 K and 2500 K – 2750 K where phase changes occurs.

4.4.3. Comparison of M3 modelled and experimental results

The same experimental results used to test the M2 model were used. Figures 64 shows M3 modelled temperature along the x-axis at the widest point of the melt pool to show melt pool half widths and

Figures 65 shows M3 modelled temperature along the z-axis at the deepest point of the melt pool to show melt pool depths.

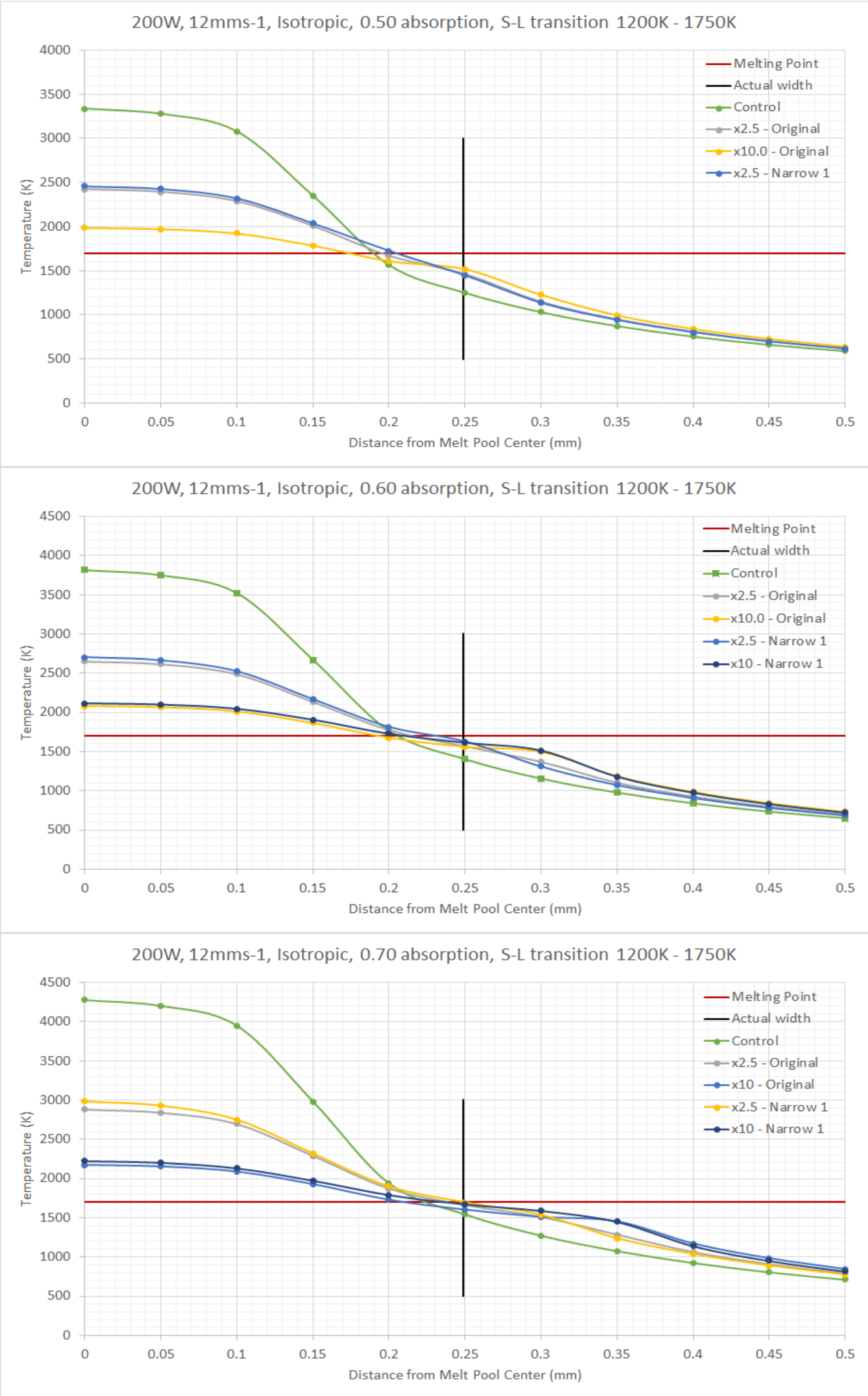

Figure 64. Melt pool half widths according to the M3 model with isotropic thermal enhancement and 0.5, 0.6 and 0.7 absorption

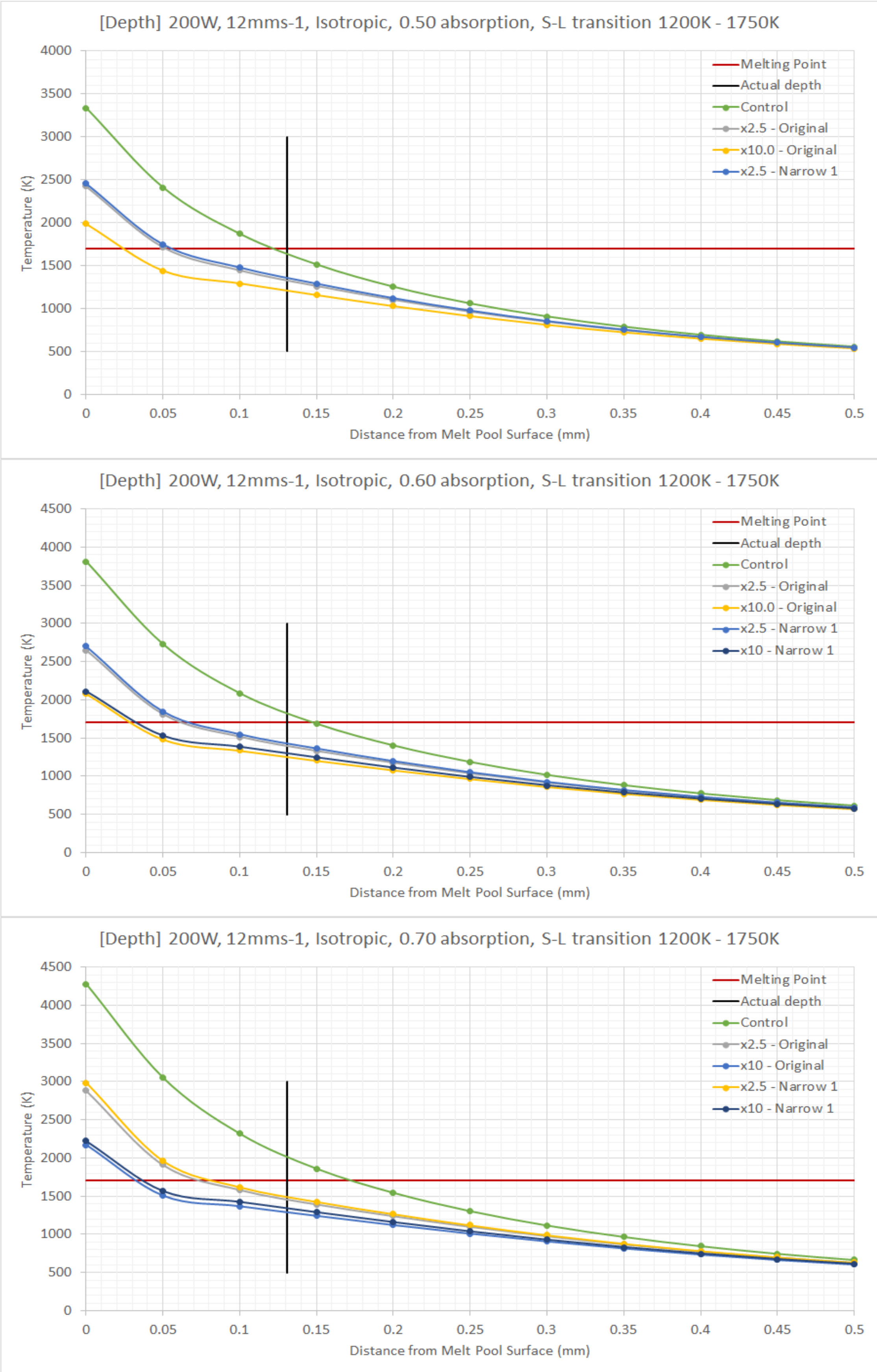

Figure 65. Melt pool depths according to the M3 model with isotropic thermal enhancement and 0.5, 0.6 and 0.7 absorption

Figure 64 and shows that the results modelled with model M3 and absorptivity values of 0.6 and 0.7 closely resemble the results obtained from the experiments. The labels 'origin' and 'narrow' in the legend of the graph indicates the temperature range at which the 'second step enhancement' occurs. For 'origin' results, the temperature range is situated between 1750 K and 3000 K, while the temperature range for 'narrow' results falls between 1750 K and 2750 K.

The reason for choosing these two different temperature ranges is that the boiling temperature of stainless steel 316 is 3090 K. Our objective in this attempt was to investigate how reducing the temperature range affected by the second step enhancement function could impact the results generated. Based on Figure 60 and Figure 62, It can be concluded that the change in temperature range has little impact on the results.

Figure 66 summarises the results. For half widths. The figure shows simulations with a range of combinations of parameters can produce a reasonable match to experiment.

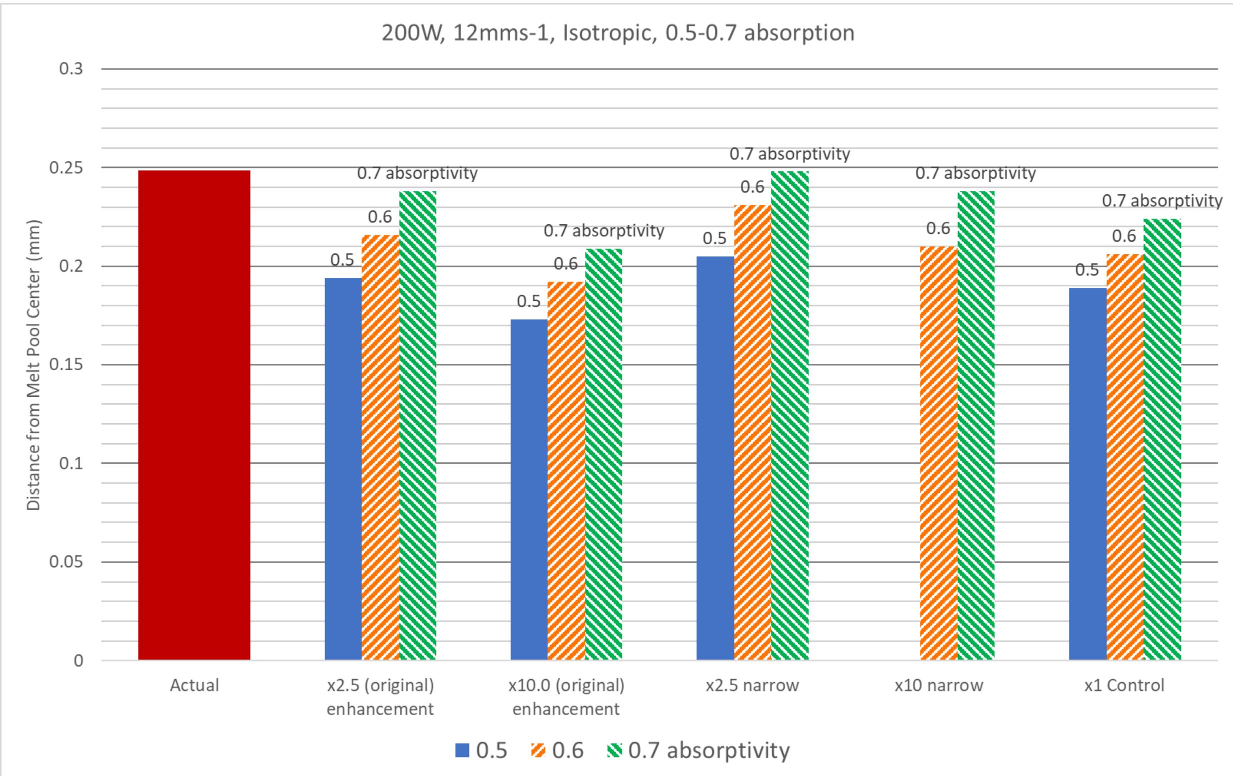

Figure 66. Experimental and simulated half width comparison using M3 with different laser absorption and thermal conductivity enhancement factors.

Figure 67 shows a comparison between the highest temperature data for the bottom surface obtained from the experiment and the simulation. The temperature data from model M3 exhibits the same trend as the data from the experiments, indicating a decrease in the highest temperature detected at the bottom surface as the laser traverse speed increases.

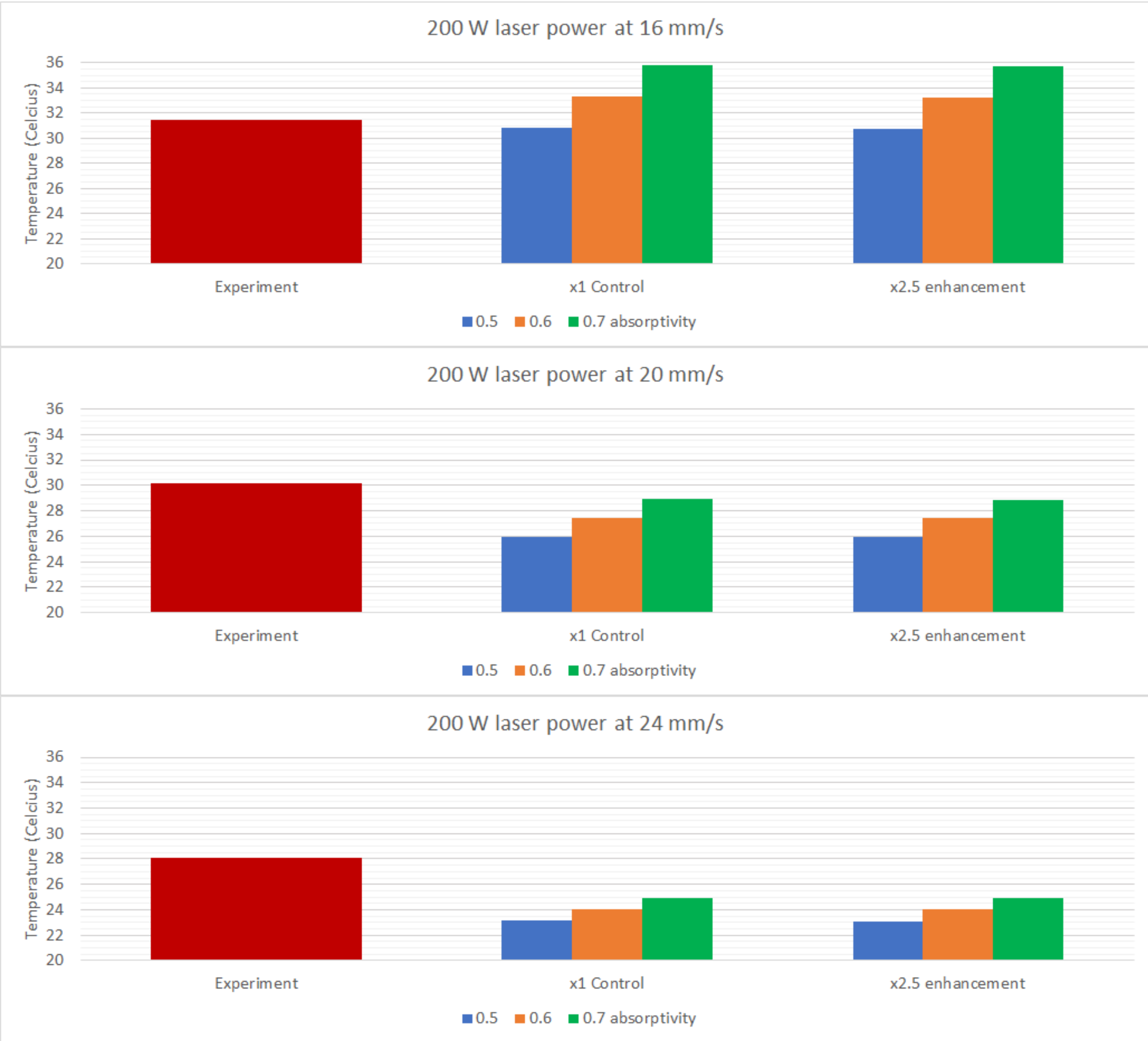

Figure 67. Highest Temperature of the bottom surface of the melt pool for different absorptions and conductivity enhancement factors

Figure 68 shows M3 modelled temperature along the x-axis at the widest point of the melt pool and Figure 69 shows M3 modelled temperature along the z-axis at the deepest point of the melt pool of samples produced at 250 W and 24 mm/s; measured pool half with and depth are also shown.

Figure 70 compares the experimental and simulated cross-sectional views of a melt track produced at 200 W and 12 mm/s using 0.7 absorptivity. The model predicts the width of the melt track to within 0.01 mm (4 % error) but under-predicts the depth by 0.05 mm (38 % error).

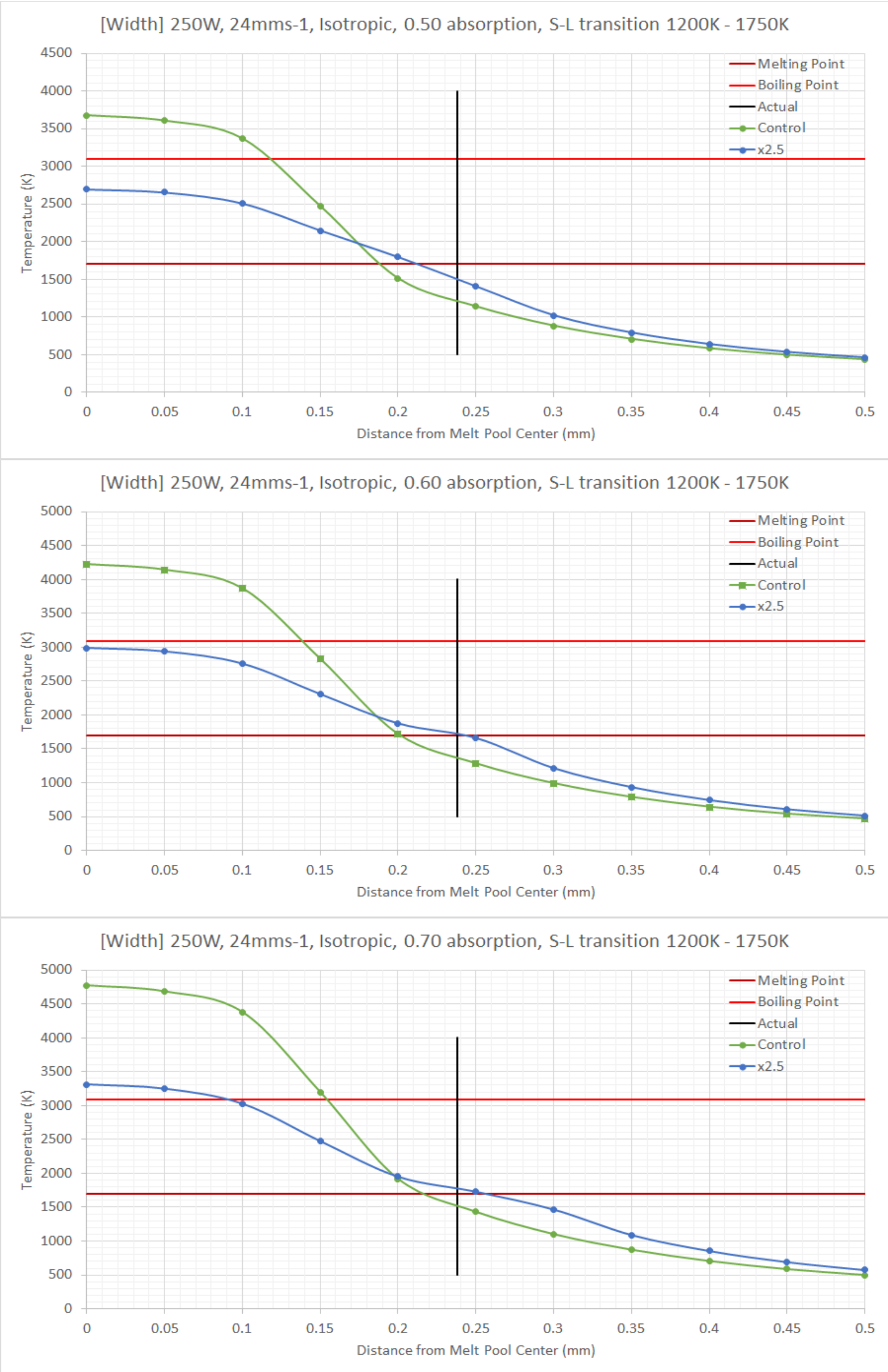

Figure 68. M3 modelled x-axis temperatures with 0.5, 0.6 and 0.7 absorption for 250 W and 24 mm/s.

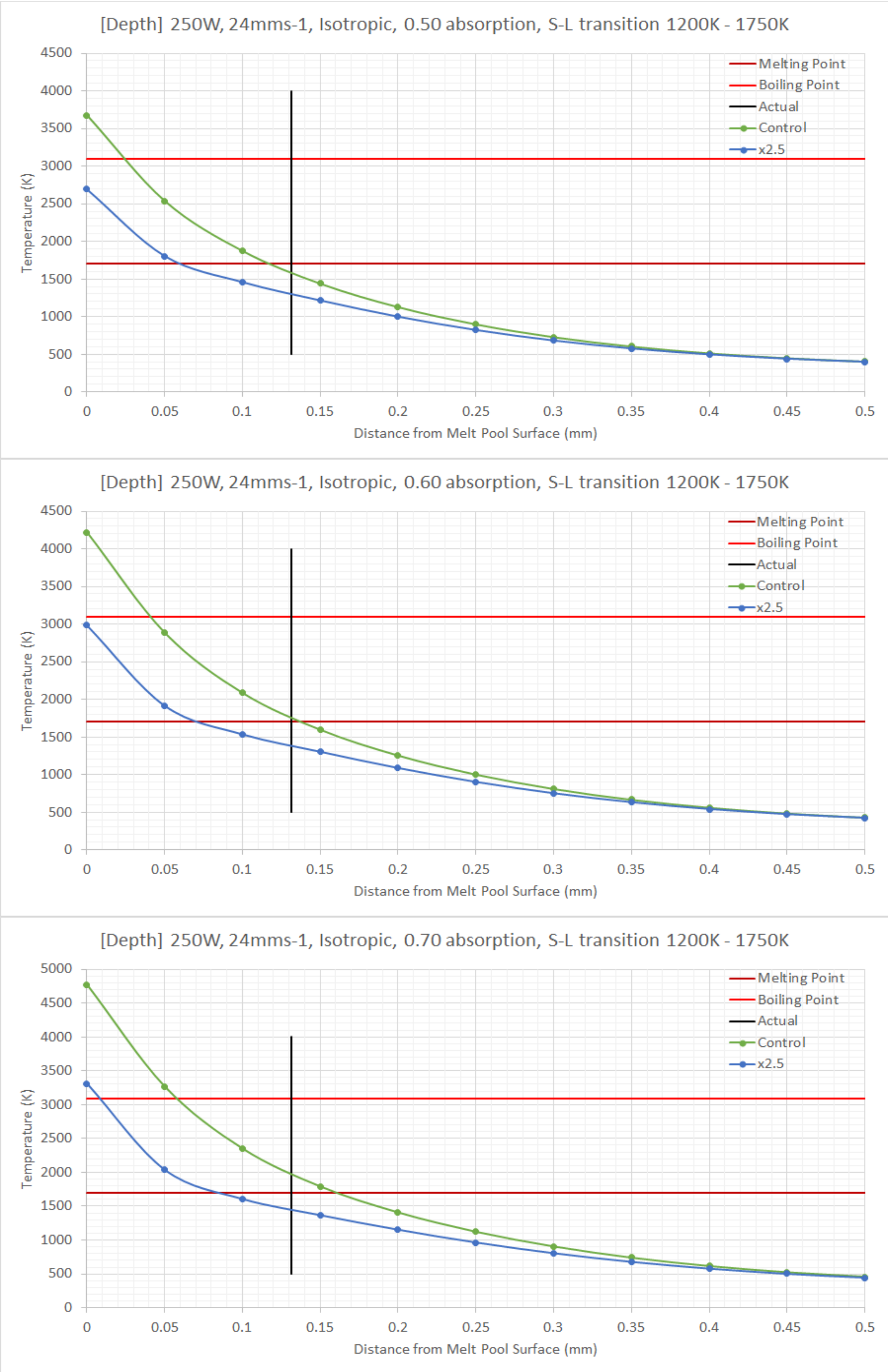

Figure 69. M3 modelled z-axis temperatures with 0.5, 0.6 and 0.7 absorption for 250 W and 24 mm/s.

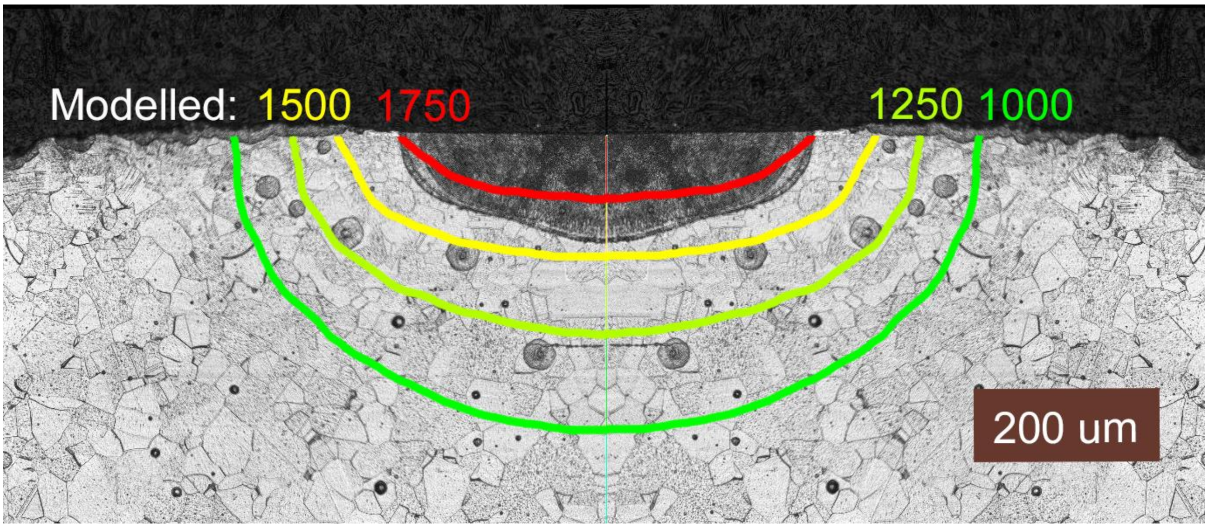

Figure 70. Approximate comparison between cross-sectional images obtained from the experiment and the simulation results for 200 W and 12 mm/s using 0.7 absorptivity.

A comparison between the simulation and experimental results yields the following observations:

- Width comparison:

  At a laser power of 200 W and a scan speed of 12 mm/s, the experimental results show a melt pool width of approximately 0.497 mm. The simulated result, on the other hand, produces a half-width of approximately 0.248 mm, corresponding to a total width of 0.496 mm. This indicates a very close agreement between the two, with a relative accuracy of 99.7%.

  The slight discrepancy observed in Figure 57 may be attributed to a misalignment in the global coordinate system—specifically, between the cross-sectional plane used for image capture and the actual y-coordinate at which the melt pool reaches its maximum width. While the data presented in Figure 55 were obtained through a systematic script designed to automatically identify and measure the widest section of the melt pool, the cross-sectional screenshot in Figure 57 was taken based on the coordinates of the most recently recorded heat flux position. This may have introduced a temporal offset, leading to the capture of a slightly smaller melt pool image due to the delay in melt pool expansion.

- Depth comparison:

  Under the same processing parameters (200 W, 12 mm/s), the experimental melt pool depth is measured at approximately 0.131 mm, while the simulation predicts a depth of 0.100 mm, corresponding to a relative accuracy of 76.3%.

4.5. Discussion

This chapter develops three single-phase finite element models and investigates the feasibility of employing them to simulate a moving melt pool.

After comparing the results obtained from models M1 and M2 with experiment, it can be concluded that these do not well predict the melt pool width. This suggests that the equations governing thermal conductivity variations may not sufficiently account for Marangoni flow within the melt pool, which plays a crucial role in heat transfer during laser melting and conduction-mode welding.

Based on the methodology of comparing modelled and measured results, model M3 demonstrates the capability to predict the width of the melt track for most conduction-based laser welding cases with laser power ranging from 200 W to 250 W. The selection of 200 W and 250 W for comparison is because power levels exceeding 250 W result in the welding process transitioning beyond the conduction-based laser welding domain, as indications of keyhole formation begin to emerge. This transition is commonly referred to as ‘mixed-mode’ laser welding.

Figure 71 to Figure 78 present a comparative analysis of the results for the 200 W and 250 W series in graphical format. Upon reviewing all results generated with laser absorption rates ranging from 35% to 80%, it is consistently observed that a laser absorption rate of 60% produces simulation results that align well with experimental trends and appear reasonable. Notably, various researchers investigating laser absorption in conduction-based and mixed-mode laser melting across diverse process parameters have collectively concluded that an acceptable range for laser absorptivity lies between 30% and 60% [77-81, 94, 132].

This trend is particularly evident in the results obtained for the 250 W series. Figure 51 and Figure 52 presents a microscopic view of the cross-section of the melt track. The experimental results for the 250 W series begin to exhibit characteristics of ‘mixed-mode’ laser melting, as the boundary between the solid region and the melt pool deviates from the smooth, semi-oval curvature observed in the 200 W series. This suggests that the temperature at the centre of the melt pool is approaching the boiling point, leading to localised vaporization and causing the laser to exhibit drilling effects, resulting in a near ‘mixed-mode’ cross-sectional shape of the melt track.

With simulation results indicating that the centre of the melt pool approaches the boiling point of the material, the M3 model provides results that are not only consistent with experimental observations but also physically reasonable within the context of conduction-based laser welding.

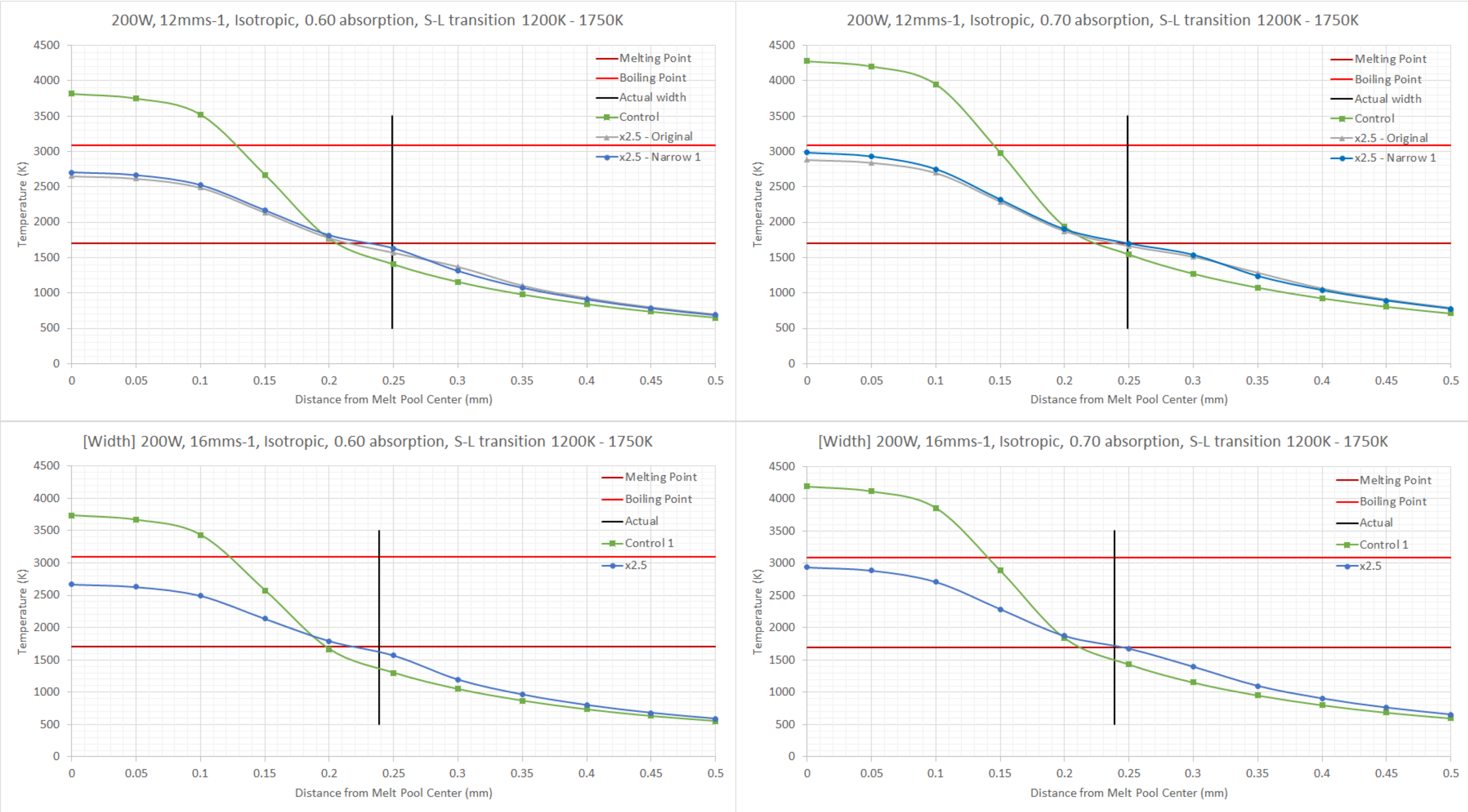

Figure 71. Half width comparison between (different enhancement factor) simulation and experiment results for 200 W with different traverse speed (part 1).

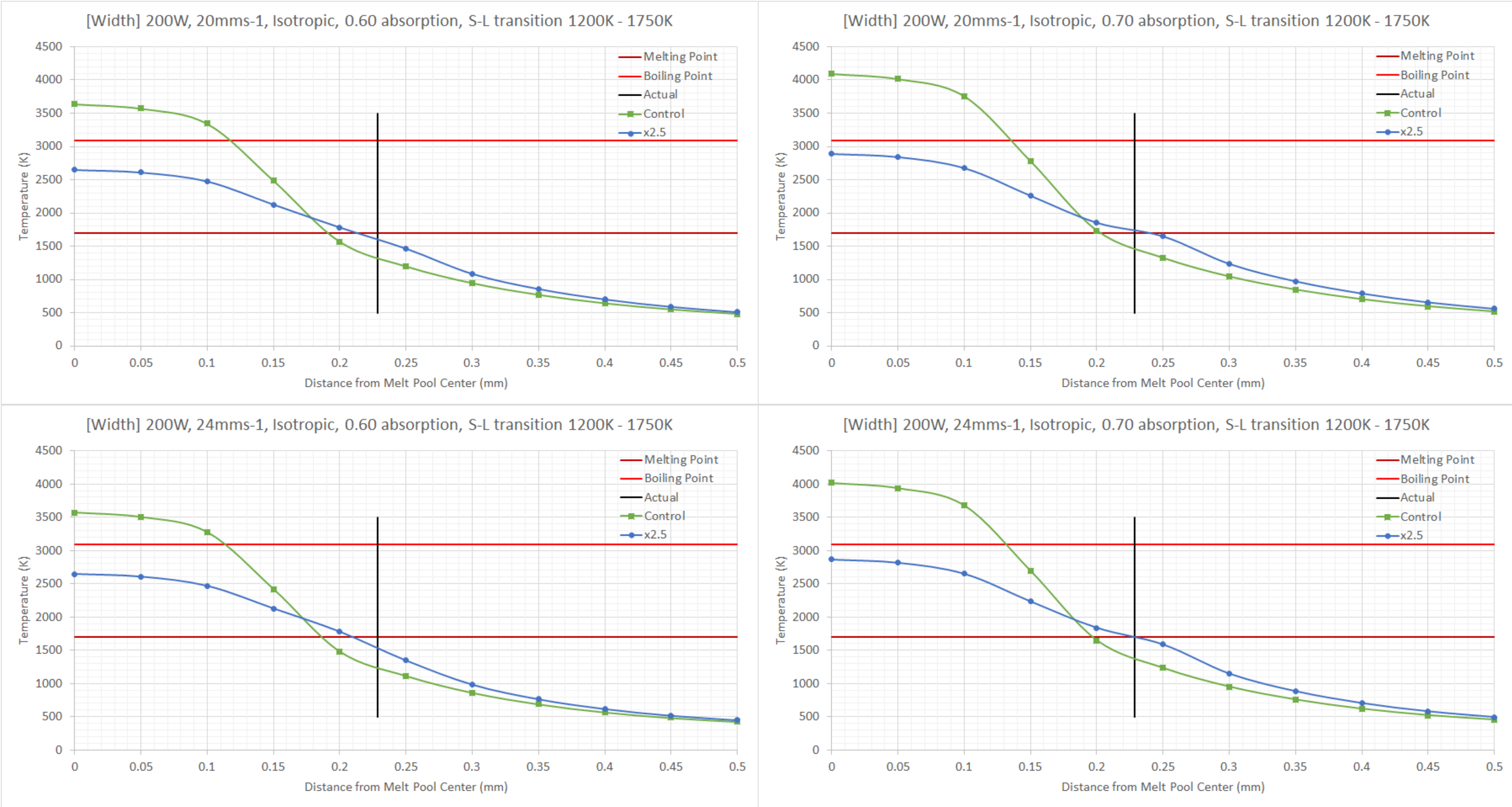

Figure 72. Half width comparison between (different enhancement factor) simulation and experiment results for 200 W with different traverse speed (part 2).

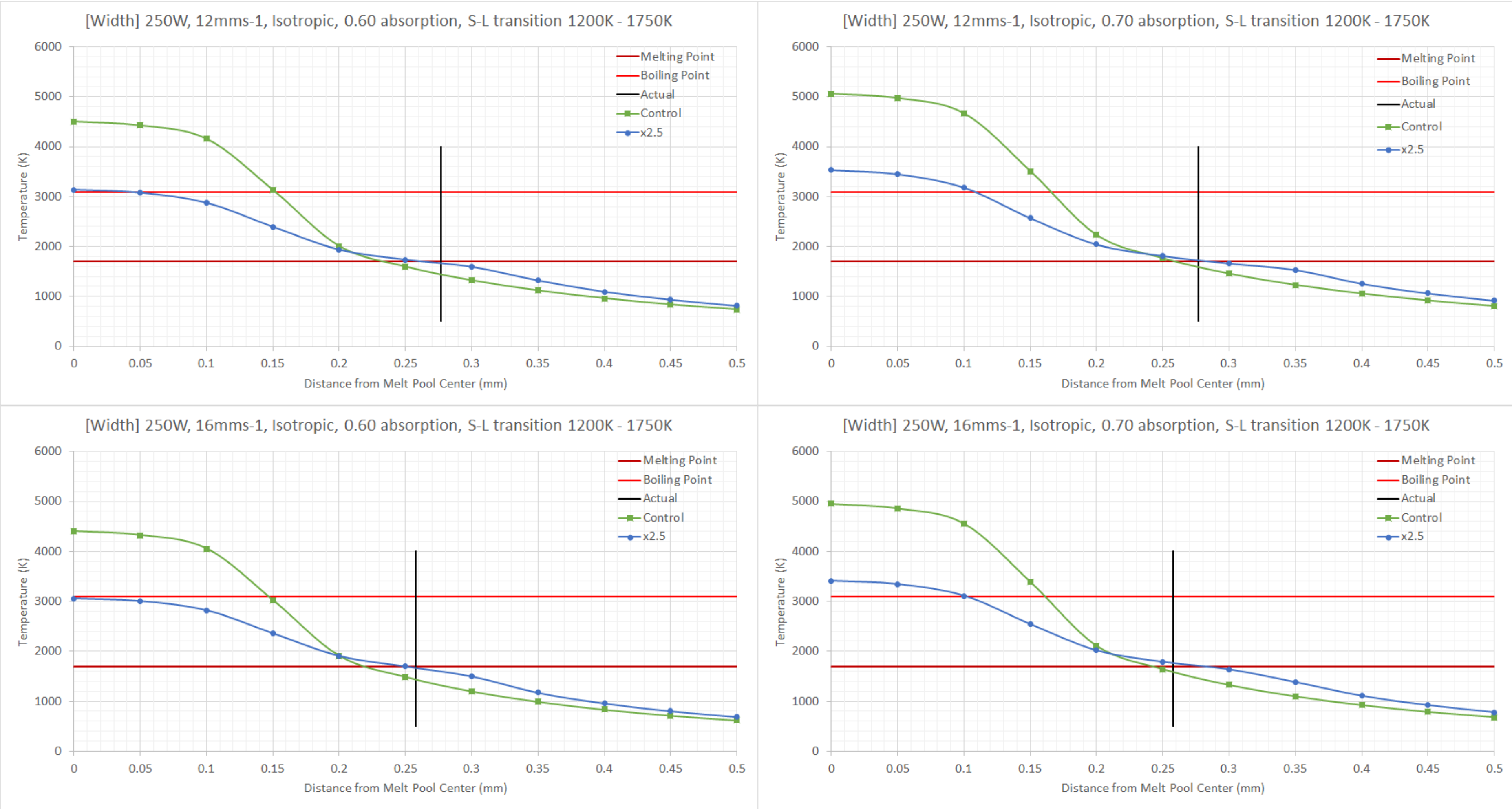

Figure 73. Half width comparison between (different enhancement factor) simulation and experiment results for 250 W with different traverse speed (part 1).

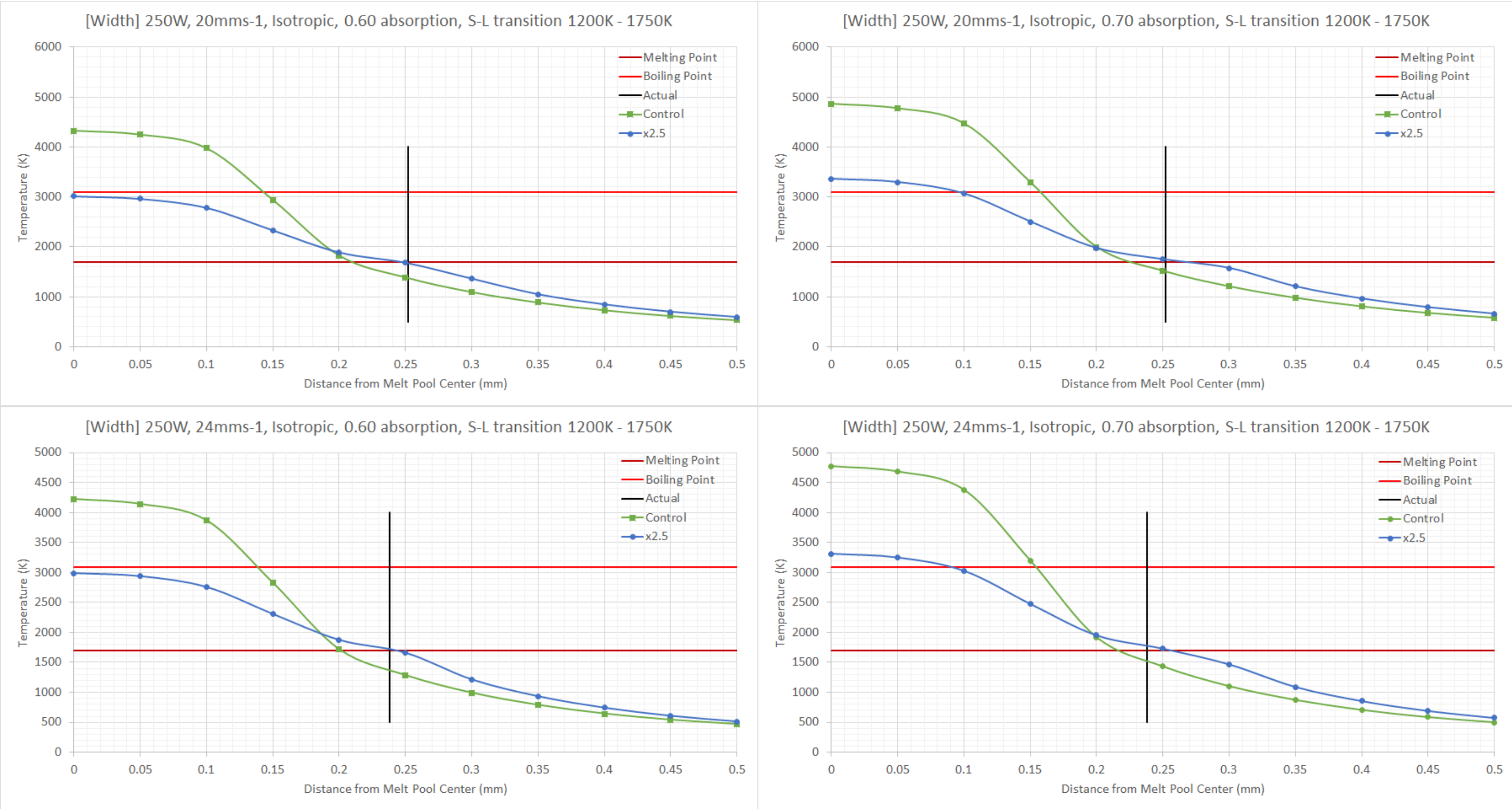

Figure 74. Half width comparison between (different enhancement factor) simulation and experiment results for 250 W with different traverse speed (part 2).

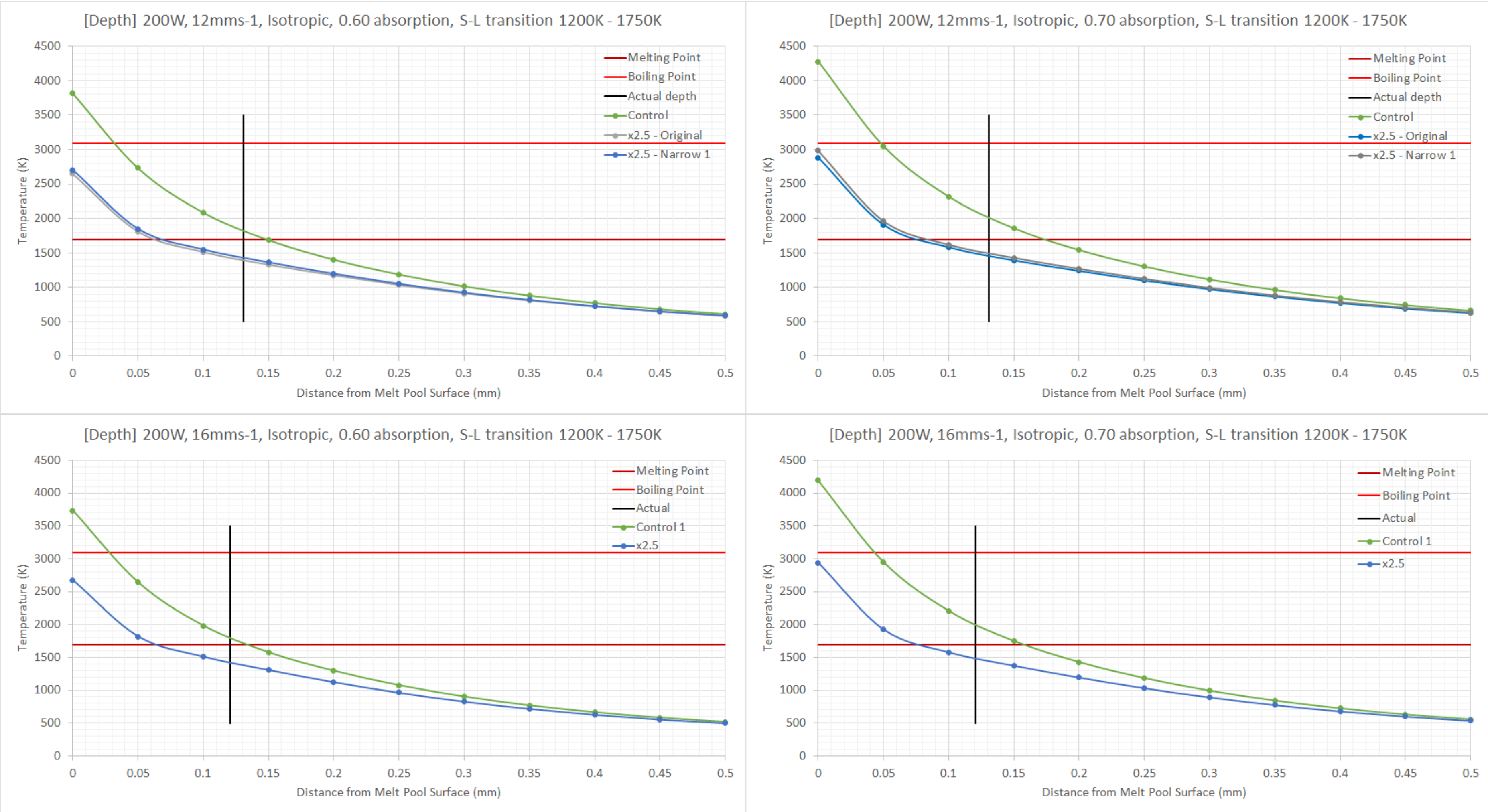

Figure 75. Depth comparison between (different enhancement factor) simulation and experiment results for 200 W with different traverse speed (part 1).

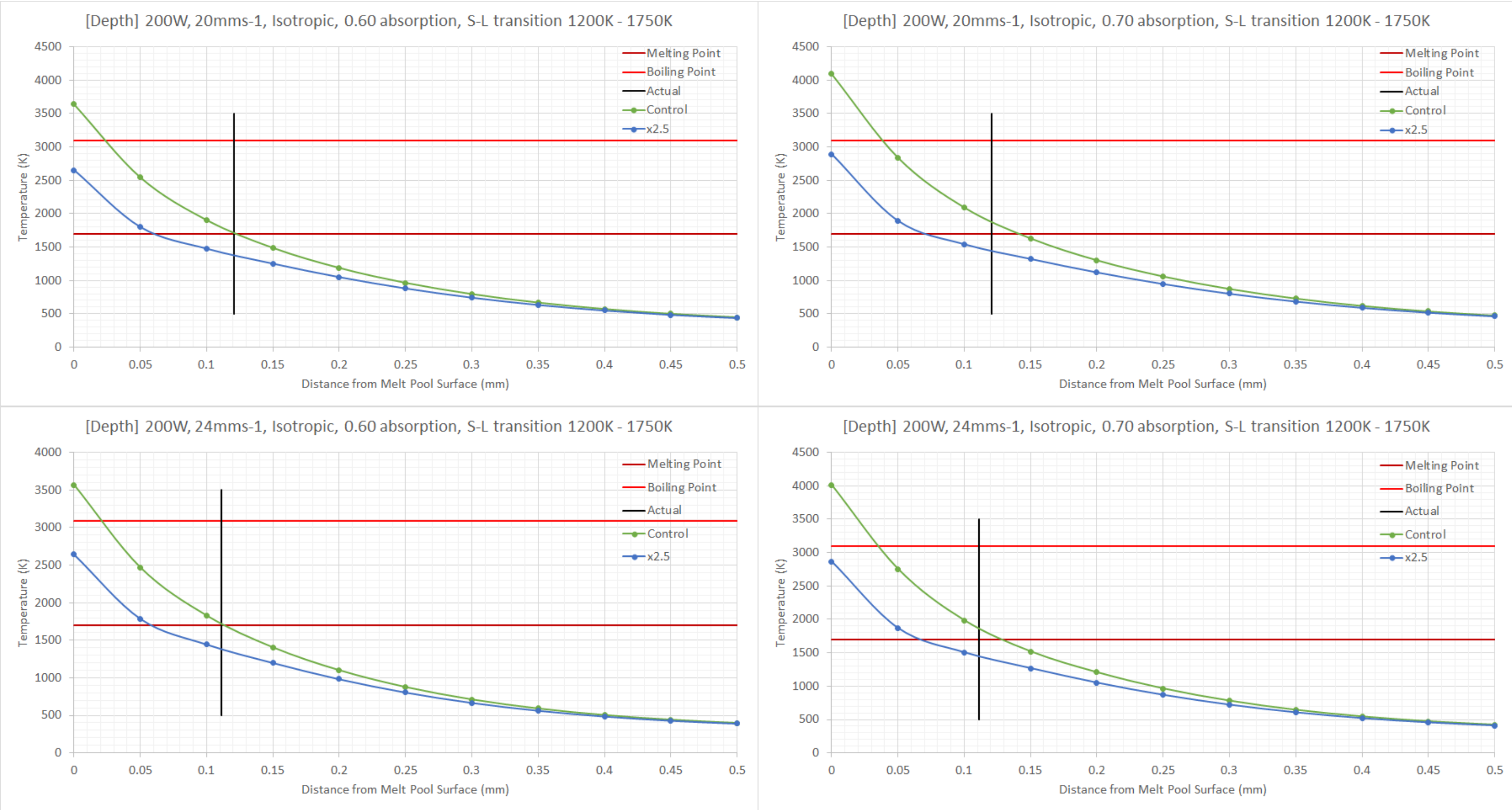

Figure 76. Depth comparison between (different enhancement factor) simulation and experiment results for 200 W with different traverse speed (part 2).

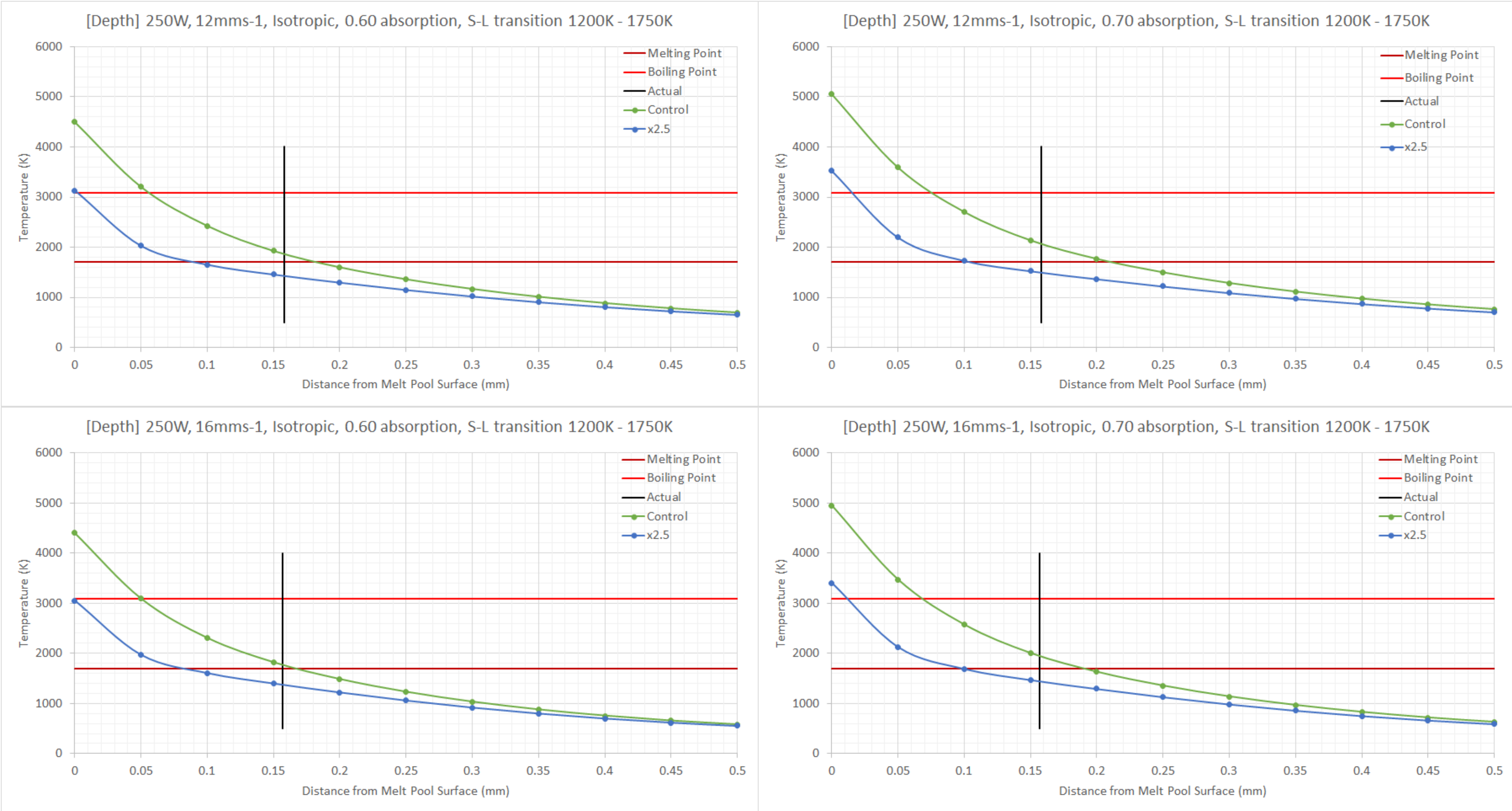

Figure 77. Depth comparison between (different enhancement factor) simulation and experiment results for 250 W with different traverse speed (part 1).

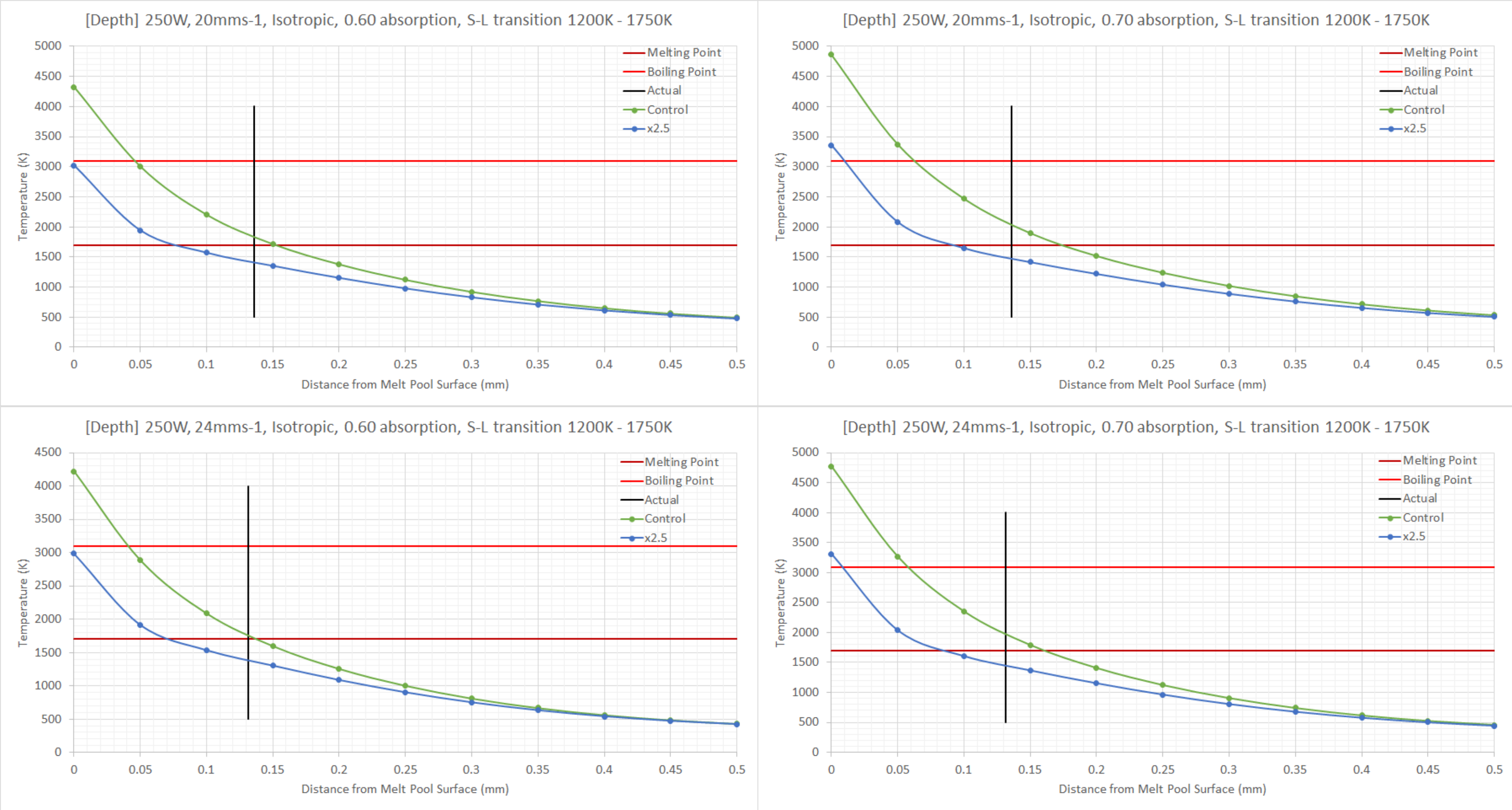

Figure 78. Depth comparison between (different enhancement factor) simulation and experiment results for 250 W with different traverse speed (part 2).

4.6. Conclusion

After analysing all the comparison results between cases involving laser power of 200 W and 250 W, in can be concluded that M3 consistently demonstrates a strong capability in predicting the width of the melt pool when the following parameters are applied:

- Laser absorption of 60%
- Thermal conductivity enhancement (multiplication) factor of 2.5 for conductivity within the temperature range of 1750 K to 2750 K. This adjustment aligns the thermal conductivity with the conductivity trend observed below the melting point.
- Thermal conductivity enhancement (multiplication) factor of 7.5 for conductivity within the temperature range of 3000 K to 3500 K. This enhancement is also implemented to maintain consistency with the conductivity trend below the melting point.

The final temperature-dependent thermal conductivity used in the simulation exhibits an incremental factor, gradually increasing from 1 until reaching a maximum multiplication factor of 18.12 at a temperature of 3000 K.

These findings indicate that the third model provides reliable predictions for the width of the melt pool by applying the isotropic enhancement principle to modify thermal conductivity during the simulation process. While the model does not fully capture the depth of the melt pool, this limitation is addressed in the next model, as discussed in the following chapter.

5. Keyhole-based and mixed-mode laser welding

5.1. Introduction

In this chapter, both keyhole-based and mixed-mode laser welding processes will be examined. Building upon the work from the previous chapter, the third model, M3, will be further refined to improve the accuracy of melt pool depth predictions. This refinement involves incorporating additional functions that determine the necessity of laser penetration and guide the depth of penetration once keyhole formation occurs.

Keyhole-based laser welding occurs when the material temperature exceeds its vaporization point, causing material vaporization and generating a drilling effect that allows the laser beam to penetrate deeper into the material. Although the vapor plume formed during this process can obstruct the laser beam and reduce energy absorption due to the inverse bremsstrahlung absorption effect, some of the laser energy that enters the keyhole is effectively trapped inside. This occurs through multiple reflections within the keyhole, significantly enhancing laser absorptivity and improving the efficiency of the welding process.

Figure 79 presents a schematic diagram of the keyhole-based laser welding process. As shown, a hot vapor plume forms when the material is heated above its vaporization point, partially obstructing the laser beam and reducing its absorption efficiency during the welding process.

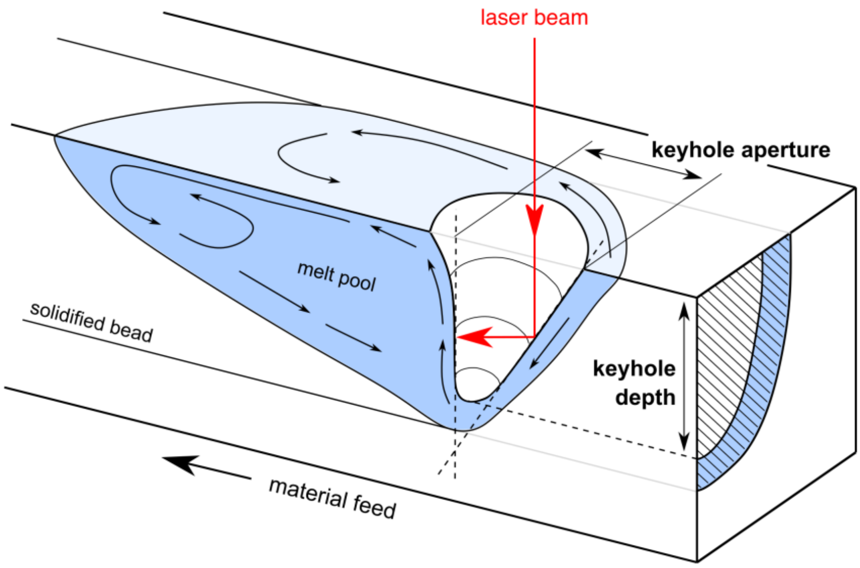

Figure 79. Schematic representation of the keyhole laser welding process [134].

5.2. Keyhole and mixed-mode model, M4

Figure 81 presents a simplified simulation flowchart for the model created to simulate the keyhole-based laser welding process. As shown in the Figure 82, the M4 model is similar to the third model created for conduction-based laser welding/melting, but there are two major differences.

In the M4 model, two new functions have been introduced to enhance the simulation of keyhole-based laser welding processes. The first function is designed to simulate the formation of keyholes during laser welding at higher power levels. The second function represents an upgraded version of the previous one, tailored to accommodate the increased depth of the melt pool that is generated during keyhole-based laser welding.

The function responsible for keyhole formation (shown in Figure 82) only triggers after the first simulation cycle has been completed. It operates by inputting initial temperature profile data to calculate the most suitable heat flux profile, which is then applied as the boundary condition in the subsequent cycle. If the most suitable heat flux profile is completely on the upper surface then the welding is purely conductive and the model operates in the same way as M3.

On the other hand, the second function serves as an extension to expand the temperature data collection range. Keyhole-based laser welding typically results in a larger melt pool compared to conduction-based laser welding. A wider temperature data collection range is necessary to cover all potential melt pool formation areas, ensuring the reliability and accuracy of the results.

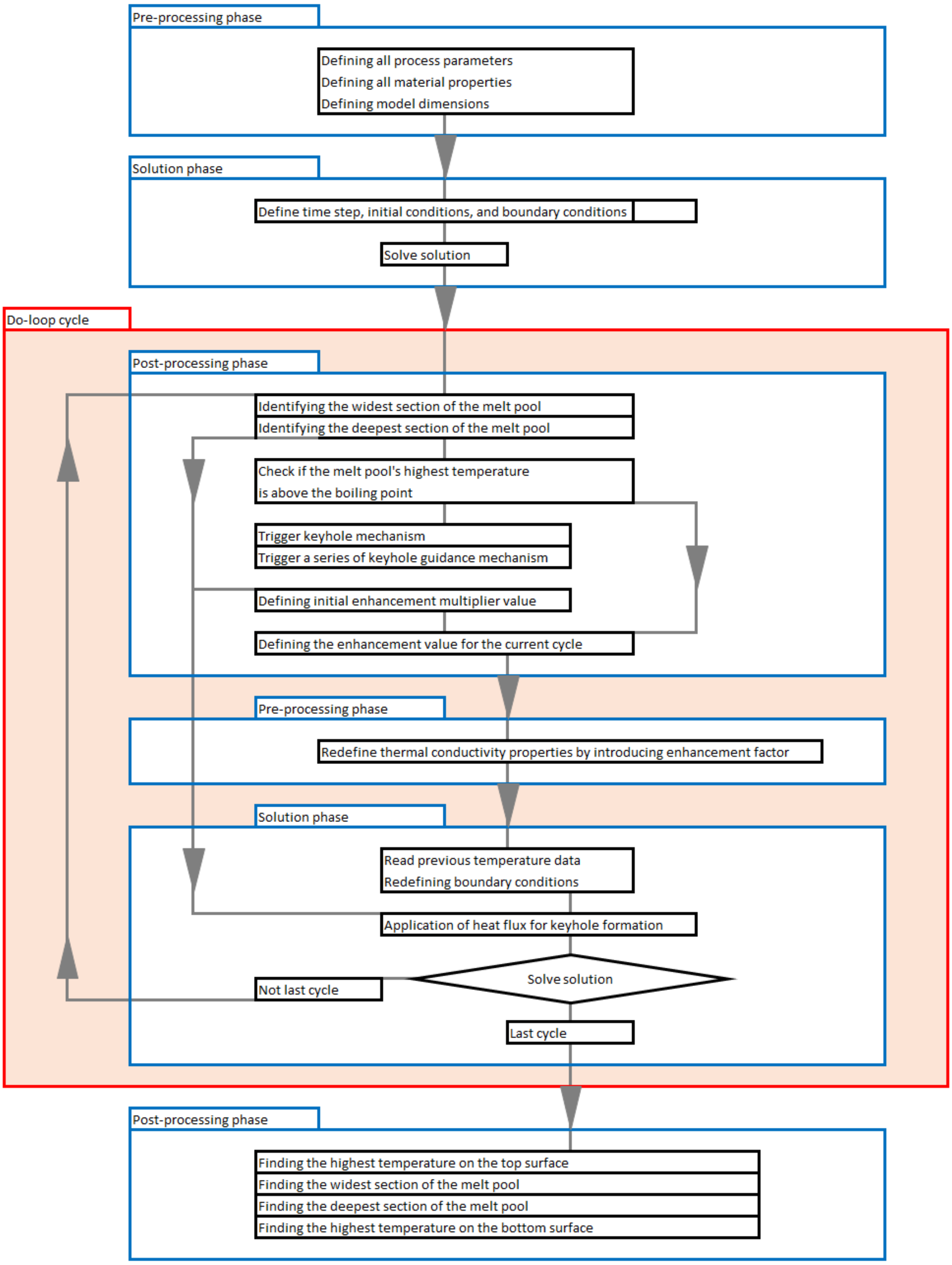

Figure 80. Simulation flowchart for the M4, mixed mode and keyhole, model.

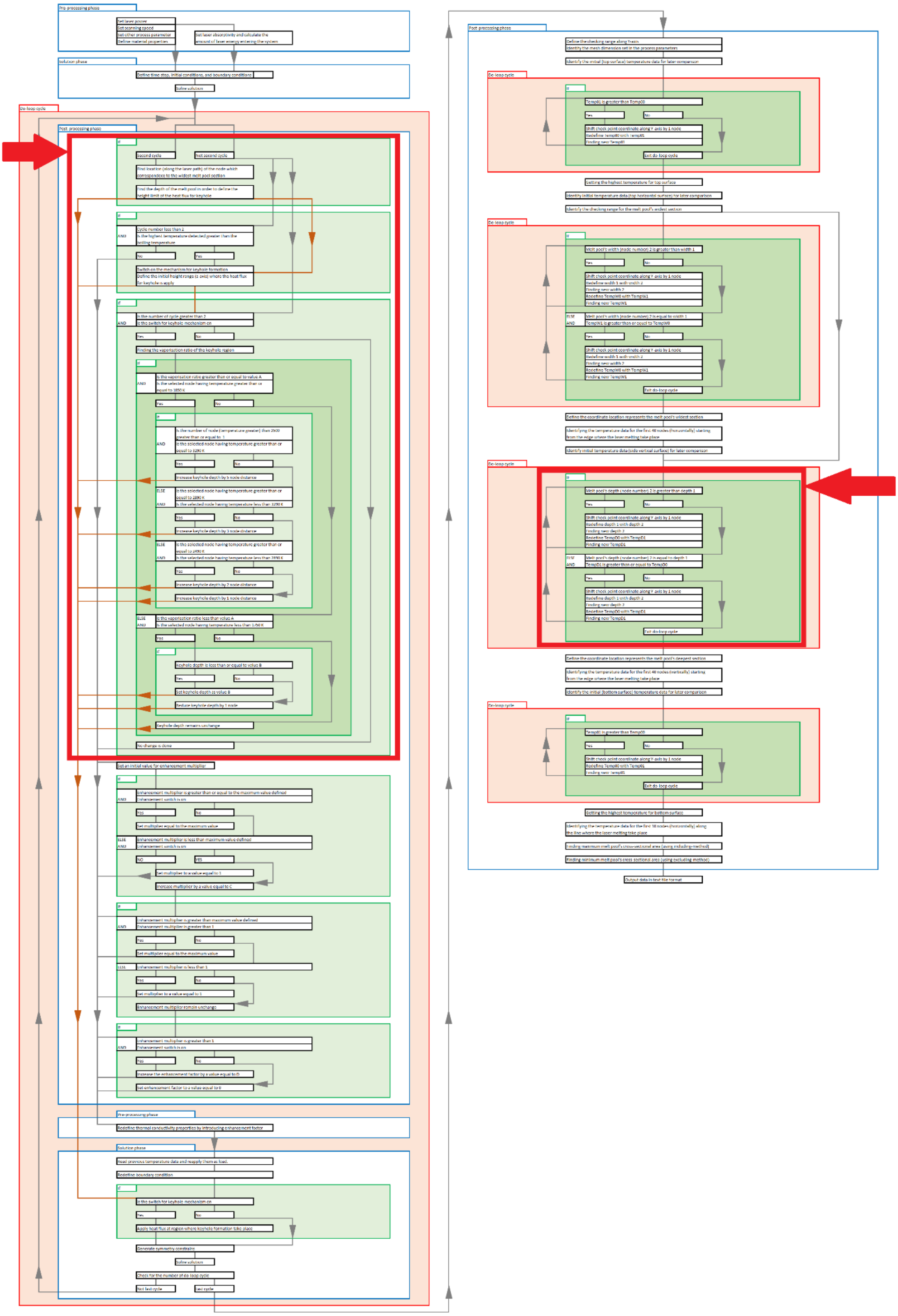

Figure 81. A detailed simulation flowchart showing the differences between models M3 and M4.

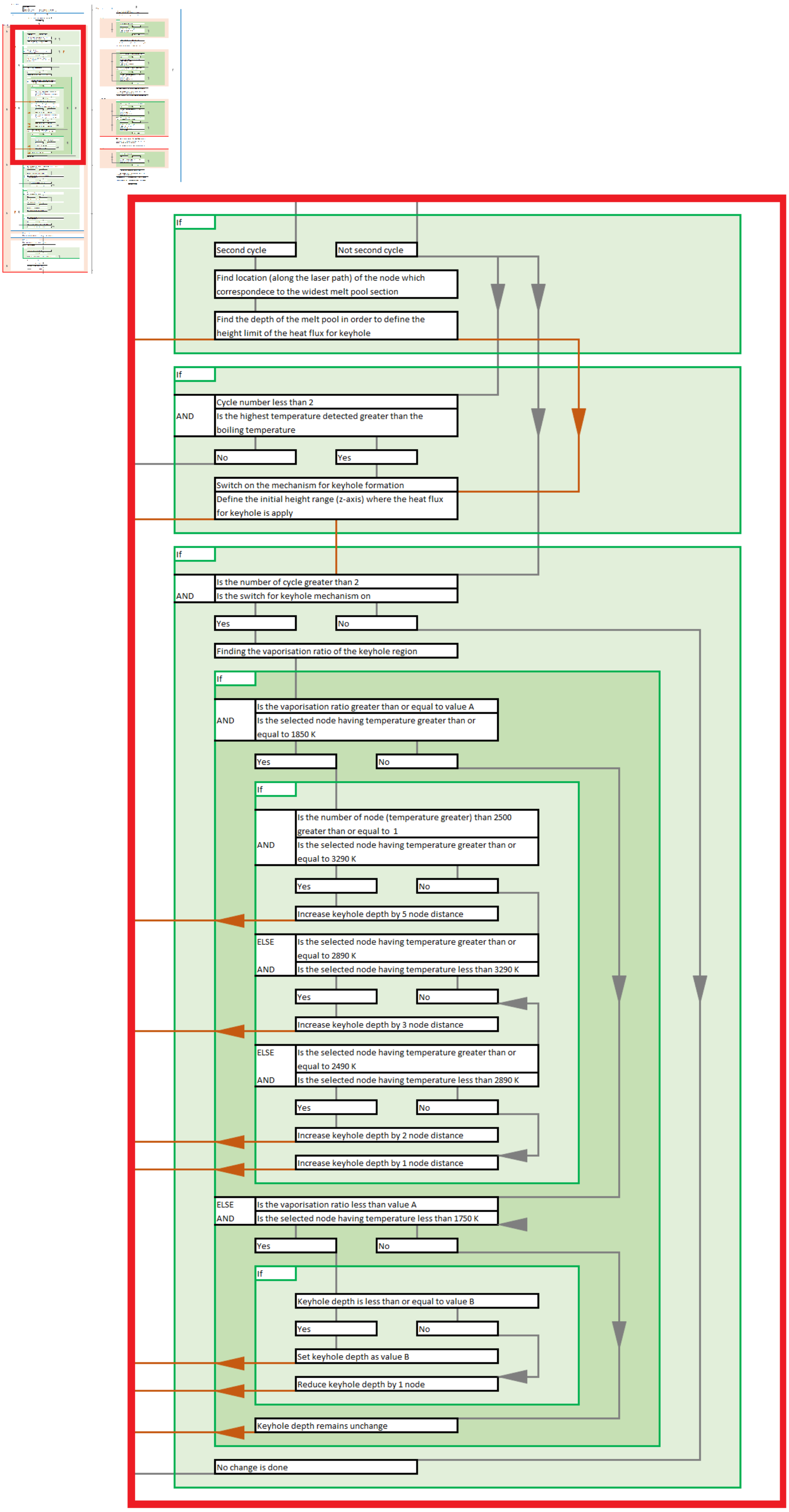

Figure 82. The location of the function responsible for the keyhole formation in model M4

Figure 83 presents a minor function that serves to identify the dimensions of the melt pool formed in the first cycle. The purpose of this function is to provide the initial data for calculating the initial heat flux profile once the trigger for the keyhole function is initiated by the subsequent function.

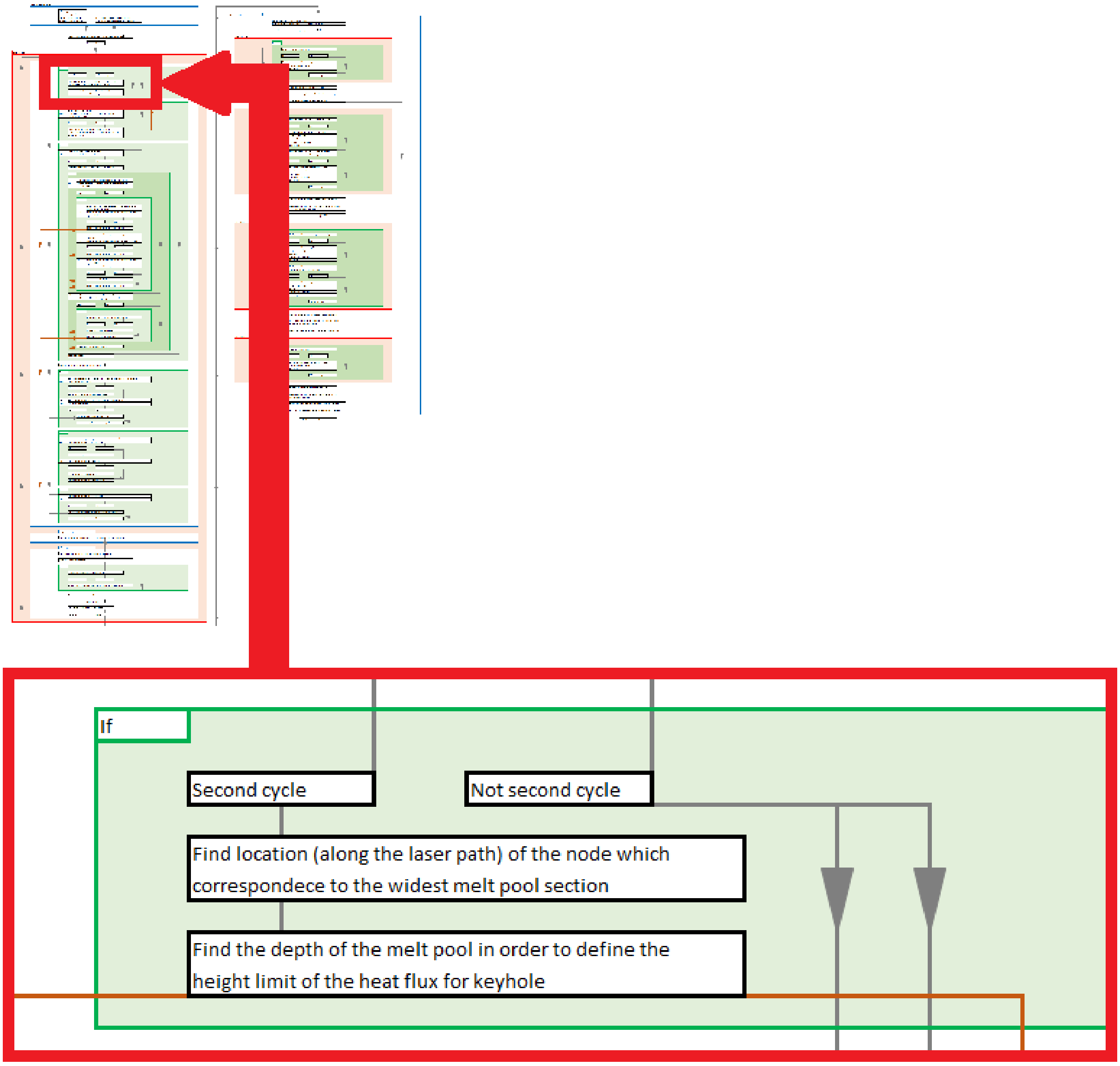

Figure 83. Analysis of the first cycle's melt pool profile for preparation of the initial input data for the calculation of the keyhole-based heat flus profile.

Figure 84 presents a minor function that serves as a safety check to determine if the temperature results of the first cycle meet the conditions for the formation of a keyhole. This function includes two conditions, both of which must be met simultaneously for it to activate the next function responsible for defining the properties of keyhole-based heat flux profile:

- The number of completed cycle must be less than 1.

- The temperature within the area where heat flux is applied during the first cycle must be greater than the boiling temperature of the material used.

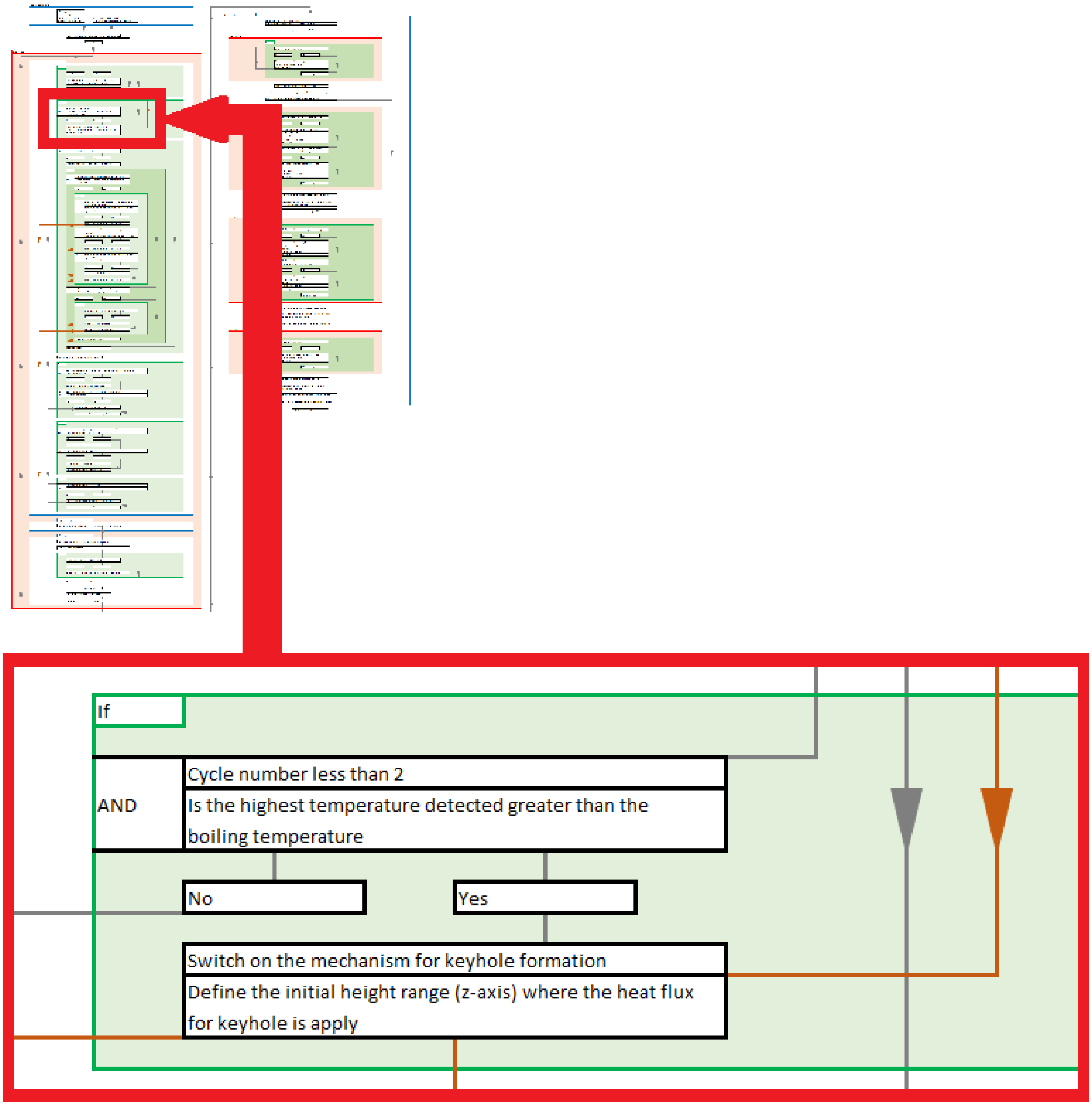

Figure 84. Trigger check for keyhole function.

Figure 85 is the main part of the routine and calculates the heat flux profile responsible for keyhole generation.

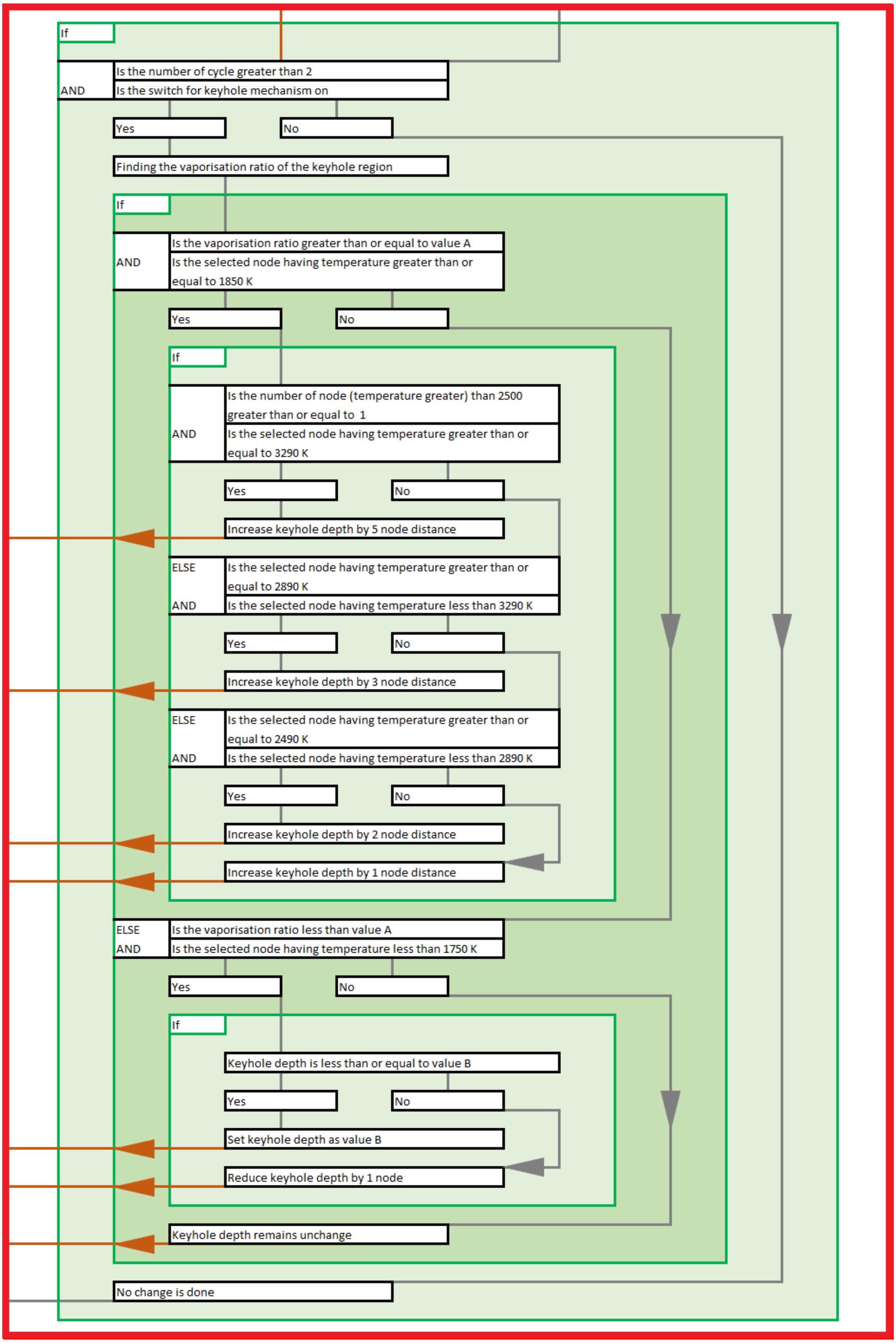

Figure 85. Calculation of the heat flux profile responsible for keyhole generation.

Together, the logics (for deciding the heat flux for keyhole formation) within Figure 83, Figure 84 and Figure 85 can be represented by the series of equations below.

Previous cycle: *i* = 1

The cycles where the following logics and equation take place: *i = i + 1*

Within Do-Loop (First level):

$$2 \leq i \leq Num\_LS$$

Define the Nodes_No_1 value based on node selection using heat radius . This value is influenced by the MeshFactor, which is defined at the beginning of the simulation.

In this case, MeshFactor is set to 20, meaning that a 1 mm distance contains 20 elements and 21 nodes..

- Define Nodes_No_2 value based on node selection at the specified location:

$$coordinate\ (x,\quad y,\quad z) = ([Half\_Width \times 2],\quad [Start\_D + (i \times Step\_Length)],\quad Half\_Thickness)$$

$$Nodes\_No\_2 = number\ of\ nodes\ with\ temperature\ \geq Melt\_Temp$$

Where Half_Width, Start_D, Step_Length, and Half_Thickness are defined at the beginning of the simulation.

- Definition of Melt_Temp1:

$$Melt\_Temp1 = \begin{cases} Melt\_Temp - 500 & if \quad i \leq 6 \\ Melt\_Temp - 400 & if \quad 6 < i \leq 12 \\ Melt\_Temp - 200 & if \quad 12 < i \leq 20 \\ Melt\_Temp & if \quad 20 < i \end{cases}$$

Where Melt_Temp is equal to 1750 K.

- Define Nodes_No_3 value based on node selection at the specified location:

$$coordinate\ (x,\quad y,\quad z) = (0,\quad [Start\_D + (i \times Step\_Length)],\quad Half\_Thickness)$$

$$Nodes\_No\_3 = number\ of\ nodes\ with\ temperature\ \geq Melt\_Temp1$$

- Define Temp_1 value through extracting temperature data from node located at the following coordinate:

$$coordinate\ (x,\quad y,\quad z) = \left(\left[(Half\_Width \times 2) - \left(\frac{Nodes\_No\_3 - 1}{1000 * MeshFactor}\right)\right],\quad [Start\_D + (i \times Step\_Length)],\quad Half\_Thickness\right)$$

$$Temp\_1 = temperature\ value\ of\ the\ selected\ node$$

- Definition of MaxNode_Behind and If_step:

$$\begin{array}{ccc} \text{MaxNode\_Behind} & = & 1 \\ \text{If\_step} & = & 1 \end{array}$$

- Within Do-Loop (Second level):

$$1 \leq \text{If\_step} \leq \text{Nodes\_No\_2}$$

  - Define Nodes_No_4 value based on node selection at the specified location:

$$coordinate\ (x,\quad y,\quad z) = (0,\quad [Start\_D + (i - MaxNode\_Behind) \times Step\_Length],\quad Half\_Thickness)$$

$$Nodes\_No\_4 = number\ of\ nodes\ with\ temperature\ \geq Melt\_Temp1$$

  - Define Temp_2 value based on node selection at the specified location:

$$coordinate \begin{pmatrix} x \\ y \\ z \end{pmatrix} = \begin{pmatrix} \left[(Half\_Width \times 2) - \left(\frac{(Nodes\_No\_4 - 1)}{(1000 \times MeshFactor)}\right)\right], \\ [Start\_D + (i - MaxNode\_Behind) \times Step\_Length], \\ Half\_Thickness \end{pmatrix}$$

$$Temp\_2 = temperature\ value\ of\ the\ selected\ node$$

  - Finding the widest section of the melt pool:

If $Temp\_2 > Temp\_1$,

$$\begin{array}{ccc} Nodes\_No\_3 & = & Nodes\_No\_4 \\ Temp\_1 & = & Temp\_2 \\ MaxNode\_Behind & = & MaxNode\_Behind + 1 \\ \text{If\_step} & = & \text{If\_step} + 1 \end{array}$$

- Redefine Nodes_No_4 value based on node selection at the specified location:

$$coordinate\ (x,\quad y,\quad z) = (0,\quad [Start\_D + (i - MaxNode\_Behind) \times Step\_Length],\quad Half\_Thickness)$$

$$Nodes\_No\_4 = number\ of\ nodes\ with\ temperature\ \geq Melt\_Temp1$$

- Redefine Temp_2 value based on node selection at the specified location:

$$coordinate\begin{pmatrix} x \\ y \\ z \end{pmatrix} = \begin{pmatrix} \left[(Half\_Width \times 2) - \left(\dfrac{(Nodes\_No\_4 - 1)}{(1000 \times MeshFactor)}\right)\right], \\ [Start\_D + (i - MaxNode\_Behind) \times Step\_Length], \\ Half\_Thickness \end{pmatrix}$$

$$Temp\_2 = temperature\ value\ of\ the\ selected\ node$$

Else, exit Do-Loop (Second level)

- Define Nodes_No_5 value based on node selection at the specified location:

$$coordinate\ (x,\quad y,\quad z) = ([Half\_Width \times 2],\quad [Start\_D + ((i - MaxNode\_Behind) \times Step\_Length)],\quad 0)$$

$$Nodes\_No\_5 = number\ of\ nodes\ with\ temperature\ \geq (Melt\_Temp1 + 250)$$

- Find the highest limitation (z-axis) where the heat flux for the keyhole can be apply:

$$KHole\_ShallowLimit = \begin{cases} \left[\dfrac{(Nodes\_No\_5) - 1}{1000 \times MeshFactor}\right] & if \quad i = 2 \\ KHole\_ShallowLimit & if \quad i \neq 2 \end{cases}$$

- Define Temp_3 value based on node selection at the specified location:

$$coordinate\ (x,\quad y,\quad z) = ([Half\_Width \times 2],\quad [Start\_D + (i - 2) \times Step\_Length],\quad Half\_Thickness)$$

$$Temp\_3 = temperature\ value\ of\ the\ selected\ node$$

- If-conditioning for deciding if the keyhole function should be switch on.

If $Temp\_3 \geq Boil\_Temp$ and $i \leq 2$

$$\begin{aligned} Keyhole\_Status &= 1 \\ Keyhole\_Depth &= [KHole\_ShadowLimit + (Heat\_Radius \times 2)] \end{aligned}$$

Where Boil_Temp is equal to 3090 K

Else if $Temp\_3 < Boil\_Temp$ and $i \leq 2$

$$\begin{aligned} Keyhole\_Status &= 0 \\ Keyhole\_Depth &= 0 \\ KHole\_ShadowLimit &= 0 \end{aligned}$$

Else

$$Keyhole\_Depth = Keyhole\_Depth$$

Where no parameters are changed.

- If-conditioning (level 1). Checking if the temperature in the keyhole section is higher than the boiling temperature. The whole IF-function is represented by Figure 85.

If $i > 2$ and $Keyhole\_Status = 1$

- Define Nodes_No_6 value based on node selection at the specified location:

$$coordinate\ (x,\quad y,\quad z) = ([Half\_Width \times 2],\quad [Start\_D + ((i-2) \times Step\_Length)],\quad [Half\_Thickness - Keyhole\_Depth])$$

$$Nodes\_No\_6 = number\ of\ nodes\ with\ temperature\ \geq Boil\_Temp$$

- Define Nodes_No_7 value based on node selection at the specified location:

$$coordinate\ (x,\quad y,\quad z) = ([Half\_Width \times 2],\quad [Start\_D + ((i-2) \times Step\_Length)],\quad 0)$$

$$Nodes\_No\_7 = number\ of\ nodes\ located\ between\ (Half\_Thickness - Keyhole\_Depth)\ and\ (Half\_Thickness)\ of\ z - axis\ direction.$$

- Definition of Vaporise_ratio:

$$\text{Vaporise\_ratio} = \frac{Nodes\_No\_6}{Nodes\_No\_7}$$

This define the vaporisation ratio within the keyhole region by dividing the number of nodes vaporised against the theoretical keyhole's depth.

- Define Temp_4 value based on node selection at the specified location:

$$coordinate \begin{pmatrix} x \\ y \\ z \end{pmatrix} = \left(\begin{matrix} [Half\_Width \times 2], \\ [Start\_D + (i-2) \times Step\_Length], \\ \left[Half\_Thickness - \left(Keyhole\_Depth - \left(\frac{5}{1000 \times MeshFactor} \right) \right) \right] \end{matrix} \right)$$

$$Temp\_4 = temperature\ value\ of\ the\ selected\ node$$

This data is used to check if the bottom of the keyhole is above the boiling point.

- Define Nodes_No_8 value based on node selection at the specified location:

$$coordinate\ (x, \quad y, \quad z) = ([Half\_Width \times 2], \quad [Start\_D + (i-2) \times Step\_Length], \quad 0)$$

$$Nodes\_No\_8 = number\ of\ nodes\ with\ temperature\ \geq 2500\ K$$

- If-conditioning (level 2). Gradually modifying the depth of the keyhole base on the situation of the ongoing cycle. The second level IF-function is represented by Figure 87.

If $Vaporise\_ratio \geq 0.1$ and $Temp\_4 \geq (Melt\_Temp1 + 100)$

  - If-conditioning (level 3). Function meant to help accelerate the keyhole formation through the definition of a series of temperature range conditions. The third level IF-function is represented by Figure 88.

If Nodes_No_8 ≥ 1 and $Temp\_4 \geq (Boil\_Temp + 200)$

- Definition of Keyhole_Depth:

$$Keyhole\_Depth = Keyhole\_Depth + \left(\frac{5}{1000 \times MeshFactor} \right)$$

Else if $(Boil\_Temp - 200) \leq Temp\_4 < (Boil\_Temp + 200)$

- Definition of Keyhole_Depth:

$$Keyhole\_Depth = Keyhole\_Depth + \left(\frac{3}{1000 \times MeshFactor} \right)$$

Else if $(Boil\_Temp - 600) \leq Temp\_4 < (Boil\_Temp - 200)$

- Definition of Keyhole_Depth:

$$Keyhole\_Depth = Keyhole\_Depth + \left(\frac{2}{1000 \times MeshFactor}\right)$$

Else if $(Melt\_Temp1 + 100) \leq Temp\_4 < (Boil\_Temp - 600)$

- Definition of Keyhole_Depth:

$$Keyhole\_Depth = Keyhole\_Depth + \left(\frac{1}{1000 \times MeshFactor}\right)$$

End If-conditioning (level 3).

Else if $Vaporise\_ratio < 0.1$ and $Temp\_4 < (Melt\_Temp1 + 100)$

- If-conditioning (level 3). Function meant to limit the heat flux for keyhole formation in order to prevent it from cancelling itself due to the keyhole heat flux reduction procedure.

If $Keyhole\_Depth \leq (KHole\_ShallowLimit + Heat\_Radius)$

- Definition of Keyhole_Depth:

$$Keyhole\_Depth = (KHole\_ShallowLimit + Heat\_Radius)$$

Else if $Keyhole\_Depth > (KHole\_ShallowLimit + Heat\_Radius)$

- Definition of Keyhole_Depth:

$$Keyhole\_Depth = Keyhole\_Depth - \left(\frac{1}{1000 \times MeshFactor}\right)$$

End If-conditioning (level 3).

Else,

- Definition of Keyhole_Depth:

$$Keyhole\_Depth = Keyhole\_Depth$$

In other words, nothing changes.

End If-conditioning (level 2)

Else,

- Definition of Khole_ShallowLimit:

$$KHole\_ShallowLimit = KHole\_ShallowLimit$$

In other words, nothing changes.

End If-conditioning (level 1)

Figure 85 presents the core of the function responsible for keyhole formation. After receiving inputs from both functions shown in Figure 83 and Figure 84, it proceeds to execute a series of nested logic functions.

The nested condition system used in this function comprises three levels of IF-conditioning:

- Level 1: The switch mechanism, which activates only after the 2nd cycle.
- Level 2: Determines the type of feedback mechanisms to activate.
- Level 3: Determines the amount of adjustment required for the keyhole depth.

In the first layer (Figure 86), the IF-condition checks for the following conditions:

- Is the number of cycle greater than 2.
- Is the switch for keyhole mechanism turn on.

If both conditions are met, it will initiate the calculation of the vaporisation ratio of the keyhole region. Once the calculation is completed, it will then enter the second level. However, if one or both conditions are false, no changes are made at this stage and this function will be skipped.

The reason for checking whether the current cycle is greater than 2 is that it requires the initial temperature profile data as input to calculate the vaporisation ratio and also to check if the bottom of the keyhole exceeds the boiling temperature of the defined material.

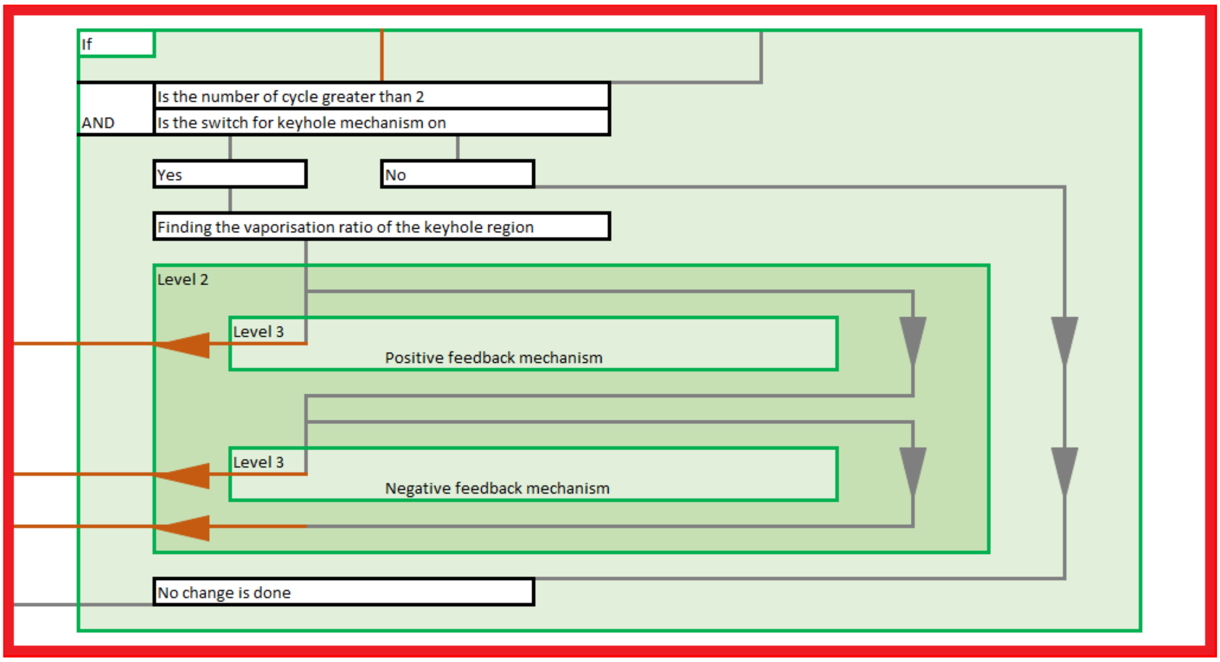

Figure 86. First layer of IF-conditioning

In the second level (Figure 87), the system will begin the initial check with the following two conditions:

- Is the vaporisation ratio greater than or equal to value A.
- Is the selected node having a temperature greater than or equal to 1850 Kelvin.

If both conditions are met, the system will then proceed to the third layer (positive feedback mechanism). If both conditions are not simultaneously fulfilled, the system will initiate the second check with another two conditions:

- Is the vaporisation ratio less than value A.
- Is the selected node having a temperature less than 1750 Kelvin.

If both conditions are met, it will also enter the third layer but for a different function (negative feedback mechanism). If both conditions are not met simultaneously, the system then determines that the current heat flux profile for keyhole formation should remain unchanged.

The purpose of the level 2 IF-conditioning is to determine whether the system should trigger the positive feedback or the negative feedback mechanism to control the depth of the keyhole formed. This enables the regulation of keyhole depth based on real-time simulation results generated during each cycle.

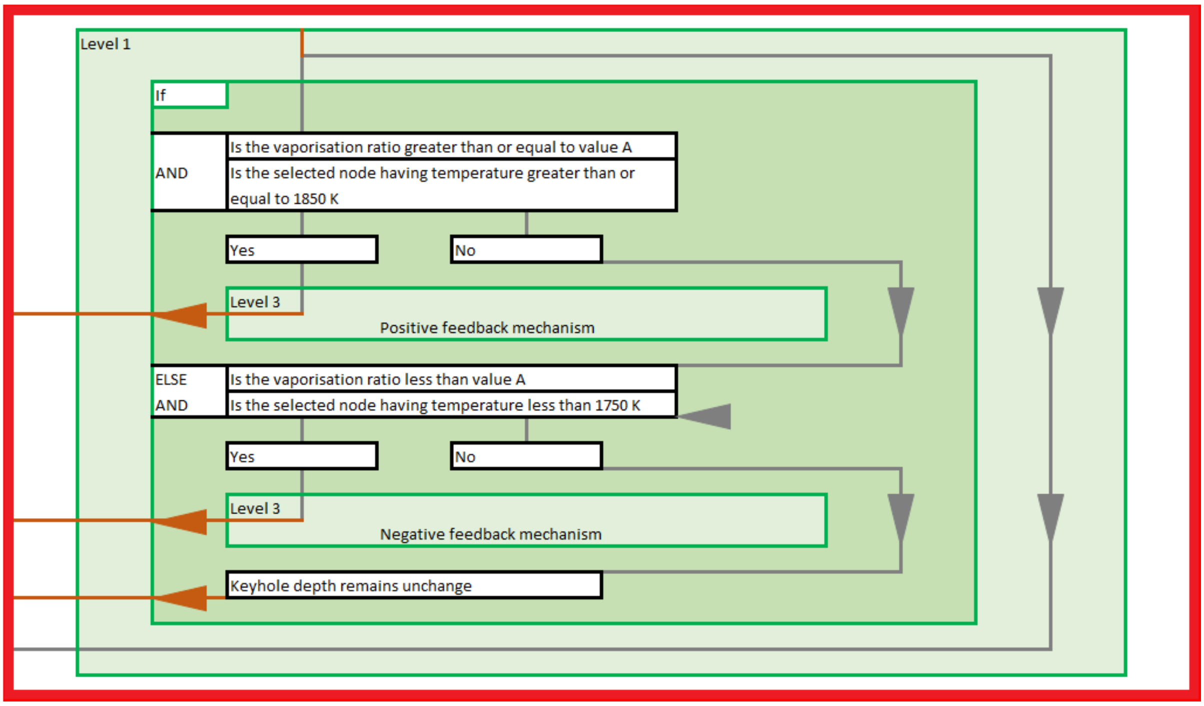

Figure 87. Second layer of IF-conditioning.

In the third level (Figure 88), there are two separate functions each with their own condition checks. The reason behind a larger condition checking range for the first function is to allow a faster expansion in keyhole depth during the initial stage of keyhole-based laser welding process.

The purpose of the first function is to act as a positive feedback mechanism; it allows the keyhole depth to increase if the heat energy accumulated within the keyhole region exceeds a threshold limit.

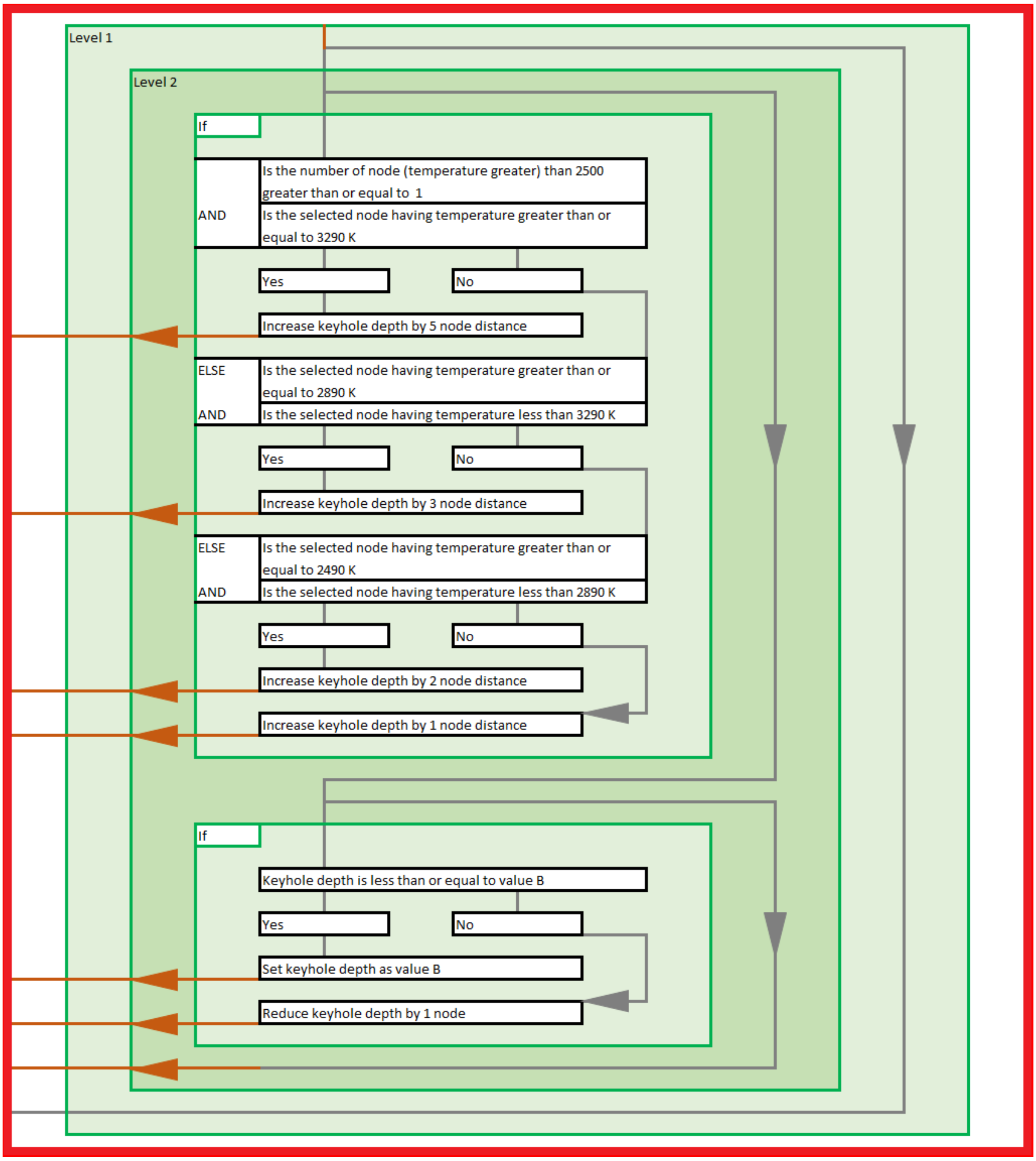

Figure 88. Third level of IF-conditioning.

Three sets of condition checking are present within this mechanism, each resulting in a different outcome. In the first condition checking, the following two conditions are presented:

- Is the number of node (temperature greater than 2500 Kelvin) greater than 1.
- Is the selected node having temperature greater than or equal to 3290 Kelvin.

If both conditions are met, the system will increase the heat flux depth by 5 nodes distance. If both conditions are not simultaneously fulfilled, the system will initiate the second check with another two conditions:

- Is the selected node having temperature greater than or equal to 2890 Kelvin.
- Is the selected node having temperature less than 3290 Kelvin.

If both conditions are met, the system will increase the heat flux depth by 3 nodes distance. If both conditions are not simultaneously fulfilled, the system will initiate the third check with another two conditions:

- Is the selected node having temperature greater than or equal to 2490 Kelvin.
- Is the selected node having temperature less than 2890 Kelvin.

If both conditions are met, the system will increase the heat flux depth by 2 nodes distance. If both conditions are not simultaneously fulfilled, the system will increase the heat flux depth by 1 node distance.

As for the second function, its purpose is to provide a negative feedback mechanism and a safety mechanism to prevent the keyhole mechanism from eliminating itself during the simulation. Only one set of condition checking is present in this mechanism:

- Is the keyhole depth less than or equal to value B

If the condition is met, the heat flux depth will be set to a value equal to value B. Otherwise, the heat flux depth will be reduced by 1 node distance.

5.3. Heat flux application

For the heat flux function for the top surface region, they are presented as follow:

- Define HFlux value based on node selection at the specified location:

$$coordinate\ (x,\quad y,\quad z)$$
$$= ([Half\_Width \times 2],\quad [Start\_D + (i-1) \times Step\_Length],\quad Half\_Thickness)$$

Reselect nodes within a circular region of radius Heat_Radius, centred at the coordinates mentioned above.

$$Heat\ Flux = \left(\frac{Laser\_P}{(\pi \times Heat\_Radius^2)}\right)$$

Where parameters Laser_P, Used_Laser_P, and Surface_Absorption are defined as follows:

$$\begin{aligned} Laser\_P &= Used\_Laser\_P \times Surface\_Absorption \\ Used\_Laser\_P &= Total\ Laser\ power\ used\ (before\ considering\ efficiency/absorptivity) \\ Surface\_Absorption &= Laser\ absorption\ rate\ on\ the\ top\ surface \end{aligned}$$

As for the heat flux function for the keyhole region which will be apply in the solution phase of the simulation process, they are presented as follow:

- If-conditioning function which decide if the heat flux for the keyhole region should be activated.
  If $Keyhole\_Status = 1$,
  - Definition of KHoleInterior_Area:

$$\text{KHoleInterior\_Area} = [Heat\_Radius \times (Keyhole\_Depth - KHole\_ShallowLimit)]$$

  - Define HFlux value based on node selection at the specified location:

$$coordinate\ (x, \quad y, \quad z) = \left([Half\_Width \times 2], \quad [Start\_D + (i-1) \times Step\_Length] - \left(\frac{Heat\_Radius}{2}\right), \quad 0\right)$$

Reselection of nodes from y-axis:

$$0 \leq Nodes\ selection \leq Heat\_Radius$$

Reselection of nodes from z-axis:

$$(Half\_Thickness - Keyhole\_Depth) \leq Nodes\ selection \leq (Half\_Thickness - KHole\_ShallowLimit)$$

Definition of heat flux for keyhole region:

$$Heat\ Flux = \left(\frac{Laser\_K}{KHoleInterior\_Area}\right)$$

Where the parameters used in calculating the heat flux are defined as follows:

$$\begin{aligned} Laser\_K &= [Used\_Laser\_P \times (Laser\_Absorption - Surface\_Absorption)] \\ Used\_Laser\_P &= Total\ Laser\ power\ used\ (before\ considering\ efficiency/absorptivity) \\ Laser\_Absorption &= Total\ Laser\ absorption\ rate \\ Surface\_Absorption &= Laser\ absorption\ rate\ on\ the\ top\ surface \end{aligned}$$

This heat flux is apply vertically in the form of a rectangular area at the side surface area defined by symmetrical boundary condition.

5.4. Experimental verification

In this section, the results obtained from the keyhole-based laser welding experiment are presented. The following process parameters were used in this experiment:

- Laser power: 500 W, 900 W and 1200 W
- Laser scanning speed: 10 and 30 mm/s
- Laser beam diameter on the surface: 0.5 mm

In addition, the following process parameters were also used at a later timeline:

- Laser power: 400 W, 600 W, 800 W, 900 W and 1000 W
- Laser scanning speed: 12, 16, 20, 24, 28, and 32 mm/s
- Laser beam diameter on the surface: 0.5 mm

The common parameters used for both experiments were:

- Gas type: Nitrogen gas
- Gas pressure: 4 bar
- Substrate material: Stainless steel 316

The two sets of process parameters were used because the experiments were conducted at different times with different experimental plans. While both experiments had the same overall goal, the second set included additional scanning speeds to provide a more comprehensive understanding of the trend and to minimise potential uncertainties. By incorporating a wider range of parameters, the experiment ensured greater flexibility in identifying the correct trend, even if some data points were affected by unforeseen issues.

Using image stitching function available in the Leica Software Application Suite (LAS) software, multiple images obtained with the Leica DFC295 digital microscope colour camera are merged into a single image that displays the entire cross-sectional area of the melt track. This enables precise measurements of the dimension and the area coverage of the melt tracks.

Images of the keyholes are shown in Figures 89-93; melt pool temperature along the y direction at the widest part of the melt pool and along the z direction at the deepest point of the melt pool are shown in Figure 94; melt dimensions from the experiments are summarised in Table 11.

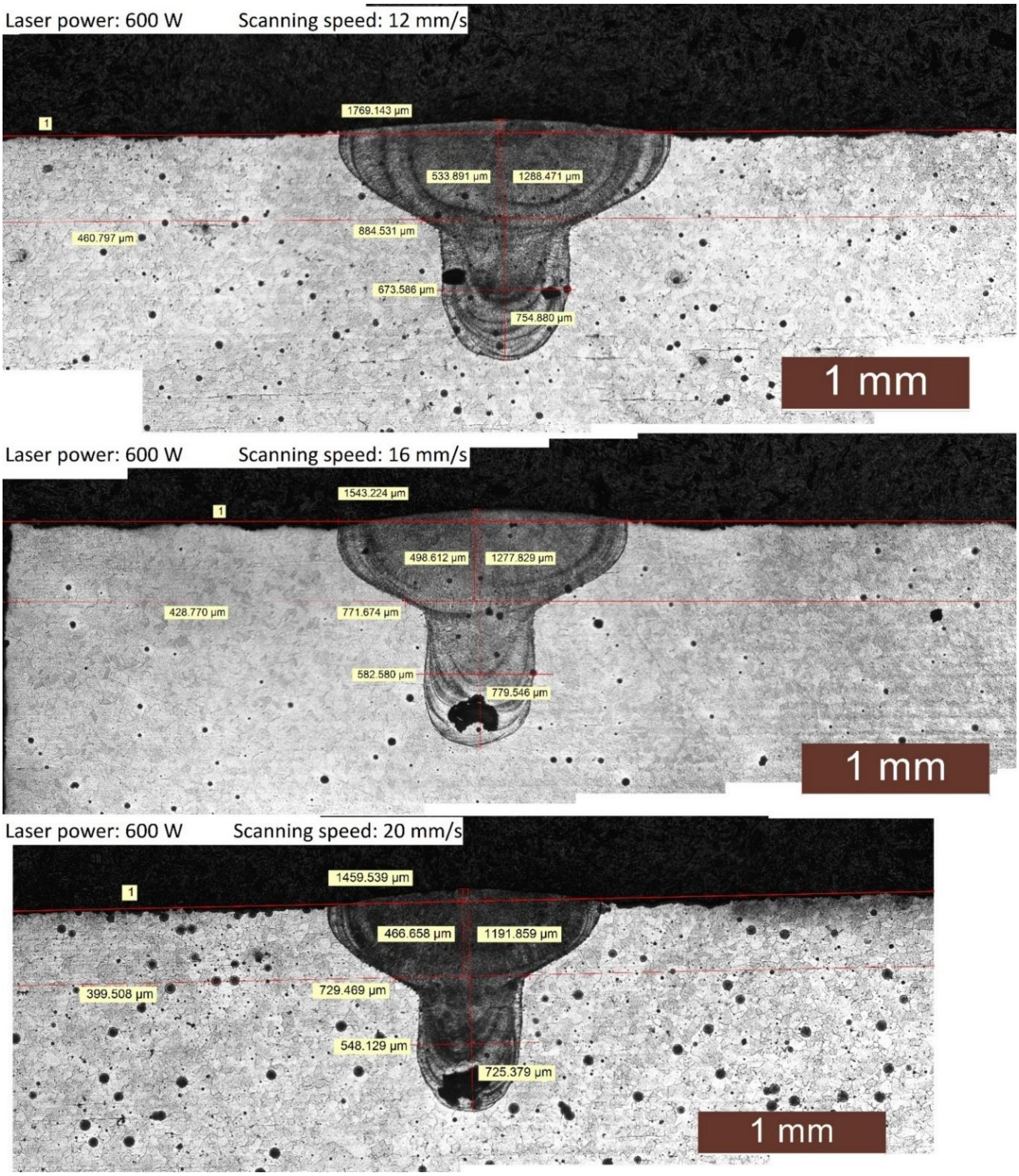

Figure 89. Keyhole-based laser melting using 600 W laser power with different scanning speed (part 1).

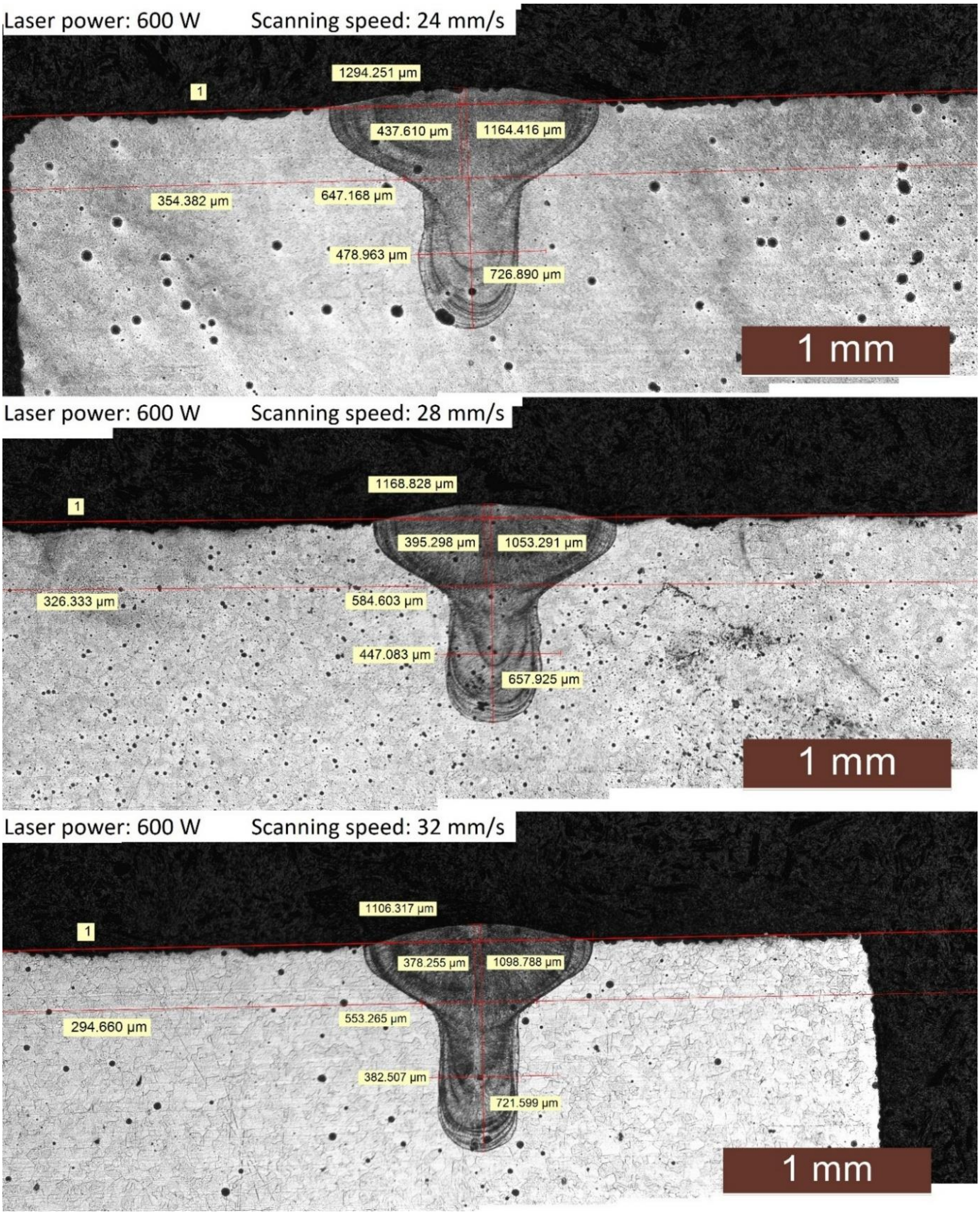

Figure 90. Keyhole-based laser melting using 600 W laser power with different scanning speed (part 2).

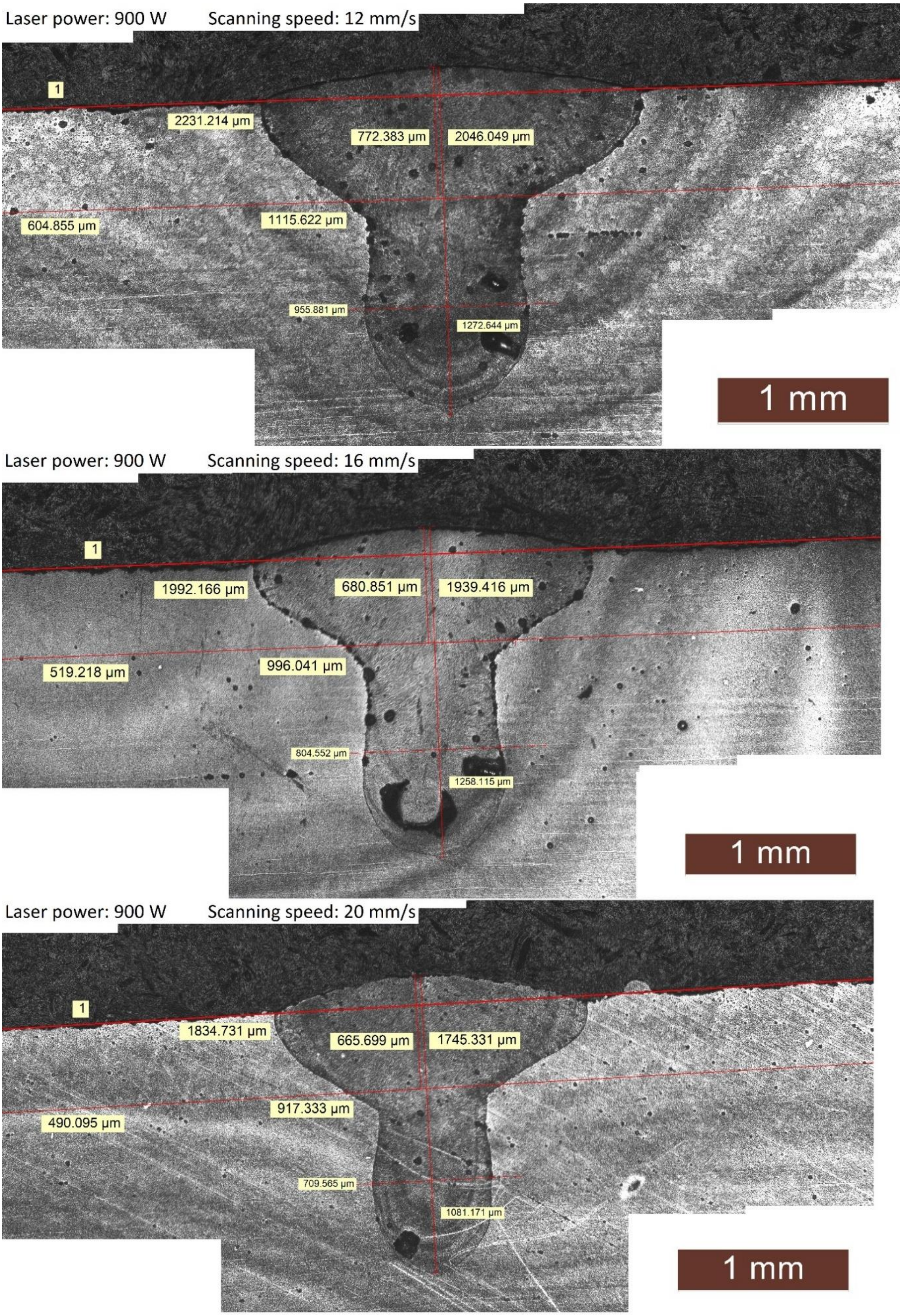

Figure 91. Keyhole-based laser melting using 900 W laser power with different scanning speed (part 1).

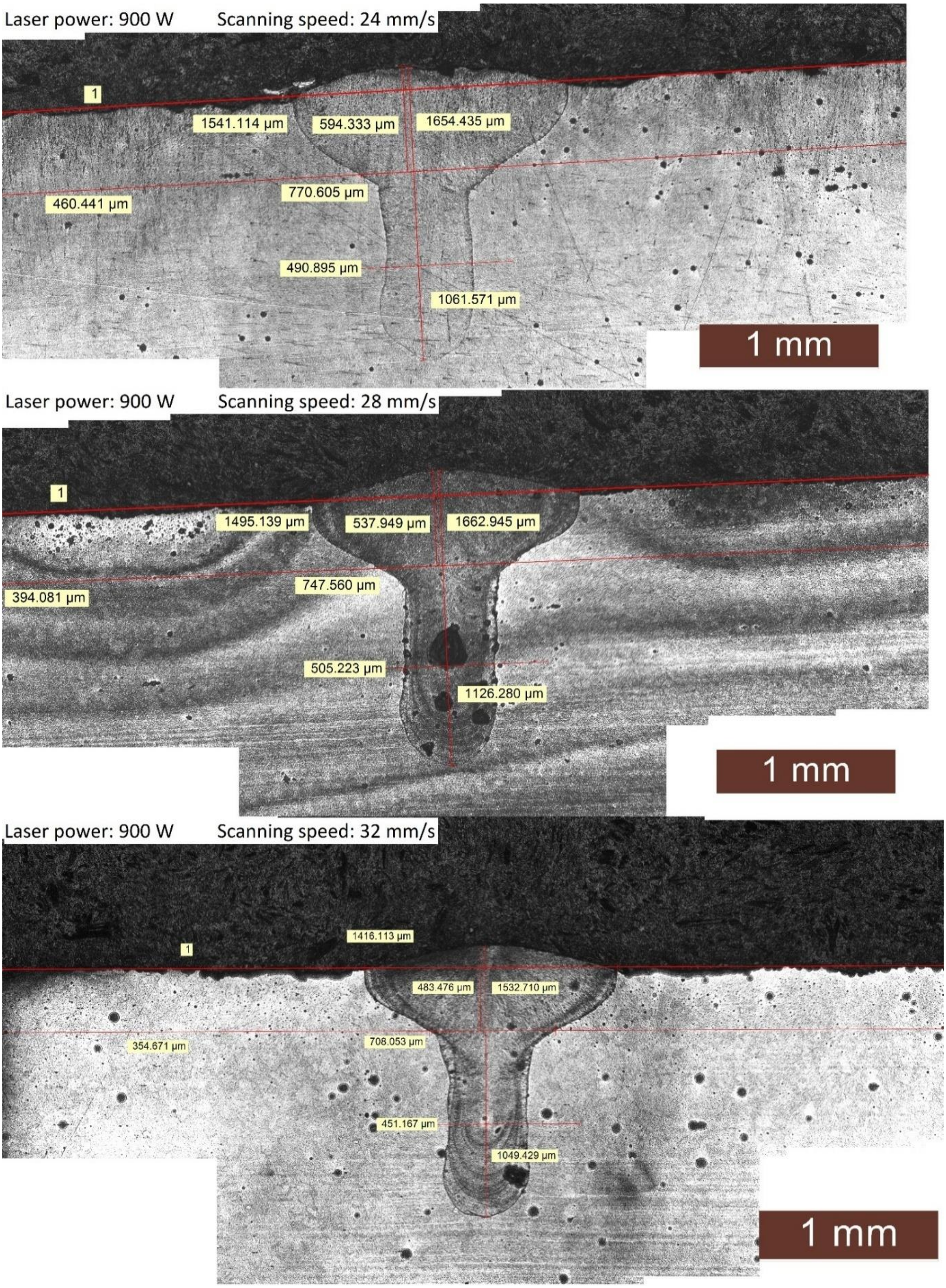

Figure 92. Keyhole-based laser melting using 900 W laser power with different scanning speed (part 2).

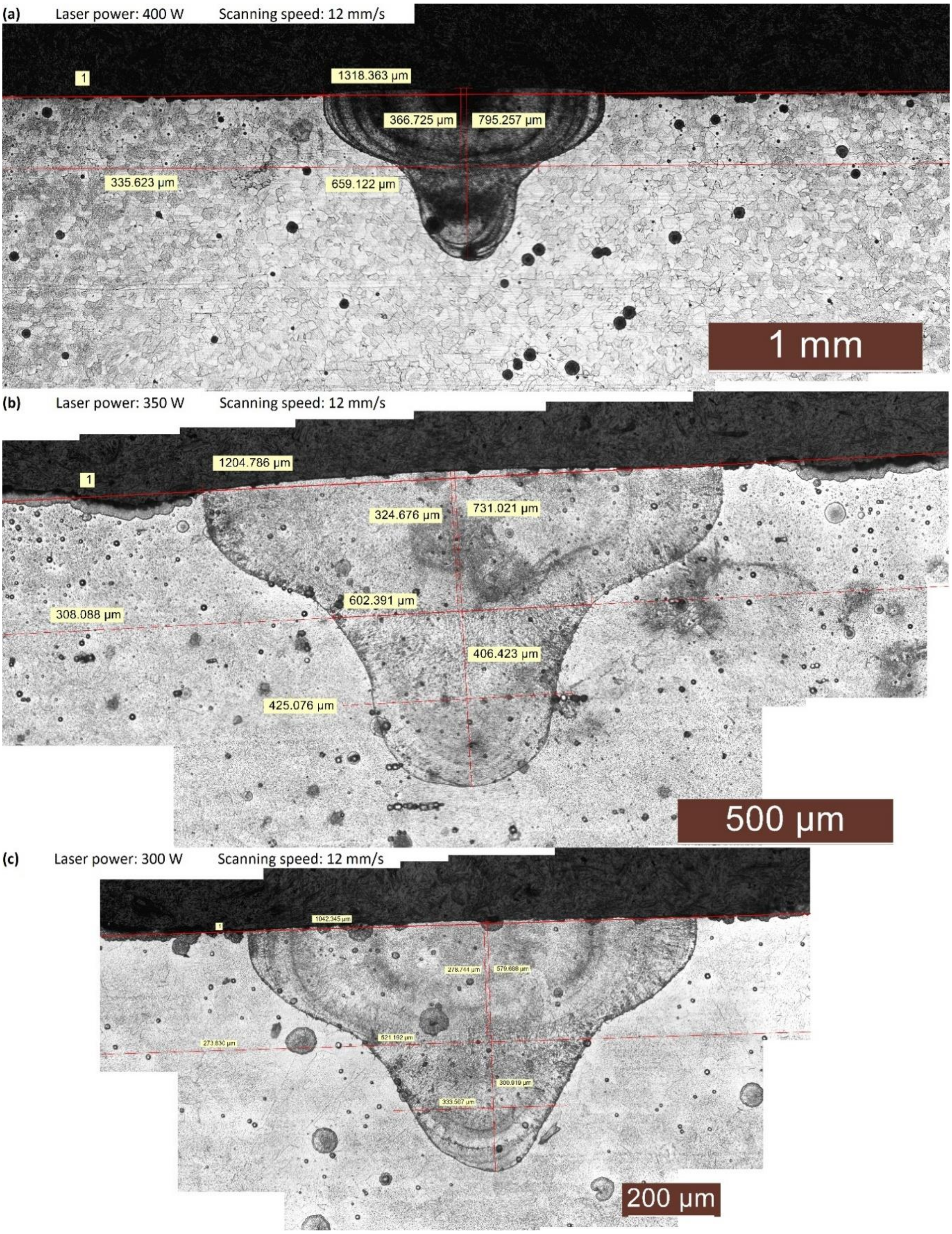

Figure 93. Transitioning from keyhole-based to mixed-mode laser melting when using 400 W, 350 W and 300 W laser power.

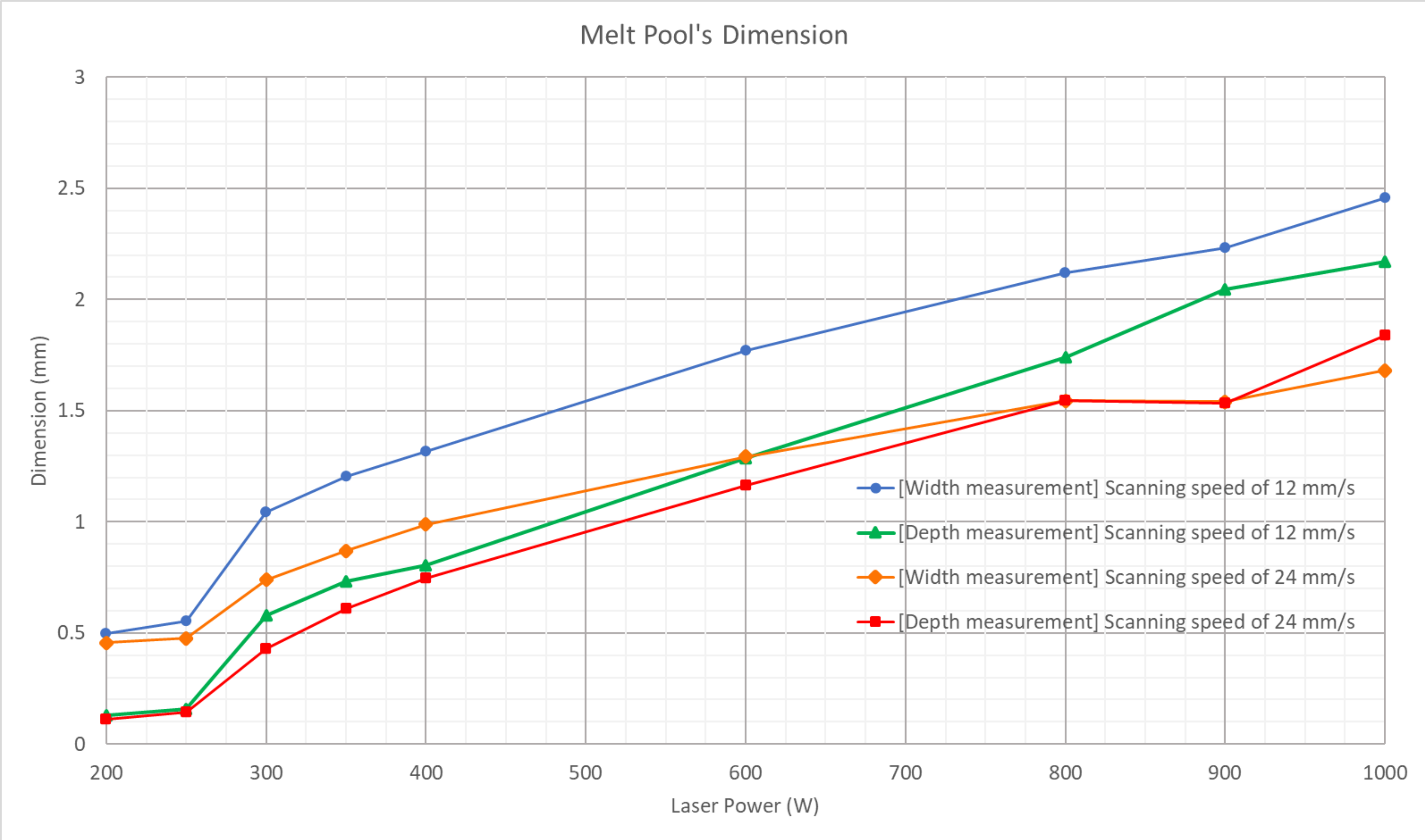

Figure 94. Change in melt pool's width and depth at laser powers of 200-1000 W and 12,24 mm/s traverse speeds.

Table 10. Melt dimensions from keyhole-based laser welding experiment.

Laser power (W)	Speed (mm/s)	Total Width (mm)	Depth (mm)	Area (mm^2)
200	12	0.50	0.13	0.050
200	16	0.48	0.12	0.044
200	20	0.46	0.11	0.040
200	24	0.46	0.11	0.040
200	28	0.42	0.11	0.037
200	32	0.43	0.10	0.035
250	12	0.55	0.17	0.066
250	16	0.52	0.16	0.060
250	20	0.50	0.15	0.055
250	24	0.48	0.14	0.049
250	28	0.47	0.14	0.046
300	12	1.04	0.58	0.342
300	16	0.94	0.49	0.271
300	20	0.84	0.43	0.216
300	24	0.74	0.43	0.192
300	28	0.70	0.42	0.181
300	32	0.68	0.41	0.167
350	12	1.21	0.73	0.497
350	16	1.07	0.66	0.398
350	20	0.97	0.62	0.325
350	24	0.87	0.61	0.288
350	28	0.86	0.57	0.270
350	32	0.77	0.61	0.251

400	12	1.32	0.81	0.600
400	16	1.22	0.81	0.535
400	20	1.06	0.76	0.439
400	24	0.99	0.75	0.383
400	28	0.90	0.71	0.352
400	32	0.89	0.69	0.325
500	10	1.62	1.15	1.085
500	20	1.28	0.93	0.645
500	30	0.99	0.86	0.437
600	12	1.77	1.29	1.240
600	16	1.54	1.28	1.056
600	20	1.46	1.19	0.917
600	24	1.29	1.16	0.772
600	28	1.17	1.05	0.650
600	32	1.11	1.10	0.589
800	8	2.42	1.98	2.815
800	10	2.21	1.86	2.388
800	12	2.12	1.74	1.998
800	14	1.94	1.78	1.871
800	16	1.82	1.62	1.567
800	18	1.68	1.72	1.469
800	20	1.69	1.49	1.087
800	22	1.60	1.67	1.320
800	24	1.54	1.55	1.185
800	26	1.44	1.53	1.094
800	28	1.45	1.43	0.980

800	32	1.34	1.38	0.860
900	10	2.57	2.07	2.824
900	12	2.23	2.05	2.396
900	14	2.02	1.94	2.084
900	16	1.99	1.94	2.019
900	18	1.88	1.80	1.749
900	20	1.83	1.75	1.628
900	22	1.66	1.70	1.404
900	24	1.54	1.53	1.233
900	26	1.45	1.64	1.153
900	28	1.50	1.66	1.172
900	30	1.38	1.59	1.014
900	32	1.42	1.53	1.008
1000	10	2.62	2.38	3.308
1000	12	2.46	2.17	2.850
1000	14	2.21	2.19	2.540
1000	16	2.10	2.01	2.246
1000	18	2.06	1.93	1.919
1000	20	1.86	1.99	1.854
1000	22	1.70	1.96	1.593
1000	24	1.68	1.84	1.489
1000	26	1.57	1.86	1.333
1000	28	1.52	1.73	1.175
1000	30	1.54	1.76	1.178
1000	32	1.40	1.73	1.070
1000	34	1.38	1.89	1.121

1200	10	2.93	2.73	4.301
1200	20	2.11	2.19	2.228
1200	30	1.61	2.07	1.444

The experimental results show a clear relationship between laser power, scanning speed, and melt pool geometry (width, depth, and cross-sectional area). As expected, increasing laser power results in greater melt pool dimensions, while increasing scanning speed leads to a reduction in both melt width and depth due to reduced energy input per unit length. These observations align with established laser welding theory, where heat transfer mechanisms shift from conduction-based melting at low power levels to keyhole welding at higher power levels.

For laser powers between 200 W and 250 W, the welding process is dominated by thermal conduction, where heat propagates primarily through conduction rather than material vaporization. The results show that within this power range, the melt pool depth remains shallow ($\leqslant$ 0.17 mm), and the cross-sectional area is small ($\leqslant$ 0.07 mm^2) even at the lowest scanning speeds.

- At 200 W and 12 mm/s, the melt pool depth is 0.1310 mm, and the area is 0.0502 mm^2, with width at 0.4975 mm.
- Increasing the scanning speed to 32 mm/s reduces the depth slightly to 0.1016 mm, indicating limited penetration.
- A similar trend is seen at 250 W, where increasing speed from 12 mm/s to 28 mm/s reduces the depth from 0.1720 mm to 0.1382 mm and width from 0.5544 mm to 0.4700 mm.

These results confirm that at lower laser power levels, heat conduction limits penetration, and material vaporization does not play a significant role. The shallow penetration depths suggest that welding in this power range is suitable for surface melting applications rather than deep-penetration welding.

At laser powers between 300 W and 400 W, the process transitions into a mixed-mode welding regime, where conduction still plays a role but localised material vaporization begins to occur, leading to increased penetration. The results show a notable increase in melt depth and cross-sectional area compared to conduction-based welding.

- At 300 W and 12 mm/s, the depth reaches 0.5797 mm, significantly greater than that at 250 W.
- Increasing power to 350 W at 12 mm/s results in further deepening of the melt pool to 0.7310 mm, with a larger cross-sectional area of 0.4973 mm^2.

- At 400 W and 12 mm/s, the depth increases to 0.8054 mm, marking the onset of a vaporization-driven melting process.

However, at higher scanning speeds (e.g., 400 W at 32 mm/s), the depth stays relatively shallow at 0.6911 mm, indicating that at these power levels, heat input is still highly dependent on speed. These results suggest that at 300–400 W, laser welding transitions from conduction to partial vaporization, producing deeper welds but still lacking a fully developed keyhole.

For laser powers above 500 W, the welding process is dominated by keyhole formation, where the energy density is high enough to cause material vaporization and plasma formation, creating a stable keyhole. This mode leads to deep penetration welding with significantly increased melt pool depth.

- At 500 W and 10 mm/s, the depth reaches 1.1511 mm, and the cross-sectional area increases to 1.0847 mm^2.
- At 600 W and 12 mm/s, the depth increases further to 1.2885 mm, showing a well-defined keyhole.
- At 800 W and 8 mm/s, the penetration depth reaches 1.9847 mm, and the area extends to 2.8148 mm^2, indicating deep keyhole formation.
- The highest power (1200 W at 10 mm/s) results in an extreme penetration depth of 2.7300 mm, with a large cross-sectional area of 4.3013 mm^2, confirming that keyhole welding is fully established.

As expected, at higher scanning speeds (e.g., 1200 W at 30 mm/s), the depth reduces to 2.0720 mm, and the area decreases to 1.4439 mm^2, demonstrating that while the keyhole mode remains dominant, scanning speed still plays a crucial role in controlling penetration depth.

Across all power levels, scanning speed has a pronounced effect on melt pool dimensions. Slower speeds allow more energy absorption, leading to wider and deeper melt pools, while higher speeds result in shallower penetration due to reduced heat input per unit length.

For example:

- At 1000 W, reducing speed from 34 mm/s to 10 mm/s increases the depth from 1.8948 mm to 2.3813 mm.
- At 600 W, reducing speed from 32 mm/s to 12 mm/s increases the depth from 1.0988 mm to 1.2885 mm.

These observations emphasise that optimal welding parameters require balancing power and scanning speed to achieve the desired penetration and melt pool dimensions while minimizing defects.

5.5. Comparison of M4 modelled and experimental results

With the new M4 model shown in Figures 80 and 81, the thermal conductivity enhancement values are based on results from chapter 4, while the depth for the keyhole is defined as a manipulated variable. The comparison between the experiment and the simulation results is conducted with the purpose of confirming the reliability of new features introduced in model M4.

5.5.1. Keyhole-based laser welding

As concluded in the previous chapter, a thermal conductivity enhancement factor of 2.5 (1750 K – 2750 K) and 7.5 (3000 K - 3500 K) will be used for the 4th simulation model, resulting in a maximum total multiplication factor of 18.12 compared to the original thermal conductivity.

The previous chapter concluded a 60% laser absorptivity for conduction-based laser melting, the simulation for keyhole-based laser melting involves the selection of two different laser absorptivity, which are 70% and 90%. This decision is based on the insights gathered from several research papers, which collectively indicate a general range between 60% and 93%, without exceeding 93% [5, 28, 44, 75, 76].

Figure 95 shows a comparison of the melt pool's width and the depth, presented for three distinct cases, each employing different variable settings in the simulation with a 70% absorptivity rate. The legend in the graph outlines three ratios for energy allocation between the surface and keyhole:

- 0.4 S : 0.7 T, allocating 40% and 30% of the total 70% thermal energy absorbed to the top surface and keyhole heat flux, respectively.
- 0.5 S : 0.7 T, allocating 50% and 20% of the total 70% thermal energy absorbed to the top surface and keyhole heat flux, respectively.
- 0.6 S : 0.7 T, allocating 60% and 10% of the total 70% thermal energy absorbed to the top surface and keyhole heat flux, respectively.

In Figure 96, a comparison of the melt pool's width and depth is presented for 5 separate cases, employing different variable settings in the simulation with a 90% absorptivity rate. The legend outlines five ratios for energy allocation towards the surface and keyhole:

- 0.2 S : 0.9 T, allocating 20% and 70% of the total 90% thermal energy absorbed to the top surface and keyhole heat flux, respectively.
- 0.3 S : 0.9 T, allocating 30% and 60% of the total 90% thermal energy absorbed to the top surface and keyhole heat flux, respectively.

- 0.4 S : 0.9 T, allocating 40% and 50% of the total 90% thermal energy absorbed to the top surface and keyhole heat flux, respectively.
- 0.5 S : 0.9 T, allocating 50% and 40% of the total 90% thermal energy absorbed to the top surface and keyhole heat flux, respectively.
- 0.6 S : 0.9 T, allocating 60% and 30% of the total 90% thermal energy absorbed to the top surface and keyhole heat flux, respectively.

Based on both Figure 95 and Figure 96, it can be concluded that the result for keyhole-based laser welding using 600W and 12 mm/s at a 70% laser absorption rate is a poor match with the results obtained from the experiment. However, for the 90% absorption rate, both cases (20% and 30% allocation to top surface heat flux) closely match the experimental results.

Figure 95 to Figure 98 present multiple graphs comparing results with different heat flux distribution ratio between the top surface and the keyhole (side). Those cases used in the comparison are:

- [Figure 95] 0.7 laser absorptivity, 600W laser power, and 12 mm/s scanning speed.
- [Figure 96] 0.9 laser absorptivity, 600W laser power, and 12 mm/s scanning speed.
- [Figure 97] 0.9 laser absorptivity, 900W laser power, and 12 mm/s scanning speed.
- [Figure 98] 0.9 laser absorptivity, 1200W laser power, and 10 mm/s scanning speed.

In Figure 98, it is observed that the depth predicted when employing a heat flux distribution of 0.3 (surface) : 0.6 (keyhole) closely matches the actual results. As for Figure 97 and Figure 98, the observed comparisons indicate that the actual results fall between the simulated results produced by heat flux distribution ratios of 0.2 : 0.7 and 0.3 : 0.6.

Upon analysing the graphs, it can be concluded that as the laser power increases from 600 W to 1200 W, the heat flux distribution gradually shifts from a ratio of 0.3 (surface) : 0.6 (keyhole) to 0.25 : 0.65. The drawback of this comparison is that for all cases the widths fail to closely match the actual results.

Figure 99 and Figure 100 show the comparison between cases using different heat flux distribution ratios with varying laser power and scanning speed. Through the use of bar charts, it is evident that a similar pattern emerges, wherein the heat flux distribution ratio gradually shifts from a ratio of 0.3 (surface) : 0.6 (keyhole) to 0.25 : 0.65 when a scanning speed of 24 mm/s is applied.

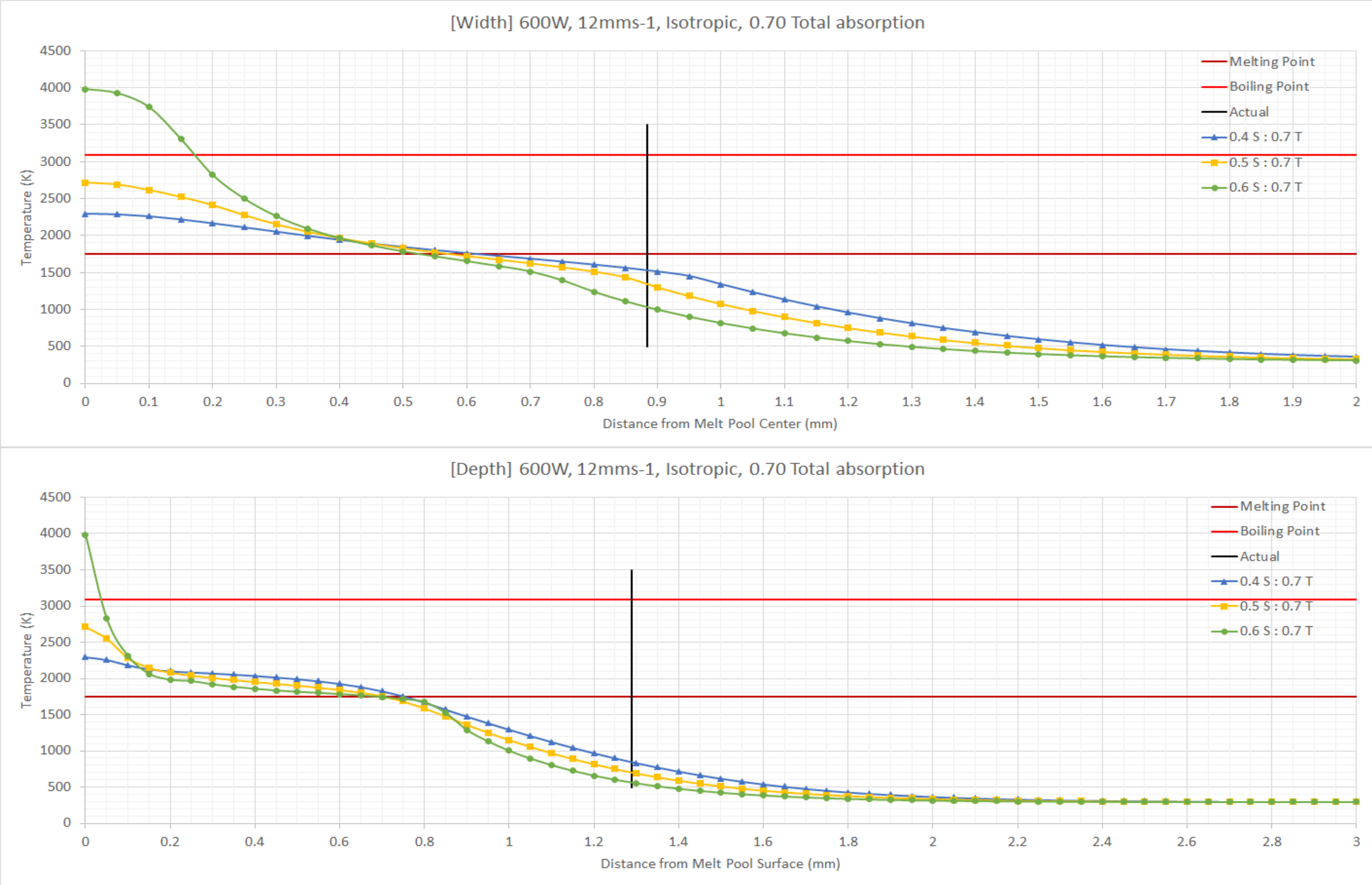

Figure 95. Simulation Results Comparison: 0.7 Laser Absorption at 600W, 12 mm/s with different heat flux distribution ratio.

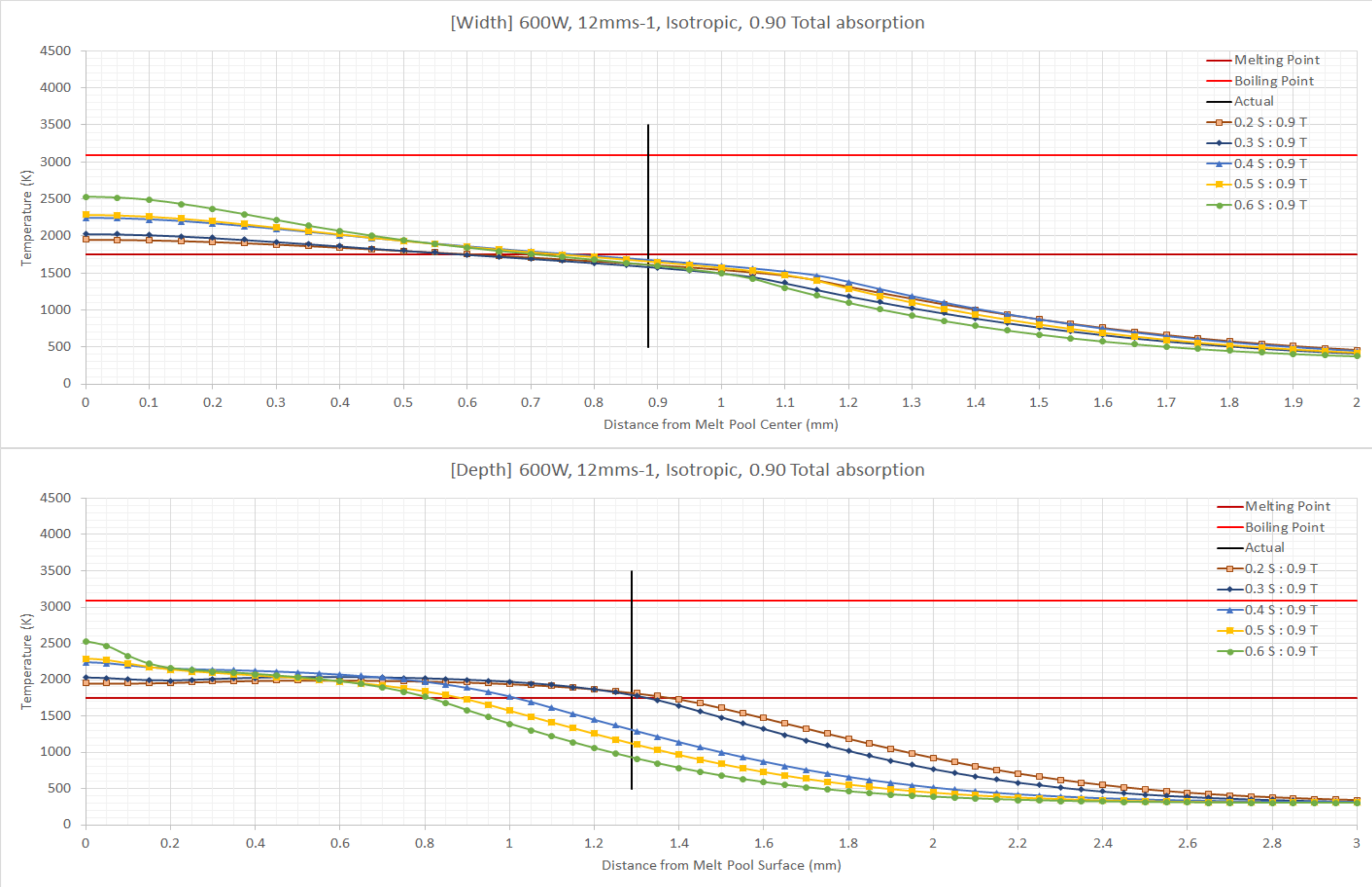

Figure 96. Experimental and M4 simulated results: 0.9 Laser Absorption at 600W, 12 mm/s with different heat flux distribution ratio.

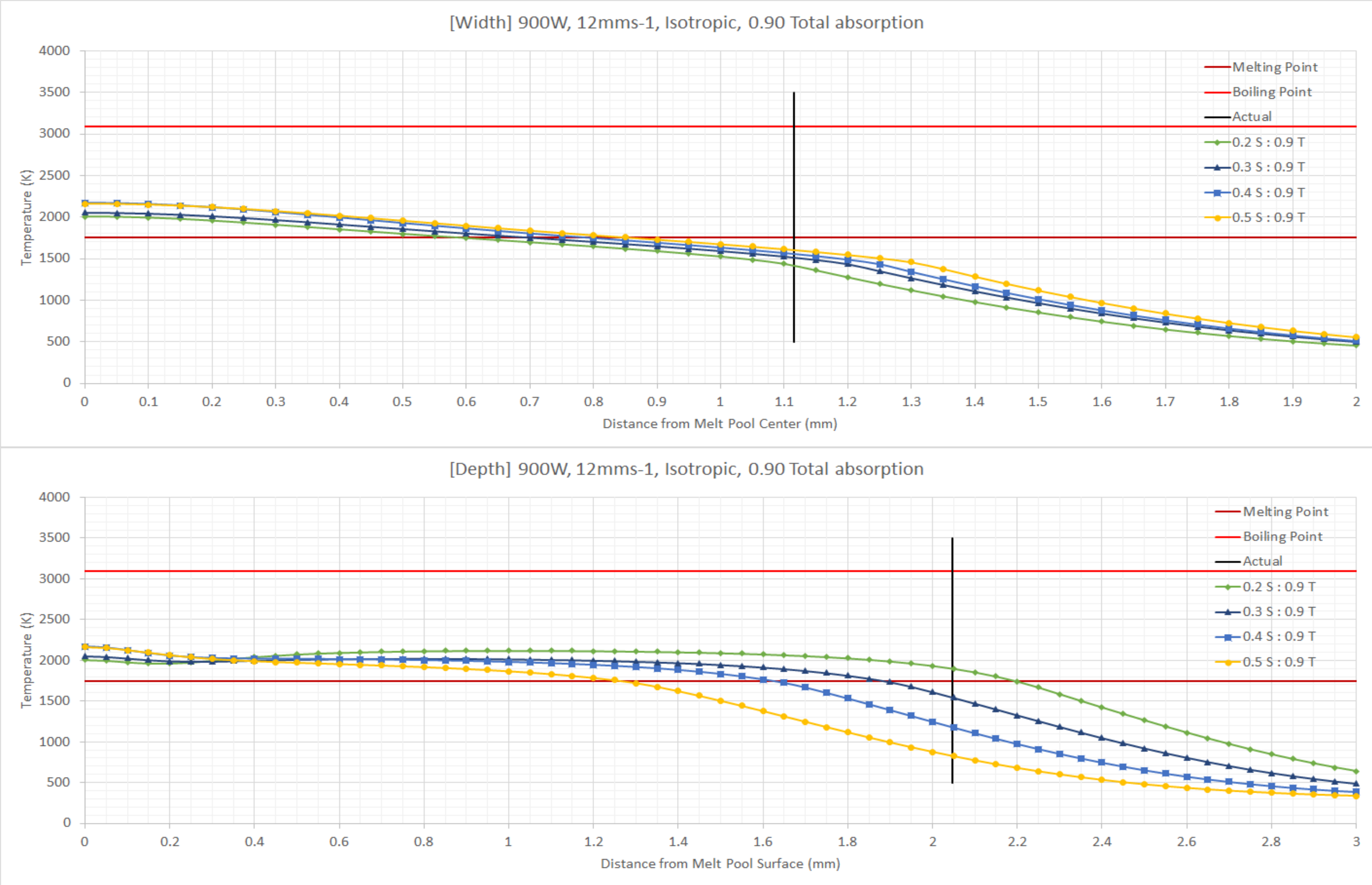

Figure 97. Experimental ad M4 simulated results: 0.9 Laser Absorption at 900W, 12 mm/s with different heat flux distribution ratio.

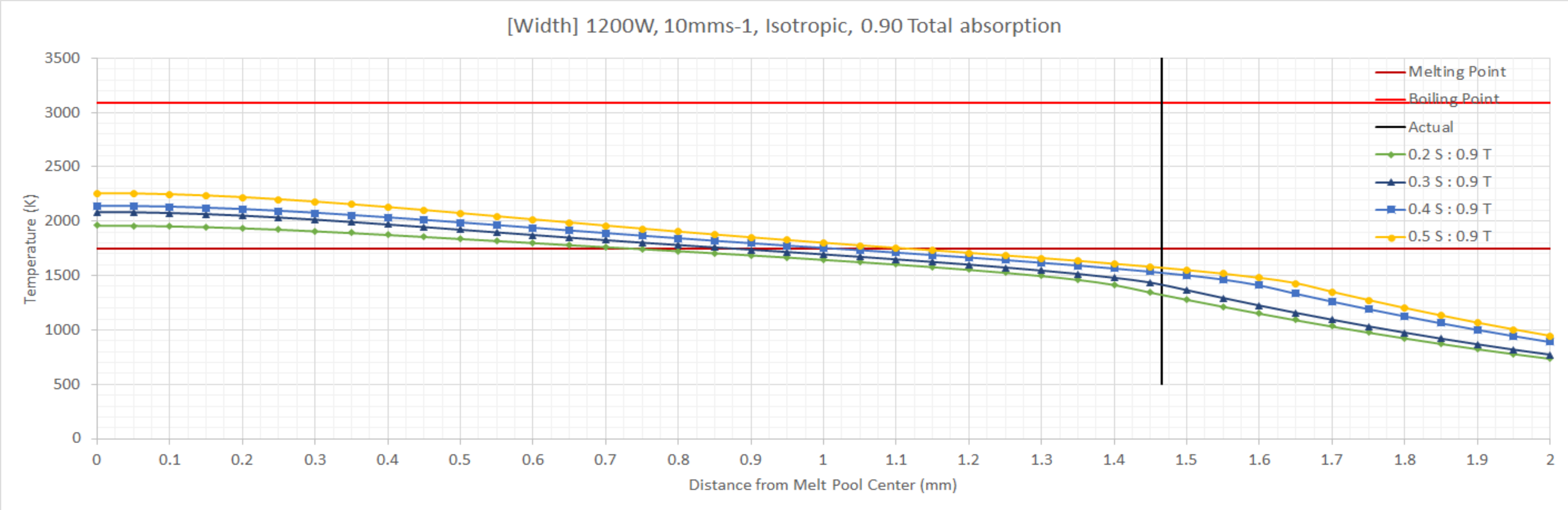

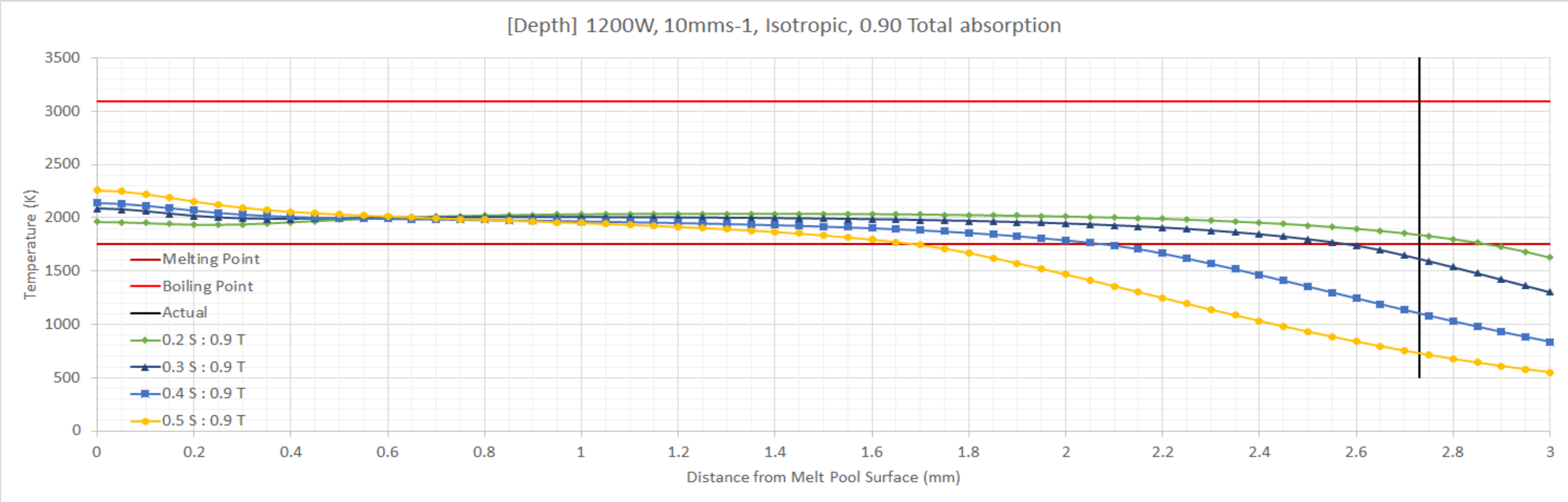

Figure 98. Experimental and M4 simulated results: 0.9 Laser Absorption at 1200W, 10 mm/s with different heat flux distribution ratio.

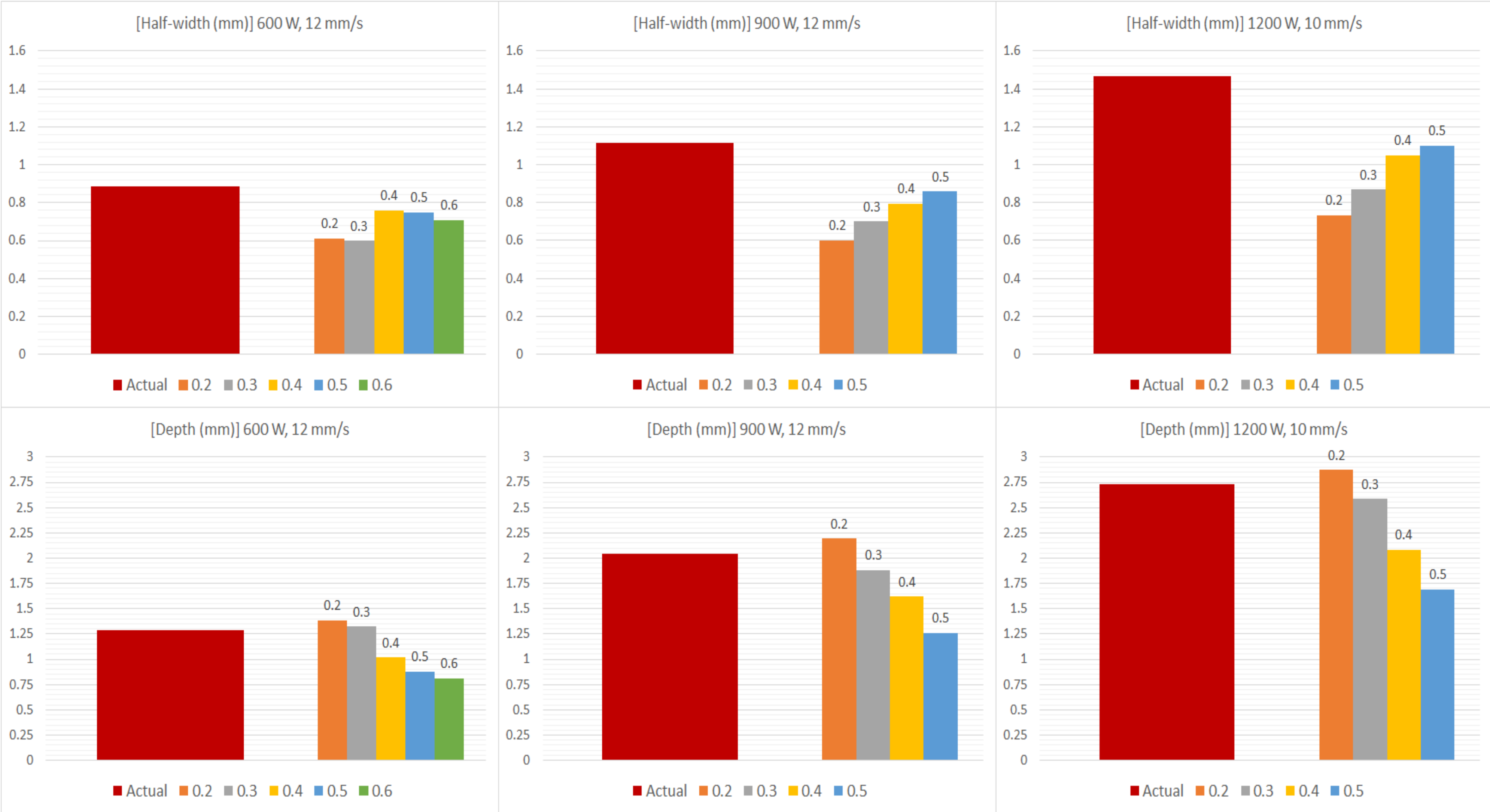

Figure 99. [0.9 absorptivity, 12 mm/s] Melt pool size comparison between different energy distribution ratio.

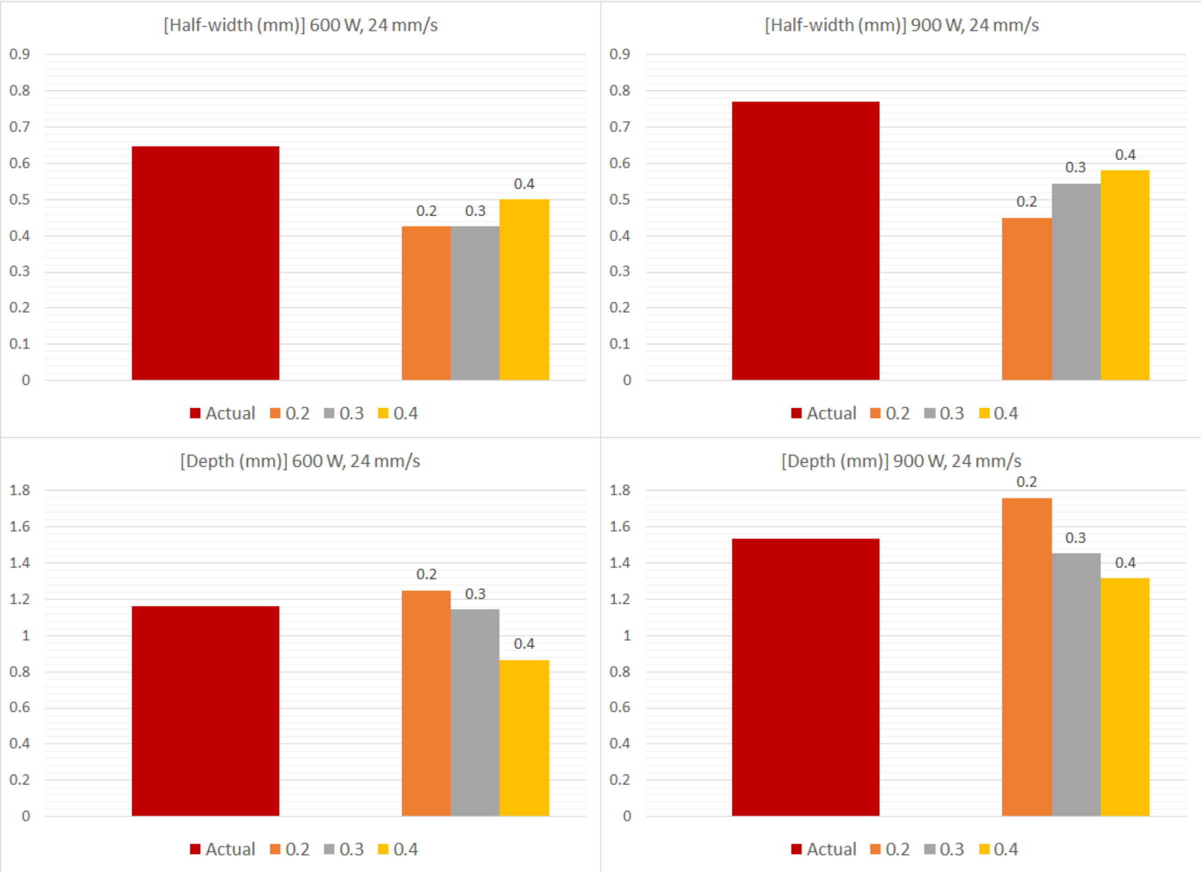

Figure 100. [0.9 absorptivity, 24 mm/s] Melt pool's size comparison between different energy distribution ratio.

It can be concluded that as laser power increases, a greater percentage of the heat energy is absorbed within the material through keyhole formation rather than surface melting.

Further validation was done using a scanning speed of 24 mm/s, laser powers of 600 W and 900 W and taking 0.9 absorption. Results are shown in Figures 101 and 102. It can be seen that:

- For the case using 600 W and 24 mm/s, the heat flux distribution with a ratio of <u>0.3 (surface) : 0.6 (keyhole)</u> shows a result closely matched with the experiment.
- For the case using 900 W and 24 mm/s, the experiment result lies between the simulation results generated using heat flux distribution ratio of <u>0.2 (surface) : 0.7 (keyhole)</u> and <u>0.3 (surface) : 0.6 (keyhole)</u>.

Based on the result analysis obtained from Figure 95 to Figure 102, it can be concluded that the ratio of heat flux distribution changes from <u>0.3 (surface) : 0.6 (keyhole)</u> to <u>0.25 (surface) : 0.65 (keyhole)</u> as the laser power increases from 600 W to 900 W.

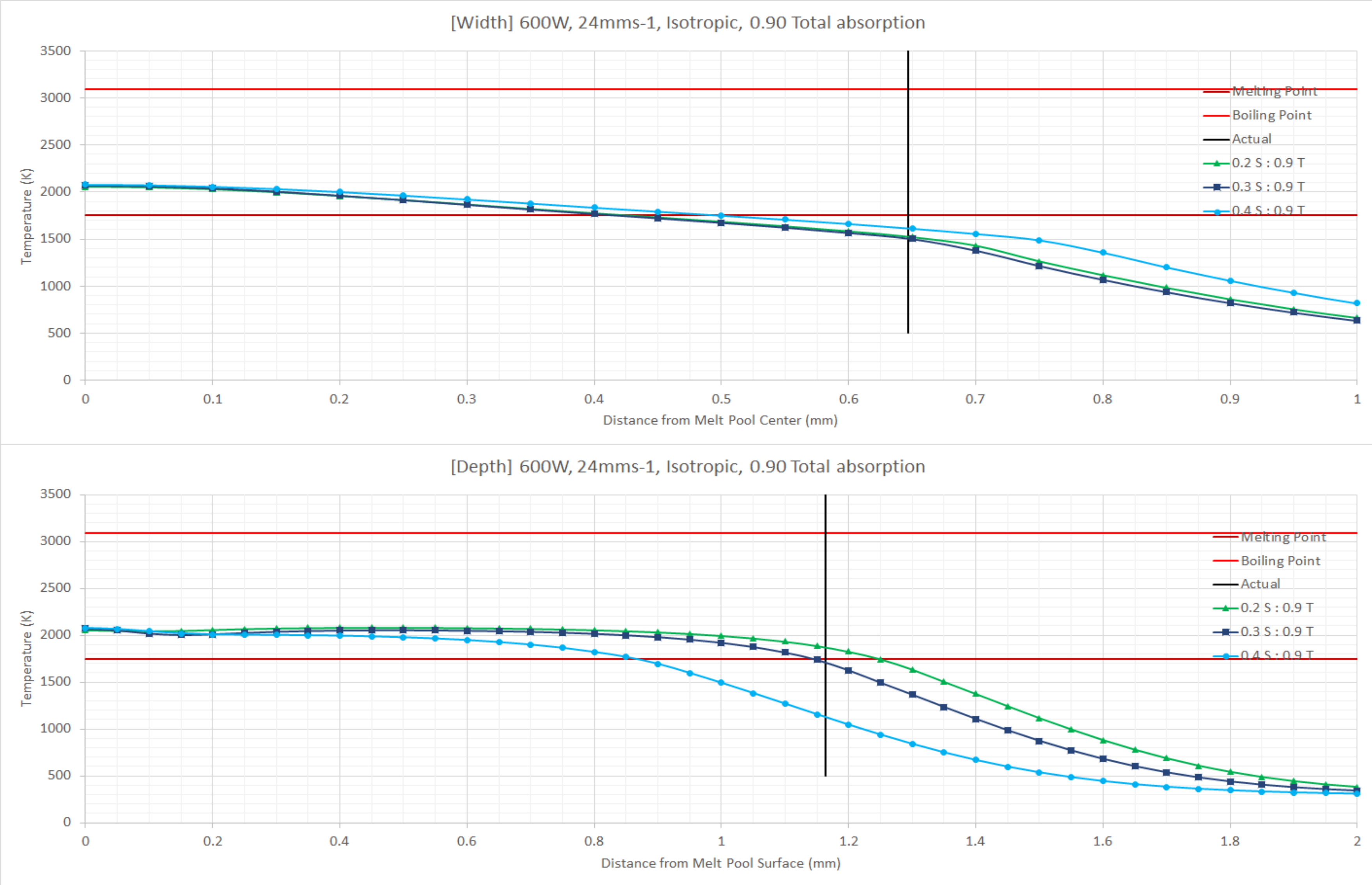

Figure 101. Simulation Results Comparison: 0.9 Laser Absorption at 600W, 24 mm/s with different heat flux distribution ratio.

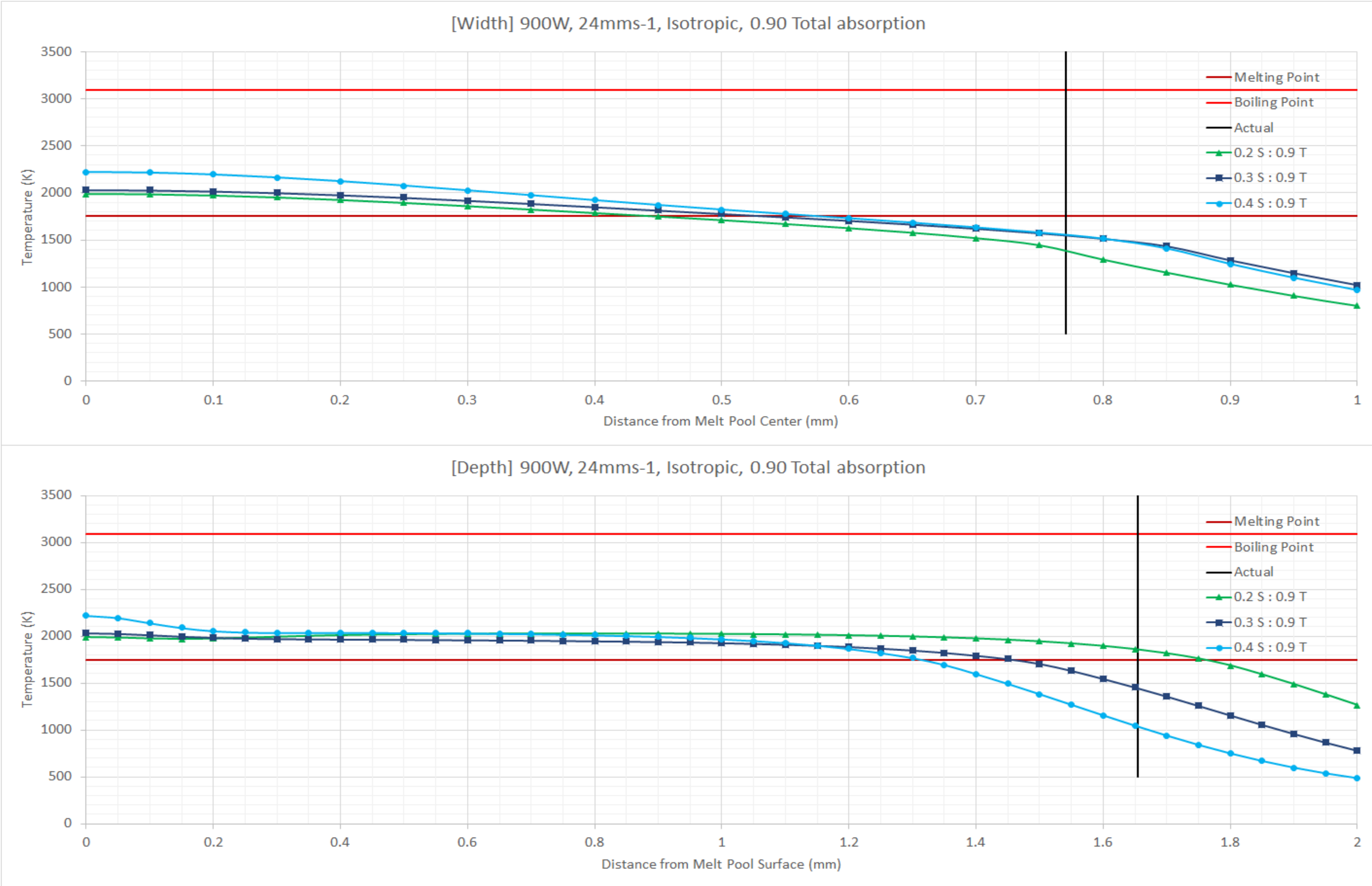

Figure 102. Simulation Results Comparison: 0.9 Laser Absorption at 900W, 24 mm/s with different heat flux distribution ratio.

5.5.2. Mixed-mode laser welding and the keyhole transition

The M4 model has demonstrated its ability to predict the melt pool's dimension for keyhole-based laser welding cases, involving the use of laser power between 600 W and 1200 W. In this section, the capabilities of M4 to simulate mixed-mode laser welding is tested.

As Figure 93 showed, the welding type transitions from mixed-mode to keyhole as the laser power increases from 300 W to 400 W. Consequently, to evaluate the efficacy of the M4 model, several simulation cases involving laser powers of 300 W and 400 W laser power were conducted.

Figure 103 shows several simulation cases conducted for laser melting using a 300 W laser power and a 12 mm/s traverse speed. It compiles results for comparing the melt pool's width and depth in four distinct cases, each employing different variable settings in the simulation with an 80% absorptivity rate. The legend in the graph outlines four ratios for energy allocation towards the surface and keyhole:

- 0.4 S : 0.8 T, allocating 40% and 40% of the total 80% absorbed thermal energy to the top surface and keyhole heat flux, respectively.
- 0.5 S : 0.8 T, allocating 50% and 30% of the total 80% absorbed thermal energy to the top surface and keyhole heat flux, respectively.
- 0.6 S : 0.8 T, allocating 60% and 20% of the total 80% absorbed thermal energy to the top surface and keyhole heat flux, respectively.
- 0.6 S : 0.8 T, allocating 70% and 10% of the total 80% absorbed thermal energy to the top surface and keyhole heat flux, respectively.

Figure 104 shows several simulation cases conducted for laser melting using a 400 W laser power and a 12 mm/s traverse speed. The legend in the graph outlines three ratios for energy allocation towards the surface and keyhole:

- 0.2 S : 0.9 T, allocating 40% and 40% of the total 80% absorbed thermal energy to the top surface and keyhole heat flux, respectively.
- 0.3 S : 0.9 T, allocating 50% and 30% of the total 80% absorbed thermal energy to the top surface and keyhole heat flux, respectively.
- 0.4 S : 0.9 T, allocating 60% and 20% of the total 80% absorbed thermal energy to the top surface and keyhole heat flux, respectively.

Figure 105 and Figure 106 shows more simulation cases conducted using 300 W and 400 W laser power. The only difference between these and the previous results is the traverse speed. To obtain results presented in Figure 105 and Figure 106, a traverse speed of 24 mm/s was used.

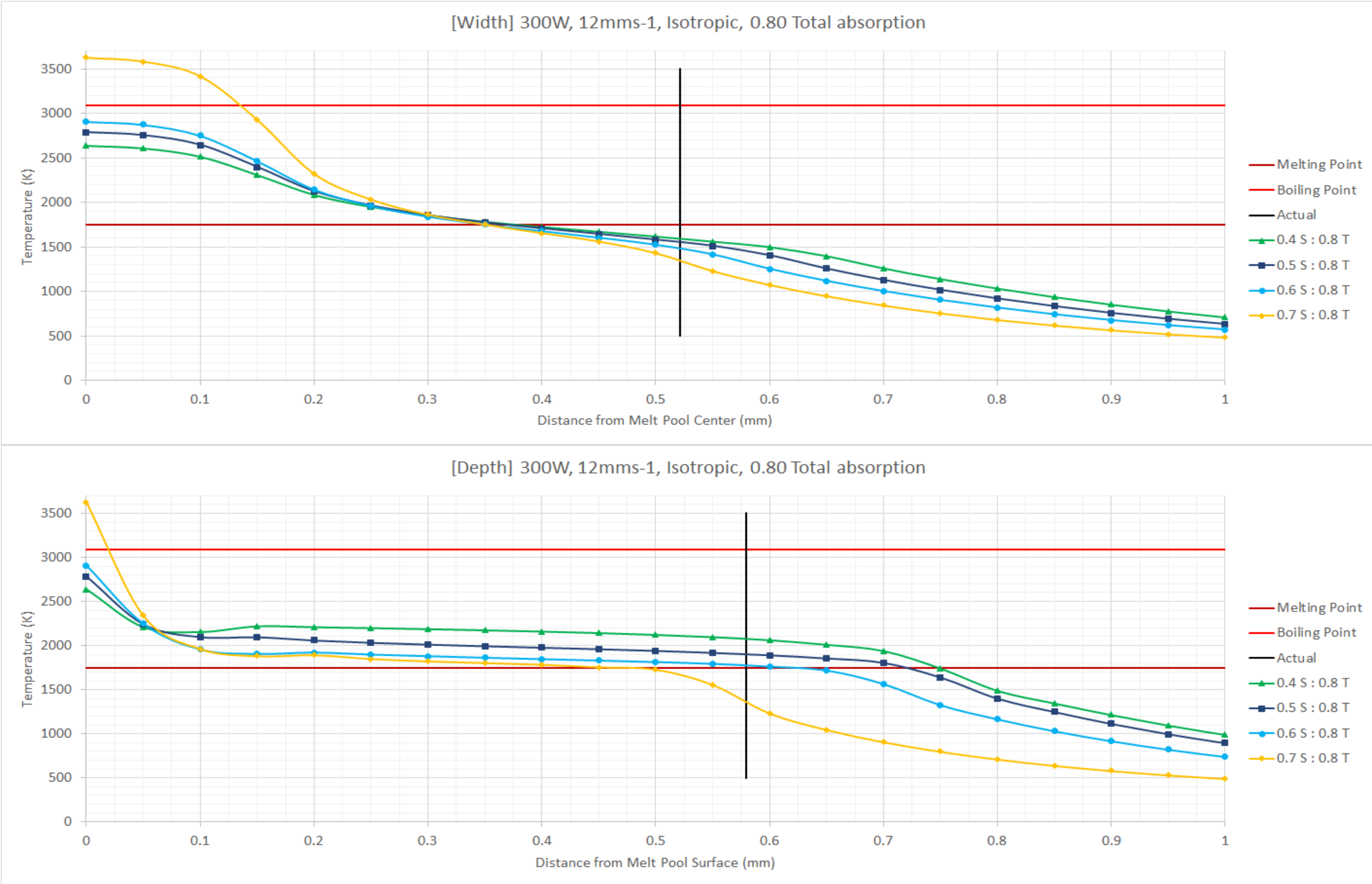

Figure 103. Simulation Results Comparison: 0.8 Laser Absorption at 300W, 12 mm/s with different heat flux distribution ratio.

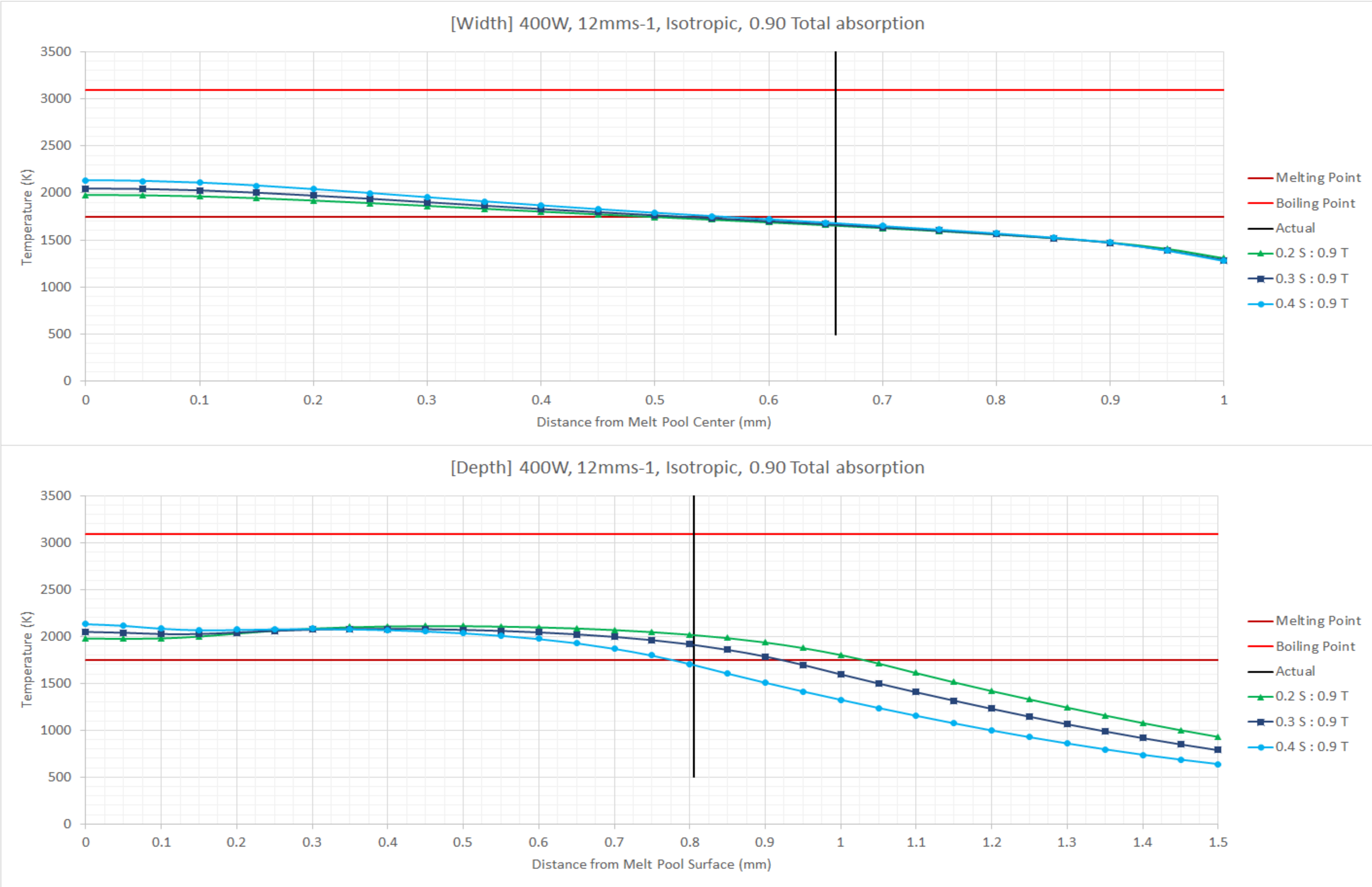

Figure 104. Simulation Results Comparison: 0.9 Laser Absorption at 400W, 12 mm/s with different heat flux distribution ratio.

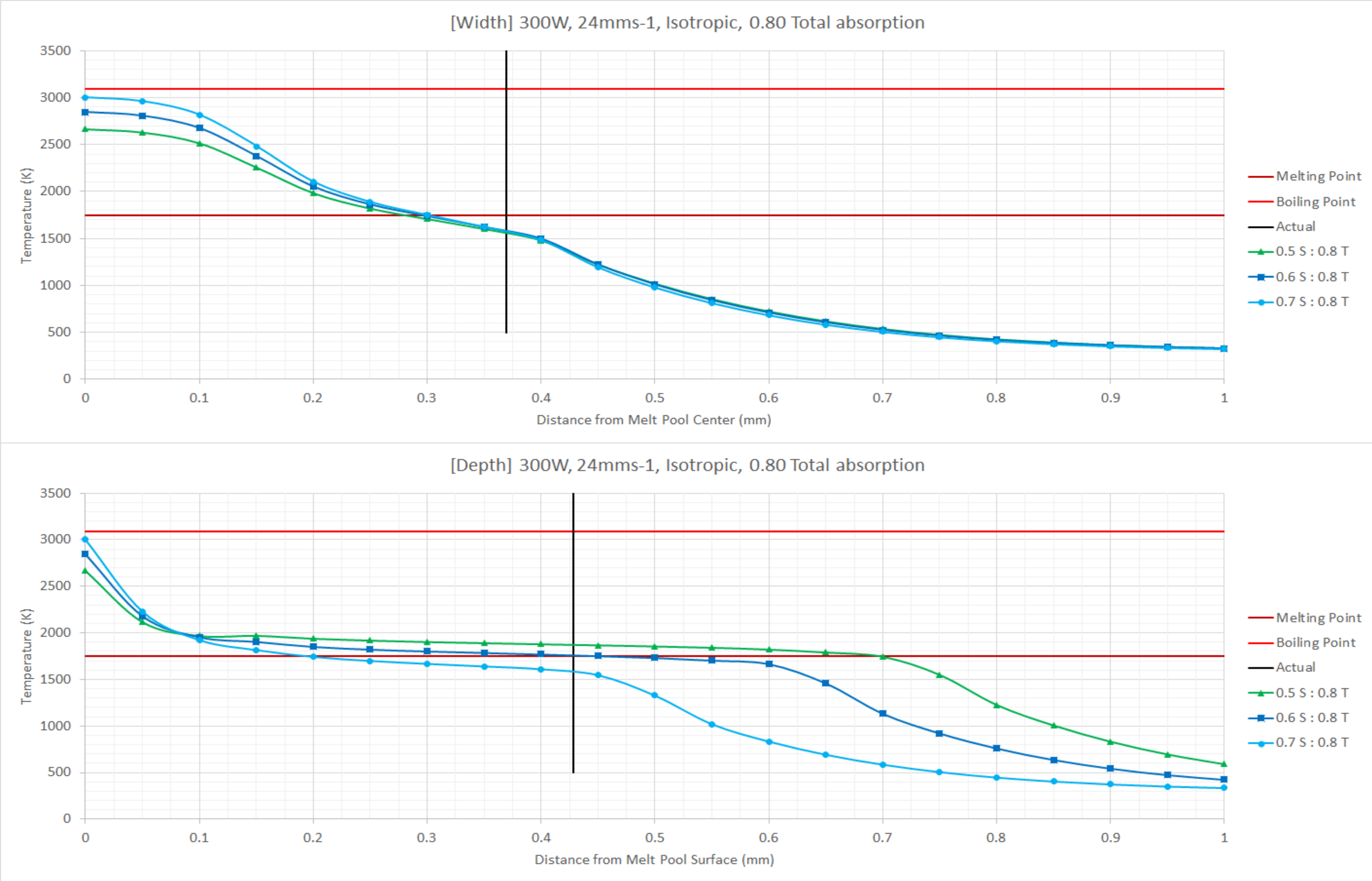

Figure 105. Simulation Results Comparison: 0.8 Laser Absorption at 300W, 24 mm/s with different heat flux distribution ratio.

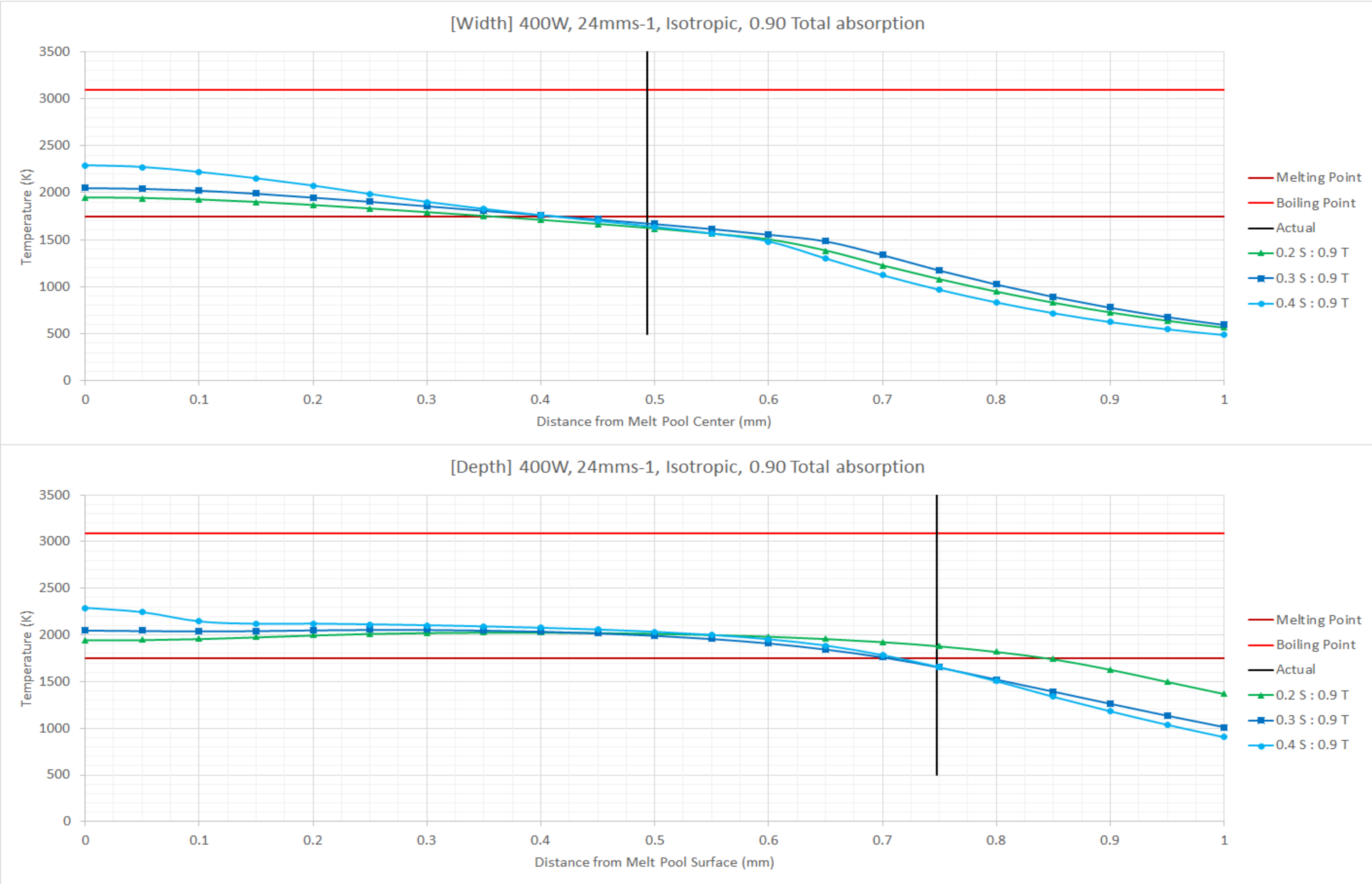

Figure 106. Simulation Results Comparison: 0.8 Laser Absorption at 400W, 24 mm/s with different heat flux distribution ratio.

For Figure 103 and Figure 105, a consistent ratio of 0.6 (surface) : 0.2 (keyhole) is obtained when the laser power is 300 W. As for Figure 104 and Figure 106, the ratio changes from 0.4 (surface) : 0.5 (keyhole) to 0.3 (surface) : 0.6 (keyhole) when the traverse speed increase from 12 mm/s to 24 mm/s.

5.6. Discussion

This chapter explores the feasibility of using a simplified model to predict the dimensions of the melt track as the welding transitions from mixed-mode to keyhole-based.

Based on the results presented in this chapter, results from the M4 model showed good agreement with experiment for most of the mixed-mode and keyhole-based laser welding cases with laser power ranging from 300 W to 1200 W. As the laser power increases from 300 W to 350 W, signs of keyhole formation begin to emerge. Upon reaching 400 W, the welding process completes its transition from mixed-mode to fully keyhole-based. In Figure 107, several cavities are identified near the centre and bottom of the nail-shaped melt pool, further confirming the existence of the keyhole formation.

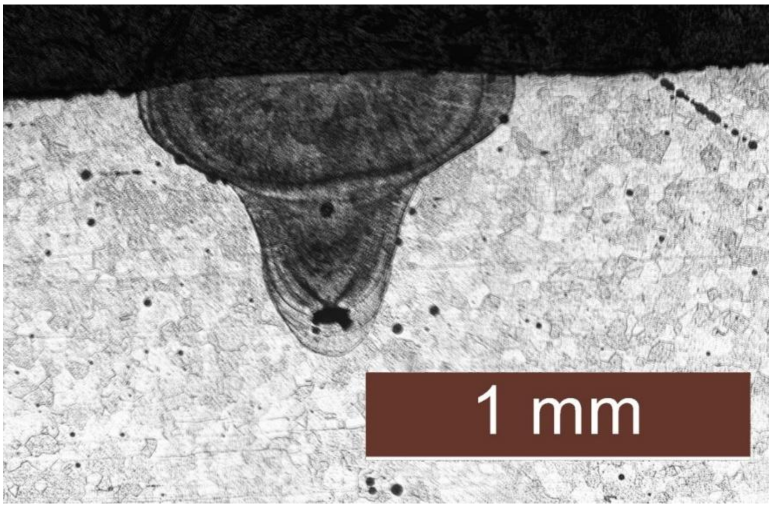

Figure 107. Cross-sectional image of the melt pool at 400 W laser power and 24 mm/s traverse speed.

After analysing the data obtained from simulations using model M4, predictions were made and shown in Figure 108 and Figure 109.

Figure 108 illustrates the predicted pattern of the heat flux distribution ratio, which is crucial information for the simulation model to predict the melt pool's dimension. Meanwhile, Figure 109 depicts the change in laser energy distribution as the laser power used during welding process increases from 200 W to 1200 W.

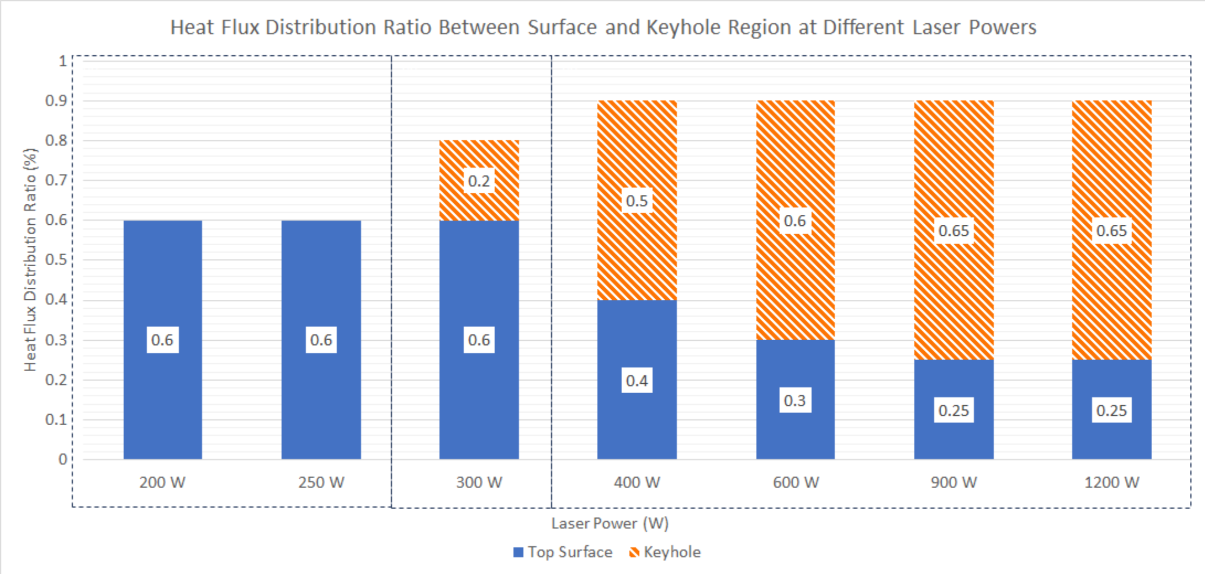

Figure 108. Estimated heat flux distribution ratio as laser power increases (applies to laser scanning speed from 12 mm/s to 24 mm/s).

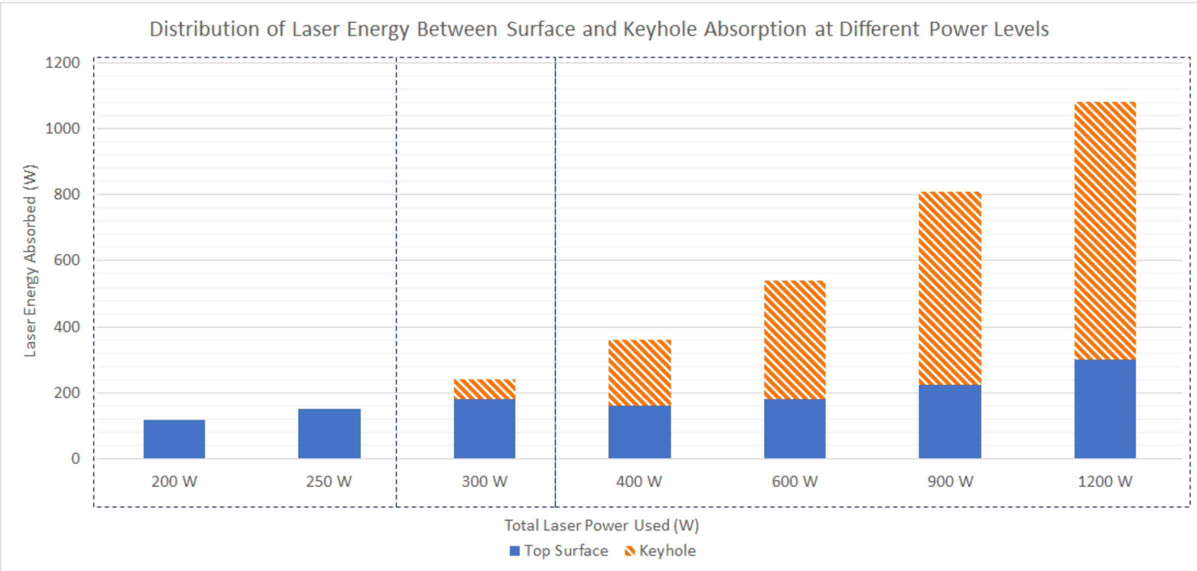

Figure 109. Estimated laser energy distribution during melt pool formation as laser power increases (applies to laser scanning speed from 12 mm/s to 24 mm/s).

5.7. Conclusion

Laser welding is widely used in manufacturing industries due to its high precision and efficiency. However, predicting energy absorption, heat transfer, and melt pool formation remains a challenge, particularly when transitioning from conduction to keyhole mode. Many existing simulation models face two major limitations. Firstly, there is often a trade-off between computational cost and accuracy—high-fidelity models provide precise predictions but require extensive computational resources and long processing times. Secondly, many models struggle to predict both melt pool width and depth simultaneously. Some models can predict the width in conduction mode but not depth in keyhole mode, and vice versa. This study addresses these challenges by proposing an alternative simulation approach that reduces computational time and resource demands while still producing qualitatively accurate results in terms of laser energy absorption, heat distribution, and keyhole formation.

Laser welding can be classified into three regimes based on the mechanisms of energy absorption: conduction mode, mixed-mode, and keyhole mode. In conduction mode, which occurs at low laser power (< 300 W), energy is absorbed at the top surface and diffuses into the material through conduction. Due to the high reflectivity of the material, only about 60% of the laser energy is absorbed. At this stage, the material temperature remains below its boiling point, preventing keyhole formation.

As laser power increases (300 W - 600 W), localised vaporization begins, and a keyhole starts to form, marking the transition into mixed-mode laser welding. At this stage, the keyhole is not fully developed, but partial laser trapping occurs, increasing absorption to approximately 80%. The energy is now distributed between the surface and the developing keyhole. Once the laser power exceeds 600 W, keyhole mode welding is fully established. A deep and stable keyhole forms, acting as a laser trap, where multiple reflections enhance energy absorption up to 90%. In this mode, heat transfer is influenced by both conduction and convection.

In comparison with existing models, the proposed simulation approach offers several improvements. Traditional models often require significant computational resources to achieve high accuracy, whereas this model achieves reasonable accuracy with reduced computational cost. Additionally, while previous models often oversimplify energy distribution, the proposed model provides a more detailed tracking of how laser energy transitions from the top surface to the keyhole region as power increases. A summary of the comparison is presented below:

- Computational Cost: The proposed model requires fewer resources compared to high-fidelity models.
- Absorption Prediction: The model improves upon simplified absorption assumptions in previous studies by providing a more detailed energy distribution analysis.
- Conduction Mode melt dimensions: The model can predict melt pool width well but has limitations in predicting depth.
- Keyhole Mode melt dimensions: The model is able to predict depth but modelled and experimental results show minor discrepancies in width.

After analysing simulation results for laser powers ranging from 300 W to 1200 W, several trends were observed. First, the absorption rate increased from 60% for conduction-based laser welding to 80% in mixed-mode welding and finally reached 90% in keyhole-based welding. Second, as the laser power increased, the distribution of laser energy shifted from the top surface toward the keyhole region. Third, the rate of increase in the amount of energy responsible for surface melting was significantly lower than the rate of increase in energy contributing to keyhole formation. This indicates that keyhole formation plays a dominant role in energy absorption at high laser powers.

Despite these improvements, one key limitation remains. The M4 model is able to predict melt pool width in conduction mode but struggles to predict depth. Conversely, in keyhole mode, it effectively predicts melt pool depth but exhibits minor inaccuracies in width prediction. This discrepancy arises due to the simplified treatment of recoil pressure and vaporization dynamics. Future work could address this limitation by incorporating more advanced physics-based models for recoil pressure effects and fluid flow interactions within the keyhole.

In conclusion, this study successfully captures energy absorption trends and keyhole formation mechanisms while reducing computational cost. By refining the approach to account for vapor pressure effects and melt pool flow dynamics, the model can be further improved to provide a more comprehensive simulation of laser welding across different power regimes.

6. General conclusion

6.1. Summary

This thesis explores the possibility of simplifying the complexity of modelling the conduction-based laser melting/welding process. This is achieved by replacing the phase change and flow movement of the material with an isotropic enhancement of temperature-dependent thermal conductivity. Additionally, the model has been expanded to simulate mixed-mode and keyhole-based laser welding by integrating a keyhole-formation function. Unlike conventional models that explicitly track phase transitions and melt pool fluid dynamics, this approach maintains the material in a single state throughout the simulation while still yielding satisfactory results.

The developed model is designed to be applicable across a range of laser welding scenarios with different power levels and welding modes. It has been validated against experimental data for laser powers ranging from 300 W to 1200 W, successfully capturing the transition from conduction-based to keyhole-based laser welding. The model effectively predicts melt pool width during conduction-mode welding and melt pool depth during keyhole-mode welding, demonstrating its capability in simulating energy absorption and distribution trends.

One of the key advantages of this approach is its ability to maintain computational efficiency while providing reasonable accuracy. The model achieves this by incorporating temperature-dependent thermal conductivity enhancement and high laser absorption rates (60–90%), compensating for the absence of explicit latent heat effects. While this simplification improves processing speed and reduces computational demand, the model's transferability depends on key factors such as material properties, laser wavelength, and beam profile. It is particularly suited for materials with similar optical and thermal properties to those studied, but further calibration may be required for highly reflective materials like Aluminium or for non-metallic materials.

The model has been compared with existing high-fidelity CFD-based simulations, which incorporate melt pool dynamics, vapor recoil pressure, and Marangoni convection. While these models achieve higher accuracy, they also demand significantly more computational power and longer simulation times. In contrast, the proposed model provides a computationally efficient alternative, offering a balance between accuracy and speed.

In terms of melt pool shape prediction, the model successfully captures the width of the melt pool during conduction-based laser welding but shows some discrepancies in predicting depth. Conversely, in keyhole-mode welding, it is able to predict melt pool depth while minor variations exist between modelled and measured width predictions. This trade-off is expected as the model simplifies some of the complex fluid interactions to enhance computational efficiency.

Overall, the developed model provides an efficient and adaptable approach to laser welding simulation, making it useful for scenarios where rapid computational results are required. While it may not fully replace high-fidelity CFD models for detailed melt pool analysis, it serves as a practical tool for process optimization and energy distribution studies, offering a compromise between accuracy and computational efficiency.

All Ansys Parametric Design Language (APDL) code developed during the project and described in the thesis is available on request. If required, the code includes a function to capture and store data and screenshots throughout the whole simulation process.

6.2. Findings

The following summarises the findings of this work:

- An increase in laser power enlarges the size of the melt pool, while an increase in traverse speed reduces its size.
- Isotropic enhancement of temperature dependent thermal conductivity has been proven feasible. In the simulation of conduction-based laser welding (200 W – 250 W), the results generated closely matched the experimental outcomes.
- The isotropic enhancement method was also applied in simulations involving mixed-mode and keyhole-based laser welding. The results demonstrated good accuracy in depth prediction but slightly inaccuracies in width prediction.
- After an extensive data-gathering process, the trend concerning the energy distribution ratio as laser welding progresses from conduction-based to keyhole-based has been identified and presented in Figure 108 and Figure 109.

6.3. Future work recommendation

At the time of writing, flaws and opportunities for further improvement in the model still exist. Therefore, the following recommendations are suggested for future work:

- The feasibility of using isotropic enhancement method to replace phase change and flow movement in simulating the expansion of the melt pool has been proven. Currently, the isotropic enhancement factor used is a constant factor, future work should explore a temperature-dependent isotropic enhancement factor, considering that the flow strength (e.g. Marangoni flow) within the melt pool changes with temperature.

- The simulation of keyhole formation without involving phase change has yielded satisfactory results. However, the model could only produce closely matched results, not an exact match with the experimental results. Further work is needed to improve the accuracy of the model's prediction capability.
- While the current model effectively predicts key thermal trends, future improvements could involve incorporating latent heat effects to further refine its accuracy, particularly for predicting melt pool depth in keyhole mode.
- Integrating semi-empirical corrections for keyhole dynamics could enhance the model's applicability across a broader range of materials and laser parameters.
- The cross-sectional shape of the melt pool generated by the model does not perfectly match the experimental results. Due to time constrain in this project, not much effort has been put into advancing the functions dedicated to heat flux application during the simulation process, resulting in a slightly inaccurate cross-sectional shape. Future work should consider improvements in the function dedicated to heat flux application.
- The logic and reasoning used during the development of this model still require further improvement as some flaws were discovered in the process of data gathering, especially when laser power ranges between 300 W and 500 W are used. This laser power range is crucial as it covers the transition from conduction-based towards keyhole-based laser welding.
- The model and its findings have been developed and validated on a single experimental system using one material and a limited range of laser parameters. To assess the generalizability and robustness of the approach, future studies should apply the model across diverse systems, materials, and broader parameter ranges.

References

1. Prashanth Konda Gokuldoss. (2020). Selective Laser Melting: Materials and Applications. Journal of Manufacturing and Materials Processing. 4 (1).

2. Néstor Catalán, Esteban Ramos-Moore, Adrian Boccardo and Diego Celentano (2022). Surface Laser Treatment of Cast Irons: A Review. Metals. 12 (4): p. 562.

3. João Pedro Oliveira and Zhi Zeng (2020). Laser Welding. Pub. MDPI - Multidisciplinary Digital Publishing Institute.

4. Torkamany M. J., Malek Ghaini F., Poursalehi R. (2015). An insight to the mechanism of weld penetration in dissimilar pulsed laser welding of niobium and Ti–6Al–4V. Optics & Laser Technology. 79: p. 100-107.

5. Torkamany M. J., Malek Ghaini F., Poursalehi R., Kaplan A.F.H. (2015). Combination of laser keyhole and conduction welding: Dissimilar laser welding of niobium and Ti-6Al-4V. Optics and Lasers in Engineering. 79: p. 9-15.

6. Udaya Kumar G.; Sivan Suresh; Sujith Kumar C.S.; Seunghyun Back; Bongchul Kang; Hee Joon Lee (2020). Applied Thermal Engineering. 174: 115274.

7. Dutta Majumdar J. and Indranil Manna (2011). Laser material processing. International materials reviews. 56 (5-6): p. 48.

8. Amy M. Elliott and Cindy Waters (2019). Additive Manufacturing for Designers - A Primer. SAE International.

9. Flemmer J., Pirch N., Gasser A., Wissenbach K., Kelbassa I. and Witzel J. (2014). LMDCAM, Computer Aided Manufacturing (CAM) Solution for Tool Path Generation for Build-up of Complex Aerospace Components by Laser Metal Deposition (LMD). Lasers in Eng. 28(5-6): p. 279-287.

10. Dinda G.P., Dasgupta A.K., Mazumderb J. (2009). Laser aided direct metal deposition of Inconel 625 superalloy: Microstructural evolution and thermal stability. Materials Science and Engineering A. 509: p. 98-104.

11. Andrew J Pinkerton, Wang W., and Li L (2008). Component repair using laser direct metal deposition. Proc. IMechE Vol. 222 Part B: J. Engineering Manufacture. 222: p. 827-836.

12. Ali K. Krumani (2014). Direct Laser Deposition for Re-Manufacturing of Components: p. 5.

13. Khalid Mahmood, Waheed Ul Haq Syed, Andrew J. Pinkerton (2010). Innovative reconsolidation of carbon steel machining swarf by laser metal deposition. Optics and Lasers in Engineering. 49: p. 240-247.

14. Khalid Mahmooda, Nicholas Stevensb, Andrew J. Pinkertona (2012). Laser surface modification using Inconel 617 machining swarf as coating material. Journal of Materials Processing Technology. 212: p. 1271-1280.

15. Renyao Qin, Xuejun Zhang, Shaoqing Guo, Bingbing Sun, Siyi Tang, Wanqing Li (2015). Laser cladding of high Co–Ni secondary hardening steel on 18Cr2Ni4WA steel. Surface & Coatings Technology. 285: p. 242-248.

16. Igor Shishkovsky, Igor Smurov (2012). Titanium base functional graded coating via 3D laser cladding. Materials Letters. 73: p. 32-35.

17. Waheed Ul Haq Syed, Andrew J. Pinkerton, Lin Li (2005). Combining wire and coaxial powder feeding in laser direct metal deposition for rapid prototyping. Applied Surface Science. 252: p. 4803-4808.

18. Kai Zhang, Xiaofeng Shang and Weijun Liu (2011). Laser Metal Deposition Shaping System for Direct Fabrication of Parts. Applied Mechanics and Materials. 66-68: p. 2202-2207.

19. Waheed Ul Haq Syed, Andrew J. Pinkerton, Zhu Liu, Lin Li (2007). Coincident wire and powder deposition by laser to form compositionally graded material. Surface & Coatings Technology. 201: p. 7083-7091.

20. Mehdi Soodi, Masood S.H. and Milan Brandt (2013). Thermal expansion of functionally graded and wafer-layered structures produced by laser direct metal deposition. Int J Adv Manuf Technol. 69: p. 2011-2018.

21. Abioye T.E., Farayibi P.K. and Clare A.T. (2015). Functionally graded Ni-Ti microstructures synthesised in process by direct laser metal deposition. Int J Adv Manuf Technol. 79: p. 843-850.

22. Mehdi Soodi, Syed H. Masood and Milan Brandt (2014). Tensile strength of functionally graded and wafer layered structures produced by direct metal deposition. Rapid Prototyping Journal. 20/5: p. 360-368.

23. Pratik R. Halani and Yung C. Shin (2011). In Situ Synthesis and Characterization of Shape Memory Alloy Nitinol by Laser Direct Deposition. Metallurgical and Materials Transactions A 43(2): p. 650-657.

24. Andrew J. Pinkerton (2015), Lasers in additive manufacturing. Optics & Laser Technology. 78: p. 25-32.

25. Donald Krantz, Sylvia Nasla, Jeff Byme, Brian Rosenberger (2001). On-Demand Spares Fabrication During Space Missions Using Laser Direct Metal Deposition. Space Technology and Applications Infernational Forum: p. 170-175.

26. Benjamin Vayre, Frédéric Vignat, François Villeneuve (2012). Metallic additive manufacturing: state-of-the-art review and prospects. Mechanics & Industry. 13(2): p. 89-96.

27. Cui C.Y., Cui X.G., Zhang Y.K., Luo K.Y., Zhao Q., Hu J.D., Liu Z., Wang Y.M. (2010). Microstructure and microhardness analysis of the hexagonal oxides formed on the surface of the AISI 304 stainless steel after Nd:YAG pulsed laser surface melting. Applied Surface Science. 256: p. 6782-6786.

28. Ziheng Wu, Guannan Tang, Samuel J. Clark, Andrey Meshkov, Subhrajit Roychowdhury, Benjamin Gould, Victor Ostroverkhov, Thomas Adcock, Steven J. Duclos, Kamel Fezzaa, Christopher Immer & Anthony D. Rollett (2023). High frequency beam oscillation keyhole dynamics in laser melting revealed by in-situ x-ray imaging. Communications Materials 4(1): p. 10.

29. Mallikarjuna Balichakra, Prasad Krishna, Vamsi Krishna Balla, Mitun Das and Srikanth Bontha (2016). Understanding Thermal Behavior in Laser Processing of Titanium Aluminide Alloys, in Proceedings of 6th International & 27th All India Manufacturing Technology, Design and Research Conference (AIMTDR-2016): College of Engineering, Pune, Maharashtra, INDIA. p. 5.

30. Zhou L., Li Z.Y., Song X.G., Tan C.W., He Z.Z., Huang Y.X., Feng J.C. (2017). Influence of laser offset on laser welding-brazing of Al/brass dissimilar alloys. Journal of Alloys and Compounds (e92). 717: p. 78-92.

31. Baoye Wu, Peng Liu, Xizhao Wang, Fei Zhang, Leimin Deng, Jun Duan, Xiaoyan Zeng (2017). Effect of laser absorption on picosecond laser ablation of Cr12MoV mold steel, 9Cr18 stainless steel and H13A cemented carbide. Optics and Laser Technology. 101: p. 11-20.

32. Shanmugarajan B., Chary J.N., Padmanabham G., Arivazhagan B., Shaju K. Albert, Bhaduri A.K. (2013). Studies on autogenous laser welding of type 304B4 borated stainless steel. Optics and Lasers in Engineering. 51: p. 1272-1277.

33. Jie Xu, Yi Luo, Liang Zhu, Jingtao Han, Chengyang Zhang, Dong Chen (2018). Effect of shielding gas on the plasma plume in pulsed laser welding. Measurement. 134: p. 25-32.

34. Masanori Miyagi, Jiye Wang (2020). Keyhole dynamics and morphology visualized by in-situ X-ray imaging in laser melting of austenitic stainless steel. Journal of Materials Processing Tech. 116673. 282(1): p. 9.

35. Wang X.-N., Chen X.-M., Sun Q., Di H.-S., Sun Li-N. (2017). Formation mechanism of δ-ferrite and metallurgy reaction in molten pool during press-hardened steel laser welding. Materials Letters. 206: p. 143-145.

36. Xiao-Long Gao, Lin-Jie Zhang, JingLiu, Jian-Xun Zhang (2012). A comparative study of pulsed Nd:YAG laser welding and TIG welding of thin Ti6Al4V titanium alloy plate. Materials Science & Engineering: A. 559: p. 14-21.

37. Pengfei Wang, Xizhang Chen, Qiuhong Pan, Bruce Madigan & Jiangqi Long (2016). Laser welding dissimilar materials of aluminum to steel: an overview. The International Journal of Advanced Manufacturing Technology. 87: p. 3081-3090.

38. Tri Le-Quang, Neige Faivre, Farzad Vakili-Farahani, Kilian Wasmer (2021). Energy-efficient laser welding with beam oscillating technique – A parametric study. Journal of Cleaner Production. 313: p. 11.

39. Zhenguo Jiang, Xi Chen, Kun Yu, Zhenglong Lei, Yanbin Chen, Shibo Wu, Zhijun Li (2019). Improving fusion zone microstructure inhomogeneity in dissimilar-metal welding by laser welding with oscillation. Materials Letters. 261: p. 4.

40. Naveed Ahsan M., Christ P. Paul, Kukreja L.M., Andrew J. Pinkerton (2010). Porous structures fabrication by continuous and pulsed laser metal deposition for biomedical applications; modelling and experimental investigation. Journal of Materials Processing Technology. 211: p. 602-609.

41. Eurico Assuncao, Stewart Williams (2013). Comparison of continuous wave and pulsed wave laser welding effects. Optics and Lasers in Engineering. 51: p. 674-680.

42. Besnea Daniel, Octavian Dontu, Mihai Avram, Alina Spanu, Ciprian Rizescu and Pascu Adrian (2016). Study on laser welding of stainless steel/copper dissimilar materials, in 7th International Conference on Advanced Concepts in Mechanical Engineering. IOP Conference Series Materials Science and Engineering 147(1): p. 8.

43. Panagiotis Karmiris-Obratański, Emmanouil-Lazaros Papazoglou, Nikolaos Karkalos, Elias Hontzopoulos and Angelos P. Markopoulos (2021). On the laser beam absorption efficiency in laser welding of aluminium thin sheet with copper pipe, in The 25th Edition of IManEE 2021 International Conference (IManEE 2021). p. 6.

44. Josefine Svenungsson, Isabelle Choquet, Alexander F. H. Kaplan (2015). Laser welding process – a review of keyhole welding modelling. Physics Procedia. 78: p. 182-191.

45. Andrew J. Pinkerton (2014). Advances in the modeling of laser direct metal deposition. Journal of Laser Applications. 27: p. 8.

46. Bedenko D.V. and Kovalev O.B. (2013). Modelling of heat and mass transfer in the laser cladding during direct metal deposition. Thermophysics and Aeromechanics. 20(2): p. 251-261.

47. Haug P., Rominger V., Speker N., Weber R., Graf T., Weigl M., Schmidt M. (2013). Influence of Laser Wavelength on Melt Bath Dynamics and Resulting Seam Quality at Welding of Thick Plates. Physics Procedia. 41: p. 49-58.

48. Rudolf Weber, Andreas Michalowski, Marwan Abdou-Ahmed, Volkher Onuseit, Volker Rominger, Martin Kraus, Thomas Graf (2011). Effects of Radial and Tangential Polarization in Laser Material Processing. Physics Procedia. 12 (1): p. 21-30.

50. Grabowski A., Lisiecki A., Dyzia M., Łabaj J., Stano S. (2022). The effect of laser wavelength on surface layer melting of the AlSi/SiC composite. Journal of manufacturing processes. 75: p. 627-636.

51. Yih-Fong Tzeng (2000). Effects of operating parameters on surface quality for the pulsed laser welding of zinc-coated steel. Journal of materials processing technology. 100 (1): p. 163-170.

52. Tsung-Yuan Kuo (2005). Effects of pulsed and continuous Nd-YAG laser beam waves on welding of Inconel alloy. Science and technology of welding and joining. 10 (5): p. 557-565.

53. Julio Coroado, Supriyo Ganguly, Stewart Williams, Wojciech Suder, Sonia Meco, Goncalo Pardal (2022). Comparison of continuous and pulsed wave lasers in keyhole welding of stainless-steel to aluminium. International journal of advanced manufacturing technology. 119 (1-2): p. 367-387.

54. Shakeel Safdar, Lin Li, Mohammed Aslam Sheikh (2007). Numerical analysis of the effects of non-conventional laser beam geometries during laser melting of metallic materials. Journal of physics. D, Applied physics. 40 (2): p. 593-603.

55. Mohammed Aslam Sheikh, Li L (2010). Understanding the effect of non-conventional laser beam geometry on material processing by finite-element modelling. Proceedings of the Institution of Mechanical Engineers. Part C, Journal of mechanical engineering science. 224 (5): p. 1061-1072.

56. Alireza Karimi, Arash Karimipour, Mohammad Akbari, Mohammad Mehdi Razzaghi, Mehdi Jamali Ghahderijani (2023). Investigating the mechanical properties and fusion zone microstructure of dissimilar laser weld joint of duplex 2205 stainless steel and A516 carbon steel. Optics and laser technology. 158: p. 12.

57. Salminen Antti , Piili Heidi , Purtonen Tuomas (2010). The characteristics of high power fibre laser welding. Proceedings of the Institution of Mechanical Engineers. Part C, Journal of mechanical engineering science. 224 (5): p. 11.

58. Cui C.Y., Cui X.G., Zhang Y.K., Zhao Q., Lu J.Z., Hu J.D., Wang Y.M. (2011). Microstructure and corrosion behavior of the AISI 304 stainless steel after Nd:YAG pulsed laser surface melting. Surface & Coatings Technology. 206: p. 1146-1154.

59. Cui C. Y., Hu J.D., Liu Y. H. and Guo Z. X. (2008). Microstructure and mechanical properties of stainless steel under Nd:YAG pulsed laser irradiation. Materials Science and Technology. 24: p. 964-968.

60. Amir Hossein Faraji, Massoud Goodarzi, Seyed Hossein Seyedein and Carmine Maletta (2015). Effects of welding parameters on weld pool characteristics and shape in hybrid laser-TIG welding of AA6082 aluminum alloy: numerical and experimental studies. Weld World. 60: p. 137-151.

61. Dongdong Gu, Donghua Dai (2016). Role of melt behavior in modifying oxidation distribution using an interface incorporated model in selective laser melting of aluminum-based material. Journal of Applied Physics. 120: p. 11.

62. Kalinga Simant Bal, Jyotsna Dutta Majumdar, Asimava Roy Choudhury (2023). Melting efficiency calculation of “finite-element-modeled” weld-bead and “experimental” weld-bead for laser-irradiated Hastelloy C-276 sheet. Welding in the World. 67: p. 1509-1526.

63. Yassine Saadlaoui, Julien Sijobert, Maria Doubenskaia, Philippe Bertrand, Eric Feulvarch and Jean-Michel Bergheau (2020). Experimental Study of Thermomechanical Processes: Laser Welding and Melting of a Powder Bed. Crystals: p. 246-265.

64. Yi Luo, Liang Zhu, Jingtao Han, Jie Xu, Chengyang Zhang, Dong Chen (2019). Effect of focusing condition on laser energy absorption characteristics in pulsed laser welding. Optics and Laser Technology. 117: p. 52-63.

65. Clare McDaniel, Aiden Flanagan, Gerard M. O’ Connor (2014). Evidence for increased incubation parameter in multi-pulse ablation of a Pt:SS alloy using a femtosecond laser at high repetition rates. Applied Surface Science. 295: p. 1-7.

66. Campbell S. W., Galloway A. M. and McPherson N. A. (2013). Arc pressure and fluid flow during alternating shielding gases. Part 2: arc force determination. Science and Technology of Welding and Joining. 18: p. 597-602.

67. Charles D. Boley, Mitchell S. C., Alexander M Rubenchik, S. S. Q. Wu (2016). Metal powder absorptivity: modeling and experiment. Applied Optics 2016. 55 (23): p. 6496-6500.

68. Maeji T., Ibano K., Yoshikawa S., Inoue D., Kuroyanagi S., Mori K., Hoashi E., Yamanoi K., Sarukura N., Ueda Y. (2017). Laser energy absorption coefficient and in-situ temperature measurement of laser-melted tungsten. Fusion engineering and design. 124: p. 287-291.

69. Germán O. Barrionuevo, Pedro M. Sequeira-Almeida, Sergio Ríos, Jorge A. Ramos-Grez, Stewart W. Williams (2022). A machine learning approach for the prediction of melting efficiency in wire arc additive manufacturing. The International Journal of Advanced Manufacturing Technology. 120: p. 3123-3133.

70. Ashok Pandarinath Tadamalle, Reddy Y.P., Ramjee E., Reddy V.K. (2014). Influence of welding speed on the melting efficiency of Nd:YAG laser welding. Advances in Production Engineering & Management. Volume 9, Number 3: p. 128-138.

71. Hongze Wang, Motoki Nakanishi, Yosuke Kawahito (2017). Effects of welding speed on absorption rate in partial and full penetration welding of stainless steel with high brightness and high power laser. Journal of Materials Processing Tech. 249: p. 193-201.

72. Yousuke Kawahito, Naoyuki Matsumoto, Youhei Abe & Seiji Katayama (2011). Laser absorption characteristics in high-power fibre laser welding of stainless steel. Welding International. 27:2: p. 129-135.

73. Binqi Liu, Gang Fang, Liping Lei (2020). An analytical model for rapid predicting molten pool geometry of selective laser melting (SLM). Applied Mathematical Modelling. 92: p. 505-524.

74. Bao Hu, Shengsun Hu, Junqi Shen, Yang Li (2014). Modeling of keyhole dynamics and analysis of energy absorption efficiency based on Fresnel law during deep-penetration laser spot welding. Computational Materials Science. 97: p. 48-54.

75. Komkamol Chongbunwatana (2014). Simulation of vapour keyhole and weld pool dynamics during laser beam welding. Production Engineering Res. Devel. 8: p. 499-511.

76. Yousuke Kawahito, Naoyuki Matsumoto, Youhei Abe, Seiji Katayama (2011). Relationship of laser absorption to keyhole behavior in high power fiber laser welding of stainless steel and aluminum alloy. Journal of Materials Processing Technology. 211: p. 1563-1568.

77. Amin Ebrahimi, Mohammad Sattari, Scholte J.L. Bremer, Martin Luckabauer, Gert-willem R.B.E. Römer, Ian M. Richardson, Chris R. Kleijn, Marcel J.M. Hermans (2022). The influence of

laser characteristics on internal flow behaviour in laser melting of metallic substrates. Materials & Design 110385. 214: p. 14.

78. Wenjun Ge, Jerry Y.H. Fuh, Suck Joo Na (2021). Numerical modelling of keyhole formation in selective laser melting of Ti6Al4V. Journal of Manufacturing Processes. 62: p. 646-654.

79. Deepak Shah, Alexey N. Volkov (2019). Combined Smoothed Particle Hydrodynamics - Ray Tracing Method for Simulations of Keyhole Formation in Laser Melting of Bulk and Powder Metal Targets, in International Mechanical Engineering Congress and Exposition IMECE2019: Salt Lake City, UT, USA. p. 8.

80. Wenda Tan, Neil S Bailey and Yung Shin (2013). Investigation of keyhole plume and molten pool based on a three-dimensional dynamic model with sharp interface formulation. Journal of Physics D: Applied Physics. 46: p. 12.

81. Quan Nguyen, Ching-yu Yang (2016). A modified Newton–Raphson method to estimate the temperature-dependent absorption coefficient in laser welding process. International Journal of Heat and Mass Transfer. 102: p. 1222-1229.

82. Waheed Ul Haq Syed, Andrew J. Pinkerton, Zhu Liu, Lin Li (2007). Single-step laser deposition of functionally graded coating by dual ‘wire–powder’ or ‘powder–powder’ feeding—A comparative study. Applied Surface Science. 253: p. 7926-7931.

83. Shaoyi Wen, Yung C. Shin (2011). Modeling of transport phenomena in direct laser deposition of metal matrix composite. International Journal of Heat and Mass Transfer. 54: p. 5319-5326.

84. Anton Kidess, Sasa Kenjeres, Bernhard W. Righolt, Chris R. Kleijn (2016). Marangoni driven turbulence in high energy surface melting processes. International Journal of Thermal Sciences. 104: p. 412-422.

85. Amir Hossein Faraji, Massoud Goodarzi, Seyed Hossein Seyedein, Giuseppe Barbieri & Carmine Maletta (2014). Numerical modeling of heat transfer and fluid flow in hybrid laser–TIG welding of aluminum alloy AA6082. The International Journal of Advanced Manufacturing Technology. 77: p. 2067-2082.

86. Shengyong Pang, Weidong Chen, Jianxin Zhou, Dunming Liao (2014). Self-consistent modeling of keyhole and weld pool dynamics intandem dual beam laser welding of aluminum alloy. Journal of Materials Processing Technology. 217: p. 131-143.

87. Saldi Z.S., Kidess A., Kenjereš S., Zhao C., Richardson I.M., Kleijn C.R. (2013). Effect of enhanced heat and mass transport and flow reversal during cool down on weld pool shapes in laser spot welding of steel. International Journal of Heat and Mass Transfer. 66: p. 879-888.

88. Yong-Hao Siao, Chang-Da Wen (2021). Examination of molten pool with Marangoni flow and evaporation effect by simulation and experiment in selective laser melting. International Communications in Heat and Mass Transfer. 125: p. 11.

89. Zhang Y. N., Xinjin Cao and Wanjara P. (2013). Microstructure and hardness of fiber laser deposited Inconel 718 using filler wire. Int J Adv Manuf Technol. 69: p. 2569-2581.

90. Eurico Assuncao, Stewart Williams, David Yapp (2012). Interaction time and beam diameter effects on the conduction mode limit. Optics and Lasers in Engineering. 50: p. 823-828.

91. Ross Cunningham, Cang Zhao, Niranjan Parab, Christopher Kantzos, Joseph Pauza, Kamel Fezzaa, Tao Sun, Anthony D. Rollett (2019). Keyhole threshold and morphology in laser melting revealed by ultrahigh-speed x-ray imaging. Science. 363: p. 849-852.

92. Xianfeng Xiao, Yanshu Fu, Xiaojun Ye, Manping Cheng, Lijun Song (2021). Analysis of heat transfer and melt flow in conduction, transition, and keyhole modes for CW laser welding. Infrared Physics & Technology. 120: p. 12.

93. Renping Wang, Yongping Lei, Yaowu Shi (2010). Numerical simulation of transient temperature field during laser keyhole welding of 304 stainless steel sheet. Optics & Laser Technology. 43: p. 870-873.

94. Ming Wei, Wen Jun Ding, Guglielmo Vastola, Yong-Wei Zhang (2022). Quantitative study on the dynamics of melt pool and keyhole and their controlling factors in metal laser melting. Additive Manufacturing. 54: p. 10.

95. Le K.Q., Tang C., Wong C.H. (2019). On the study of keyhole-mode melting in selective laser melting process. International Journal of Thermal Sciences. 145: p. 9.

96. Ramesh Roop Rai, Elmer J. W., Todd A Palmer and Tarasankar Debroy (2007). Heat transfer and fluid flow during keyhole mode laser welding of tantalum, Ti–6Al–4V, 304L stainless steel and vanadium. Journal of Physics D: Applied Physics. 40: p. 15.

97. Shengyong Pang, Xin Chen, Jianxin Zhou, Xinyu Shao, Chunming Wang (2015). 3D transient multiphase model for keyhole, vapor plume, and weld pool dynamics in laser welding including the ambient pressure effect. Optics and Lasers in Engineering. 74: p. 47-58.

98. Sohail Muhammad, Sang-Woo Han, Suck-Joo Na, Andrey Gumenyuk & Michael Rethmeier (2014). Characteristics of weld pool behavior in laser welding with various power inputs. Weld World. 58: p. 269-277.

99. Yilin Wang, Ping Jiang, Jintian Zhao, Shaoning Geng, Boan Xu (2021). Effects of energy density attenuation on the stability of keyhole and molten pool during deep penetration laser welding process: A combined numerical and experimental study. International Journal of Heat and Mass Transfer 176(50): p. 13.

100. Alessandro Franco, Luca Romoli, Alessandro Musacchio (2014). Modelling for predicting seam geometry in laser beam welding of stainless steel. International Journal of Thermal Sciences. 79: p. 194-205.

101. Shakeel Safdar, Andrew J. Pinkerton, Lin Li, Mohammed A. Sheikh, Philip J. Withers (2012). An anisotropic enhanced thermal conductivity approach for modelling laser melt pools for Ni-base super alloys. Applied Mathematical Modelling. 37: p. 1187-1195.

102. Shuhai Chen, Jihua Huang, Jun Xia, Xingke Zhao, Sanbao Lin (2015). Influence of processing parameters on the characteristics of stainless steel/copper laser welding. Journal of Materials Processing Technology. 222: p. 43-51.

103. Niyanth Sridharan, Anil Chaudhary, Peeyush Nandwana, and Sudarsanam Suresh Babu (2016). Texture Evolution During Laser Direct Metal Deposition of Ti-6Al-4V. JOM. 68: p. 772-777.

104. Sudip Bhattacharya, Guru P. Dinda, Dasgupta A.K., Jyoti Mazumder (2010). Microstructural evolution of AISI 4340 steel during Direct Metal Deposition process. Materials Science and Engineering A. 528: p. 2309-2318.

105. Garrett J. Marshall, Joseph Young W., Scott M Thompson, Nima Shamsaei, Steve R Daniewicz, and Shuai Shao (2016). Understanding the Microstructure Formation of Ti-6Al-4V During Direct Laser Deposition via In-Situ Thermal Monitoring. JOM. Vol. 68, No. 3: p. 778-790.

106. Tian X.J., Zhang S.Q., Wang H.M. (2014). The influences of anneal temperature and cooling rate on microstructure and tensile properties of laser deposited Ti–4Al–1.5Mn titanium alloy. Journal of Alloys and Compounds. 608: p. 95-101.

107. Sudip Bhattacharya, Guru P. Dinda, Ashish K. Dasgupta, Jyoti Mazumder (2013). A comparative study of microstructure and mechanical behavior of CO2 and diode laser deposited Cu–38Ni alloy. J Mater Sci. 49: p. 2415-2429.

108. Amir Reza Ansari Dezfoli, Weng-Sing Hwang, Wei-Chin Huang & Tsung-Wen Tsai (2017). Determination and controlling of grain structure of metals after laser incidence: Theoretical approach. Scientific Reports. 7(1): p. 11.

109. Grigoryants A.G., Shiganov I.N., Misyurov A.I., Melnikov D.M., Kholopov A.A., Shtereverya D.S. (2021). Features of laser impact treatment application with low-energy sources to reduce residual tensile stresses in the welds of aluminium alloys. Welding international. 35 (10-12): p. 389-396.

110. Xinjin Cao, Benjamin Rivaux, Mohammad Jahazi, Jonathan Cuddy, Birur A. (2009). Effect of pre- and post-weld heat treatment on metallurgical and tensile properties of Inconel 718 alloy butt joints welded using 4 kW Nd:YAG laser. Journal of Materials Science. 44 (17): p. 4557-4571.

111. Hebble T. L., David S. A., Vitek J. M., Reed R. W. (1987). Effect of Rapid Solidification on Stainless Steel Weld Metal Microstructures and Its Implications on the Schaeffler Diagram. Welding Journal. 66.

112. Mingming Ma, Zemin Wang, Xiaoyan Zeng (2017). A comparison on metallurgical behaviors of 316L stainless steel by selective laser melting and laser cladding deposition. Materials Science & Engineering A. 685: p. 265-273.

113. Moat R.J., Andrew J. Pinkerton, Li L., Withers P.J., Preuss M. (2011). Residual stresses in laser direct metal deposited Waspaloy. Materials Science and Engineering A. 528: p. 2288-2298.

114. Mallikarjuna Balichakra, Srikanth Bontha, Prasad Krishna and Vamsi Krishna Balla (2019). Laser surface melting of γ-TiAl alloy: an experimental and numerical modeling study. Materials Research Express. 6: p. 9.

115. Sun G.F., Liu C.S., Lijun Song, and Jyoti Mazumder (2010). Microstructure and Wear Behavior of Laser-Aided Direct Metal Deposited Co-285 and Co-285 +WC Coatings. Metallurgical and Materials Transactions A 41(6): p. 1592-1603.

116. Long R.-S., Sun S., Zhenzhong Lian (2016). Crack restriction mechanism of thin wall metal parts fabricated by laser direct deposition shaping. Materials Science and Technology. 32(6): p. 523-539.

117. Labudovic M., Hu D., Radovan Kovacevic (2003). A three dimensional model for direct laser metal powder deposition and rapid prototyping. Journal of Materials Science. 38: p. 35-49.

118. Syed H. Riza, Masood S. H., Cuie Wen, Dong Ruan, Shanqing Xu (2014). Dynamic behaviour of high strength steel parts developed through laser assisted direct metal deposition. Materials and Design. 64: p. 650-659.

119. Jie Liu, Martin Dahmen, Volker Ventzke, Nikolai Kashaev, Reinhart Poprawe (2013). The effect of heat treatment on crack control and grain refinement in laser beam welded β-solidifying TiAl-based alloy. Intermetallics. 40: p. 65-70.

120. Myriam Gharbi, Patrice Peyre, Cyril Gorny, Muriel Carin, Simon Morville, Philippe Le Masson, Denis Carron, Rémy Fabbro (2013). Influence of various process conditions on surface finishes induced by the direct metal deposition laser technique on a Ti–6Al–4V alloy. Journal of Materials Processing Technology. 213: p. 791-800.

121. Myriam Gharbi, Patrice Peyre, Cyril Gorny, Muriel Carin, Simon Morville,Philippe Le Masson, Denis Carron, Rémy Fabbro (2014). Influence of a pulsed laser regime on surface finish

induced by the direct metal deposition process on a Ti64 alloy. Journal of Materials Processing Technology. 214: p. 485-495.

122. Lidong Yu, Yang Bai, TianXuan Bian, YunTeng Qu, ZhiWei Xu, Yi Li, Heng Zhang (2023). Influence of laser parameters on corrosion resistance of laser melting layer on C45E4 steel surface. Journal of Manufacturing Processes. 91: p. 1-9.

123. Sayed Hamid Hashemi, Seyed Ali Mousavi, Reza Shoja Razavi, Amin Nourollahi, Ali Ashrafi (2023). Laser surface melting of Al–Co–rare earth (Ce–La) alloys for improving corrosion resistance. Optics & Laser Technology. 162: p. 11.

124. Cui C.Y., Xia C.D., Cui X.G., Zhou J.Z., Ren X.D., Wang Y.M. (2015). Novel morphologies and growth mechanism of Cr2O3 oxide formed on stainless steel surface via Nd: YAG pulsed laser oxidation. Journal of Alloys and Compounds. 635: p. 101-106.

125. Cui C.Y., Cui X.G., Ren X.D., Qi M.J., Hu J.D., Wang Y.M. (2014). Surface oxidation phenomenon and mechanism of AISI 304 stainless steel induced by Nd:YAG pulsed laser. Applied Surface Science. 305: p. 817-824.

126. Adams D.P., Hodges V.C., Hirschfeld D.A., Mark A Rodriguez, McDonald J.P., Paul G Kotula (2013). Nanosecond pulsed laser irradiation of stainless steel 304L: Oxide growth and effects on underlying metal. Surface and Coatings Technology. 222: p. 1-8.

127. Li Z.L., Zheng H.Y., Teh K.M., Liu Y.C., Lim G.C., Seng H.L., Yakovlev N.L. (2009). Analysis of oxide formation induced by UV laser coloration of stainless steel. Applied Surface Science. 256: p. 1582-1588.

128. Arkadiusz J. Anton´czak, Dariusz Kocoń, Maciej Nowak, Paweł Kozioł, Krzysztof M. Abramski (2013). Laser-induced colour marking—Sensitivity scaling for a stainless steel. Applied Surface Science. 264: p. 229-236.

129. László Nánai, Róbert Vajtai, Thomas F. George (1997). Laser-induced oxidation of metals: state of the art. Thin Solid Films. 298: p. 160-164.

130. Lijin Huang, Xueming Hua, Dongsheng Wu, and Fang Li (2019). Experimental Investigation and Numerical Study on the Elimination of Porosity in Aluminum Alloy Laser Welding and Laser–GMA Welding. Journal of Materials Engineering and Performance. 28(3): p. 1618-1627.

131. Vienna, I.A.E.A. (2008). Thermophysical Properties of Materials For Nuclear Engineering: A Tutorial and Collection of Data, Austria: IAEA.

132. Unocic R. R. and DuPont J. N. (2004). Process Efficiency Measurements in the Laser Engineered Net Shaping Process. Metallurgical and Materials Transactions B. 35(1): p. 143-152.

133. Kangda Hao, Geng Li, Ming Gao, Xiaoyan Zeng (2015). Weld formation mechanism of fiber laser oscillating welding ofaustenitic stainless steel. Journal of Materials Processing Technology 225. p. 77-83

134. Yaasin A. Mayi, Morgan Dal, Patrice Peyre, Michel Bellet and Remy Fabbro (2023). Physical mechanisms of conduction-to-keyhole transition in laser welding and additive manufacturing processes. Optics & Laser Technology. 158 (1).

135. Minkailu Kamara, Wang W, Marimuthu S, and Li L (2011). Modelling of the melt pool geometry in the laser deposition of nickel alloys using the anisotropic enhanced thermal conductivity approach. Proceedings of the Institution of Mechanical Engineers Part B Journal of Engineering Manufacture 225(B1): J. Engineering Manufacture. P. 87

136. Sagar Nikam, Hao Wu, Ryan Harkin, Justin Quinn, Rocco Lupoi, Shuo Yin, Shaun McFadden (2022). On the application of the anisotropic enhanced thermal conductivity

approach to thermal modelling of laser-based powder bed fusion processes. Additive Manufacturing 55: 102870.

137. Aritra Ghosh, Dipten Misra, Sanjib Kumar Acharyya (2019). Experimental and Numerical Investigation on Laser Welding of 2205 Duplex Stainless Steel. Lasers in Manufacturing and Materials Processing 6: p. 228–246.

138. Yong-Hao Siao, Chang-Da Wen (2021). Thermal analysis of anisotropic heat conduction model with experimental validation on molten pool during selective laser melting. Materials Today Communications 27: 102425.

139. Shiwen Liu, Haihong Zhu, Gangyong Peng, Jie Yin, Xiaoyan Zeng (2018). Microstructure prediction of selective laser melting AlSi10Mg using finite element analysis. Materials and Design 142: p. 319-328.

140. Ancellotti S., Fontanari V., Molinari A., Iacob E., Bellutti P., Luchin V., Zappini G., Benedetti M. (2019). Numerical/experimental strategies to infer enhanced liquid thermal conductivity and roughness in laser powder-bed fusion processes. Additive Manufacturing 27: p. 552-564.